Séquence d'activité des failles et dynamique du prisme himalayen : apports de la thermochronologie et de la modélisation numérique

Xavier Robert

Université Joseph Fourier - Grenoble - France
Observatoire des Sciences de l'Univers de Grenoble
Laboratoire de Géodynamique des Chaînes Alpines

Thèse

présentée à
l'**Université Joseph Fourier - Grenoble - France**
pour obtenir le grade de
Docteur de l'Université Joseph Fourier - Grenoble - France
spécialité « Sciences de la Terre et de l'Univers »

par

Xavier ROBERT

Séquence d'activité des failles et dynamique du prisme himalayen : apports de la thermochronologie et de la modélisation numérique

Thèse soutenue publiquement le 27 Novembre 2008 devant le jury composé de :

M.	R. Cattin	Géosciences Montpellier	(Rapporteur)
M.	S. Willett	ETH Zürich	(Rapporteur)
M.	J. Braun	Géosciences Rennes	(Examinateur)
M.	A. Pêcher	LGCA Grenoble	(Examinateur)
M.	P. Van der Beek	LGCA Grenoble	(Directeur de thèse)
M.	J.-L. Mugnier	LGCA Grenoble	(Directeur de thèse)

"Nierez-vous qu'on ait trouvé des coquilles sur les montagnes ? Qui les y a mises, sinon le Déluge ? Elles n'ont pas coutume, je crois, de pousser toutes seules dans la terre comme des carottes ! (...) A moins que ce ne soit encore une des découvertes de la science ?"

Gustave Flaubert *dans* ***Bouvard et Pécuchet***

Remerciements

Cette thèse n'aurait jamais abouti sans le soutien scientifique et amical de nombreuses personnes. Je tiens à les remercier ici, et j'espère n'avoir omis personne...

Je voudrais tout d'abord exprimer mes plus profonds remerciements à mes deux encadrants, Jean-Louis et Peter, qui m'ont beaucoup apporté au niveau méthodologique et scientifique pour acquérir le recul nécessaire à la synthèse de ces travaux. Je tiens à noter à la fois leur grande disponibilité pour toute discussion, et leurs nombreux coups de pouces dans les moments de difficultés. J'ai aussi énormément apprécié le rôle qu'ils ont tenu pour m'introduire dans la communauté internationnale de géomorphologie/tectonique récente et m'y confronter.

Merci aussi à Rodolphe Cattin et Sean Willett d'avoir accepter de rapporter cette thèse, ainsi qu'à Jean Braun et Arnaud Pêcher qui ont bien voulu être examinateur de mon travail. J'espère que la lecture de mon manuscrit ne sera pas trop difficile, vous intéressera, et que j'aurai su exprimer ma passion pour ce projet.

Bien entendu, cette thèse n'aurait pu être menée à bien sans l'équipe du LGCA que je remercie beaucoup. Je souhaite mettre en exergue la qualité et la rapidité du travail des secrétaires qui ont tout mis en oeuvre pour me simplifier les tâches administratives, et trouver les meilleurs arrangements possibles. Mes remerciements vont aussi à Erica, Matthias, Bardhyl, François et Françis, sans qui je n'aurais jamais pu mener à bien les datations que j'ai effectuées.

Cette thèse n'aurait pu avoir lieu sans mission de terrain dans des pays dans lesquelles les conditions de travail ne sont pas évidentes. Je remercie Ananta Gajurel pour nous avoir grandement facilité la mission de novembre 2005 au Népal,

ainsi que Djorge Grujic qui a fait son maximum pour organiser et négocier une mission au Bhoutan.

Un autre aspect important a été le volet modélisations numériques. Il a pu être mené grâce à l'investissement de Jean qui a souvent mis la main à la pâte pour résoudre mes problèmes quotidiens, malgré son éloignement. Qu'il en soit ici encore remercié !

Je remercie aussi l'ensemble des chercheurs et des thésards du laboratoire pour les bons moments passés ensemble, au laboratoire, en montagne, en avion, ou dans les bars, ainsi que pour leur aide

Mention spéciale au Vieux Baron, Roi de la Thermodynamique et de la culture générale, qui a supporté mes frasques un peu plus de quatre ans, cinq jours sur sept, ainsi qu'à Kiki, pour sa grande amitié.

Merci aussi à tous les amis de Grenoble, de la LaiTUE, à mes nombreux colocataires et à ma famille !

Je remercie enfin une seconde famille, les fous-furieux des Vulcains et assimilés, avec qui j'ai passé de nombreux moments, des fois difficiles, mais inoubliables, forgeant de solides amitiés. Grâce à eux, j'ai très souvent eu l'occasion de me vider la tête de tous les problèmes temporaires liés à l'avancement de mon projet de thèse.

Grenoble, le 5 décembre 2008.

Table des matières

Introduction

1

Sommaire

Ce chapitre introduit la problématique et donne les éléments géographiques, géologiques et géophysiques nécessaires à la compréhension du manuscrit, du raisonnement et des techniques utilisées.

This chapter introduces the study and provides the geographical, geophysical and geological background necessary to understand the manuscript, the reasoning and the techniques used.

1.1 Approche générale

A la surface du globe, les zones de convergence possèdent des signatures tectoniques, magmatiques et morphologiques qui varient à la fois dans l'espace et dans le temps. Les déformations associées observées actuellement permettent dans certains cas d'évaluer l'état de contraintes (Zoback 1992). Cette dynamique des continents est régie par des forces s'établissant principalement en limite de plaques. Ces moteurs principaux de la tectonique des plaques entrent dans les conditions aux limites responsables de la dynamique continentale (Turcotte et Schubert 1982), et donc de la déformation continentale.

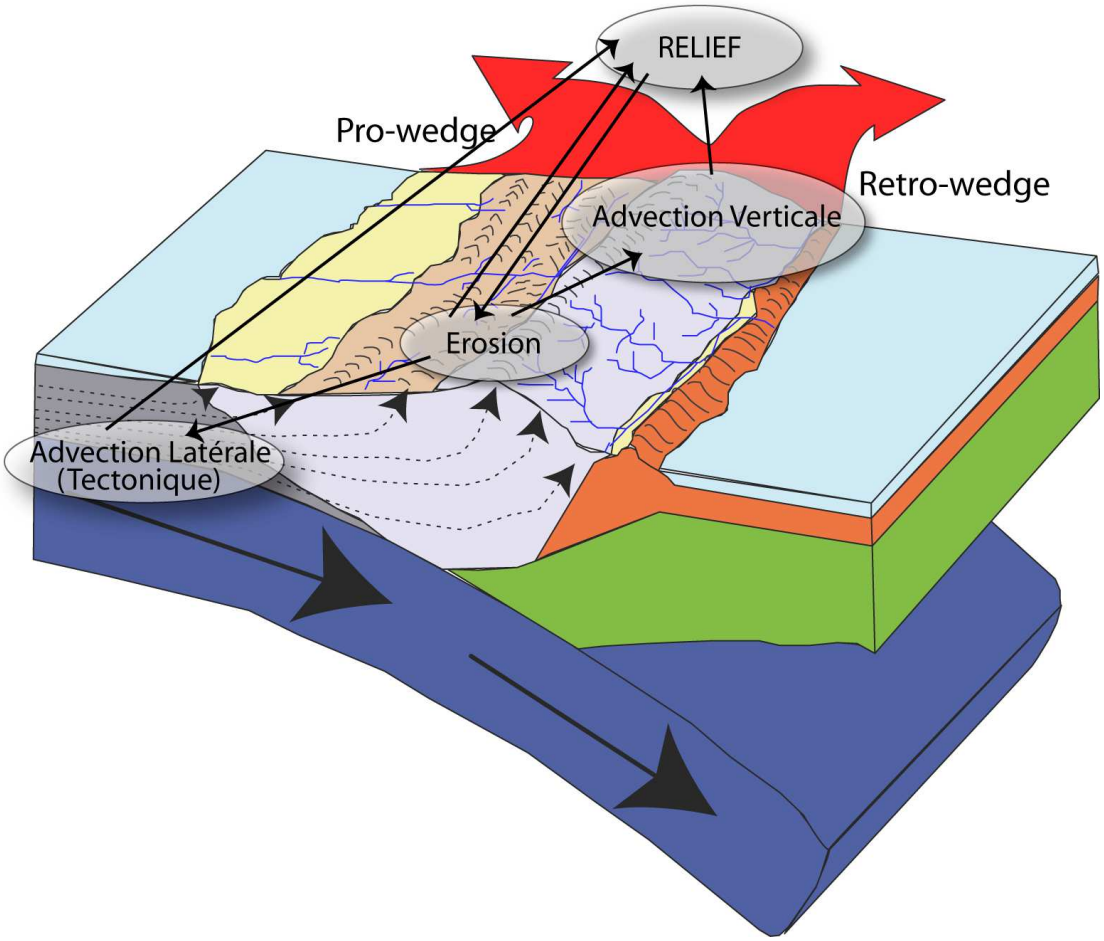

FIG. 1.1 – *Relations entre advections latérale et verticale, relief et érosion au niveau d'un orogène actif. La tectonique (advection latérale et verticale) déplace les masses crustales qui forment des reliefs. Ces reliefs entrainent une augmentation des précipitations sur l'un de leurs côtés (pro-wedge ou retro-wedge), ce qui entraine leur érosion. L'advection verticale (exhumation) est en partie due à la réponse à l'érosion via les méchanismes isostatiques et à la tectonique ; modifié d'après Stolar et al. (2006).*

Or, cette déformation est influencée par la dynamique externe des chaînes de

montagnes via les processus d'érosion et de sédimentation (Burbank (1992), Avouac et Burov (1996), Finlayson et al. (2002) , Fig. 1.1). Il a été mis en évidence dans les Andes, par exemple, que des variations climatiques à grande échelle sont répercutées dans les caractéristiques topographiques (Montgomery et al. 2001). Cependant, des études ont montré la coïncidence des zones d'érosion intense (fortes pentes et précipitations intenses) avec les zones d'exhumation rapide (Finlayson et al. 2002). En effet, l'influence de l'érosion sur la localisation de la déformation dans une chaîne de montagnes est un phénomène souvent envisagé à la suite de modélisations analogiques (Konstantinovskaia et Mallavieille 2005) et numériques (Beaumont et al. 1992, Willett 1999, Beaumont et al. 1999; 2001). Par redistribution des masses de surface, les processus superficiels permettraient des variations de contraintes gravitationnelles et moduleraient donc les flux de matières en profondeur (Beaumont et al. 1992, Avouac et Burov 1996, Beaumont et al. 1994). En conséquence, la structure thermique est modifiée. Par compensation thermique, cette modification permet l'élévation des plus hauts sommets (Zeitler et al. 2001, Koons 1989). D'un autre côté, l'incision rapide et profonde des vallées permet d'élever les plus hauts sommets par réduction de la masse de la chaîne et donc par compensation isostatique (Burbank 1992, Fielding et al. 1994, Masek et al. 1994). Ceci perturbe le système climatique et l'érosion (Molnar et England 1990, Brozovic et al. 1997).

Or, les données géologiques pertinentes en faveur de cette hypothèse sont encore fort peu nombreuses. Nous proposons de tester cette hypothèse en acquérant des données :

1. A une échelle de temps allant du cycle sismique, considéré comme l'incrément de déplacement élémentaire à l'échelle géologique à celle de la déformation finie (de l'ordre du million d'années),
2. Sur un objet géologique soumis à des conditions de déplacements à ses limites simples,
3. Sur un objet géologique soumis à des conditions climatiques et érosives variables latéralement.

La zone externe de l'Himalaya constitue un objet géologique adapté pour tes-

ter cette influence de l'érosion sur la tectonique (Fig. 1.2). Elle est soumise à une convergence continue et de valeur constante depuis plusieurs dizaines de millions d'années (Mugnier et al. 2004, Yin 2006). Elle est en revanche soumise à un gradient climatique d'Est en Ouest (transversalement par rapport à la direction de convergence), variable au cours du temps (Finlayson et al. 2002, Thiede et al. 2004; 2005, Bookhagen et Burbank 2006). Aussi, la mise en évidence d'une évolution temporelle et/ou spatiale (transversalement à la chaîne) de la déformation dans le prisme himalayen constituerait un observable clef pour tester l'influence de l'érosion sur la localisation de la déformation tectonique à l'échelle d'une chaîne de montagnes.

1.2 Géologie et structure de la chaîne himalayenne

1.2.1 Aspects topographiques

En première approche, la chaîne himalayenne présente une structure topographique relativement cylindrique. Du sud au nord, le relief définit plusieurs unités (Fig. 1.3) :

- La plaine du Gange qui est à une altitude de l'ordre de 100 à 200 m, et qui présente un relief très plat.
- Du front de la chaîne à $75 - 100$ km au nord du front, l'altitude augmente régulièrement, avec un relief, calculé sur un rayon 5 km, compris entre 0.5 et 1.5. L'altitude moyenne est de l'ordre de 2000 m (Duncan et al. 2003, Bookhagen et Burbank 2006).
- De 100 à 150 km du front de la chaîne, le relief devient très important, souvent supérieur à 2.5, les pentes sont très fortes. C'est dans cette zone que se situent la majorité des plus hauts sommets de l'Himalaya (supérieurs à 8000 m). L'altitude moyenne est de l'ordre de 5000 m.
- Plus au nord, et ce sur plus de 1000 km, nous repassons à une zone de faible relief, correpondant au plateau du Tibet. En revanche, l'altitude moyenne reste élevée, de l'ordre de 4500 à 5000 m.

Mais cette cylindricité au niveau du relief n'est qu'une première approche. En effet, il faut distinguer deux zones bien différentes, à savoir l'Himalaya central au Népal central et l'Himalaya oriental au Bhoutan. Duncan et al. (2003) montrent que

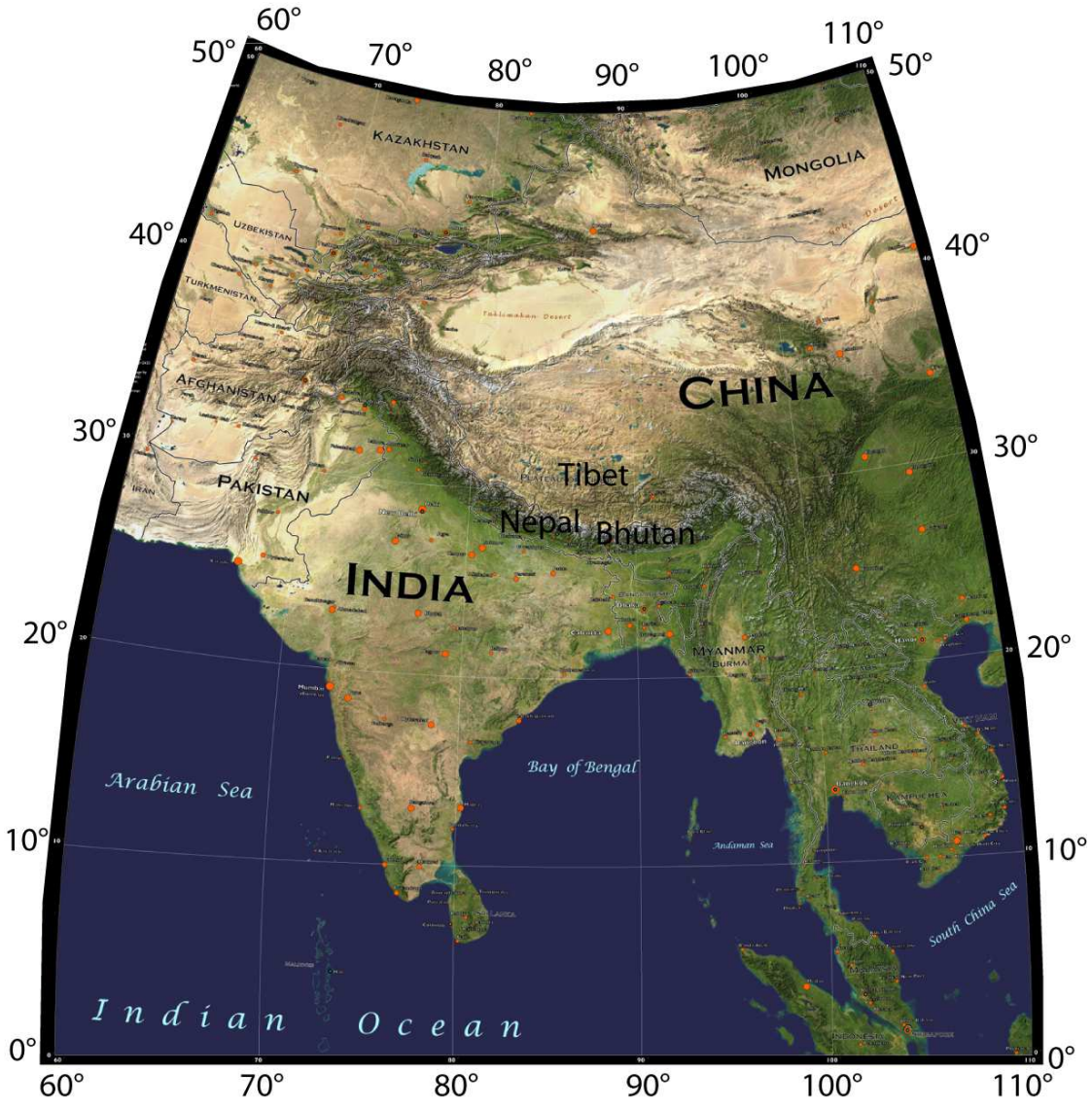

FIG. 1.2 – *Situation sur une image Landsat plaquée sur un modèle numérique de terrain du Népal, du Tibet, du Bhoutan et de l'Inde. La chaîne Himalayenne est constituée de l'ensemble des reliefs formant la ceinture nord indienne ; modifié d'après William Bowen*

cette topographie diffère notablement dans les pentes le long de transects nord - sud. Au Népal central, ils mettent en évidence un saut topographique, ou transition physiographique, au sud de la zone des hauts sommets (High Himalaya). En moins de 10 km, nous passons d'une altitude moyenne de l'ordre de 2000 m au sud à une altitude moyenne de l'ordre de 5000 m. Au Bhoutan, la pente est beaucoup plus régulière du sud au nord (Bookhagen et Burbank (2006), Fig. 1.4).

Il est possible de mettre en vis-à-vis ces données de relief et les précipitations moyennes pour la période récente (après 1998, voir Fig. 1.3). Les fortes pluies semblent induites par le premier saut topographique majeur. Mais le contrôle précis exercé par la topographie sur les précipitations reste peu documenté (Bookhagen et Burbank 2006). Les régions sans bande de précipitations fortes présentent un relief plus raide et les fortes précipitations sont plutôt focalisées au front de la chaîne.

Différentes interprétations en terme géométrique, géologique, tectonique et érosif existent pour expliquer la zone de fort relief observée en Himalaya central (Lavé et Avouac 2000, Duncan et al. 2003, Wobus et al. 2006). Pour la zone du Népal central, nous pouvons montrer qu'il y a une relation évidente entre la géométrie profonde des structures et la topographie observée.

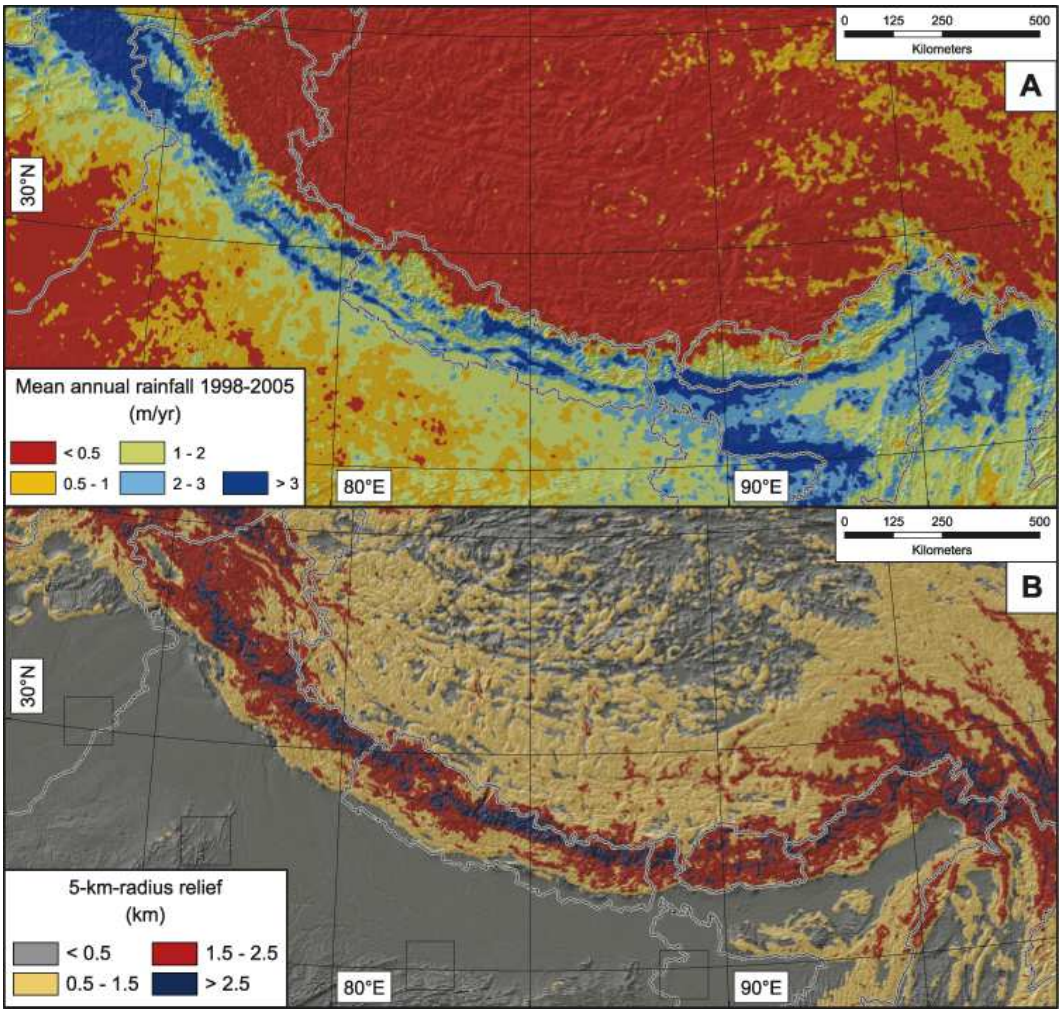

FIG. 1.3 – *(a) Moyenne calibrée par TRMM des précipitations lors de la mousson, de janvier 1998 à décembre 2005. Les données prennent en compte la mesure instantanée de précipitations avec une résolution spatiale de l'ordre de* $5 * 5$ *km. En Himalaya central, deux bandes de fortes précipitations sont en exergue. (b) Relief calculé sur un rayon de* 5 *km à partir des données topographiques issues des données SRTM V2 et des images et modèles numériques de terrain ASTER avec une résolution spatiale de* 90 *m. En Himalaya central,* 75 *à* 100 *km au nord du front de la chaîne, une bande à fort relief est marquée. En revanche, ce fort relief est beaucoup moins marqué en Himalaya de l'est (Bhoutan) ; modifié d'après Bookhagen et Burbank (2006).*

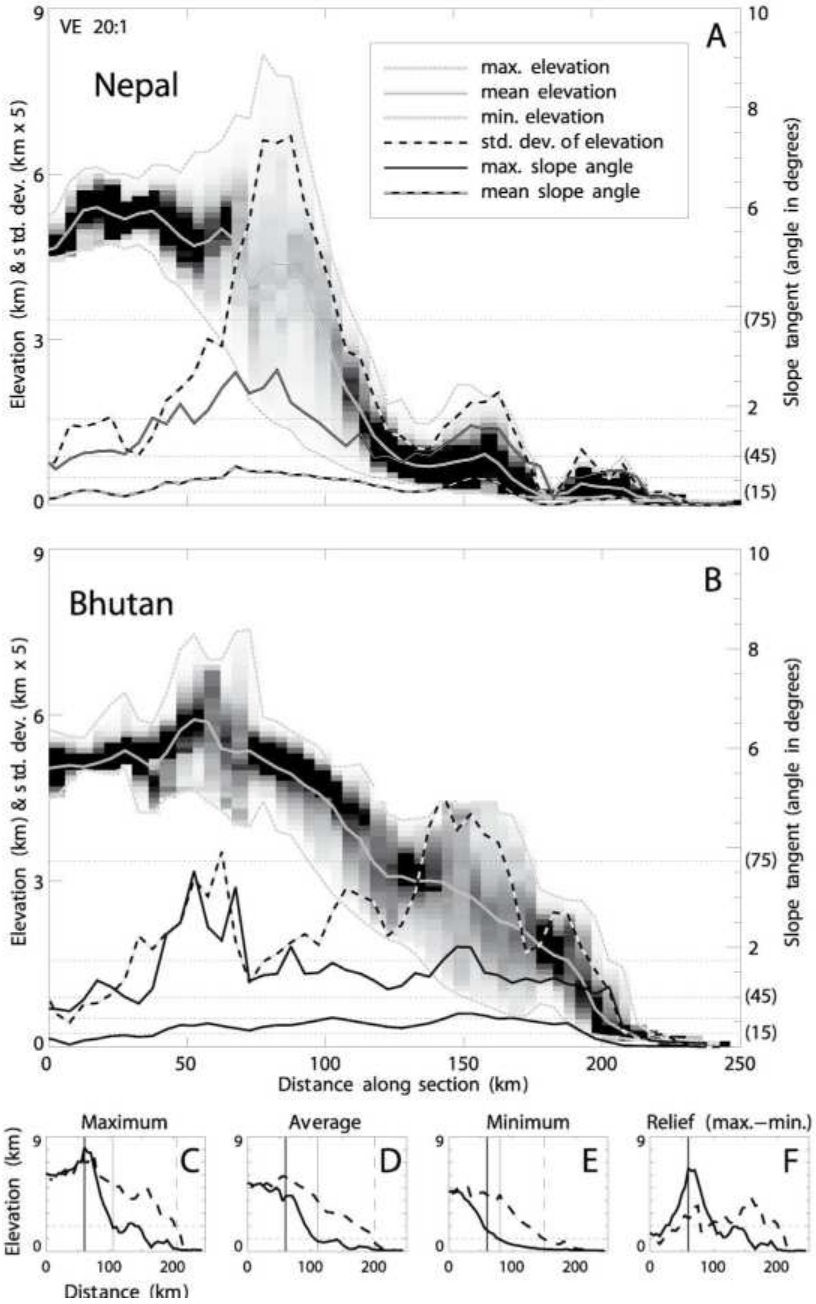

FIG. 1.4 – *Profils nord - sud d'altitude et de pente moyennes sur une largeur de* 50 *km au Népal (a) et au Bhoutan (b). L'échantillonnage est effectué tous les* 5 *km. Pour chaque profil, il est représenté l'altitude maximale, minimale et moyenne, et la pente. Le relief est calculé comme la déviation standard de l'altitude. (c) à (f) : Comparaison de profil du Népal et du Bhoutan alignés sur les hauts sommets et le MFT. Les lignes verticales pleines (Népal) et tiretées (Bhoutan) correspondent aux intersections des profils avec les altitudes* 1 *et* 2 *km, marquées par des lignes horizontales en pointillé ; modifié d'après Duncan et al. (2003).*

1.2.2 Aspects géologiques

L'orogène himalayen est produit par la collision cénozoïque entre les blocs continentaux asiatique et indien. L'Inde possède une altitude moyenne inférieure à 1000 m, alors que le plateau tibétain est un bassin endoréïque de relief très faible, mais d'altitude supérieure à 5000 m (Fielding et al. 1994). Le front topographique est représenté par la chaîne himalayenne.

La chaîne himalayenne est définie par la suture du Tsangpo au nord, la faille sénestre du Chaman à l'Ouest, la faille dextre de Sagaing à l'Est et le Main Frontal Thrust (MFT) au sud (Le Fort 1975) (Fig. 1.5). Le système tectonique est un peu plus large : il contient en plus de la chaîne himalayenne proprement dite, le bassin d'avant chaîne actif (dépression Indus - Gange) et les cônes alluviaux du Bengale et de l'Indus. L'orogène en lui-même est composé de systèmes de chevauchements d'échelle crustale, parallèles en première approximation et séparant différentes unités lithologiques (Fig. 1.5).

Dans la littérature, les divisions géographiques, structurelles et stratigraphiques sont la plupart du temps interchangeables (Le Fort 1975; 1996) et basées sur le travail de Heim et Gansser (1939) qui, à partir de l'étude de la région du Kumaun (Inde du nord - ouest), divisent l'Himalaya en 4 ceintures géographiques correspondant exactement à 4 domaines géologiques distincts. Nous verrons que cette amalgame, correct au premier ordre, masque en fait des observations importantes. Ces divisions sont considérées continues le long de l'orogène (Gansser 1964, Le Fort 1975) et incluent (du sud au nord) :

- Les Siwaliks (Sub-Himalaya), composés de dépôts de bassins d'avant-pays d'âges Miocène à Quaternaire (Burbank 1996), plissés lors de la propagation frontale de la déformation. Ils consistent en des alternances de grès, d'argiles et de conglomérats. Trois unités sont distinguées, de la plus jeune à la plus ancienne, les Upper Siwaliks (conglomérats), les Lower Siwaliks (grès - conglomérats) et les Lower Siwaliks (grès - argiles). Ce système chevauchant récent est disymétrique d'Est en Ouest : il est très large au Népal occidental (de l'ordre de 40 km) avec des chevauchements intermédiaires (Main Dun Thrust, MDT), mais étroit au Bouthan (de l'ordre de 10 km) (Chalaron et al. 1995,

Leturmy et al. 1999, Mugnier et al. 2004). Au Pakistan (ouest de la chaîne), les Siwaliks sont les plus larges.

– Le Bas Himalaya ou Moyen Pays (Lesser Himalaya, LH), formé de roches sédimentaires déposées sur la marge indienne : 12 kilomètres de roches précambriennes sont non-fossilifères et 3 kilomètres sont représentés par des sédiments fossilifères Permo-Carbonifères à Eocène. L'ensemble de ces roches possèdent un faible degré métamorphique (faciès schistes verts) (Stocklin 1980). La partie nord du Lesser Himalaya est constituée de métapélites à assemblage grenat-biotite-sillimanite (Pecher et Le Fort 1986, Mcfarlane 1995, Vannay et Hodges 1996, Godin et al. 1998, Godin 2003). Plus récement, Beyssac et al. (2004) quantifient, à partir de spectroscopie raman sur du matériel carboné, les températures maximales atteintesle long d'un transect nord - sud dans le Lesser Himalaya, et montrent un gradient inverse métamorphique du sud vers le nord.
– Le Haut Himalaya (Higher/Greater Himalaya, HH ou GH ou GHS), composé de métasédiments datant du Protérozoïque supérieur à Cambrien (Gansser 1983) intrudés par des complexes cristallins. Le degré de métamorphisme est moyen à fort (faciès amphibolites). Cette zone forme une partie des plus hauts sommets himalayens.
– L'Himalaya Téthysien (Tethyan Himalaya, TH), roches sédimentaires marines déposées sur la marge indienne entre le Cambrien et l'Eocène. Elles sont présentes dans la partie sud du plateau du Tibet, entre la suture du Tsangpo et les hauts sommets himalayens. Le métamorphisme de la série décroît rapidement du sud vers le nord du faciès schistes verts (biotite-muscovite) à la base de la formation, au faciès schistes verts basse température (Garzanti et Pagni Frette 1991, Crouzet et al. 2007). La transition entre le Lesser Himalaya et le Tethyan Himalaya est brutale, de l'ordre de quelques centaines de mètres (Garzanti et Pagni Frette 1991).

Les contacts entre ces divisions sont définis par :

– Le Main Frontal Thrust (MFT) délimitant les Siwaliks de la plaine du Gange,
– Le Main Boundary Thrust (MBT) dont le mur est constitué par le sub-Himalaya et le toit par le Lesser Himalaya,

– Le Main Central Thrust (MCT) dont le footwall est constitué par le Lesser Himalaya et le hangingwall par le Higher Himalaya. Le footwall est marqué par un fort gradient métamorphique inverse (Heim et Gansser 1939, Le Fort 1975, Pecher 1989, Hubbard 1989). Le MCT en lui-même est traditionnellement défini comme une zone de cisaillement ductile de largeur variable de quelques dizaines de mètres à quelques kilomètres (Le Fort 1975, Brunel 1986).
– Le South Tibetan Detachment (STD ou STDS) dont le hangingwall est constitué par le Tethyan Himalaya et le footwall par le Higher Himalaya. A l'opposé des autres failles, celle-ci est une faille normale.

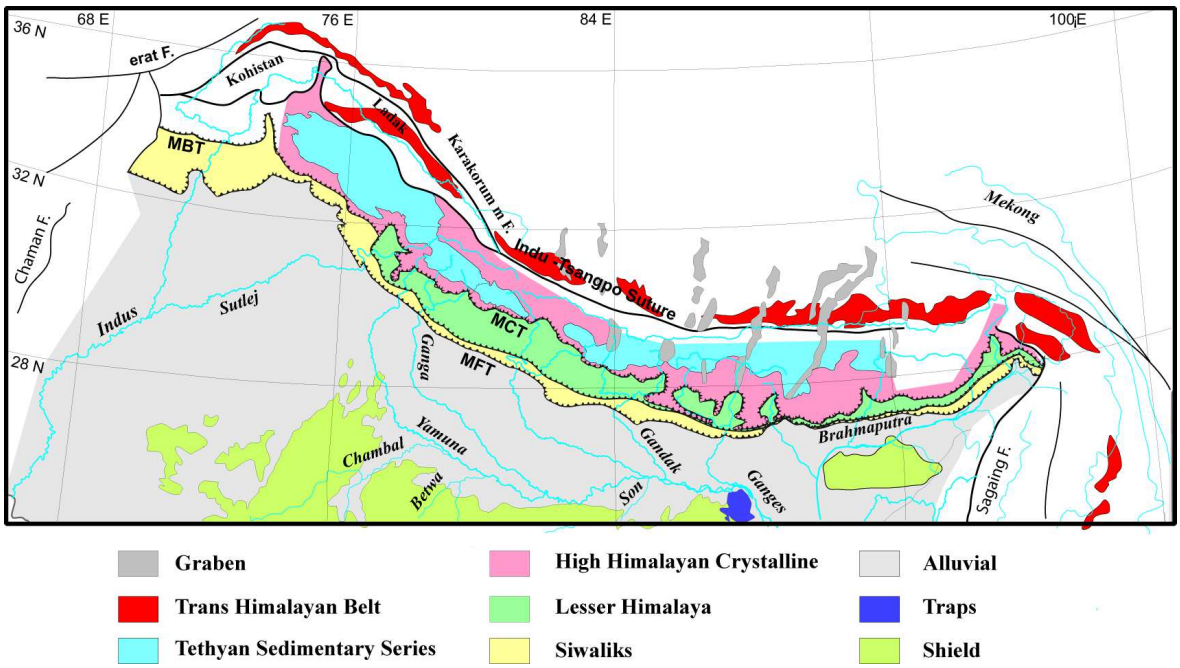

FIG. 1.5 – *Structure générale simplifiée de la chaîne himalayenne mettant en exergue les unités géologiques principales et les grandes structures tectoniques ; modifié d'après Galy (1999).*

1.2.3 Etat actuel des connaissances sur la tectonique

Timing et déformation dans le prisme himalayen

Il y a $120 - 130$ *Ma*, la plaque Indienne s'est séparée du Gondwana, puis de Madagascar 36 à 46 *Ma* plus tard (Metcalfe 1996). Son déplacement vers le nord à une vitesse de 15 $cm.an^{-1}$ entraîne la fermeture progressive d'une portion de l'Océan Téthys, qui disparaît alors en subduction le long de la limite Asie - Inde (Dercourt et al. 1993). La collision et la formation de l'Himalaya débutent aux alentours de $50 - 53$ *Ma*, et s'accompagnent d'un ralentissement du mouvement de l'Inde (Row-

ley 1996, Searle et al. 1997, De Sigoyer et al. 2000, Yin 2006). Lorsque la totalité de l'océan a disparu, la partie continentale de la plaque indienne entre à son tour en subduction. Sous l'effet des forces liées à la dynamique interne, l'Inde continue son mouvement vers le nord, forçant la marge continentale à descendre dans la zone de subduction. Or la croûte continentale indienne étant moins dense que le manteau, elle s'oppose à la subduction. Il en résulte une désolidarisation du manteau et de la croûte au niveau de la zone de subduction. La chaîne himalayenne commence à se former par empilement successif de croûte. A partir de 35 Ma, la vitesse de convergence se stabilise à environ 5 $cm.an^{-1}$ (Guillot et al. (2003), Fig. 1.6). Ces changements de vitesses s'accompagnent souvent de changements de direction de convergence.

Najman et al. (1997) démontrent grâce à des datations $^{40}Ar/^{39}Ar$ qu'au front de la collision, l'Himalaya ne se développe vraiment que depuis 20 à 30 Ma. Auparavant, d'autres épaississements de croûte ont probablement été actifs et ont contribué à la formation du plateau tibétain. Mais la formation de cette structure ne suffit pas à expliquer les 1500 km de convergence de l'Inde depuis le début de la collision. Un autre processus tectonique joue un rôle majeur, à savoir l'extrusion vers l'est de morceaux de continents, poussés par l'Inde, grâce au jeu de grandes failles décrochantes. Ce modèle est appuyé par des expériences analogiques (Tapponnier et al. 1982) et par la datation de déformations sur le terrain (Lacassin et al. 1997) (Fig. 1.7).

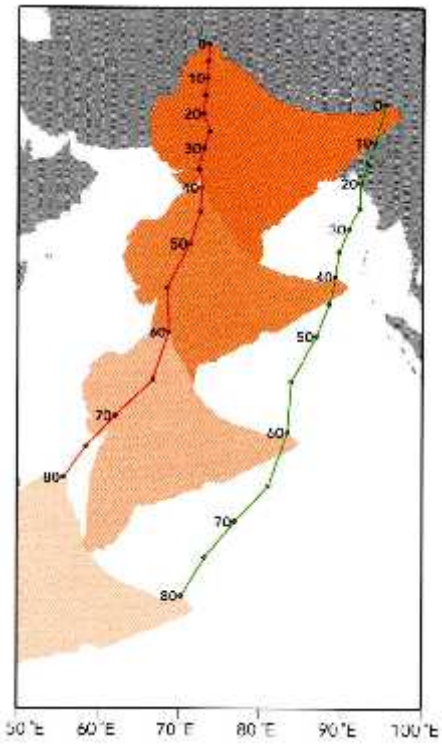

(a) Mouvement de l'Inde par rapport à la plaque eurasienne depuis 80 *Ma* par intervalles de 5 *Ma* déduit de la combinaison des mouvements relatifs Inde-Afrique, Afrique-Amérique du Nord, Amérique du Nord-Eurasie

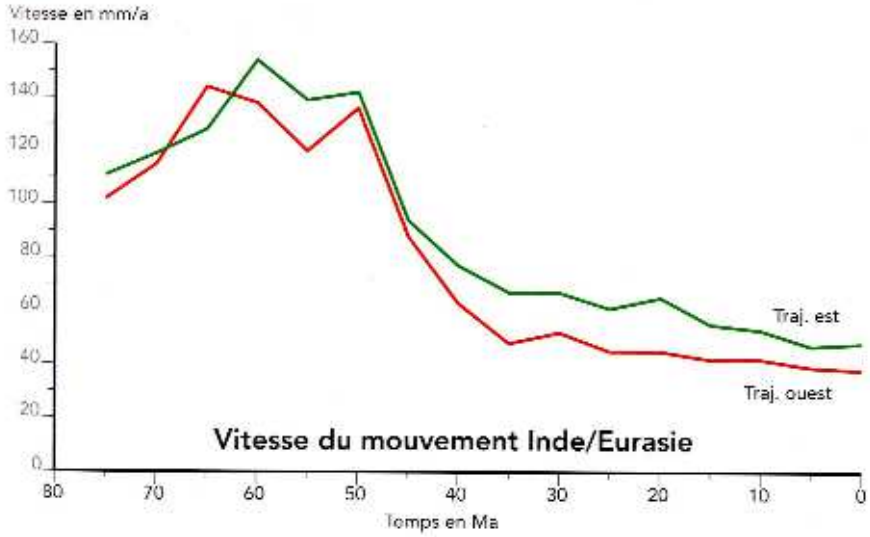

(b) Variations au cours du temps de la vitesse de rapprochement de l'Inde par rapport à l'Eurasie. Les trajectoires et la vitesse sont calculées pour deux points situés sur la suture himalayenne, en rouge pour le point ouest et en vert pour le point est

FIG. 1.6 – *Déplacement et vitesse de l'Inde par rapport à l'Eurasie ; d'après Royer et Patriat (2002).*

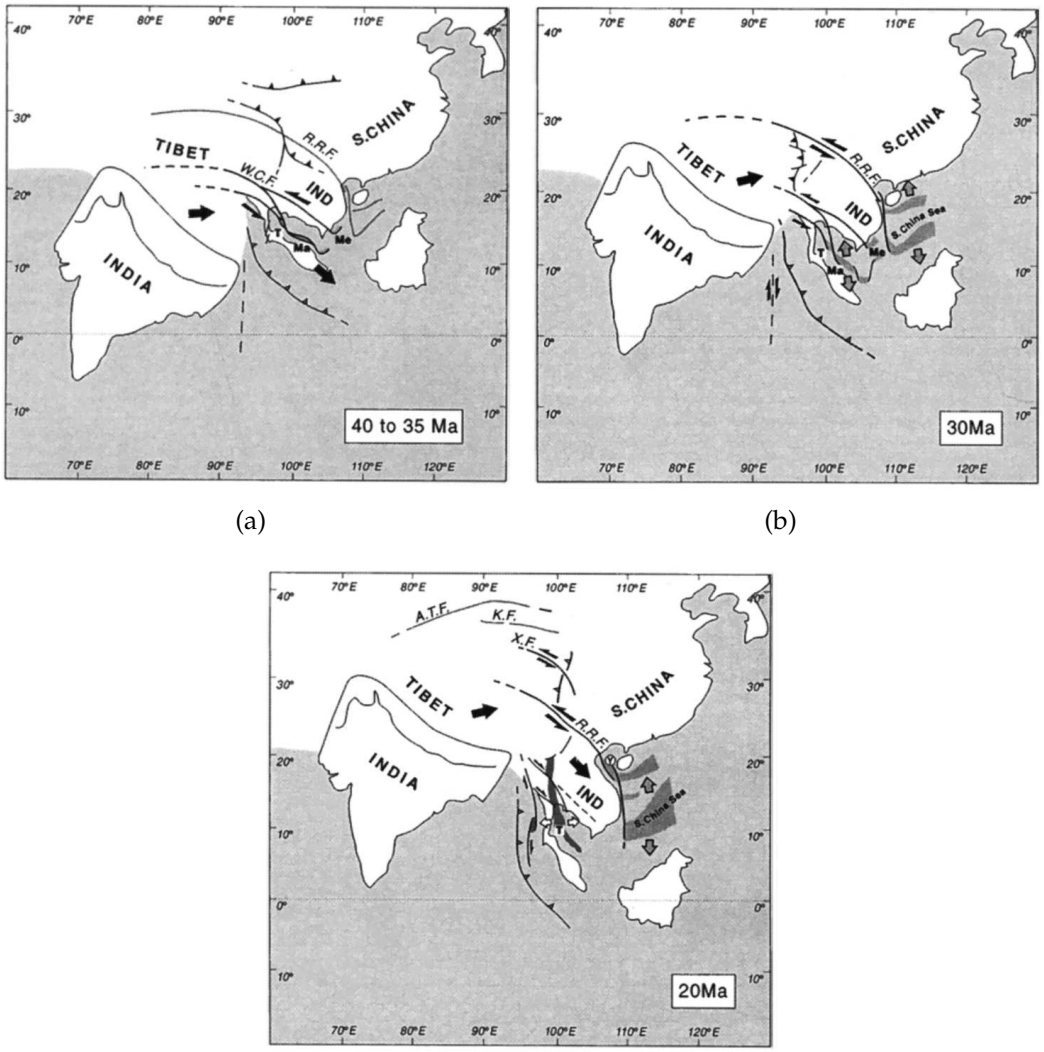

FIG. 1.7 – *Modèle spéculatif d'extrusion en Himalaya entre l'Eocène et le Miocène. Les vitesses sont relatives à l'Inde. (a) Situation des plaques et des blocs continentaux à l'Eocène supérieur (40 à 35 Ma) avec le début du mouvement sénestre le long de la faille Wang Chao (WCF), l'extrusion de l'Indochine du sud-ouest et l'ouverture corrélée du delta du Mekong (Me) et d'une partie du golfe de Thailande (T). (b) A l'Oligocène inférieur (30 Ma), l'extrusion de l'Indochine (IND) est majeure, avec un mouvement sénestre sur la faille du Fleuve Rouge (RRF) et l'ouverture de la mer de Chine du sud. (c) Au Miocène inférieur (20 Ma), le mouvement sénestre le long de la faille du Fleuve Rouge continue avec l'ouverture de la mer de Chine du sud et de bassins en pull-apart (Y = Yinghehai) ; d'après Lacassin et al. (1997).*

Le MCT est initié au minimum entre $23 - 20$ Ma (Hubbard 1989, Hodges et al. 1996). Simultanément, le STDS s'initie aussi (Burchfiel et al. 1992, Hodges et al. 1996). Certains auteurs comme Beaumont et al. (2001) le relient à un modèle de channel flow, modèle qui exhume la zone comprise entre le MCT et le STDS avec une érosion très intense (supérieure à 10 $mm.an^{-1}$). D'après ces modélisations numériques, la rhéologie de cette zone est obligatoirement définie par un angle de friction très faible (entre 5 et 10°). Le hangingwall du MCT est alors érodé lorsqu'il arrive à la surface au dessus de la rampe. Ce modèle de channel flow est compatible avec une subduction plate de la lithosphère indienne, mais est peu compatible avec plusieurs constatations : il n'existe aucune preuve géologique de l'élévation du plateau tibétain de 8 km permettant ce mécanisme, les observations de terrain ne sont pas compatibles avec des unités téthysiennes avec un angle de friction aussi faible (Ratschbacher et al. 1994), la géométrie prédite du MCT avec une seule rampe sous le front d'érosion est incohérente avec les observations dans le moyen pays (Yin 2006), le taux d'érosion invoqué semble trop élevé (Yin 2006), l'augmentation abrupte des taux d'érosion et l'initiation du MCT ne sont pas corrélées temporellement (Hubbard 1989, Yin 2006). Ce modèle n'explique pas le gradient inverse de métamorphisme.

A partir de datations $^{40}Ar/^{39}Ar$ sur hornblendes et $U - Pb$ sur zircons, Hubbard (1989), Hodges et al. (1992), Parrish et Hodges (1996), Coleman et Hodges (1998), Godin et al. (2001) suggèrent que le gradient inverse métamorphique observé et daté de 20 à 23 Ma est contemporain de la déformation induite le long du MCT pendant son activité. Des études thermochronologiques montrent qu'au Miocène Moyen, la déformation était terminée (Hubbard 1989, Copeland et al. 1991). Bollinger et al. (2004) expliquent ce métamorphisme par la formation d'un duplex.

Pour ce qui est des chevauchements frontaux, peu de données contraignent leur initiation. D'après des données sédimentologiques et géochimiques datant l'exhumation du Bas Himalaya et le début de l'augmentation de son érosion, Huyghe et al. (2001) montrent que le système chevauchant du Lesser Himalaya aurait été initié il y a environ 10 à 12 Ma. Pour Delcaillau (1997), l'initiation du MBT serait plus tardive (8 Ma). Il faut noter que pour Huyghe et al. (2001), le MBT n'est

que l'un des des chevauchements du Lesser Himalaya, ce qu ipeut expliquer cette différence d'âges. Cette activité est actuellement discrète (Delcaillau 1997).

Le MFT est actuellement actif (décalage de terrasses récentes par des failles) avec des vitesses de raccourcissement de 14 à 20 $mm.an^{-1}$ (Lavé et Avouac 2000, Mugnier et al. 2004), tandis que la mesure de la déformation instantanée par GPS indique un bloquage intersismique du chevauchement (Banerjee et Burgmann 2002, Jouanne et al. 2004). Le MFT aurait été initié aux environs de 2 *Ma* d'après Mugnier et al. (2004), van der Beek et al. (2006) au Népal.

Une synthèse de la cinématique des derniers 22 *Ma* est proposée sur la Fig. 1.8 (DeCelles et al. 2001).

La reconstruction de la tectonique des plaques basée sur des données paléomagnétiques de l'orogène himalayen suggère une convergence totale post collision de 2600 ± 900 *km* entre l'Eurasie et l'Inde, dont 1700 ± 610 *km* accommodés par le raccourcissement nord-sud du plateau tibétain et de l'expulsion latérale (Patriat et Achache 1984, Achache et al. 1984, Besse et Courtillot 1988; 1991). Les 900 *km* de différence entre ces valeurs moyennes peuvent être pris en compte pour le raccourcissement frontal himalayen (Le Pichon et al. 1992). Patzelt et al. (1996) estiment ce raccourcissement en se basant sur des données paléomagnétiques entre $\sim$ 700 *km* et 1500 *km*.

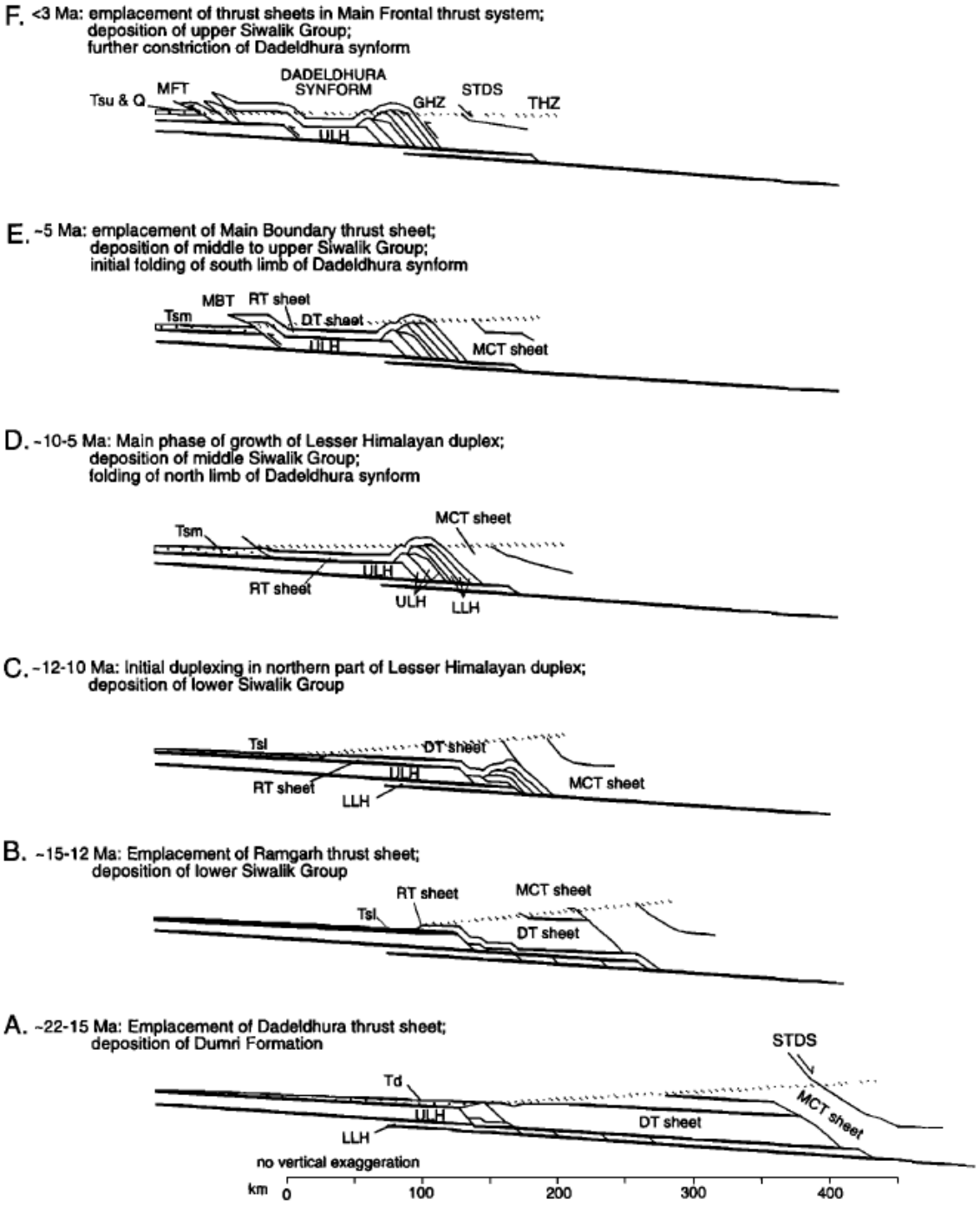

FIG. 1.8 – *Reconstruction incrémentale de coupes équilibrées du front du prisme Himalayen de 22 Ma à 3 Ma. La ligne pointillée représente la position approximative de la surface. LLH = Lower Lesser Himalaya, ULH = Upper Lesser Himalaya, RT = Ramgarh thrust, DT = Dadeldhura Thrust, GHZ = Greater Himalayan zone, THZ = Tibetan Himalayan zone ; d'après DeCelles et al. (2001).*

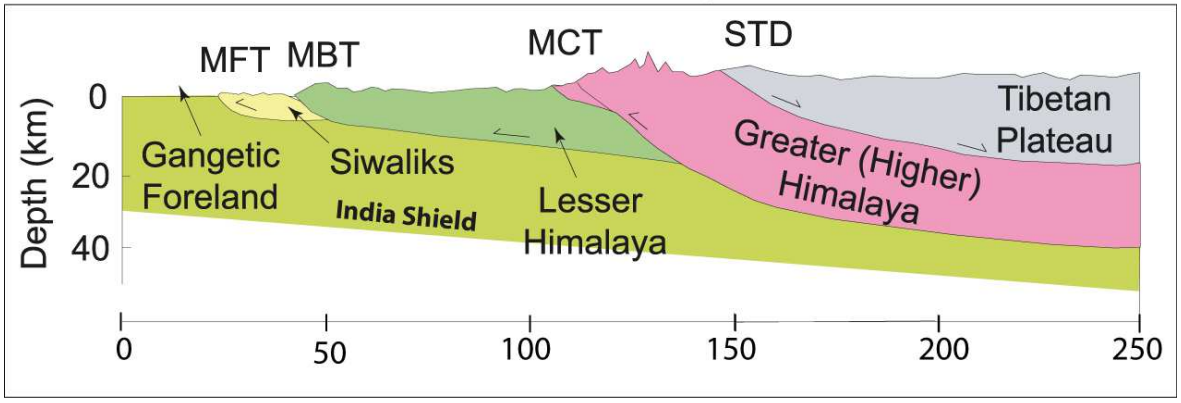

FIG. 1.9 – *Coupe simplifiée de la chaîne himalayenne centrale montrant la connection des chevauchements principaux sur le MHT et les principales zones tectonostratigraphiques ; modifiée d'après Bookhagen et Burbank (2006).*

Géométrie profonde des grandes structures tectoniques himalayennes

Les 3 chevauchements majeurs MCT, MBT et MFT sont connectés en profondeur au Main Himalayan Thrust (MHT) qui accommode l'essentiel de la déformation actuelle (Fig. 1.9). Il s'enracine dans une zone de cisaillement ductile sub-horizontale située sous le Sud-Tibet (Avouac 2003) (Fig. 1.10, Fig. 1.11, Fig. 1.12 et Fig. 1.13). La microsismicité absorbe une fraction négligeable des déformations observées, ces déformations élastiques finissent alors par être transférées sur le MHT lors des séismes himalayens majeurs (Avouac 2003). Dans la suite, nous montrons que cette géométrie est susceptible de varier latéralement.

Communément, il est admis que la zone du MHT possède une géométrie en plat - rampe - plat (Lyon-Caen et Molnar 1985, Schelling et Arita 1991, Schelling 1992, DeCelles et al. 2001). Cette géométrie ne peut être appliquée à l'ensemble de l'Himalaya (Berger et al. 2004), cette chaîne présentant une variation latérale de morphologie, et sa définition repose sur des observations peu contraignantes. Les paragraphes suivants passent en revue les principales zones de l'Himalaya.

Au niveau du Népal central : Dans la littérature, il y a peu de données permettant de contraindre la géométrie précise du MHT au Népal central. Il a été mis en évidence sous le Tibet (Fig. 1.10) par des études de réfraction sismique et imagé par les profils sismiques profonds INDEPTH (Zhao et Nelson 1993, Brown et al. 1996, Nelson 1996). La structure sous l'Himalaya du Népal central a été imagée et interprétée par Lemonnier et al. (1999) (Fig. 1.10). A partir de ces données, Avouac (2003), propose que le MHT soit constitué d'une géométrie en rampe - plat - rampe. La rampe la plus au sud aurait un pendage de l'ordre de 30°, et son émergence à la surface correspond à la trace du MFT. La seconde rampe, plus conjecturale serait située à une profondeur correspondant à la croûte moyenne, et située entre le front et la haute chaîne. Son pendage vers le nord est estimé à environ 15°. Cette géométrie et ces valeurs sont qualitativement cohérentes avec les données de microsismicité (Fig. 1.10, Fig. 1.11 et Fig. 1.12).

Des articles récents appuient ces hypothèses grâce à l'imagerie en fonction-récepteur migrée le long du profil 85°E de l'expérimentation Hi-CLIMB (Schulte-Pelkum et al. 2005, Hetenyi et al. 2007).

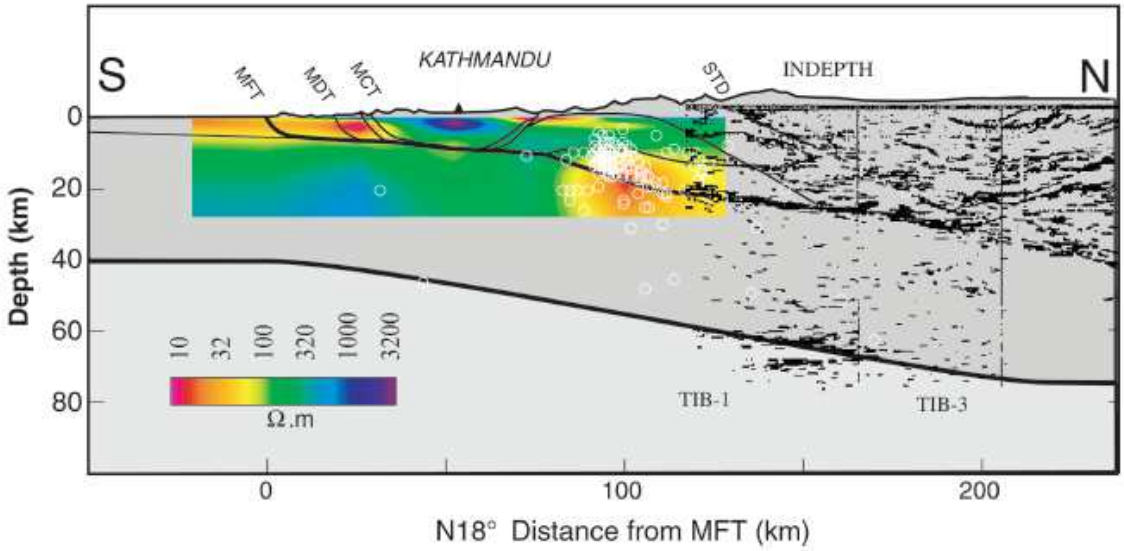

FIG. 1.10 – *Contraintes géophysiques sur la structure sous le Népal central ; la coupe condutimétrique a été obtenue à partir d'expériences magnétotelluriques (Lemonnier et al. 1999) ; il est aussi reporté la coupe sismique INDEPTH (Zhao et Nelson 1993, Brown et al. 1996, Nelson 1996). Toutes les failles sont branchées à leur racine à la zone de transition fragile - ductile qui correspond au reflecteur principal à mi-croûte ; les ronds blancs correspondent à la microsismicité enregistrée le long de ce transect (Figure d'après Avouac (2003)).*

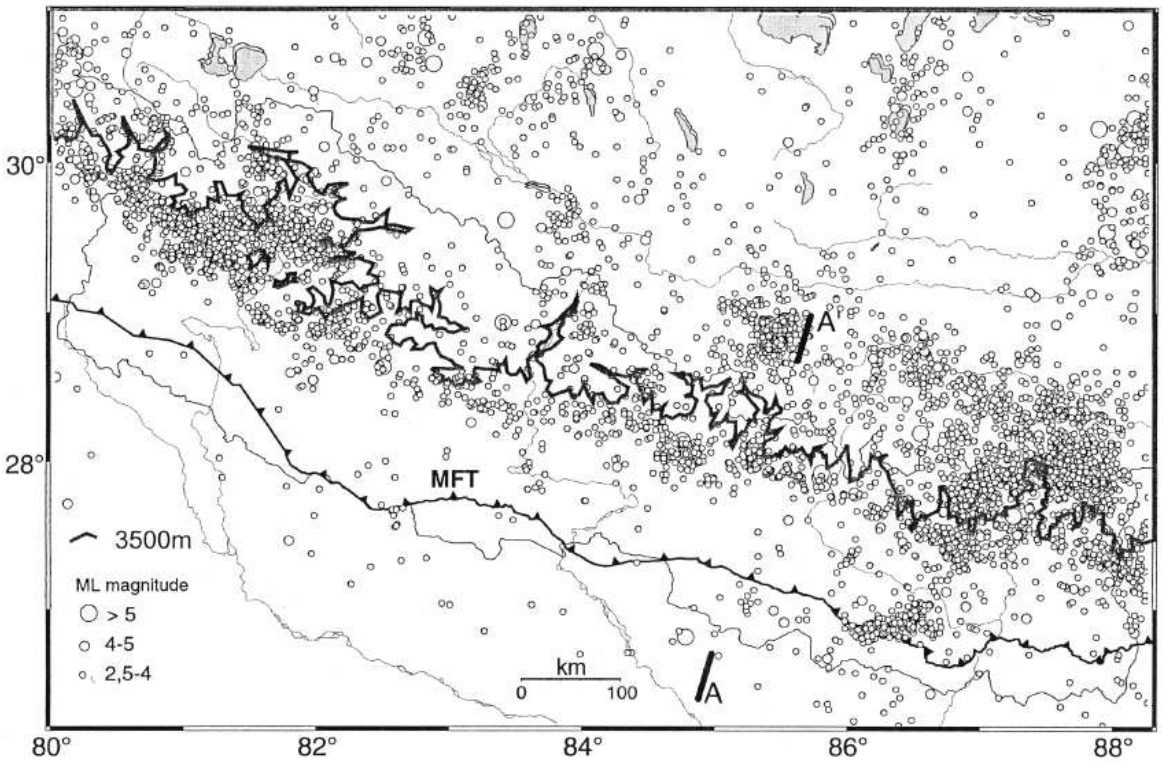

FIG. 1.11 – *Sismicité du Népal (Himalaya central) enregistrée par le réseau sismologique du DMG entre le 04/01/1995 et le 10/12/1999 (Pandey et al. 1999) ; la ligne noire foncée correspond à la ligne de niveau 3500 m (Figure d'après Avouac (2003)).*

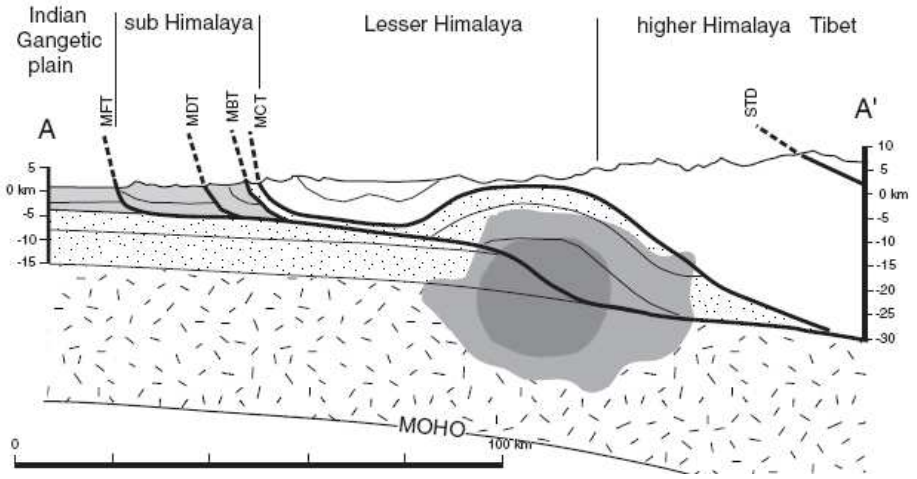

FIG. 1.12 – *Coupe à travers le Népal central et projection de l'activité microsismique ; l'aire du maximum de microsismicité est interprétée comme la conséquence des contraintes liées à un mouvement nord - sud le long du MHT (Figure d'après Jouanne et al. (2004)).*

Berger et al. (2004) proposent un modèle de morphologie du MHT au Népal à partir de modélisations numériques de la déformation intersismique. Au Népal, les longueurs des plats et la pente des rampes varieraient latéralement, ce qui entrainerait des rampes latérales dans la croûte indienne (Fig. 1.14).

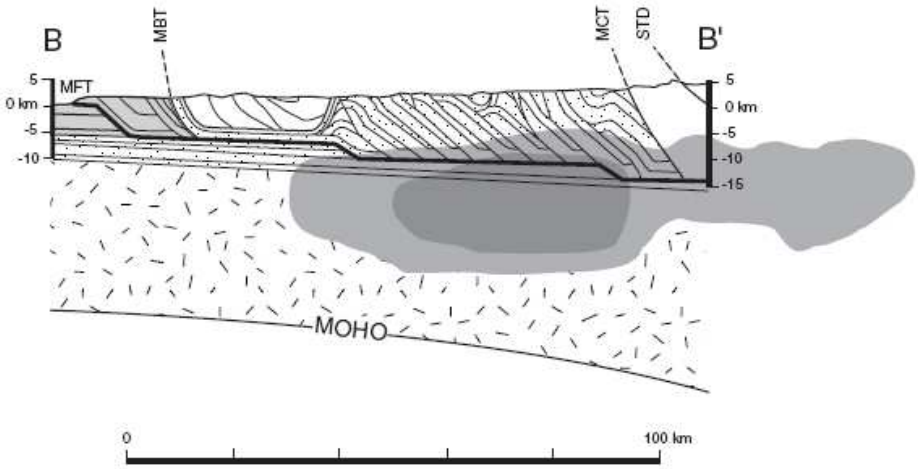

FIG. 1.13 – *Coupe à travers le Népal de l'Ouest et projection de l'activité microsismique ; l'aire du maximum de microsismicité est interprétée comme la conséquence des contraintes liées à un mouvement nord - sud le long du MHT (Figure d'après Jouanne et al. (2004)).*

Au niveau de Kathmandu, la coupe nord-sud de l'Himalaya est caractérisée par une écaille cristalline située au sommet des unités du moyen pays (Stocklin 1980). Cette unité fait partie de la klippe de Kathmandu qui forme le relief important de la chaîne du Mahabarat avec des altitudes supérieures à $2500 - 3000\ m$ juste au nord de l'avant pays Siwalik. Ces unités cristallines sont datées du Cambrien

à l'Ordovicien par Scharer et Allegre (1983) et représenteraient l'extension sud du High Himalaya (Stocklin 1980).

Au niveau du Népal de l'ouest : Au niveau des Annapurnas, il n'y a pas de klippe de Higher Himalaya dans le Lesser Himalaya comme au niveau de Kathmandu. De plus, la Fig.1.13 représentant la microsismicité dans l'extrême ouest - Népal ne montre pas la même structure qu'au niveau de Népal central. La structure, interprétée par Jouanne et al. (2004) comporterait 3 rampes de moindre ampleur et moins profondes. La structure générale reste proche de celle du Népal central.

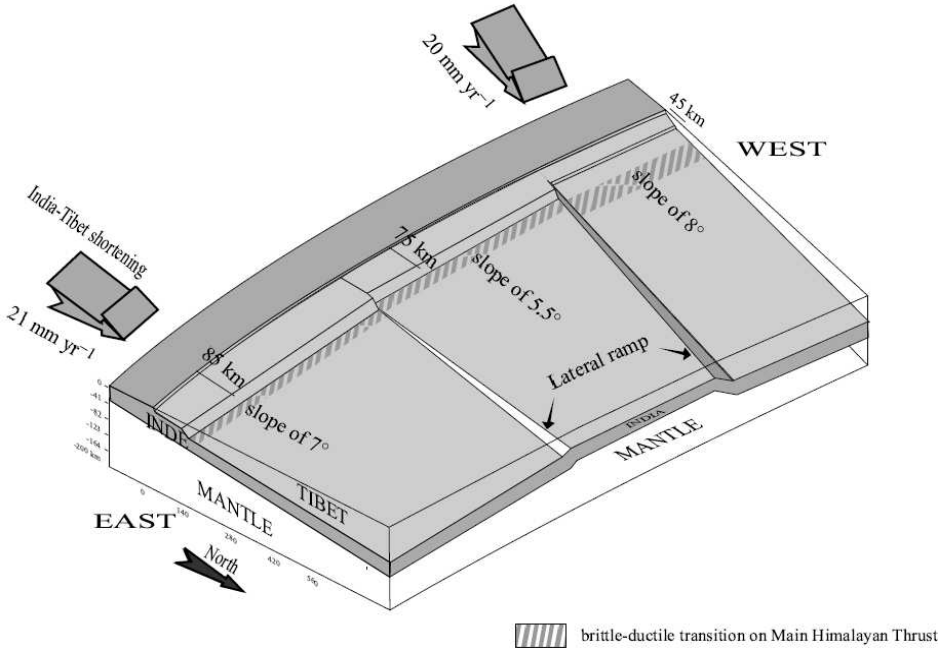

FIG. 1.14 – *Extension 3D des modèles finaux issus de la modélisation de la déformation intersismique. Cette interprétation implique un changement brutal de géométrie entre chaque zone et la présence de rampes crustales latérales ; d'après Berger et al. (2004).*

Coupe du Bhoutan : La structure profonde de l'Himalaya du Bhoutan est assez peu documentée. Hauck et al. (1998) présentent les seules images géophysiques de la structure crustale de l'Himalaya aux alentours de la longitude 90° Est, obtenues à partir d'un profil de reflection sismique (Fig. 1.15). Ils dessinent une géométrie du MHT sans rampe bien distincte.

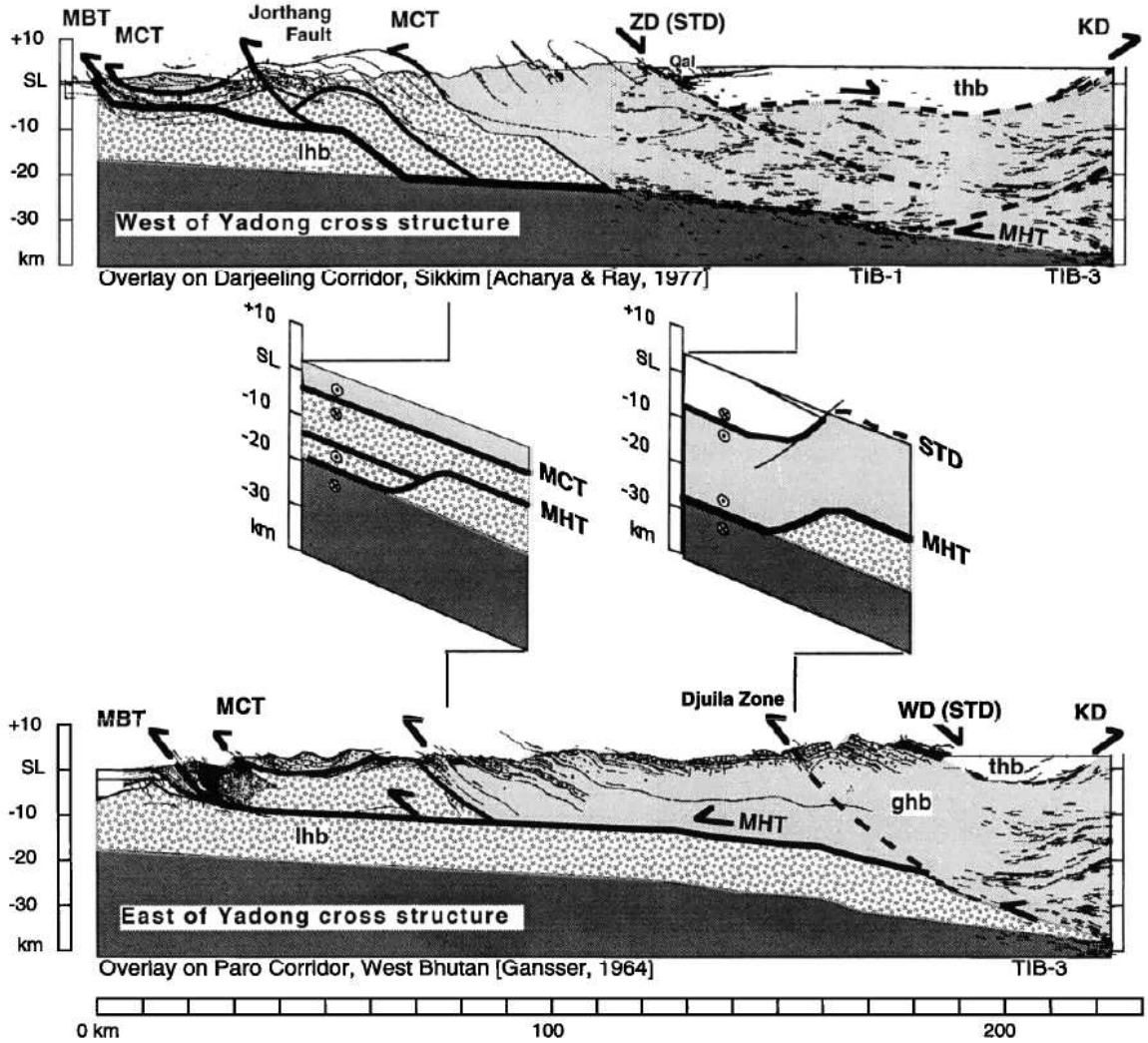

FIG. 1.15 – *Coupe géologique interprétée à travers le Népal de l'est et l'ouest du Bhutan à partir des données de réflexion sismique et des coupes de Acharaya et Ray (1977), Gansser (1964). KD est l'interprétation du détachement de Kangmar. (Figure d'après Hauck et al. (1998)).*

1.3 Problématique

1.3.1 Fonctionnement du prisme himalayen

Avant tout, il est nécessaire de se poser la question du mécanisme selon lequel se déforme le prisme de la chaîne himalayenne : la déformation s'effectue-t-elle selon une rampe et un chevauchement frontal (modèle de Bollinger et al. (2004), Avouac (2003), Lavé et Avouac (2000; 2001) : Fig. 1.16(a)), des anciens chevauchements internes sont-ils réactivés (modèle de Hodges et al. (2004) ; Fig. 1.16(b)) ? Et si des réactivations hors-séquences sont initiées, quelle est la proportion de raccourcissement associé ? Un outil pouvant répondre à ces interrogations est la reconstruction de l'histoire thermique des unités mises en jeu. Intuitivement, ces deux scénarii ne devraient pas avoir la même signature thermo-cinématique, et donc, les enregistrements thermochronologiques devraient nous permettre de trancher entre ces différentes hypothèses. Sur de tels phénomènes, récents, les températures mises en jeu sont basses (50 à 200°C), ce qui nous incite à utiliser des marqueurs de basses températures. Nous utiliserons alors le système traces de fissions sur apatites dont la température de fermeture est de 110°C. De plus, toute la déformation n'est pas nécessairement accommodée uniquement par un raccourcissement au niveau du prisme, mais aussi par une composante de sous-plaquage qui joue un rôle dans la structure thermique d'après Bollinger et al. (2006). Dans quelle mesure cette composante de sous-plaquage affecte-t-elle la signature thermique et thermochronologique de la tectonique de prisme ?

Une deuxième question se pose aussi : comment se déforme le prisme frontal et récent, *id est* au niveau des Siwaliks, et quelle est la part de l'érosion dans ce système dynamique ?

Dans un premier temps, nous allons justifier et présenter les techniques utilisées, à savoir la thermochronologie par traces de fission sur apatites et la modélisation numérique directe et inverse.

Dans un second temps, nous allons étudier la dynamique globale du prisme himalayen en appliquant les techniques décrites précédemment, *id est* en modélisant l'état thermique du prisme selon les trois scénarii proposés ci-dessus, et en calculant les âges thermochronologiques associés (traces de fission sur apatites et

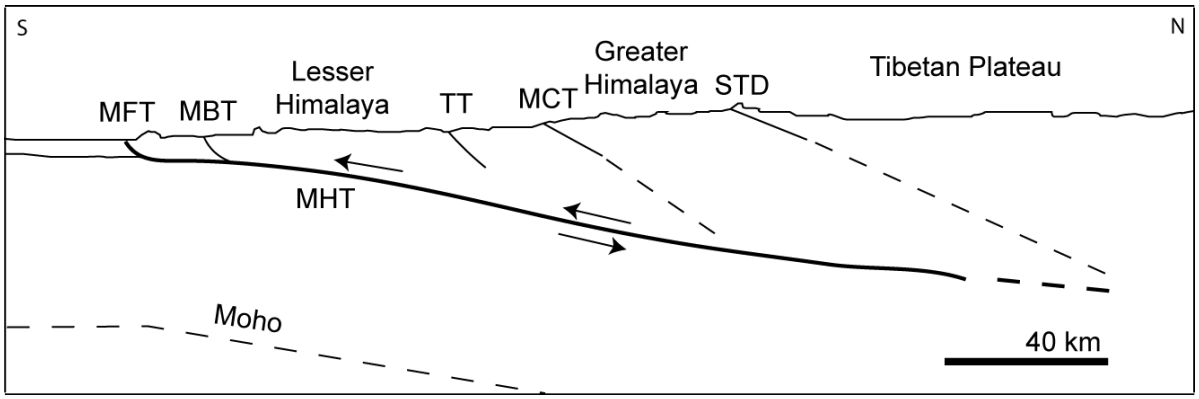

(a)

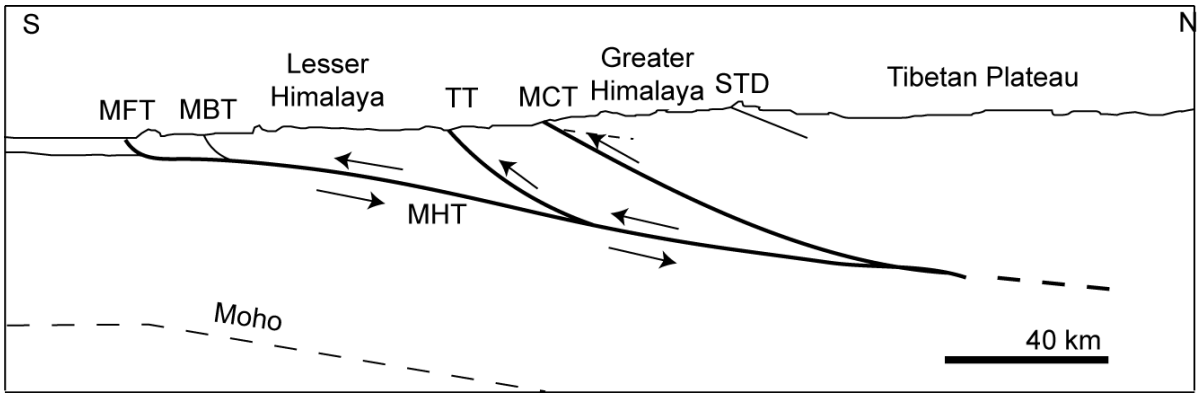

(b)

FIG. 1.16 – *Modèles de déformation du front de la chaîne himalayenne. a) Modèle de Lavé et Avouac (2001) : la déformation est principalement accommodée au front de la chaîne grâce au MHT - MFT. b) Modèle de Hodges et al. (2004) : la déformation est accommodée à la fois au front de la chaîne par le couple MHT - MFT, mais aussi grâce à une réactivation hors séquence au niveau du front topographique. (Schémas modifiés d'après Hodges et al. (2004)).*

données Argon). La chaîne himalayenne étant complexe autant d'un point de vue structures que d'un point de vue processus, nous allons simplifier le problème en étudiant des transects Nord - Sud, en se restreignant à un modèle cinématique et en implémantant un modèle de processus de surface simple dans un premier temps.

Pour ces volets, nous confronterons les résultats aux données de terrain (Traces de fission sur Apatites). En effet, j'ai accumulé par mesures et par un travail bibliographique plusieurs jeux de données : un transect Nord - Sud au niveau du Langtang, un transect Nord - Sud au niveau des Annapurnas et un début de transect Nord - Sud dans l'Est-Bhoutan. Deux transects plus restreints mais de résolution temporelle plus importante, dans les Siwaliks, à savoir au niveau de la Karnali et de la Bakeia nous contraindront mieux le dernier stade de déformation de la chaîne himalayenne. Nous disposons de plus de données $^{40}Ar/^{39}Ar$ sur muscovites déjà publiées par Arita et al. (1997), Rai (1998) et Bollinger et al. (2004). Ces données seront aussi la base d'une inversion des problèmes.

1.3.2 Kinematic models of the central Himalaya : A critical evaluation

Au cours des derniers 10 ans, quelques modèles numériques élaborés ont vu le jour pour tenter d'expliquer par la cinématique l'histoire du front himalayen (Beaumont et al. 2001; 2004, Jamieson et al. 2004, Brewer et Burbank 2006, Wobus et al. 2006, Bollinger et al. 2006, Whipp et al. 2007). Ces modèles ne sont pas décrits exactement dans les mêmes référentiels, utilisent des données similaires, mais leurs conclusions sont divergentes. La question qui se pose est de savoir quelle différence réelle il y a entre ces modèles. Il est donc important d'en faire un état des lieux, en décrivant tous ces modèles dans un même repère. C'est l'objet de l'article qui suit. Cet article sera soumis à *Earth and Planetary Science Letters*.

Kinematic models of the central Himalaya: A critical evaluation

Xavier Robert[1], Peter van der Beek[1], Jean Braun[2], Jean-Louis Mugnier[3]

1. Laboratoire de Géodynamique des Chaînes Alpines, Université Joseph Fourrier, Grenoble, France
2. Géosciences Rennes, Université de Rennes 1, Rennes, France
3. Laboratoire de Géodynamique des Chaînes Alpines, CNRS, Le Bourget-du-Lac, France

To be submitted to Earth and Planetary Science Letters

Word count (22/10/2008): Main text - 6829

Abstract

Thermo-mechanical and thermo-kinematic models are commonly used to examine the tectonic evolution of orogenic belts. In the central Himalaya, different models that aim to reproduce thermochronological and geological datasets acquired mainly in central Nepal have been published over the last decade. The models support different tectonic mechanisms, such as crustal channel flow, underplating or out-of-sequence faulting, and reproduce geological observations and thermochronological data more or less well, but have not led to unambiguous conclusions as to the dynamics or kinematics of the central Himalaya. A detailed comparison of five different proposed models shows that these can be resumed to two fundamentally different classes of models (crustal underplating or out-of-sequence faulting) when expressed in the same reference frame, and that the geological or geophysical evidence to discriminate between them is currently lacking. The divergence and/or ambiguity in these models can be explained by the location of existing thermochronological datasets, which strongly concentrate on the Greater Himalayan Sequence, whereas a significantly discriminative tectonic signal should rather be recorded in the Lesser Himalaya, where relatively few data are available.

Keywords: Himalaya, Nepal, Tectonics, Thermochronology, Numerical modelling, Review.

1. Introduction

An improved understanding of the dynamics and kinematics of orogenic belts is an essential component of research into collisional tectonics. Major questions concern the behaviour of the lithospheric mantle and pathways of crustal deformation and flow. These processes drive

mountain building and strongly interact with the evolving topography, both global and regional-scale climate, and erosion processes (e.g., Willett, 1999; Zeitler et al., 2001; Whipple and Meade, 2006). To understand active mountain building at the scale of a mountain belt, one needs to be able to track particle paths during long timescales. Access to the structure and behaviour of the upper crust is provided by structural and thermochronological data. Surface observations, however, force us to extrapolate to infer the architecture of the subsurface (upper) crust.

Because of its rapid convergence and exhumation rates, the central Himalaya provides an excellent natural laboratory to study evolving orogenic systems and mountain building processes. Numerous balanced-cross sections have been constructed to infer the geological structure of the central Himalaya and to develop scenarios for its kinematic development (Schelling and Arita, 1991; DeCelles et al., 2001; Robinson et al., 2006; Yin, 2006). During the last twenty years, important thermochronological datasets have been published that constrain exhumation rates and pathways along several transects across the range (e.g., Copeland et al., 1991; Catlos et al., 2001; Bollinger et al., 2004; Thiede et al., 2004; Vannay et al., 2004; Grujic et al., 2006). The thermal history recorded by bedrock cooling ages provides strong constraints on the kinematics and evolution through time of the architecture of the mountain belt. However, in active orogens the thermal field is multidimensional and commonly transient with rock exhumation paths. The lateral rock movement, in combination with effects of erosion and topography, will deflect isotherms and produce local, non-linear, geothermal gradients (Batt and Braun, 1997; Willett et al., 2003; Ehlers, 2005). Thus, to extract maximum information from thermochronological data, the lateral and vertical components of advection have to be specified. Furthermore, topography strongly influences

low-temperature thermochronometers in rapidly exhuming regions (Manktelow and Grasemann, 1997; Braun, 2002; Ehlers, 2005) and thus needs to be taken in account

The large-scale structure of active mountain ranges is efficiently described, to a first order, by the doubly-vergent critical-wedge concept (Willett et al., 1993; Batt and Braun, 1997; Beaumont et al., 2000; Figure 1a). In this model, the upper and middle crust of the underthrusting ("pro-") plate is effectively decoupled from the underlying mantle, which undergoes continental subduction underneath the "retro"-plate. Particle paths within the crust define a deforming double wedge in which material is transported from the pro- to the retro-wedge. Recent geophysical data has highlighted continental subduction of Indian lithosphere beneath Tibet (Schulte-Pelkum et al., 2005; Hetényi, 2007). However, exhumation in the central Himalaya is strongly focussed in the frontal part of the orogenic pro-wedge (Lavé and Avouac, 2001; Avouac, 2003). This differs from smaller-scale orogens such as Taiwan or the Southern Alps of New Zealand, where erosion is focused in the retro-wedge (Willett, 1999; Batt et al., 2000; Willett et al., 2003), as predicted by the doubly-vergent wedge model. The locus of maximum exhumation in an orogenic wedge is controlled by climate, in particular by the asymmetry of precipitation due to orographic effects (Willett, 1999; Stolar et al., 2007) and orogaphic focusing of precipitation is particularly strong in the Himalaya (Bookhagen and Burbank, 2006). However, models suggest that orographic precipitation focused on the pro-wedge may shift the locus of maximum exhumation toward the central part of the orogen, as observed for instance in the Olympic Mountains of the western US (Willett, 1999; Batt et al., 2001), but it is difficult to shift this locus further into the pro-wedge. Two possibilities have been proposed to explain the translation of the locus of maximum exhumation to the front of the pro-wedge: crustal channel flow (Beaumont et al., 2001; 2004; Figure 1b) or underplating (Avouac, 2003; Bollinger et al., 2006; Figure 1c).

Numerical models that have been developed in recent years to improve our understanding of the central Himalaya are mostly thermo-kinematic (Bollinger et al., 2006; Brewer and Burbank, 2006; Wobus et al., 2006; Whipp et al., 2007), i.e., the kinematics are explicitly described through an *a-priori* crustal structure and a kinematic rule set; the model predicts the associated thermal structure and cooling/exhumation pathways. Some thermo-mechanical models, in which the crustal kinematics are predicted from a set of boundary conditions and rheological flow laws, have also been developed (Cattin and Avouac, 2000; Beaumont et al., 2001; 2004; Jamieson et al., 2004). Most models are two-dimensional (2D) and model a crustal profile (Cattin and Avouac, 2000; Beaumont et al., 2001; 2004; Jamieson et al., 2004; Bollinger et al., 2006; Wobus et al., 2006). Some three-dimensional (3D) or pseudo-3D approaches, which take in account 3D topography in order to better predict the influence of topography on the near-surface thermal field, have also been developed (Brewer and Burbank, 2006; Whipp et al., 2007). In contrast to the thermo-kinematic models, which concentrate on the most recent evolution of the central Himalaya (i.e., the last few million years), the thermo-mechanical models of Beaumont et al. (2001; 2004) and Jamieson et al. (2004) model the evolution of the central Himalaya over the entire (50-60 My) orogenic phase.

Numerical model predictions have mostly been tested against thermochronological data for systems with different closure temperatures (i.e. apatite and zircon fission-track, mica Ar-Ar data) and peak pressures and temperatures recorded by metamorphic rocks. Model applications have been heavily concentrated on central Nepal because this region concentrates the most extensive thermochronological and metamorphic datasets (Macfarlane, 1995; Arita et al., 1997; Fraser et al., 2000; Catlos et al., 2001; Bollinger et al., 2004; Blythe et al., 2007)

together with good constraints on crustal geometry (Cattin et al., 2001; Avouac, 2003; Schulte-Pelkum et al., 2005).

However, although model parameters are similar and models are tested against the same datasets, results and interpretations of model predictions strongly differ amongst authors. Avouac (2003) and Bollinger et al. (2006) argue for frontal propagation of the deformation combined with crustal underplating that forms a major duplex. In contrast, Beaumont et al. (2004) and Jamieson et al. (2004) invoke a channel-flow model to explain the spatial distribution of peak metamorphic conditions. Hodges et al. (2004) suggest out-of-sequence thrusting to explain patterns of low-temperature thermochronologic ages, but implicitly associate this model with channel flow (cf. Hodges, 2006). It thus appears timely at this stage to synthesise, compare and critically evaluate these different models in order to understand their key points and real or supposed differences. This exercise is a necessary starting point for new modelling studies.

Here, we compare the different recent thermo-kinematic and thermo-mechanical models, exploring their differences and potentially hidden similarities, as well as their limits and their application to the central Himalaya. We start out by defining some generally loosely used terms and building a common reference frame. We briefly review what is known about the tectonic evolution of the central Nepal Himalaya before reviewing in detail the different model studies. This review leads us to suggest that model outcomes may be more similar than suggested by their authors, to define what the fundamental differences between the models are and to propose a strategy to discriminate between the different scenarios proposed in the literature.

2. Orogen kinematics: definitions and reference frames

In this section, we examine the different components of convergent motion that have been proposed for the central Himalaya. Although we follow previous analyses of this type (DeCelles and DeCelles, 2001; Avouac, 2003; Simoes et al., 2007), we prefer to define terms explicitly here as they remain rather loosely applied. We analyse an orogenic prism overriding a crustal-scale flat-ramp-flat thrust (Figure 2), such as envisaged in the central Himalaya (Avouac, 2003; Schulte-Pelkum et al., 2005; Hetényi, 2007). For a reference frame fixed to the (Indian) footwall or pro-plate, this motion can be subdivided into the following fundamental modes:

(1) Overthrusting (Figure 2a): the fault is fixed with respect to the footwall; the convergence velocity (V) equals the overthrusting velocity. Material is exhumed from the hangingwall; no deformation occurs in the footwall. Overthrusting can take place along the main basal detachment, as illustrated in Figure 2a, or along a surface-breaking fault within the overriding hanging-wall block, in which case it is termed “out-of-sequence”;

(2) Underthrusting (Figure 2b): the fault is fixed with respect to the hangingwall and thus moves in the direction of the underthrusting block with a velocity $V_u = V$ (in the case of pure underthrusting). In this case, no material from the footwall is exhumed by the fault and no deformation occurs in the hangingwall. Both modes (1) and (2) exclude material transfer from one block to the other and are clearly two extreme cases of the possible kinematics. Amongst the numerous possible cases that relax this condition, the following are usually inferred:

(3) Underplating (with potential duplex formation; Figure 2c): the deep ramp part of the fault moves toward the footwall at a velocity of V_{up}. Footwall material is thus incorporated into the hangingwall via an underplating window that represents a ‘porous’ part of the crustal

fault where matter can cross from the footwall to the hangingwall and eventually be exhumed, if underplating is combined with overthrusting. Duplex formation is a special case of underplating where matter crosses the underplating window discontinuously through time. This scheme is invoked by Avouac (2003) and Bollinger et al. (2004) to explain strong exhumation of the pro-wedge in the Himalaya. Note that pure underplating is not sustainable through time because the deep crustal ramp will rapidly 'overtake' the surface-breaking frontal fault;

(4) Frontal fault propagation (Figure 2d) is likened to underplating, but in this case it is the upper ramp and the surface-breaking front of the fault that moves toward the footwall at a velocity V_p. Material coming from the upper part of the underthrusting plate is incorporated in the frontal prism and can be exhumed at the front if frontal propagation is associated with overthrusting. In terms of critical-wedge kinematics, modes (3) and (4) are often referred to as "basal accretion" and "frontal accretion", respectively (e.g., Batt et al., 2001; Simoes et al., 2007);

(5) Channel flow (Figure 2e) denotes the kinematic situation where the velocity along a single thrust fault (in a reference frame fixed to the pro-plate) is greater than the overall convergence rate. There is no horizontal advection of the main fault, but a high velocity zone in the overthrusting block builds a channel that forces rocks to be exhumed. The thrust at the base of the channel is necessarily associated with a normal fault in its hangingwall, which forms the 'roof' of the channel, in order to satisfy the definition that the velocity in the channel is greater than the overall convergence rate. In the scenario inferred for the central Himalaya (Beaumont et al., 2001; 2004; Jamieson et al., 2004), channel flow occurs in a position of out-of-sequence thrusting, but this is not necessarily the case. The only kinematic difference between (out-of-sequence) channel flow and out-

of-sequence overthrusting is the necessity for concomitant extensional faulting in the former.

Note that of the above modes of convergence, only overthrusting and channel flow will lead to exhumation of rocks (for steady-state topography), whereas fault propagation and underplating provide mechanisms for transferring material from the footwall to the hangingwall. The kinematics of mountain building can be described by any combination of these processes (but not by any single process on its own). The questions are: are all of them compatible with each other, can the fundamental mode change through time and what are the controls on which mode operates?

3. Tectonic setting of the central Himalaya

3.1. Structure

The Himalayan orogen is characterized by a north-dipping, southward-propagating, crustal-scale thrust sequence (Figure 3). Major thrusts delimit three distinct units that are, from south to north: the Siwaliks foreland fold-and-thrust belt between the Main Frontal (MFT) and the Main Boundary (MBT) thrusts; the metasediments of the Lesser Himalaya between the MBT and the Main Central Thrust (MCT); the Greater Himalayan crystalline thrust sheet with overlying Tethyan sediments (Gansser, 1964; Le Fort, 1975). The latter unit is separated from the Tibetan or Tethyan Himalayan zone by the extensional South Tibetan Detachment System (STDS). Structural and geochronological data indicate that the MCT and STDS were simultaneously active during middle Miocene times (Burchfiel et al., 1992; Hodges, 2000), whereas the more frontal thrusts have been sequentially activated since that time (cf. next section). Geophysical and structural studies suggest that all major faults in the central Himalaya, including the MFT, MBT and MCT, branch at depth to a single major mid-crustal décollement, the Main Himalayan Thrust (MHT; Hirn and Sapin, 1984; Zhao et al., 1993;

Makovsky et al., 1996; Schulte-Pelkum et al., 2005). The MHT is characterized by a ramp-flat geometry, probably with two major ramps. One is shallow and corresponds to where the fault emerges with a dip angle of around 30° at the surface (MFT). The other is envisaged at mid-crustal depth beneath the sharp topographic front of the high range (Avouac, 2003; Figure 3). Although geophysical data suggest a dip angle of ~15° for this ramp (Lemonnier et al., 1999; Pandey et al., 1999), mechanical modelling based on the present-day displacement field (Berger et al., 2004) rather suggests a ramp angle of ~30°. The Lesser Himalaya forms a crustal scale antiformal stack or duplex (Schelling and Arita, 1991; DeCelles et al., 2001; Figure 3b) on top of which klippen of Greater Himalayan rocks are locally preserved in synclinal structures (the largest one of which is the Kathmandu klippe in central Nepal).

Ten to thirty kilometres south of the MCT zone in central Nepal, a sharp physiographic transition marks the morphology by separating a northern high-relief zone at a mean elevation >3000 m and a southern zone of more moderate relief at a mean elevation <1500 m (Lavé and Avouac, 2001; Duncan et al., 2003; Wobus et al., 2003). This physiographic transition is situated above the inferred deep ramp of the MHT and is interpreted in different ways, related to the kinematic models proposed for the central Himalaya: either as a result of overthrusting over the mid-crustal MHT ramp (Lavé and Avouac, 2001), as a result of underplating and duplex formation at the ramp (Avouac, 2003; Bollinger et al., 2006) or as reflecting Quaternary out-of-sequence thrusting in the MCT zone (Wobus et al., 2003; Hodges et al., 2004).

3.2. Kinematics

Determinations of present-day convergence across the Himalaya from GPS measurements range from 13 to 21 $mm.y^{-1}$ (Bilham et al., 1997; Larson et al., 1999; Jouanne et al., 2004).

GPS measurements show a west-to-east increase in convergence rate, qualitatively consistent with the location of the rotation pole of the India-Asia collision (Paul et al., 2001). Lavé and Avouac (2000) and Mugnier et al. (2004) infer Holocene shortening rates of 14-21 $mm.y^{-1}$ across the MFT in Nepal from folded and uplifted river terraces. Quaternary convergence rates across the Siwaliks in Nepal, as derived from balanced cross-sections, are ~19 $mm.y^{-1}$ (Mugnier et al., 2004). On longer time-scales, Mio-Pliocene rates of convergence across the Lesser Himalaya are 19-22 $mm.y^{-1}$ (DeCelles et al., 2001) and propagation rates of the Ganges foreland basin during the same time interval are 10-24 $mm.y^{-1}$ (Lyon-Caen and Molnar, 1985; Mugnier and Huyghe, 2006).

Although the above rates are all quantitatively similar, they do not all reflect the same components of motion. The present-day and Holocene convergence rates reflect the sum of underthrusting of India and overthrusting of the Himalaya, whereas the Quaternary and longer-term shortening rates should reflect overthrusting plus forward propagation of the frontal fault. The propagation rate of the Ganges foreland basin, in contrast, reflects forward propagation and/or underthrusting (DeCelles and DeCelles, 2001). Different estimates for the overthrusting velocity have been published: present-day geodetic uplift rates as well as short-term fluvial incision rates have been interpreted to suggest overthrusting rates equal to the total convergence of ~21 $mm.y^{-1}$ (Cattin and Avouac, 2000; Lavé and Avouac, 2001), whereas in contrast, Bollinger et al. (2006) and Brewer and Burbank (2006) argue that thermochronological ages of both Greater and Lesser Himalayan rocks require overthrusting rates of no more than 5-6 $mm.y^{-1}$. In the latter case, the underthrusting velocity thus has to be ~15 $mm.y^{-1}$. Thrusts in the Lesser Himalaya indicate a forward propagating sequence that initiated after cessation of activity on the MCT (which was active at 20-25 Ma). Thrusts in the internal Lesser Himalayas are active between ~12 and 15 Ma (DeCelles et al., 2001; Robinson

et al., 2006) and the Lesser Himalayan duplex was built since ~10 Ma (DeCelles et al., 2001; Huyghe et al., 2005; Robinson et al., 2006). The MBT is active around 5 Ma (Meigs et al., 1995; DeCelles et al., 2001; Huyghe et al., 2001) and the MFT since ~2 Ma (Mugnier et al., 2004; van der Beek et al., 2006), suggesting long-term frontal propagation at a (poorly constrained) rate of 5-15 $mm.y^{-1}$.

4. Thermo-kinematic and thermo-mechanical models for the central Himalaya

4.1. Model Setup

The thermo-kinematic models we discuss here generally consist of three components: (1) a kinematic model that prescribes particle paths and nodal advection velocities; (2) a thermal (finite-element) model that tracks the calculated temperature field through time; and (3) a thermochronometer age-prediction model. Extension along the STDS is ignored in all thermo-kinematic models and no crustal channel flow, located between MCT and STD is considered. This is in contrast to the thermo-mechanical models of Beaumont et al. (2001; 2004) and Jamieson et al. (2004), which mainly focus on this channel flow.

The crustal geometry of all thermo-kinematic models is based on the crustal cross-section proposed by Avouac (2003) (Figure 4). The major difference consists of the presence of an underplating window in the models of Wobus et al. (2006) and Bollinger et al. (2006). These models apply a linear, gently dipping MHT (10-18°) whereas models that only model over- and underthrusting (Brewer and Burbank, 2006; Whipp et al., 2007) include a ramp with higher dip (18-28°; Figure 4; Table 1). The ramp dip and location control the exhumation rate and pattern for simple overthrusting models, whereas these are controlled by the locus and rate of underplating in the underplating models. The underplating window extends from 70 to

150 km north from the MFT in Bollinger et al. (2006). In Wobus et al. (2006), the size of the underplating window is not specified but appears to encompass the entire MHT ramp. Whipp et al. (2007) explicitly test the existence of out-of-sequence faulting in the MCT zone by including a surface-breaking fault above the MHT ramp and partitioning the overthrusting velocity between this fault and the MHT.

The size of the model domain differs somewhat between different models, especially in length, from 100 km (Wobus et al., 2006) to 220 km (Bollinger et al., 2006). This may affect predicted particle and time-temperature paths. For a model including an overthrusting rate of 5 km.My^{-1} since 20 Ma, a particle currently at the surface has been displaced laterally by 100 km. When the modelled domain is smaller in length than 100 km (e.g., Wobus et al., 2006), this may affect predicted ages. However, Wobus et al. (2006) do not explicitly predict thermochronological ages and particle paths, but rather focus on the (steady-state) thermal structure of the orogen.

As concerns the thermal calculations, only Bollinger et al. (2006) consider a transient thermal field; the other three models use thermal steady state. Thermal parameters used in the different models are grossly similar (Table 1). The most important difference consists in the value of the basal heat flow, which varies by a factor of two (15 to 30 mW.m^{-2}) at a pre-defined depth (50 or 100 km). The imposed basal heat flow may strongly affect thermal predictions. Whipp et al. (2007) show that increasing the heat flux into the base of the thermal model increases the maximum temperature within the model domain and steepens the thermal gradient near the surface. In consequence, the distance from a given closure isotherm to the surface is reduced and the predicted thermochronological age pattern at the surface is

uniformly younger. However, varying the basal heat flow only shifts the isotherms up or down and does not deform them.

To compare the kinematics of the different models, it is important to describe all of them in the same reference frame. Because of the high overall convergence velocity in the Himalaya, using the (Indian) footwall plate as a reference frame, as we did in Section 2, would require modelling an excessively large hangingwall domain (e.g., 400 km for a model applying a 20 $mm.y^{-1}$ convergence for 20 My). Therefore, all models use a reference frame in which the MHT ramp is fixed, and have the surface trace of either the MBT or the MFT for origin. Because all models also include steady-state topography, they implicitly assume that the topography is advected with the hangingwall rocks at the velocity of frontal propagation and/or underthrusting. Figure 4 shows characteristic particle paths and Table 1 writes out the kinematic rule set for each model. To a first order, the four models presented follow a similar scheme, with convergence partitioned into ~5 $mm.y^{-1}$ of overthrusting and ~15 $mm.y^{-1}$ of underthrusting velocities. This partitioning appears to be required in order to fit the thermochronological data, as tested explicitly by Brewer and Burbank (2006).

The kinematics of the Wobus et al. (2006) model consists of an underthrusting and overthrusting velocity, which are both specified parallel to the MHT fault plane. These are combined with an accretion velocity (equivalent to the underplating velocity in our terminology) by vector summing. The detailed particle trajectories along the MHT are unclear in this model – it appears that accretion can take place along the entire fault plane, which would seem inconsistent with the definition of the MHT as a major crustal discontinuity. Bollinger et al. (2006) take a similar approach as Wobus et al. (2006) but limit accretion to a spatially restricted underplating window within the MHT, which appears physically more

plausible. In both models, however, the geometry of the MHT does not change with time. This implies forward propagation of the fault at the same rate as underthrusting (cf. Figure 2), although neither model includes such propagation.

In the model of Whipp et al. (2007), all faults are stable with respect to an external reference frame. The crustal block between the MFT and MCT is thus isolated from the rest of the model, but has its own internal kinematics, which are discontinuous from the underthrusting plate and from the hangingwall of the MCT. No underplating is included in the model, which implies that either (1) the mass conservation equation is not respected, (2) there must be extension at the surface of the block between the MCT and MFT, or (3) crustal material crosses the MCT. Thus, the kinematics of the Whipp et al. (2007) model does not appear entirely self-consistent, but this choice is made for numerical simplicity. To solve this problem, either the MCT should be advected along the MHT with the same velocity as that of the block between the MCT and MFT, or there should be underplating on the MHT ramp.

The "channel-flow" models of Beaumont et al. (2001, 2004) and Jamieson et al. (2004) differ from the other models because they are thermo-mechanical rather than thermo-kinematic (Figure 5). They are also run over much longer times (typically >50 My) than the kinematic models. Deformation is driven by underthrusting of the Indian plate by the full convergence velocity of 20 $mm.y^{-1}$ to the left of a velocity discontinuity or "S-point", whereas basal velocity is 0 to the right of this point. The model reference frame is built around this point, which itself is not fixed but moves in time toward the Tibetan retrowedge (which is fixed with respect to an external reference frame). Figure 5 presents some representative particle paths for this model. The thermal field is calculated, using similar thermal parameters as in the thermo-kinematic models, over the full subducting lithosphere. The models are characterized

by a weakened layer in the middle crust that allows channel flow and a time-dependent surface denudation model that is function of slope and relief. They typically evolve through an initial crustal-thickening phase of 20-30 My duration in which there is no surface erosion. Subsequently, a phase of focused erosion at the Himalayan front sets up the channel flow and exhumation of middle crustal material. In order to predict peak metamorphic temperatures and times of cooling that are compatible with observations in the central Himalaya, denudation rates need to drop considerably over the last ~15 Ma. The crustal kinematics is strongly controlled by gravity forcing from the overthickened Tibetan retro-wedge.

There has been some confusion about whether inferred out-of-sequence reactivation of the MCT zone in central Nepal (Wobus et al., 2003; Hodges et al., 2004; Wobus et al., 2005) can be likened to channel flow. The predicted crustal geometry and kinematics of most models presented by Beaumont et al. (2004) and Jamieson et al. (2004) is comparable to out-of-sequence thrusting in that the channel reaches the surface inboard of the deformation front, but the main period of activity of the channel takes place during the intermediate stages of the model run rather than in the recent past; therefore, the model does not explain the inferred recent reactivation of the MCT zone.

4.2. Model constraints

To constrain the predictions of thermo-kinematic models, authors use either *in-situ* (Bollinger et al., 2006; Whipp et al., 2007) or detrital (Brewer and Burbank, 2006; Wobus et al., 2006) low temperature thermochronological data, which record the cooling history of exhumed samples. Thermochronological systems used are mostly muscovite Ar-Ar and apatite fission track, with respective closure temperatures of ~350 °C and ~110 °C. Most of this data is from the Marsyandi River in central Nepal and was collected in the High Himalaya and/or the

MCT zone (transition High Himalaya – Lesser Himalaya). There is very few data from the southern part of the Lesser Himalaya, due mainly to unfavourable lithologies. Both AFT and Ar-Ar ages are very young in the MCT zone (typically <2 Ma and <4 Ma respectively; Copeland et al., 1991; Bollinger et al., 2004; Huntington and Hodges, 2006; Blythe et al., 2007) and increase both toward the north and toward the south to ~8 Ma for AFT and ~20 Ma for mica Ar-Ar. Bollinger et al. (2006) use the observed linear southward increase in mica Ar-Ar ages at a rate of ~0.24 $My.km^{-1}$ to place constraints on the overthrusting rate (~5 $km.My^{-1}$) in their model.

Both Brewer and Burbank (2006) and Wobus et al. (2006) use detrital mica Ar-Ar thermochronologicy data to fit their model, from the Marsyandi and the Burhi Gandaki, Trisuli and Bhote Kosi rivers in central-west and central Nepal, respectively. Whereas Brewer and Burbank (2006) concentrate on the high-exhumation MCT zone and the Higher Himalaya, Wobus et al. (2006) report a major break in detrital mica Ar-Ar ages from a mode of ~8 Ma north of the physiographic transition to modal ages of 1.0-2.0 Ga immediately south of it. This strong transition between young and completely unreset mica Ar-Ar ages places strong constraints on their model. However, it seems surprising to find such unreset Proterozoic mica Ar-Ar ages in Lesser Himalayan rocks mostly younger than 1.9 Ga (DeCelles et al., 2000; Yin, 2006 and references therein), because no pre-Himalayan Ar-Ar ages have been reported from *in-situ* bedrock samples in this part of the Lesser Himalaya and the Kathmandu nappe (Arita et al., 1997; Rai, 1998; Bollinger et al., 2004). Further west, in the Marsyandi region and in far-western Nepal, some pre-Himalayan mica Ar-Ar ages have been reported for rocks from the Lesser Himalaya at location 15-30 km south of the MCT but not closer to it (Copeland et al., 1991; Catlos et al., 2001; Robinson et al., 2006). An extensive detrital Ar-Ar study within the Marsyandi catchment (Brewer et al., 2006), encompassing the

Tethyan, Greater and Lesser Himalaya, did not report any pre-Himalayan cooling ages. Moreover, given the recorded peak metamorphic temperatures of >350°C for Lesser Himalayan rocks in central Nepal (Bollinger et al., 2004), mica Ar-Ar ages should be reset during Himalayan tectonism. Thus, we do not understand the origin of these exceedingly old detrital mica Ar-Ar ages, nor their geological significance.

Petrologic constraints have also been used. Bollinger et al. (2006) incorporate the distribution of peak metamorphic temperature documented from Raman Spectroscopy of Carbonaceous Material (RSCM) thermometry (Beyssac et al., 2004; Bollinger et al., 2004); peak metamorphic temperatures vary typically between 550°C near the MCT to about 350°C in the southernmost samples. Beaumont et al. (2001) and Jamieson et al. (2004) use peak metamorphic pressure-temperature estimates and in situ Ar-Ar ages to constrain the earlier (Miocene) phases of model evolution, but not the more recent phases.

4.3. Model conclusions

Channel-flow models (Beaumont et al., 2001; 2004; Jamieson et al., 2004), in which a low – viscosity crustal channel is extruded due to the gravitational force of the overthickened Tibetan Plateau coupled to focused surface denudation, provide an internally self-consistent explanation for many observed features of the Himalayan – Tibetan system (Nelson et al., 1996; Hodges, 2000). Model predictions agree fairly well with peak metamorphic ages from both the Greater and the Lesser Himalaya and with Lesser Himalayan cooling ages (Jamieson et al., 2004). However, the model requires significant slowing down of erosion after ~20 Ma in order to provide these fits (Beaumont et al., 2001; Jamieson et al., 2004). Even so, predicted Greater Himalayan cooling ages are 5 to 10 Ma younger than measured ages.

Bollinger et al. (2006) show that observed peak metamorphic temperatures and cooling ages are equally well explained by a model of continuous underplating coupled to spatially variable erosion at the Himalayan topographic front since ~10 Ma. As the model assumes steady-state topography, it requires sustained high and spatially variable erosion rates that equal rock uplift rates throughout the last 10 My, in contrast to the channel-flow model predictions. The underplating model also provides an internally consistent explanation for the occurrence of Greater Himalayan klippen. This model does not include late MCT reactivation nor disproves it, but suggest that this process may not be essential to explain the first-order observations of structure and metamorphism for the Kathmandu transect. The model predicts a gradient of exhumation ages (increasing toward the south), which is controlled by overthrusting velocity and can thus be used to constrain the latter.

Although the model of Bollinger et al. (2006) is geometrically and kinematically very similar to that of Wobus et al. (2006), the latter authors' conclusions differ from the previous. Wobus et al. (2006) allow for out-of-sequence thrusting and compare model predictions for both underplating and out-of-sequence thrusting models. They show that continuous accretion (underplating) and discrete (out-of-sequence) surface faulting are both plausible mechanisms for producing the observed pattern of mica Ar-Ar cooling ages in the central Himalaya. But out-of-sequence surface thrusting at the physiographic transition provides the simplest explanation for the distribution of cooling ages they use to constrain their model. In particular, the very old detrital Ar-Ar ages they report just south of the physiographic transition can only be explained by a limited set of conditions in the underplating model, but follows directly from the kinematics of the out-of-sequence thrusting model regardless of overthrusting velocities. They suggest that the kinematics of the central Himalaya may evolve in time from underplating and duplex formation to focussed out-of-sequence thrusting and that spatial

variations between the two styles of deformation are present due to the laterally varying depth of erosion.

Whipp et al. (2007) compared a scenario of simple ramp overthrusting (without underplating) with an out-of-sequence model. They applied their model to the Marsyandi valley and also show that existing thermochronology data cannot be used to discriminate between these two models. Predicted ages depend more on the erosion rate generated by the kinematic model than on the kinematic scenario. A major conclusion of this study is that there have been no major changes in the topographic relief since the samples cooled through their closure temperature because the model topography is in steady state and the model yields predicted ages that fit the data. This is compatible with other models.

Finally, Brewer and Burbank (2006) did not set out to test the existence or absence of out-of-sequence faulting at the physiographic transition. They use a simple ramp overthrusting model in order to search for a kinematic scenario that allows to explain the observed pattern in detrital mica Ar-Ar ages throughout the Higher Himalaya, which young from north to south (i.e. toward the MCT). Mean detrital Ar-Ar ages provide fairly tight constraints on the rate of overthrusting and the ramp dip (~5 km.My^{-1} and ~18° respectively), although tradeoffs clearly exist between these two parameters. Finally, the models do not predict the observed detrital age distribution very well, implying additional complexity in the response of the detrital signal that is not captured by the model.

5. Discussion and conclusion

Although the models discussed above have led the authors to very different and sometimes opposing conclusions, none of them provide unambiguous arguments in favour or against the different kinematic hypotheses for the central Himalaya. In fact, the models are not extremely different in terms of kinematics or thermal parameters. Three main classes of kinematic models can be distinguished: channel flow or out-of-sequence thrusting (which are kinematically similar, at least south of the STDZ), ramp overthrusting and underplating. As explained below, the latter two are probably linked at long timescales.

All models are able to predict the available thermochronologic data relatively well. The least successful in this respect is the channel-flow model, which requires erosion to be nearly "shut off" over the last 10-15 My and yet predicts too young mica Ar-Ar ages throughout the Greater Himalayan Sequence. The model also does not take into account the Miocene to present forward propagation of deformation from the MCT toward the MFT. It therefore appears that this model is best applied to the Miocene evolution of the Himalaya, when the MCT was probably the frontal thrust of the system, but not the more recent tectonic history. However, Robinson et al. (2006) and Kohn (2008) provide detailed criticisms of the channel-flow model with respect to the outcrop pattern and deformation history of the Greater Himalayan Sequence. In particular, they argue that the model cannot explain the existence of Greater Himalayan klippen far to the south of the present-day trace of the MCT, and that it is inconsistent with the parallel stacked pattern of Greater and Lesser Himalayan rocks in the MCT zone, because it predicts viscous mixing of these at the base of the crustal channel.

The different thermo-kinematic models all predict reasonable patterns of thermochronological ages, which thus cannot be used to discriminate between them. The simplest model of overthrusting on a crustal-scale ramp permits to explain both low- (apatite fission-track) and intermediate (mica Ar-Ar) temperature thermochronology data (Brewer and Burbank, 2006; Whipp et al., 2007) as well as more elaborate models that include underplating or out-of-sequence thrusting.

However, as noted by Bollinger et al. (2004) and Wobus et al. (2006), a simple overthrusting model cannot explain the inverse metamorphic gradient observed in the Lesser Himalaya south of the MCT (e.g., Pêcher, 1989; Macfarlane, 1995; Beyssac et al., 2004), as this would predict that, given sufficient time (i.e. 10-20 My at rates of overthrusting of ~5 $km.My^{-1}$) a continuous southward increase in peak metamorphic temperature and pressure should be established. It therefore needs to be combined with either underplating or out-of-sequence thrusting / channel flow in the long term.

Both thermo-kinematic models for underplating (Bollinger et al., 2006; Wobus et al., 2006) model the process as continuous transfer of material from the underthrusting to the overthrusting plate. For reasons of numerical simplicity, they do not include discrete forward movement of the ramp (according to the definition of underplating in Section 2 and Figure 2) even though Avouac (2003) and Bollinger et al. (2004) envisaged this to be the physical process taking place. The nature of the Lesser Himalayan duplex, which is inferred to result from underplating and which is composed of discrete thrust packages (Schelling and Arita, 1991; DeCelles et al., 2001), clearly indicates the discontinuous nature of the process. Neither of the underplating models in fact includes a ramp in the MHT, as the kinematics is simply controlled by vector addition of an overthrusting and accretion rate (Figure 4c, d). Note,

however, that such kinematics predicts shortening to the north of the underplating window (converging particle paths) and extension to the south of it (diverging particle paths), which is not readily observed in the field.

Another important aspect of the thermo-kinematic models is the partitioning of convergence into overthrusting and underthrusting. All models take the MHT ramp as the reference frame in order to limit the horizontal extent of the model. The idea behind this reference frame is that the topography (which is assumed in steady state in all models) is controlled by the interplay between tectonic advection of rocks and erosion, and the former term is controlled by the crustal geometry. Underthrusting implies that the Indian plate undergoes significant deformation beneath the crustal ramp in the MHT. Although this idea contradicts the paradigm of "undeformable footwalls" in structural geology, there is seismological evidence for such deformation of the underthrusting Indian plate beneath the High Himalaya (de la Torre et al., 2007).

In a more intuitive reference frame fixed to the Indian plate, underthrusting is difficult to distinguish from underplating and simultaneous forward propagation at the same rate (the difference lying in the particle paths of points in the underthrusting Indian plate, which are either depressed by the overriding Himalaya (overthrusting) or are incorporated into it (underplating and forward propagation; cf. Figure 2). This is also evident from the different geological measures of "convergence" or "shortening" rate discussed in Section 3.2, which, when combined, show that they cannot independently estimate the underthrusting or forward propagation rate, only some combination of the two. In a reference frame fixed to India, the Himalayan topography is thus advected by the total convergence rate minus the horizontal

projection of the erosion rate. As shown by Brewer and Burbank (2006), it is in fact this latter quantity that is equivalent to the “overthrusting” rate (Figure 6).

One reason for the divergence or lack of conclusions from the different thermo-kinematic models is that they are mainly constrained by data from the Greater Himalaya, and the history of the Lesser Himalayan rocks remains essentially unconstrained. Low–temperature thermochronological ages in the hanging wall are very young (typically <2 Ma for AFT ages and <4 Ma for mica Ar-Ar) so that it will be very difficult to extract a signal of potential out-of-sequence faulting from them. Furthermore, particle paths in the hanging wall of the MCT are fairly similar in both trajectory and velocity in both models. In contrast, the shape of a thermochronological age transect through the Lesser Himalaya and the topographic transition should be more discriminative regarding the presence or absence of out-of-sequence faulting in the MCT zone (Figure 7), as in one case there should be a clear jump in both low- and intermediate-temperature ages, whereas in the other both should show a continuous decrease toward the MCT zone. Thus, to better constrain the recent kinematics of the central Himalaya, new data from the southern part of the Lesser Himalaya (Figure 7) should be collected and the whole transect from the MFT in the south to the Greater Himalaya in the north modelled. Given the unfavourable lithologies that characterize most of the Lesser Himalaya, this will be no easy task.

Acknowledgements

This research was funded by INSU-CNRS through the *Reliefs de la Terre* programme. J.-P. Avouac and L. Bollinger are thanked for constructive discussions.

References

Arita, K., Dallmeyer, R.D. and Takasu, A., 1997. Tectonothermal evolution of the Lesser Himalaya, Nepal: Constraints from $^{40}Ar/^{39}Ar$ ages from the Kathmandu Nappe. Isl. Arc, 6: 372-385.

Avouac, J.P., 2003. Mountain building, erosion and the seismic cycle in the Nepal Himalaya. Adv. Geophys., 46: 1-79.

Batt, G.E., Brandon, M.T., Farley, K.A. and Roden-Tice, M., 2001. Tectonic synthesis of the Olympic Mountains segment of the Cascadia wedge, using two-dimensional thermal and kinematic modeling of thermochronological ages. J. Geophys. Res., 106: 26731-26746.

Batt, G.E. and Braun, J., 1997. On the thermo-mechanical evolution of compressional orogens. Geophys. J. Int., 128: 364-382.

Batt, G.E., Braun, J., Kohn, B.P. and McDougall, I., 2000. Thermochronological analysis of the dynamics of the Southern Alps, New Zealand. Geol. Soc. Am. Bull., 112: 250-266.

Beaumont, C., Jamieson, R.A., Nguyen, M.H. and Lee, B., 2001. Himalayan tectonics explained by extrusion of a low-viscosity channel coupled to focused surface denudation. Nature, 414: 738-742.

Beaumont, C., Jamieson, R.A., Nguyen, M.H. and Medvedev, S., 2004. Crustal channel flows: 1. Numerical models with applications to the tectonics of the Himalayan-Tibetan orogen. J. Geophys. Res., 109: B06406, doi:10.1029/2003JB002809.

Beaumont, C., Kooi, H. and Willett, S., 2000. Progress in coupled tectonic - surface process models with applications to rifted margins and collisional orogens. In: M.A. Summerfield (Editor), Geomorphology and Global Tectonics, Wiley, Chichester, pp. 29-56.

Berger, A., Jouanne, F., Hassani, R. and Mugnier, J.L., 2004. Modelling the spatial distribution of present-day deformation in Nepal: how cylindrical is the Main Himalayan Thrust in Nepal? Geophys. J. Int., 156: 94-114.

Beyssac, O., Bollinger, L., Avouac, J.-P. and Goffé, B., 2004. Thermal metamorphism in the lesser Himalaya of Nepal determined from Raman spectroscopy of carbonaceous material. Earth Planet. Sci. Lett., 225: 233-241.

Bilham, R., Larson, K., Freymueller, J. and Project IDYLHIM Members, 1997. GPS measurements of present-day convergence across the Nepal Himalaya. Nature, 386: 61-64.

Blythe, A., Burbank, D.W., Carter, A., Schmidt, K.L. and Putkonen, J., 2007. Plio-Quaternary exhumation history of the central Himalaya: 1. Apatite and zircon fission-track and apatite [U-Th]/He analyses. Tectonics, 26: TC3002, doi:10.1029/2006TC001990.

Bollinger, L. et al., 2004. Thermal structure and exhumation history of the Lesser Himalaya in central Nepal. Tectonics, 23: TC5015, doi:10.1029/2003TC001564.

Bollinger, L., Henry, P. and Avouac, J.P., 2006. Mountain building in the Nepal Himalaya: Thermal and kinematic model. Earth Planet. Sci. Lett., 244: 58-71.

Bookhagen, B. and Burbank, D.W., 2006. Topography, relief, and TRMM-derived rainfall variations along the Himalaya. Geophys. Res. Lett., 33: doi:10.1029/2006GL026037.

Braun, J., 2002. Quantifying the effect of recent relief changes on age-elevation relationships. Earth Planet. Sci. Lett., 200: 331-343.

Brewer, I.D. and Burbank, D.W., 2006. Thermal and kinematic modeling of bedrock and detrital cooling ages in the central Himalaya. J. Geophys. Res., 111: doi:10.1029/2004JB003304.

Brewer, I.D., Burbank, D.W. and Hodges, K.V., 2006. Downstream development of a detrital cooling-age signal: Insights from $^{40}Ar/^{39}Ar$ muscovite thermochronology in the Nepalese Himalaya. In: S.D. Willett, N. Hovius, M.T. Brandon and D.M. Fisher (Editors), Tectonics, Climate, and Landscape Evolution. Geological Society of America Special Paper, 398, pp. 321-338.

Burchfiel, B.C. et al., 1992. The South Tibetan detachment system, Himalayan orogen: Extension contemporaneous with and parallel to shortening in a collisional mountain belt. Geological Society of America Special Paper, 269, 41 pp.

Catlos, E.J. et al., 2001. Geochronologic and barometric constraints on the evolution of the Main Central Thrust, central Nepal Himalaya. J. Geophys. Res., 106: 16177-16204.

Cattin, E. and Avouac, J.P., 2000. Modeling mountain building and the seismic cycle in the Himalaya of Nepal. J. Geophys. Res., 105: 13389-13408.

Cattin, R. et al., 2001. Gravity anomalies, crustal structure and thermo-mechanical support of the Himalaya of Central Nepal. Geophys. J. Int., 147: 381-392.

Copeland, P. et al., 1991. An Early Pliocene thermal disturbance of the Main Central Thrust, central Nepal: Implications for Himalayan tectonics. J. Geophys. Res., 96: 8475-8500.

de la Torre, T.L., Monsalve, G., Sheehan, A.F., Sapkota, S. and Wu, F., 2007. Earthquake processes of the Himalayan collision zone in eastern Nepal and the southern Tibetan Plateau. Geophys. J. Int., 171: 718-738 doi:10.1111/j.1365-246X.2007.03537.x.

DeCelles, P.G. and DeCelles, P.C., 2001. Rates of shortening, propagation, underthrusting, and flexural wave migration in continental orogenic systems. Geology, 29: 135-138.

DeCelles, P.G., Gehrels, G.E., Quade, J., LaReau, B. and Spurlin, M., 2000. Tectonic implications of U-Pb zircon ages of the Himalayan orogenic belt in Nepal. Science, 288: 497-499.

DeCelles, P.G. et al., 2001. Stratigraphy, structure, and tectonic evolution of the Himalayan fold-thrust belt in western Nepal. Tectonics, 20: 487-509.

Duncan, C., Masek, J. and Fielding, E., 2003. How steep are the Himalaya? Characteristics and implications of along-strike topographic variations. Geology, 31: 75-78.

Ehlers, T.A., 2005. Crustal thermal processes and thermochronometer interpretation. In: P.W. Reiners and T.A. Ehlers (Editors), Low-temperature Thermochronology: Techniques, Interpretations, and Applications, Mineralogical Society of America/Geochemical Society Reviews in Mineralogy and Geochemistry, 58, pp. 315-350.

Fraser, G., Worley, B. and Sandiford, M., 2000. High-precision geothermobarometry across the High Himalayan metamorphic sequence, Langtang Valley, Nepal. J. Metam. Geol., 18: 665-681.

Galy, A., 1999. Etude géochimique de l'érosion actuelle de la chaîne himalayenne. Ph.D. Thesis, Institut National Polytechnique de Lorraine, Nancy, 433 pp.

Gansser, A., 1964. Geology of the Himalayas. John Wiley and Sons Ltd., London, 289 pp.

Grujic, D. et al., 2006. Climatic forcing of erosion, landscape, and tectonics in the Bhutan Himalayas. Geology, 34: 801-804.

Hetényi, G., 2007. Evolution of deformation of the Himalayan prism: from imaging to modelling, Ph.D. Thesis, Ecole Nationale Supérieure, Paris, 400 pp.

Hirn, A. and Sapin, M., 1984. The Himalayan zone of crustal interaction; suggestions from explosion seismology. Ann. Geophys., 2: 123-130.

Hodges, K.V., 2000. Tectonics of the Himalaya and southern Tibet from two perspectives. Geol. Soc. Am. Bull., 112: 324-350.

Hodges, K.V., 2006. A synthesis of the Channel Flow-Extrusion hypothesis as developed for the Himalayan-Tibetan orogenic system. In: R.D. Law, M.P. Searle and L. Godin (Editors), Channel Flow, Ductile Extrusion and Exhumation in Continental Collision Zones, Geological Society, London, Special Publication, 268, pp. 71-90.

Hodges, K.V., Wobus, C.W., Ruhl, K., Schildgen, T. and Whipple, K.X., 2004. Quaternary deformation, river steepening, and heavy precipitation at the front of the Higher Himalayan ranges. Earth Planet. Sci. Lett., 220: 379-389.

Huntington, K.W. and Hodges, K.V., 2006. A comparative study of detrital mineral and bedrock age-elevation methods for estimating erosion rates. J. Geophys. Res., 111: doi:10.1029/2005JF000454.

Huyghe, P., Galy, A., Mugnier, J.L. and France-Lanord, C., 2001. Propagation of the thrust system and erosion in the Lesser Himalaya: Geochemical and sedimentological evidence. Geology, 29: 1007–1010.

Huyghe, P., Mugnier, J.L., Gajurel, A.P. and Delcaillau, B., 2005. Tectonic and climatic control of the changes in the sedimentary record of the Karnali River section (Siwaliks of Western Nepal). Isl. Arc, 14: 311-327.

Jamieson, R.A., Beaumont, C., Medvedev, S. and Nguyen, M.H., 2004. Crustal channel flows: 2. Numerical models with implications for metamorphism in the Himalayan-Tibetan orogen. J. Geophys. Res., 109: B06407, doi:10.1029/2003JB002811.

Jouanne, F. et al., 2004. Current shortening across the Himalayas of Nepal. Geophys. J. Int., 157: 11-14.

Kohn, M.J., 2008. P-T-t data from central Nepal support critical taper and repudiate large-scale channel flow of the Greater Himalayan Sequence. Geol. Soc. Am. Bull., 120: 259-273.

Larson, K.M., Bürgmann, R., Bilham, R. and Freymueller, J.T., 1999. Kinematics of the India-Eurasia collision zone from GPS measurements. J. Geophys. Res., 104: 1077-1093.

Lavé, J. and Avouac, J.P., 2000. Active folding of fluvial terraces across the Siwaliks Hills (Himalayas of central Nepal). J. Geophys. Res., 105: 5735-5770.

Lavé, J. and Avouac, J.P., 2001. Fluvial incision and tectonic uplift across the Himalayas of central Nepal. J. Geophys. Res., 106: 25561-25593.

Le Fort, P., 1975. Himalaya: the collided range. Present knowledge of the continental arc. Am. J. Sci., 275: 1-44.

Lemonnier, C. et al., 1999. Electrical structure of the Himalaya of central Nepal: High conductivity around the mid-crustal ramp along the MHT. Geophys. Res. Lett., 26: 3261–3264.

Lyon-Caen, H. and Molnar, P., 1985. Gravity anomalies, flexure of the Indian plate and the structure, support and evolution of the Himalaya and Ganga Basin. Tectonics, 4: 513-538.

Macfarlane, A.M., 1995. An evaluation of the inverted metamorphic gradient at Langtang National Park, Central Nepal Himalaya. J. Metam. Geol., 13: 595-612.

Makovsky, Y., Klemperer, S.L., Liyan, H., Deyuan, L. and Project INDEPTH Team, 1996. Structural elements of the southern Tethyan Himalaya crust from wide-angle seismic data. Tectonics, 15: 997-1005.

Manktelow, N.S. and Grasemann, B., 1997. Time-dependent effects of heat advection and topography on cooling histories during erosion. Tectonophysics, 270: 167-195.

Meigs, A.J., Burbank, D.W. and Beck, R.A., 1995. Middle-Late Miocene (> 10 Ma) formation of the Main Boundary Thrust in the western Himalaya. Geology, 23: 423-426.

Mugnier, J.-L. and Huyghe, P., 2006. Ganges basin geometry records a pre-15 Ma isostatic rebound of Himalaya. Geology, 34: 445-448.

Mugnier, J.L., Huyghe, P., Leturmy, P. and Jouanne, F., 2004. Episodicity and rates of thrust sheet motion in the Himalayas (western Nepal). In: K.C. McClay (Editor), Thrust Tectonics and Petroleum Systems, American Association of Petroleum Geologists Memoir 82, pp. 1-24.

Nelson, K.D. et al., 1996. Partially molten middle crust beneath Southern Tibet: Synthesis of Project INDEPTH results. Science, 274: 1684-1688.

Pandey, M.R., Tandukar, R.P., Avouac, J.P., Vergne, J. and Héritier, T., 1999. Seismotectonics of the Nepal Himalaya from a local seismic network. J. As. Earth Sci., 17: 703-712.

Paul, J. et al., 2001. The motion and active deformation of India. Geophys. Res. Lett., 28: 647-650.

Pêcher, A., 1989. The metamorphism in the Central Himalaya. J. Metam. Geol., 7: 31-41.

Rai, S.M., 1998. Les Nappes de Kathmandou et du Gosainkund, Himalaya du Népal central (Etude cartographique, structurale, métamorphique, géochimique et radiochronologique). Ph.D. Thesis, Université Joseph Fourier, Grenoble, 150 pp.

Robinson, D.M., DeCelles, P.G. and Copeland, P., 2006. Tectonic evolution of the Himalayan thrust belt in western Nepal: Implications for channel flow models. Geol. Soc. Am. Bull., 118: 865-885.

Schelling, D. and Arita, K., 1991. Thrust tectonics, crustal shortening, and the structure of the far eastern Nepal Himalaya. Tectonics, 10: 851-862.

Schulte-Pelkum, V. et al., 2005. Imaging the Indian subcontinent beneath the Himalaya. Nature, 435: 1222-1225.

Simoes, M. et al., 2007. Mountain building in Taiwan: A thermokinematic model. J. Geophys. Res., 112: B11405, doi:10.1029/2006JB004824.

Stolar, D.B., Roe, G.H. and Willett, S.D., 2007. Controls on the patterns of topography and erosion rate in a critical orogen. J. Geophys. Res., 112: F04002, doi:10.1029/2006JF000713.

Thiede, R.C., Bookhagen, B., Arrowsmith, J.R., Sobel, E.R. and Strecker, M.R., 2004. Climatic control on rapid exhumation along the Southern Himalayan Front. Earth Planet. Sci. Lett., 222: 791-806.

van der Beek, P.A. et al., 2006. Late Miocene – Recent exhumation of the central Himalaya and recycling in the foreland basin assessed by apatite fission-track thermochronology of Siwalik sediments, Nepal. Basin Res., 18: 413–434 doi: 10.1111/j.1365-2117.2006.00305.x.

Vannay, J.-C. et al., 2004. Miocene to Holocene exhumation of metamorphic crustal wedges in the NW Himalaya: Evidence for tectonic extrusion coupled to fluvial erosion. Tectonics, 23: TC1014, doi:10.1029/2002TC001429.

Whipp, D.M. et al., 2007. Plio-Quaternary exhumation history of the central Nepalese Himalaya: 2. Thermokinematic and thermochronometer age prediction model. Tectonics, 26: TC3003, doi:10.1029/2006TC001991.

Whipple, K.X. and Meade, B.J., 2006. Orogen response to changes in climatic and tectonic forcing. Earth Planet. Sci. Lett., 243: 218-228.

Willett, S.D., 1999. Orogeny and orography: The effects of erosion on the structure of mountain belts. J. Geophys. Res., 104: 28957-28981.

Willett, S.D., Beaumont, C. and Fullsack, P., 1993. Mechanical model for the tectonics of doubly vergent compressional orogens. Geology, 21: 371-374.

Willett, S.D. and Brandon, M.T., 2002. On steady state in mountain belts. Geology, 30: 175-178.

Willett, S.D., Fisher, D., Fuller, C., En-Chao, Y. and Chia-Yu, L., 2003. Erosion rates and orogenic-wedge kinematics in Taiwan inferred from fission-track thermochronometry. Geology, 31: 945-948.

Wobus, C.W., Heimsath, A., Whipple, K.X. and Hodges, K.V., 2005. Active out-of-sequence thrust faulting in the central Nepalese Himalaya. Nature, 434: 1008-1011.

Wobus, C.W., Hodges, K.V. and Whipple, K.X., 2003. Has focused denudation sustained active thrusting at the Himalayan topographic front? Geology, 31: 861-864.

Wobus, C.W., Whipple, K.X. and Hodges, K.V., 2006. Neotectonics of the central Nepalese Himalaya: Constraints from geomorphology, detrital $^{40}Ar/^{39}Ar$ thermochronology, and thermal modeling. Tectonics, 25: doi:10.1029/2005TC001935.

Yin, A., 2006. Cenozoic tectonic evolution of the Himalayan orogen as constrained by along-strike variation of structural geometry, exhumation history, and foreland sedimentation. Earth-Sci. Rev., 76: 1-131.

Zeitler, P.K. et al., 2001. Erosion, Himalayan geodynamics, and the geomorphology of metamorphism. GSA Today, 11: 4-9.

Zhao, W., Nelson, K.D. and Project INDEPTH Team, 1993. Deep seismic reflection evidence for continental underthrusting beneath southern Tibet. Nature, 366: 557-559.

Figure and table captions

Figure 1: Illustration of the kinematics envisaged for a convergent orogen, driven by plate subduction and accretion in a doubly-vergent critical wedge (modified from Beaumont et al., 2000; Willett and Brandon, 2002). Crustal deformation is focused above point S. Dashed lines represent particle paths. (a) Convergent orogen without any channel flow or underplating mechanisms: the exhumation zone and erosional flux concern the whole deforming orogen (pro- and retro-side) and may vary spatially according to orographic focussing of precipitation and erosion. (b) Convergent orogen with channel flow: the exhumation zone and erosional flux are concentrated on the front of the pro-wedge. (c) Convergent orogen with underplating induces focussing of exhumation zone and erosional flux in the pro-wedge.

Figure 2: Different components of motion that can be involved in Himalayan kinematics, in a reference frame fixed to the underthrusting (Indian) plate. The underthrusting (Indian) block is in light blue and the overthrusting (Himalayan) block in yellow. The geometry of the fault plane is voluntary exaggerated for clarity. Five points (A to E) are followed to illustrate particle trajectories (grey lines). Red bars mark high exhumation zones. (a) Overthrusting: the fault is fixed with respect to the footwall; the convergence velocity (V) equals the overthrusting velocity (V_o) Point C is exhumed along the fault, the other points do not move. (b) Underthrusting: the fault is fixed with respect to the hangingwall and moves in the direction of the underthrusting block with a velocity $V_u = V$. Points B and D are deflected downwards, points C and E are passively transported. There is no exhumation. (c) Underplating: the deep ramp part of the fault moves toward the footwall at a velocity of V_{up}. Upper crust Indian material (point D) is thus transferred to the hangingwall. There is no exhumation. (d) Frontal propagation: the upper ramp and the surface-breaking front of the

fault move toward the footwall at a velocity V_p. Indian material (point B) is incorporated in the frontal prism. There is no exhumation. (e) Channel flow: there is no horizontal advection of the main fault, but a high velocity zone builds a channel (V_c) that forces deep crustal rocks (point E) to be exhumed over the deep ramp

Figure 3: (a) Simplified Geologic map of the Himalaya, modified from Galy (1999). Inset show location of Nepal in southern Asia. (b) Simplified geological cross-section across the Himalaya of central Nepal, modified from Bookhagen and Burbank (2006). MFT: Main Frontal Thrust, MBT: Main Boundary Thrust, MCT: Main Central Thrust, STDS: South Tibetan Detachment System, ITS: Indus-Tsangpo Suture.

Figure 4: Geometries, model domains, kinematics and particle paths of the different models that little differ from the geometry described by Avouac (2003). Notations as in Figure 3. Black arrows refer to the velocity vectors and black dashed lines represent particle paths. $\boldsymbol{V}_o$ represents overthrusting velocity, $\boldsymbol{V}_u$ underthrusting velocity and $\boldsymbol{V}_{ac}$ the accretion (= underplating) velocity. The grey shaded zone represents the underplating window where the hangingwall velocity is set at $\boldsymbol{V}_o - \boldsymbol{V}_{ac}$ and the footwall velocity $\boldsymbol{V}_u + \boldsymbol{V}_{ac}$. All geometries are from the original publications of (a) Brewer and Burbank (2006; (b) Whipp et al. (2007); (c) Bollinger et al. (2006); (d) Wobus et al. (2006).

Figure 5: Initial conditions for the thermo-mechanical model of Beaumont et al. (2001; 2004) and Jamieson (2004). Only the central region of the model is shown here; the full model width is 2000 km. (a) Passive marker grid and mechanical layers. (b) Thermal layers and instantaneous velocity vectors; q represents heat flow, A_i, the heat production of the layer i, K the thermal conductivity and Φ_{eff} the effective internal angle of friction. Surface denudation

rate is function of local surface slope. (c) Relationship between mechanical and thermal layers and summary of parameters (a, b, c from Beaumont et al., 2004). (d) Thermal structure (isotherms) and particle paths (arrows) for points (A, B and C) originating in different parts of the model that are exhumed together at ca. 51 My (from Beaumont et al., 2001).

Figure 6: Conceptual sketch illustrating the passage from a reference frame fixed to the MHT to a reference frame fixed to the underthrusting Indian plate. Notations as in Figure 2. The 5 $mm.y^{-1}$ overthrusting velocity and 15 $mm.y^{-1}$ underthrusting velocity in the MHT-fixed reference frame translate to 20 $mm.y^{-1}$ of underthrusting combined underplating and forward propagation (which take up an unknown amount of the 20 $mm.y^{-1}$ convergence). Erosion of the topographic front has a horizontal component of 5 $mm.y^{-1}$ (equal to the overthrusting velocity in the MHT-fixed reference frame) so that the topography is advected toward the Indian plate at a velocity of 15 $mm.y^{-1}$ (equal to the underthrusting velocity in the MHT-fixed reference frame). This model also allows to explain puzzling variations in overthrusting velocity recorded in the frontal Siwalik chain (~20 $mm.y^{-1}$; Lavé and Avouac, 2000; Mugnier et al., 2004) compared to those in the High Himlaya (~5 $mm.y^{-1}$; Bollinger et al., 2004; Brewer and Burbank, 2006), which are simply related to varying erosion rates between the little indurated Siwalik sediments and the resistant Greater Himalayan crystalline rocks.

Figure 7: Sketch of the two kinematic scenario envisaged for the central Himalaya (modified from Hodges et al., 2004) with the expected thermochronological age trends. (a) In the model of Avouac and co-workers (e.g., Avouac 2003; Bollinger et al., 2006), shortening is concentrated on the Main Himalayan Thrust (MHT), which includes a crustal ramp below the High Himalaya where Indian plate material is underplated to the overriding plate. Both low- and high-temperature thermochronologic age trends should show continuous younging from

the MFT to the topographic transition zone and MCT zone. (b) In the model of Hodges and co-workers (e.g., Wobus et al., 2003; 2005; Hodges et al., 2004), out-of-sequence faulting occurs in the MCT zone on the topographic transition (TT). The sharp topographic transition and a jump in cosmogenic ages have been used to support such a model. Both low- and high-temperature thermochronologic age trends should also present a jump in the topographic transition and/or in the MCT zone.

Table 1: Thermal and kinematic parameters of different recent themrmo-kinematic models. Grey lines mark the most important differences between the models. When a parameter is set from "*x to y*", that means several runs were performed with different values of this parameter between *x* and *y*.

Model	Brewer and Burbank, 2006	Wobus et al., 2006	Bollinger et al., 2006	Whipp et al., 2007
		Model geometry		
Geometry	2D – 3D	2D (Avouac)	2D (Avouac)	3D (Avouac)
Box size (L[W*]D)*	190 * ? * 50 km	100 * 60 km	220 * 60 km	140 * 84 * 50 km
Ramp angle (α)	13 to 23°	18°	10 °	MCT: 28° ; MFT: 20°
		Thermal parameters		
Basal heat flow	15 $mW.m^{-2}$ at 50 km	30 $mW.m^{-2}$ at 100 km	15 $mW.m^{-2}$ at 100 km	20 to 50 $mW.m^{-2}$ at 50 km
Heat production	0 to 2.5 $\mu W.m^{-3}$	1 to 2 $\mu W.m^{-3}$	0.4 to 2.5 $\mu W.m^{-3}$	0.8 to 3 $\mu W.m^{-3}$
Thermal diffusivity	$0.8.10^{-6}$ $m^2.s^{-1}$	1.10^{-6} $m^2.s^{-1}$	1.10^{-6} $m^2.s^{-1}$	$1.1.10^{-6}$to $1.4.10^{-6}$ $m^2.s^{-1}$
Thermal conductivity	3 $W.M^{-1}.K^{-1}$	2.5 $W.M^{-1}.K^{-1}$	2.5 $W.M^{-1}.K^{-1}$	2.5 to 3 $W.M^{-1}.K^{-1}$
Surface temperature	0°C	Non-explicit	0°C	14 to 7°C/km times elevation
Topography	Steady state	Steady state	Steady state	Steady state
Thermal structure	Steady state	Steady state ?	Transient	Steady state
		Kinematic parameters		
Convergence rate(V)	20 $mm.y^{-1}$	20 $mm.y^{-1}$	21 $mm.y^{-1}$	20 $mm.y^{-1}$
Underthrusting velocity(V_u)	15 $mm.y^{-1}$	15 $mm.y^{-1}$	17 +/- 0.5 $mm.y^{-1}$	5 to 19 $mm.y^{-1}$
Overthrusting velocity (V_o)	5 $mm.y^{-1}$	5 $mm.y^{-1}$	4 +/- 0.5 $mm.y^{-1}$	V_{MFT}: 1 to 15 $mm.y^{-1}$ V_{MCT}: 0 to 8 $mm.y^{-1}$
Accretion rate (underplating, V_{ac})	No	1 to 4 mm/yr	1 to 1.5 $mm.y^{-1}$	No
Out of sequence fault	No	Possible	No	V_{MCT}: 0 to 8 mm/yr
Mass conservation	$\vec{\nabla}.\vec{V} = \vec{0}$	Non-explicit	$\vec{\nabla}.\vec{V} = \vec{0}$	$\vec{\nabla}.\vec{V} = \vec{0}$ (?)
Velocity	Fault parallel	*Footwall*: **V**=**V**u +**V**ac *Hanging wall*: **V**=**V**o +**V**ac	V = Vu + Vo *Footwall*: V=-tgα.Vu +Vac(x) **V**=**V**u +**V**ac *Hanging wall*: V=tgα.Vo +Vac(x) **V**=**V**o +**V**ac	V = Vo+Vu Vo = V_{MFT}+V_{MCT} Fault parallel *MFT*: V=(V_{MFT} + Vu) / cosα_{MFT} *MCT:* V=V_{MCT} / cosα_{MCT}
Running time	20 Myr	>10 Myr	20 Myr	20 Myr ?
Fixed point / reference	MHT	MHT	MHT	MHT - MCT

Table 1: Robert et al

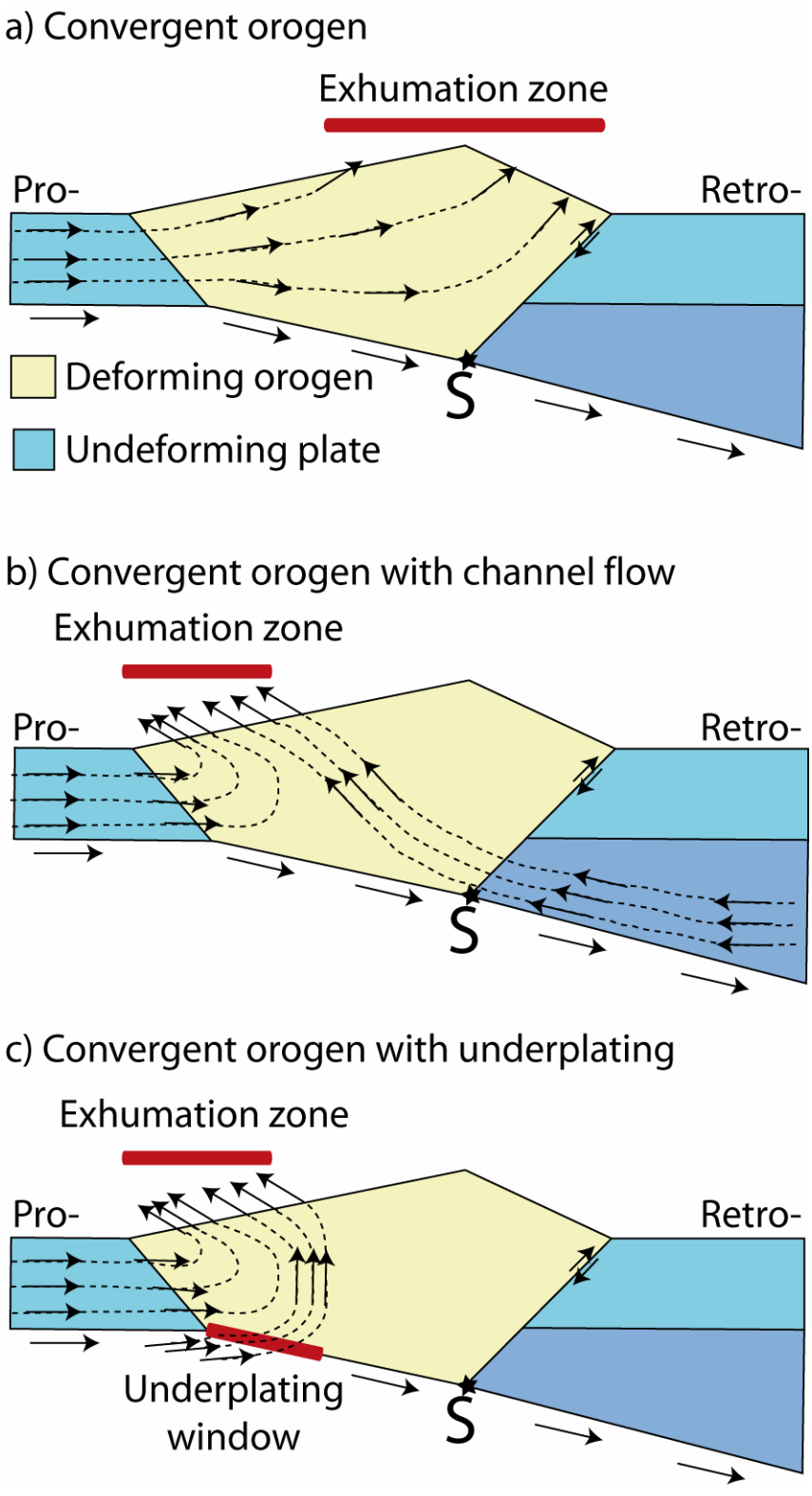

Figure 1: Robert et al

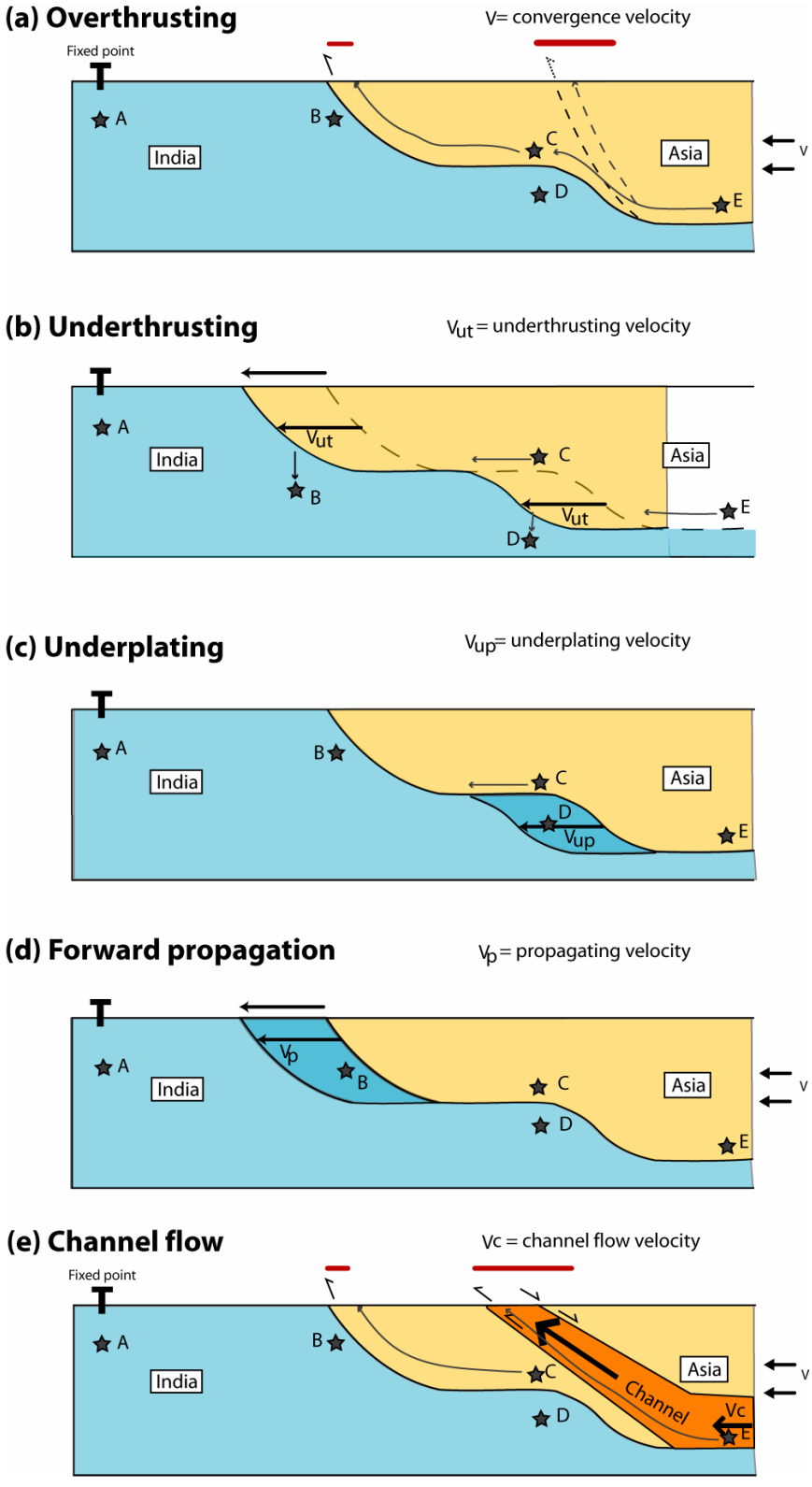

Figure 2: Robert et al.

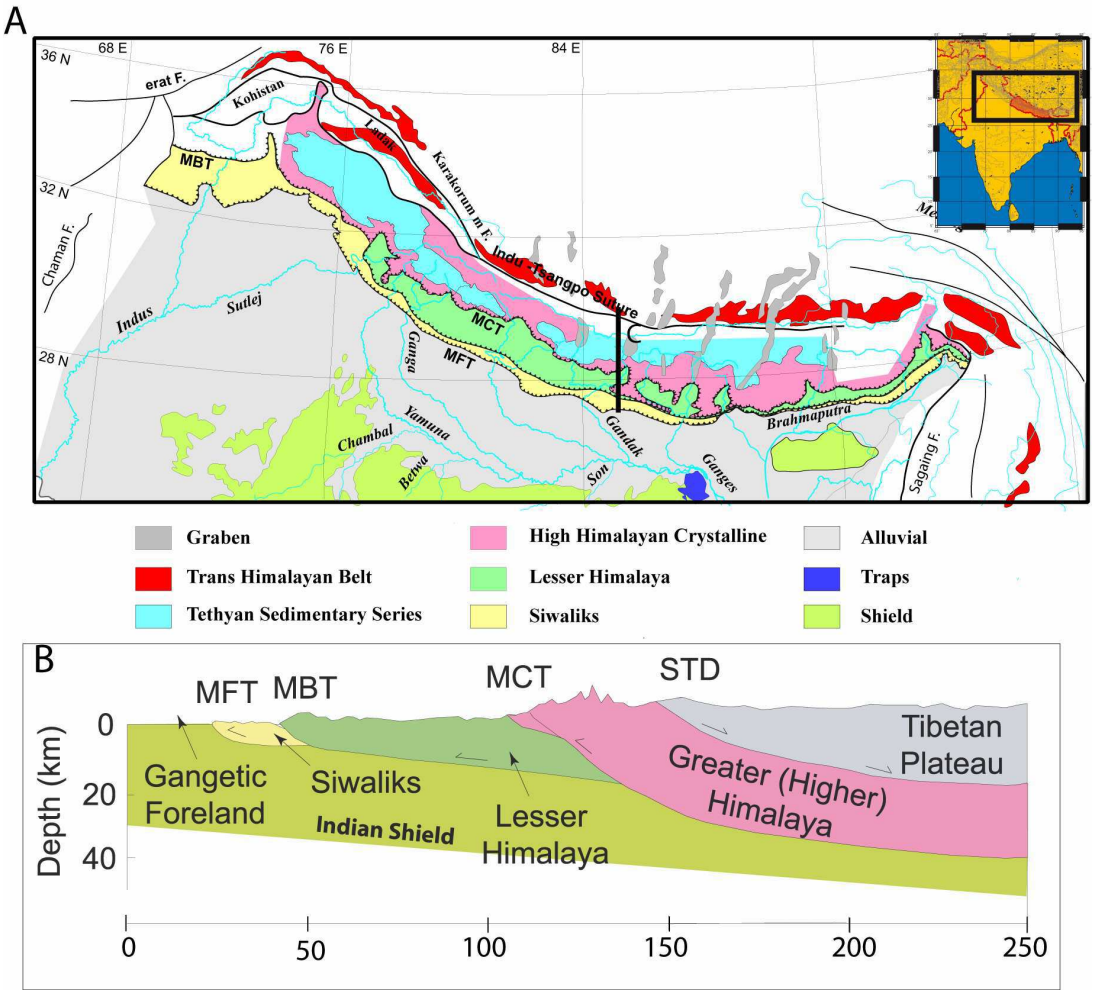

Figure 3: Robert et al.

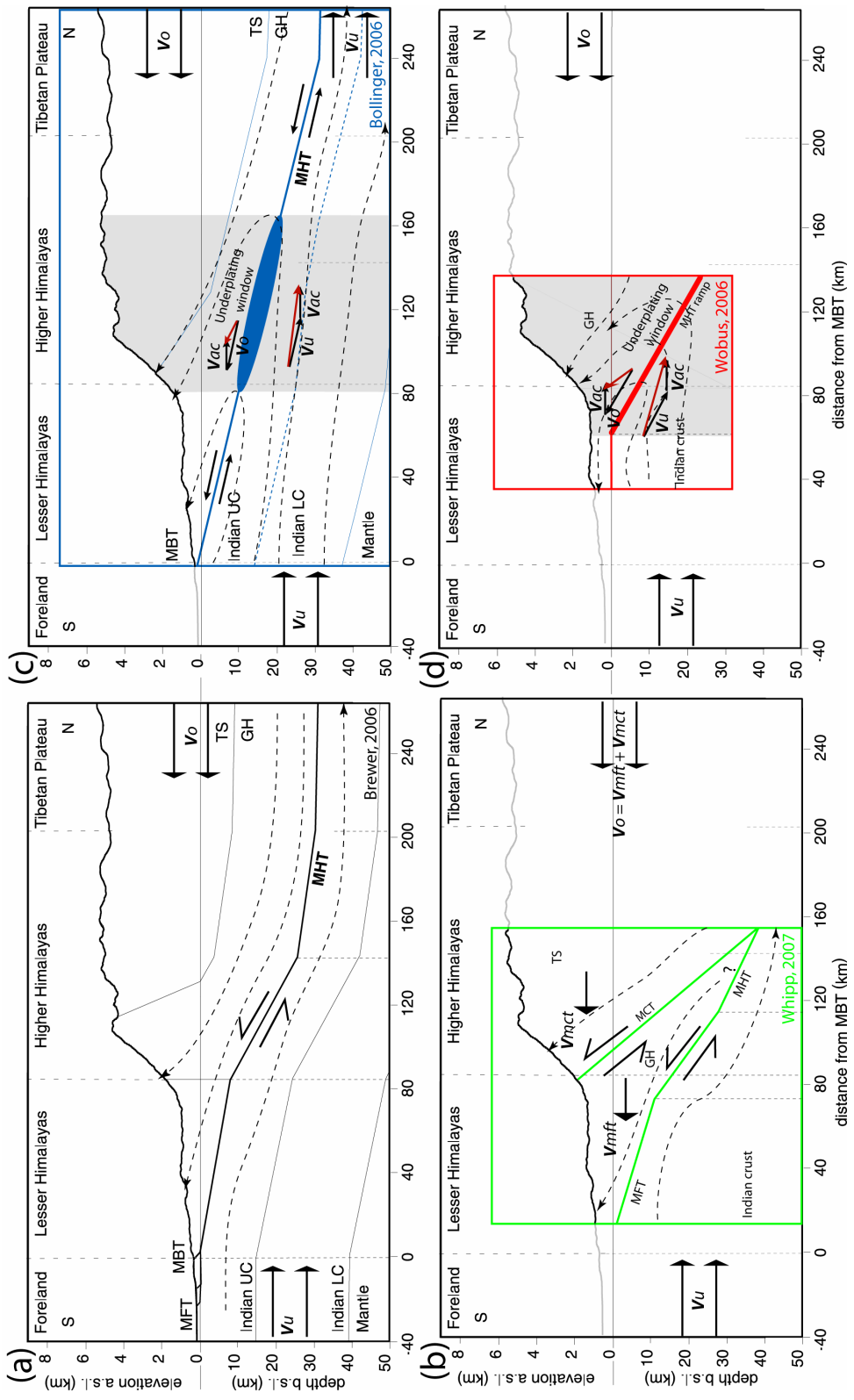

Figure 4: Robert et al.

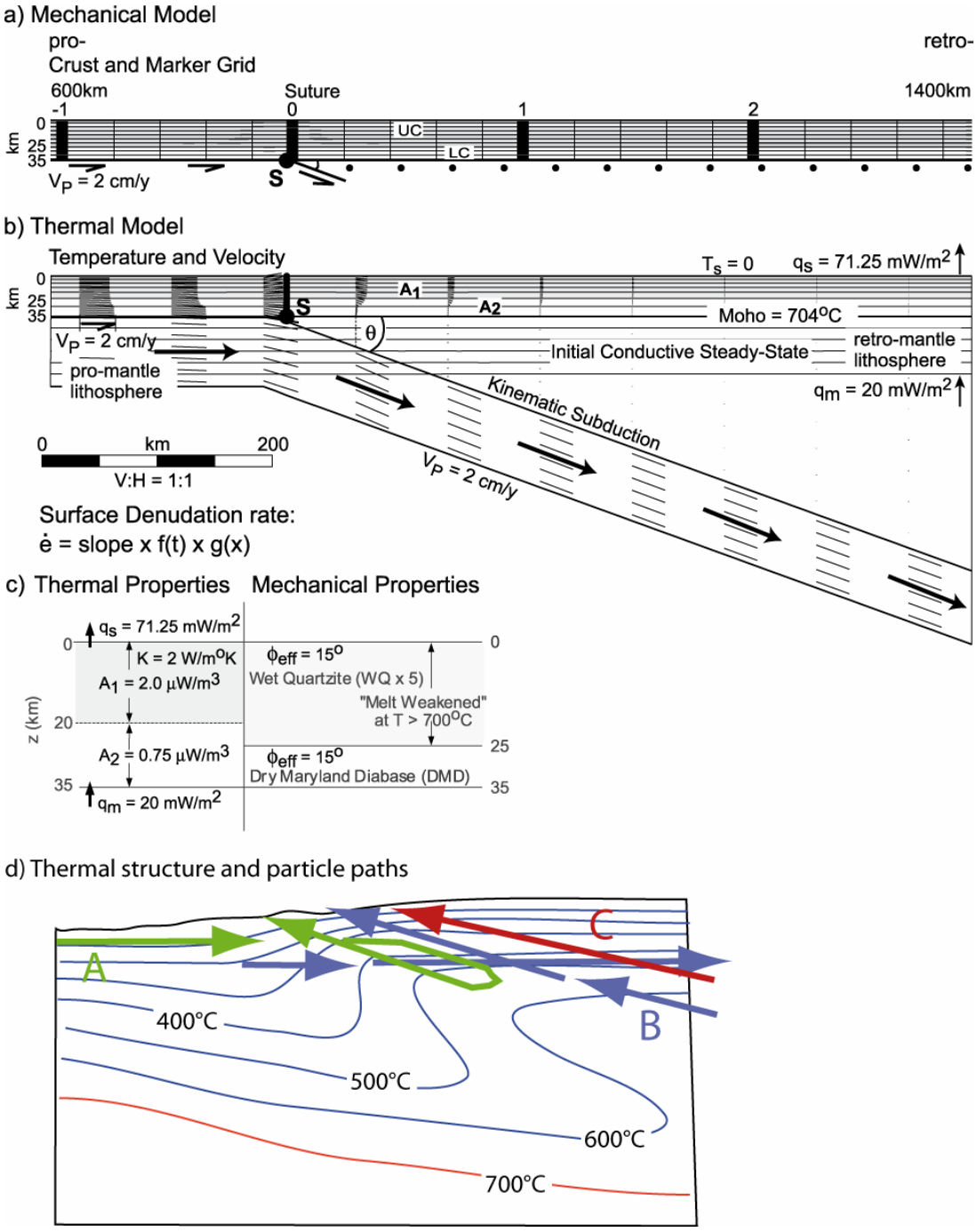

Figure 5: Robert et al.

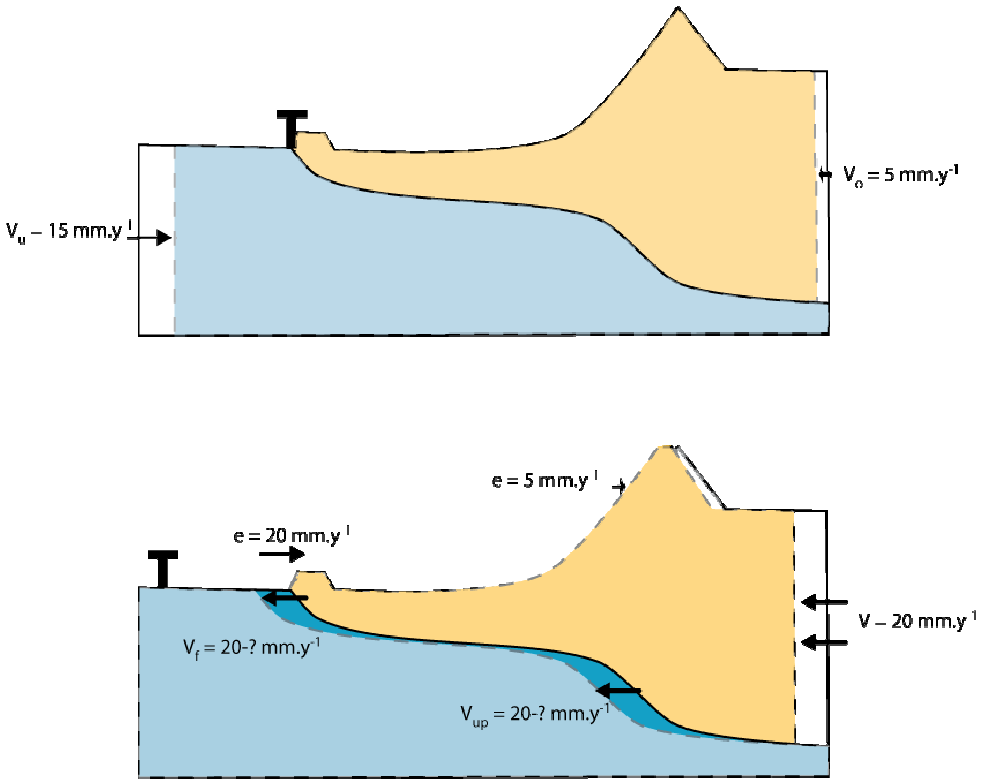

Figure 6: Robert et al.

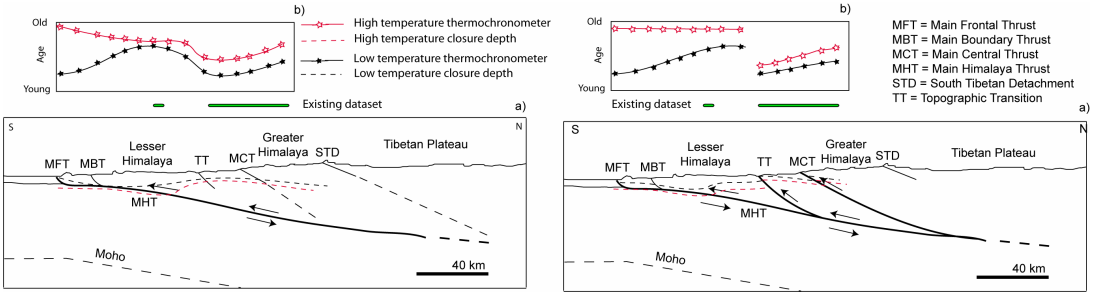

Figure 7: Robert et al.

Transition

Le Népal central est relativement bien documenté et est la base de nombreuses modélisations numériques. Mais les conclusions des ses modélisations basées sur des données similaires sont interprétées très différement selon les auteurs. Cela impose donc de construire une base de données plus précise pour mieux contraindre les différentes hypothèses, et de mener de nouveaux tests numériques. Ce sera le fil guide de nos parties suivantes.

Pour répondre à ces questions, nous commencerons (partie 2) à mettre en place toutes les notions et les méthodes utilisées permettant la compréhension des différentes études. Nous pourrons alors, en partie 3, mettre en évidence l'importance de la géométrie des accidents à l'échelle crustale sur les objets étudiés, ce qui sera la base de démonstration, en partie 4 qu'en Himalaya, cette structure profonde varie latéralement de façon importante. Cela nous amènera à traiter en partie 5 la variation latérale du front d'un prisme orogénique, toujours en s'appuyant sur l'exemple himalayen.

Principes et Méthodologie 2

Sommaire

Ce chapitre explique le raisonnement suivi, démontre le bien-fondé des objets utilisés, puis décrit les techniques analytiques et numériques mises en application.

This chapter documents the logic of the work and the choice of the objects studied. The second part explains the analytical and numerical techniques used throughout this work.

2.1 Principes de l'étude

De nombreuses études montrent que les deux scénarii proposés pour expliquer la cinématique récente du prisme himalayen possèdent des signatures cinématiques et thermiques de basse température bien distinctes (Avouac 2003, Bollinger et al. 2004; 2006, Whipp et al. 2007) (Fig. 2.1).

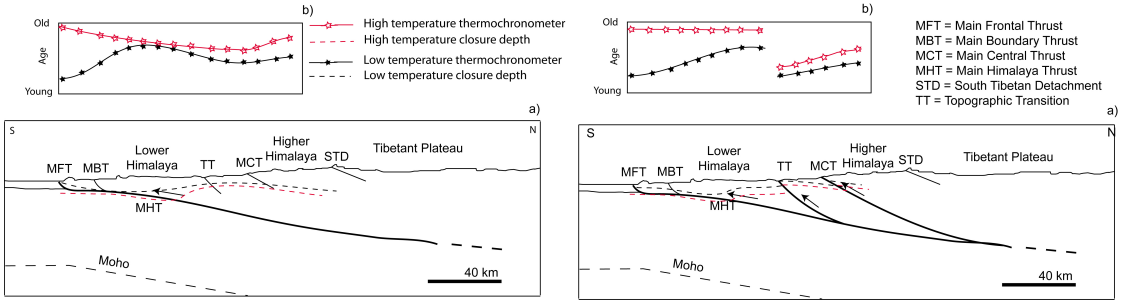

FIG. 2.1 – *Positions attendues des températures de fermeture* 110°C *(AFT) et* 350°C *(Ar) pour les modèles de la cinématique himalayenne de Avouac (2003) et de Hodges et al. (2004). Cette prédiction permet de proposer des profils thermochronologiques respectivement associés à des thermochronomètres de basses et hautes températures. Dans le cas d'un mécanisme hors séquence (Hodges et al. 2004), il y a un saut d'âges à proximité de la transition topographique.*

Pour tenter de répondre à cette problématique, il faut donc acquérir des observables permettant de reconstruire la cinématique et la structure thermique de la région étudiée. Il existe de nombreuses méthodes pour connaître un gradient thermique, mais toutes les méthodes ne permettent pas d'obtenir une carte des isothermes à l'échelle du prisme orogénique : les températures mises en jeu dans ces phénomènes sont de l'ordre de la centaine de degrés, pour des profondeurs de quelques kilomètres à quelques dizaines de kilomètres. L'utilisation de forages profonds permet d'obtenir des valeurs de températures pour des profondeurs de quelques centaines de mètres, ce qui est lourd et coûteux à mettre en oeuvre et qui n'est pas suffisant pour cette problématique. De plus, la mesure du gradient thermique donne uniquement un instantanné de la structure thermique. Pour en déduire une cinématique, il est nécessaire d'associer la mesure du gradient thermique à une étude de son évolution. Une possiblité serait alors d'utiliser des marqueurs du métamorphisme associés à sa datation. Plusieurs problèmes se posent alors : d'abord, les températures concernant le métamorphisme sont élevées (400°C) et ne donnent des informations que pour la zone profonde. De plus, les données déjà existantes (Hubbard 1989, Hodges et al. 1992, Parrish et Hodges 1996, Coleman et

Hodges 1998, Godin et al. 2001) concernent des étapes de l'évolution de la chaîne himalayenne plus anciennes (20 Ma) que celle qui nous intéresse.

Il reste les systèmes thermochronologiques de basse température qui représentent à la fois un système thermique, et son évolution dans le temps. Un thermochronomètre est un système permettant de dater le passage d'une roche à une température donnée, appelée température de fermeture. Cette température correspond à la température maximale en dessous de laquelle est enregistrée la décroissance d'un isotope radioactif qui permet la datation. A différents systèmes correspondent différentes températures de fermeture (Reiners et Brandon (2006) and Fig.2.2) :

$^{40}Ar/^{39}Ar$ ***sur muscovites :*** $T_{ferm} = 380°C$ (Robbins 1972, Hames et Bowring 1994)

Traces de fission sur zircons : $T_{ferm} = 232°C$ (Brandon et al. 1998)

Traces de fission sur apatites : $T_{ferm} = 116°C$ (Ketcham et al. 1999)

$(U-Th)/He$ ***sur zircons :*** $T_{ferm} = 183°C$ (Reiners et al. 2004)

$(U-Th)/He$ ***sur apatites :*** $T_{ferm} = 67°C$ (Farley 2000)

Dans la littérature, il est possible de trouver des données $^{40}Ar/^{39}Ar$ sur muscovites (Rai 1998, Arita et al. 1997) ou traces de fission sur apatites (Copeland et al. 2000, Blythe et al. 2007, Crouzet et al. 2007). Or, la majorité de ces données sont situées au nord de la zone du MCT, et la conclusion est que ces données à ces endroits-là ne permettent pas de discriminer correctement les deux scénarii (Brewer et Burbank 2006, Bollinger et al. 2006, Blythe et al. 2007, Whipp et al. 2007).

Intuitivement, la différence dans la signature thermique de ces deux scénarii devrait se trouver au sud de la zone du MCT. Il faut donc acquérir des données thermochronologiques de basse température le long de transects nord - sud au travers du prisme frontal himalayen. A cause de la nature des roches dans le Lesser Himalaya (gneiss, quartzites, schistes, dolomies, ...), il est difficile de trouver des apatites et des zircons de bonne qualité (contenance en inclusions faible, automorphes, sains, ...). Il est donc difficilement envisageable d'effectuer des transects avec les systèmes $(U-Th)/He$ sur apatites ou sur zircons. Nous nous focaliserons sur les traces de fission sur apatites.

L'idéal aurait été d'obtenir des trajets temps - température, et donc temps - profondeur. Ceci est possible avec le système traces de fission sur apatites en tra-

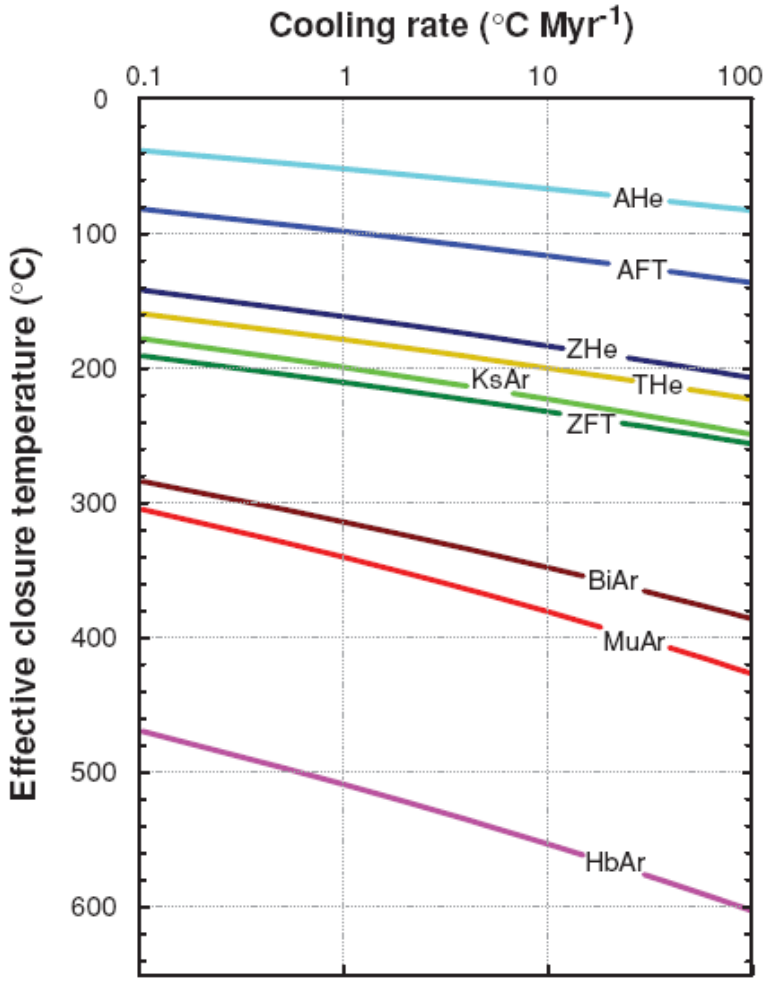

FIG. 2.2 – *Estimation de la température de fermeture effective en fonction du taux de refroidissement pour les thermochronomètres He, FT at Ar (Reiners et Brandon 2006).*

vaillant sur des analyses statistiques de longueurs de traces observées. Or, pour ces analyses, nous avons besoin d'un nombre important de traces par échantillon. Ceci n'est possible que pour des échantillons suffisamment âgés avec une teneur en uranium correcte. Or dans les études précédentes, les âges obtenus dans les autres études (Burbank et al. 2003, Blythe et al. 2007) sont très jeunes ($\leq$ 1.5 *Ma*). Il en résulte que le nombre de traces permettant la mesure de longueurs de traces reste trop faible pour ce type d'échantillon. De plus, la qualité des échantillons est telle qu'il n'est pas possible d'appliquer cette technique pour l'étude du Lesser Himalaya.

Une solution à ce problème est de modéliser la cinétique du prisme frontal himalayen, de prédire le champ de température associé à chaque modèle, et de calculer des âges thermochronologiques respectivement associés. La modification

du code PECUBE de Braun (2003) permet cela. Une inversion des paramètres cinématiques permet alors de contraindre la cinétique et le timing des failles. Ceci est effectué grâce au Neighbourhood Algorithm de Sambridge (1999a;b). Le principe général de la méthodologie employée est présenté Fig. 2.3.

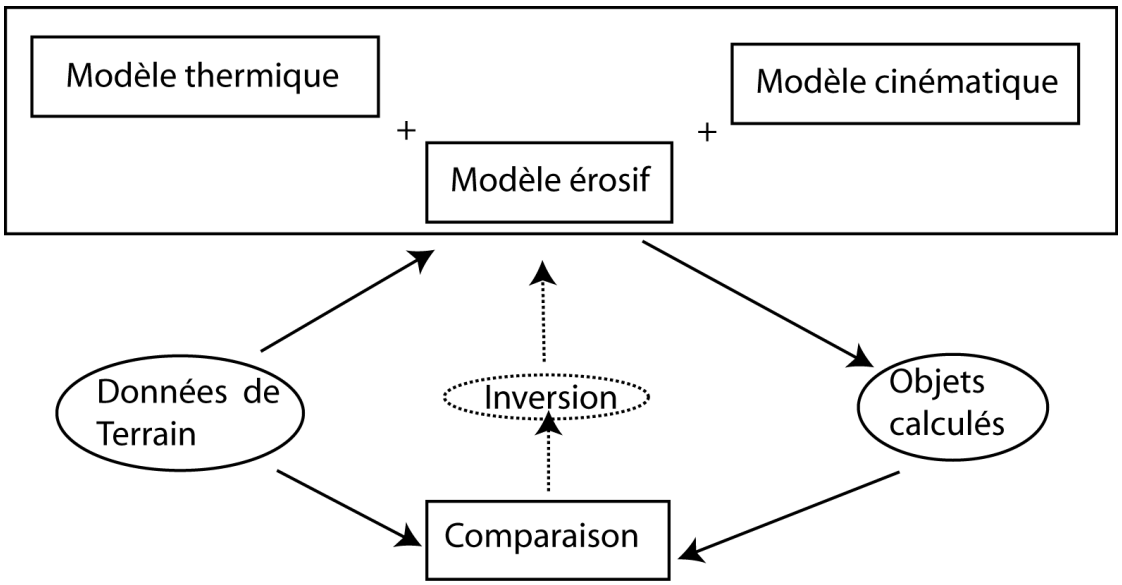

FIG. 2.3 – *Principe général des relations données - modèles - inversions : les inversions permettent de contraindre des paramètres caractéristiques du modèle.*

Les deux prochaines sections décrivent les méthodes d'analyse des Traces de Fission sur Apatites et les méthodes de modélisation utilisées.

2.2 Analyse thermochronologique à partir du système Traces de Fission sur Apatites

Les campagnes de terrain au Népal et au Bhoutan nous ont permis d'obtenir des données thermochronologiques sur le thermochronomètre traces de fission sur apatites. Avant de donner les résultats, nous présentons la méthode utilisée.

Cette analyse permet de reconstruire l'histoire thermique de basse température de roches magmatiques, métamorphiques et sédimentaires (Gallagher et al. 1998) par la datation du passage de cette roche à une température spécifique au système étudié, température appelée *température de fermeture*. Cette reconstitution thermique permet l'accès à différents types d'estimations :

– Estimation de taux de dénudation dans les zones orogéniques et dans les

zones continentales stables (Gallagher et al. 1994, Fitzgerald et al. 1995, Gallagher et al. 1998, Carter 1999) ;

- Reconstitution de l'évolution de bassins sédimentaires (Gallagher et al. 1998, van der Beek et al. 2006) ;
- Datation de l'activité de failles (Garver et al. 1999, van der Beek et al. 2006) ;
- Traçages de sédiments (Garver et al. 1999, Najman et al. 2005, van der Beek et al. 2006, Bernet et al. 2006) ;

La méthode de traces de fission sur apatites (AFT) est basée sur la décroissance radiocative de ^{238}U. Cette décroissance est enregistrée sous certaines conditions de température (température inférieure à la température de fermeture du système) par création et maintien de dommages du réseau cristallin (Fleischer et al. (1975), Fig. 2.4). Ces dommages peuvent être mis en exergue afin de les visualiser (traces observables au microscope optique). L'âge est alors estimé en déterminant la densité des traces dans ces minéraux ainsi que leur teneur en uranium.

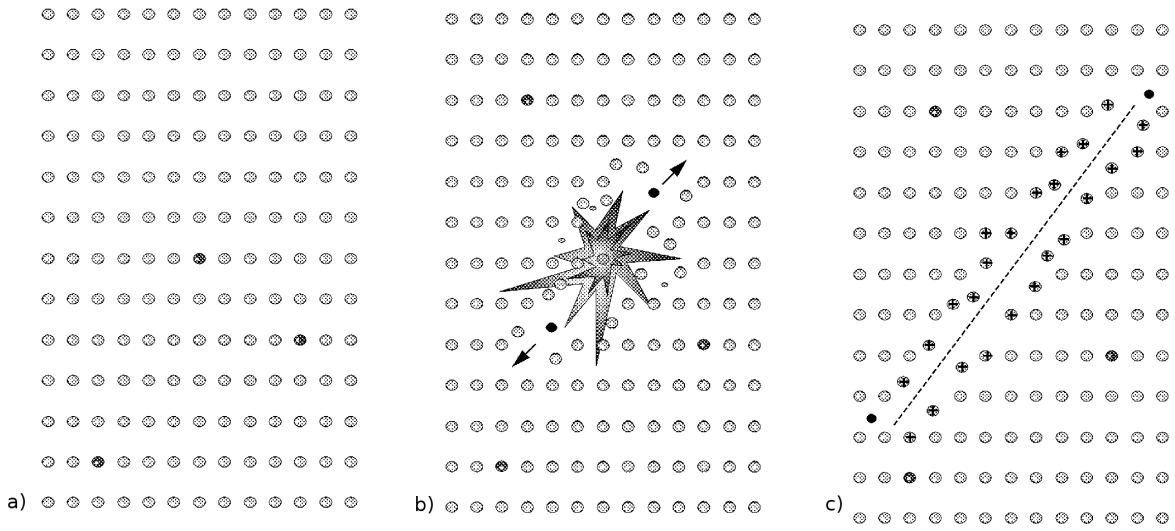

FIG. 2.4 – *Modèle de création de dommages dans un réseau cristallin par la fission d'un atome d'*^{238}U*. a) Réseau cristallin contenant des traces d'*^{238}U *(points noirs). b) La fission spontanée d'un atome d'*^{238}U *produit 2 particules lourdes chargées et relache une énergie de l'ordre de* 200 *MeV. Il y a répulsion entre ces deux particules chargées qui interagissent (échanges d'électrons et/ou ionisations) avec les atomes environnants. Cela entraîne une déformation du réseau. c) les particules ionisées sont ralenties par la capture d'électrons, elles ralentissent et commencent à interagir avec le réseau par des collisions atomiques, jusqu'à leur arrêt. Ceci laisse un dommage rectiligne appelé trace de fission latente. Cette trace ne peut être observée en microscopie optique sans attaque chimique. D'après Gallagher et al. (1998).*

La température joue un rôle sur le maintien au cours du temps du dommage dans le réseau cristallin : à haute température, les traces de fission sont *recuites*

(détruites partiellement) ou effacées totalement. Ce processus peut être contraint par la mesure des longueurs de traces de fission. Pour l'apatite, des modèles cinétiques ont été proposés par Green et al. (1989b), Carlson (1990), Crowley et al. (1991), Ketcham et al. (1999). Green et al. (1985), Crowley et al. (1991), Carlson et al. (1999) et Barbarand et al. (2003b) ont montré que la température à laquelle les traces de fission s'effacent totalement est influencée par la variation de la composition chimique, et principalement par la proportion de chlore (Cl). Pour les mêmes conditions, les traces de fission dans les apatites riches en Cl sont plus résistantes au raccourcissement que celle riches en OH et fluor F (Green et al. 1985, Crowley et al. 1991, Carlson et al. 1999). Or, le paramètre D_{par} correspondant à la moyenne arithmétique du diamètre des traces projetées parallèlement à l'axe c de l'apatite est corrélé avec la proportion en Cl, OH et F (Donelick 1993; 1995, Burtner et al. 1994). Carlson et al. (1999) montrent qu'il est possible d'obtenir une estimation des effets de la composition chimique sur les variations des longueurs de traces, en mesurant le D_{par}. Si le D_{par} est inférieur à 1.7 μm dans les conditions d'attaque utilisées, il caractérise plutôt des fluoroapatites (les plus répandues). Si le D_{par} est supérieur à cette valeur, ce sont plutôt des chlorapatites.

Pour les apatites, l'anisotropie cristallographique joue aussi un rôle important (Donelick et al. 1999, Carlson et al. 1999, Ketcham et al. 1999). La température en dessous de laquelle les traces ne sont pas effacées totalement est de l'ordre de $120°C$, et elles sont recuites entre 60 et $110°C$. Ce domaine de température définit la zone de rétention (ou recuit) partielle (PAZ pour *Partial Annealing Zone*) (Gleadow et al. 1986, Green et al. 1989a, Gallagher et al. 1998). A des températures inférieures, les traces gardent leur stabilité et l'influence de la température est minime (Fitzgerald et Gleadow 1990). Il est alors possible de contraindre l'évolution thermique des roches entre $\sim 60 - 110°C$ en utilisant des approches ou des modèles d'inversion stochastique (Gallagher 1995, Ketcham et al. 2000, Ketcham 2005).

Ci-dessous, nous exposons synthétiquement la méthode de datation. Plus de détails peuvent être obtenus à partir de Wagner et Van Den Haute (1992), Gallagher et al. (1998), Tagami (2005), Donelick et al. (1999).

2.2.1 Notion de traces de fission sur apatites et de datations

Les apatites sont des minéraux contenant des atomes d'^{238}U (99.3 % dans la nature) et d'^{235}U (0.7 % dans la nature). Cet ^{238}U se désintègre spontanément au cours du temps, soit par émission d'une particule alpha, soit par fission, c'est-à-dire en libérant deux ions fils dits *fragments de fission*. A environ deux millions de désintégrations alpha correspond une seule fission spontanée.

Ces deux fragments de fission, libérés avec une énergie cinétique de l'ordre de 200 MeV, sont alors éjectés selon des directions opposées. La plupart des minéraux se comportent comme des détecteurs solides non conducteurs et sont capables d'enregistrer le déplacement de ces fragments : ce phénomène induit une désorganisation locale du réseau cristallin par ionisation des atomes le long du trajet des produits de fission (modèle du pic d'explosion ionique de Fleischer et al. (1965)). Par répulsions électrostatiques, une zone linéaire de défauts métastables à faible densité d'atomes se forme. Sa taille est de l'ordre de la centaine d'angströms en diamètre, et de 15 à 25 μm de long, ce qui définit une trace latente.

Le diamètre d'une trace latente est très faible, ce qui fait qu'il n'est pas possible d'observer de tels défauts au microscope optique. Pour les visualiser, il faut les révéler, *id est* il est nécessaire de les élargir grâce à une attaque chimique appropriée. Pour cela, il faut que le produit de l'attaque puisse pénétrer dans les défauts. Un moyen est de mettre à nu une surface interne polie du minéral qui recoupe les traces latentes. Nous travaillons donc sur une surface coupant le minéral en son milieu, surface interne obtenue par polissage.

D'après Fleischer et Price (1963a;b), la morphologie des traces révélées est très variable et dépend du rapport entre la vitesse d'attaque des traces V_t et celle du minéral V_g. $\frac{V_g}{V_t}$ est toujours inférieur à 1 et caractérise la forme de la trace. Dans le cas des apatites, ce rapport est faible, ce qui explique la forme en pointe de flèche observée. La morphologie des traces est aussi à relier à leur orientation par rapport à l'orientation cristallographique du minéral. En effet, dans un plan parallèle à l'axe cristallographique c, les traces parallèles à c sont très fines alors qu'elles se présentent avec un V plus ouvert perpendiculairement à c. Ceci s'explique par le fait que V_t est plus élevée parallèlement à c que dans les autres directions (Fleischer

et Price 1963a;b). Pour les apatites, l'attaque chimique sélective est effectuée avec de l'acide nitrique à 5 N pendant 20 s à une température de 20°C.

La population d'un isotope *père* instable, comme l'^{238}U, décroît avec le temps en suivant une loi exponentielle. Il en résulte que le nombre de traces latentes qui s'accumulent dans un minéral voit son nombre augmenter avec le temps. Ce temps depuis lequel ces traces ont commencé à être enregistrées et la concentration d'^{238}U dans le minéral déterminent la densité ρ_s (nombre de traces/cm^2) de traces de fission spontanées, révélées sur une surface interne du minéral obtenue par polissage. Il en résulte que la détermination de ce nombre de traces permet de calculer un temps correspondant pour l'échantillon à l'âge de son passage à travers la température de fermeture du système.

2.2.2 Mesure d'âge de traces de fission sur apatites

Pour une détermination effective de l'âge, il faut connaître l'abondance relative des éléments pères et fils, id est le nombre d'atomes d'^{238}U et le nombre de traces spontanées par unité de volume, comptées sur la face polie du grain. Une donnée manquante est dans le cas de la thermochronologie par traces de fission sur apatites, la concentration initiale en ^{238}U du minéral. Elle n'est pas fournie par l'information ρ_s. Pour cela, nous connaissons le rapport $\frac{^{238}U}{^{235}U}$ qui est constant dans la nature et égal à 137.88 (Gallagher et al. 1998). L'idée est de trouver la quantité d'$^{238}U_{init}$ en mesurant la quantité d'^{235}U. L'^{235}U est aussi instable et se désintègre par émission alpha et par fission spontanée. Mais cet isotope est peu abondant et sa période de désintégration par fission spontanée est supérieure à celle de l'^{238}U. Sa contribution aux traces de fission spontanée est donc négligeable ($\prec 1/10000$ de celle de l'^{238}U). En revanche, cet isotope est le seul qui fissionne par capture de neutrons thermiques. Cette propriété permet de déterminer sa proportion dans le minéral étudié. Pour cela, nous irradions le minéral dans un flux contrôlé de neutrons thermiques en réacteur nucléaire. Au laboratoire de Grenoble, nous utilisons le canal P1 (neutrons thermiques) du réacteur Orphée du Centre d'Etudes Nucléaires de Saclay (France). La fluence mesurée ϕ ($neutrons/cm^2$) et la teneur en ^{235}U du minéral déterminent la densité de traces de fission induites ρ_i dans un minéral irradié.

L'âge de trace de fission est alors donné par l'équation :

$$t = \frac{1}{\lambda_d} \ln(1 + \frac{\rho_s g \lambda_\alpha \phi \sigma I}{\rho_i \lambda_f}) \tag{2.1}$$

où :

- t est l'âge ;
- ρ_s et ρ_i sont respectivement les densités de traces (nombre de traces/unité de surface) spontanées et induites ;
- λ_f représente la constante de décroissance radioactive par fission spontanée de l'^{238}U ($8.216\ 10^{-17}\ ans^{-1}$) ;
- λ_α représente la constante de décroissance radioactive par émission α de l'^{238}U ($1.55125\ 10^{-10}\ ans^{-1}$) ;
- g est un facteur de géométrie du minéral dépendant de la technique de datation utilisée ;
- ϕ est la fluence neutronique ;
- σ est la section efficace de fission de l'^{235}U par capture de neutrons thermiques ($570.8\ 10^{-22}\ cm^{-2}$) et
- I le rapport $\frac{^{235}U}{^{238}U}$ égal à $7.2527\ 10^{-3}$.

Nous assurons la dosimétrie neutronique grâce à des pastilles de verres ou *moniteurs*, renfermant une quantité précise et connue d'Uranium, irradiés conjointement aux minéraux à dater. Comme dans les minéraux, au cours de l'irradiation, il s'y produit des fissions d'^{235}U. Dans ces moniteurs, la densité ρ_d des traces induites révélées est proportionnelle à la fluence :

$$\phi = B * \rho_d \tag{2.2}$$

avec B une constante caractéristique du dosimètre.

L'équation d'âge 2.1 devient :

$$t = \frac{1}{\lambda_d} \ln(1 + \frac{\rho_s g \lambda_\alpha B \rho_d \sigma I}{\rho_i \lambda_f}) \tag{2.3}$$

Dans l'équation 2.3, deux termes sont difficiles à évaluer :

- le terme B (Gallagher et al. 1998),
- λ_f n'est connue qu'avec une incertitude de 15%

Nous contournons ces difficultés par l'introduction d'un paramètre ζ de substitution, déterminé par calibration avec un échantillon d'âge connu (Gallagher et al. 1998) :

$$\zeta = \frac{B\sigma I}{\lambda_f} \tag{2.4}$$

Ce qui donne la formule finale de l'équation d'âge :

$$t = \frac{1}{1+\lambda_d} \ln(\lambda_d \frac{\rho_s}{\rho_i} \rho_d \zeta g) \tag{2.5}$$

Dans le cas où les densités de traces fossiles(ρ_s) et induites (ρ_i) sont mesurées dans un échantillon standard (minéraux ou verres volcaniques) d'âges bien connus t_{st}, alors, nous pouvons calculer ζ à partir de l'équation :

$$\zeta = \frac{e^{\lambda_\alpha t_{st}} - 1}{\frac{\rho_{s(st)}}{\rho_{i(st)}} \rho_d \lambda_\alpha g} \tag{2.6}$$

Chaque utilisateur doit donc déterminer sa propre valeur de ζ qui dépend, pour un réacteur nucléaire et une position d'irradiation donnés, des conditions de révélation et d'observation des traces. Dans une certaine mesure, des critères de reconnaisance des traces adoptés doivent aussi être pris en compte. Une dernière dépendance est le type de verre utilisé. Nous utilisons alors des échantillons étalons (standards, voir Tab. 2.1) dont les âges sont reconnus internationalement.

Standard	Origine	Age (Ma) $\pm 2\sigma$	Référence(s)
Durango	Mexique	31.40 ± 0.72 31.44 ± 0.18	Naeser et Fleischer (1975) McDowell et al. (2005)
Fish Canyon Tuff	Colorado, USA	27.74 ± 0.30 28.13 ± 0.47	Steven et al. (1967) Hurford et Hammerschmidt (1985) Kunk et al. (1985) Dazé et al. (2003)

TAB. 2.1 – *Valeurs des âges traces de fission des standards utilisés, associés à leurs références bibliographiques.*

2.2.3 Méthode du détecteur externe : détermination de l'abondance en ^{235}U

Pour déterminer l'abondance en ^{235}U, la méthode utilisée est celle du *détecteur externe* (Fig. 2.5). La surface d'un minéral donné est polie et attaquée par de l'acide en conditions appropriées, ce qui révèle les traces de fission spontanées intersectant ce qui était une surface interne. Un détecteur sans uranium (muscovite typiquement) est collé à la surface polie. L'échantillon est alors irradié grâce à des neutrons thermiques de basse énergie dans un réacteur nucléaire. Cette irradiation induit spécifiquement la fission des atomes d'^{235}U, et donc une expulsion de deux fragments de fission par atome d'^{235}U. Pour les atomes de la surface du grain, cette éjection crée une trace de fission latente à la fois sur le grain et sur le mica. Il se produit alors sur le mica une image miroir du grain original. Ensuite, seul le mica est attaqué à l'acide, ce qui révèle les traces induites sur chaque grain de l'échantillon par l'irradiation. Le grain originel est exempt de trace induite révélée. Le comptage de traces sur le mica permet la mesure de l'abondance en ^{235}U.

2.2.4 Mesure de longueurs et de largeurs de traces de fission sur apatites

La méthode présentée précédemment ne suffit pas à remonter à une histoire thermique. Cette dernière est approchée par l'*étude des longueurs de traces de fission* sur ces mêmes minéraux car d'autres informations sur l'histoire thermique sont contenues dans ces longueurs (Gleadow et al. 1986) : les longueurs des traces de fission sont diminuées par augmentation de la température ou diminution de la vitesse de passage par la zone de rétention partielle (PAZ pour Partial Annealing Zone) lors de l'exhumation (Carter et Gallagher (2004), Fig. 2.6. Cette information contenue dans les spectres de longueurs de traces de fission permet de renseigner des histoires complexes de faible température (Carter et Gallagher 2004). Pour un même âge thermochronologique donné et différentes histoires thermiques, les spectres de longueurs de traces peuvent être différents et un enfouissement trop important efface en grande partie l'histoire thermique précédente (Fig. 2.6).

La mesure de longueurs s'effectue sous microscope optique, grâce à une tablette digitale et un curseur équipé d'une diode électroluminescente (DEL) de forte inten-

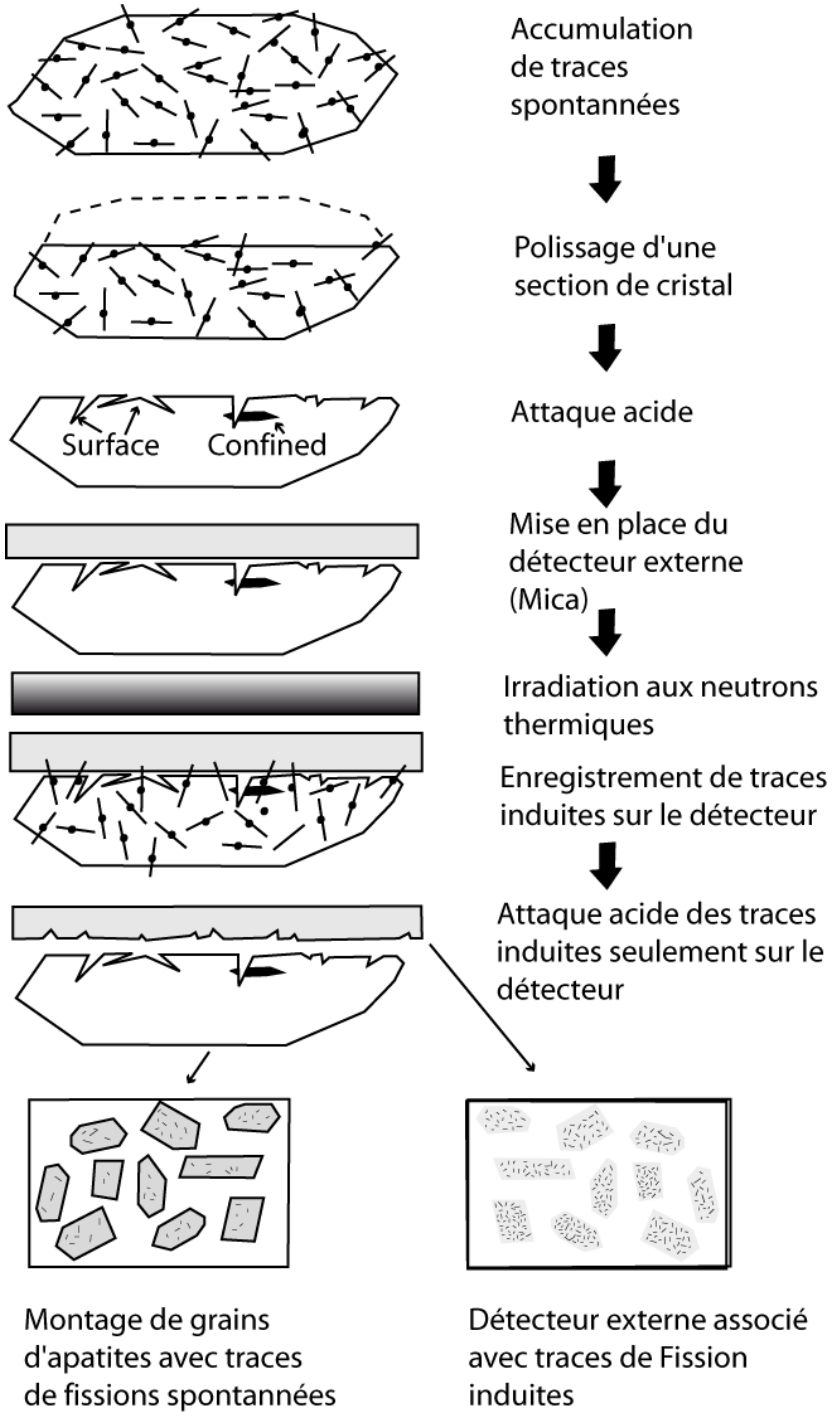

FIG. 2.5 – *Méthode du détecteur externe (d'après Gallagher et al. (1998)).*

sité, visible dans le microscope via un système de miroirs. Les mesures effectuées sur les échantillons sont calibrées par une séance de mesures effectuées sur des standards. Les longueurs mesurées n'ont de sens que sur des traces ne recoupant pas la surface du minéral, c'est-à-dire des *traces confinées*. Celles-ci ne peuvent être révélées que si elles sont en contact avec le milieu extérieur via une autre trace non confinée ou une fracture ou une surface de clivage, ce qui permet l'accès (et donc l'attaque) pour l'acide révélateur. Seules les traces confinées parallèles au plan d'observation sont mesurées.

De plus, la composition en Cl, F, et OH des apatites joue dans le contrôle du taux de recuit lors du passage dans la PAZ (Gleadow et Duddy 1981, Donelick 1991) et influe sur l'efficacité de l'attaque acide lors de la révélation des traces (Barbarand et Pagel 2001). La largeur des traces de fission non confinées donne une approche de la composition des apatites (Gleadow et Duddy 1981, Donelick 1991, Donelick et al. 1999, Barbarand et al. 2003). C'est pourquoi l'étude de la distribution des largeurs des traces de fission est nécessaire en parallèle à celle des longueurs de traces, de manière à contraindre au mieux les histoires thermiques. La méthode de mesure des largeurs est similaire à celle de mesure des longueurs de traces, sauf qu'on les mesure sur des traces non confinées et séquentes au plan poli d'observation.

Pour des échantillons très jeunes et/ou ayant une teneur en U faible, il n'est pas possible d'effectuer ces mesures complémentaires de longueurs de trace de fission, car les traces de fission confinées sont moins nombreuses que les traces séquentes à la surface. Lorsque les échantillons sont trop jeunes et/ou possèdent une teneur en uranium trop faible, il est possible de favoriser la révélation de traces confinées en irradiant les échantillons au californium 252 (^{252}Cf). Cette irradiation induit des zones de dommages dans le minéral qui permettent à l'acide de pénétrer et donc d'augmenter la probabilité de révéler et d'observer plus de traces de fissions confinées.

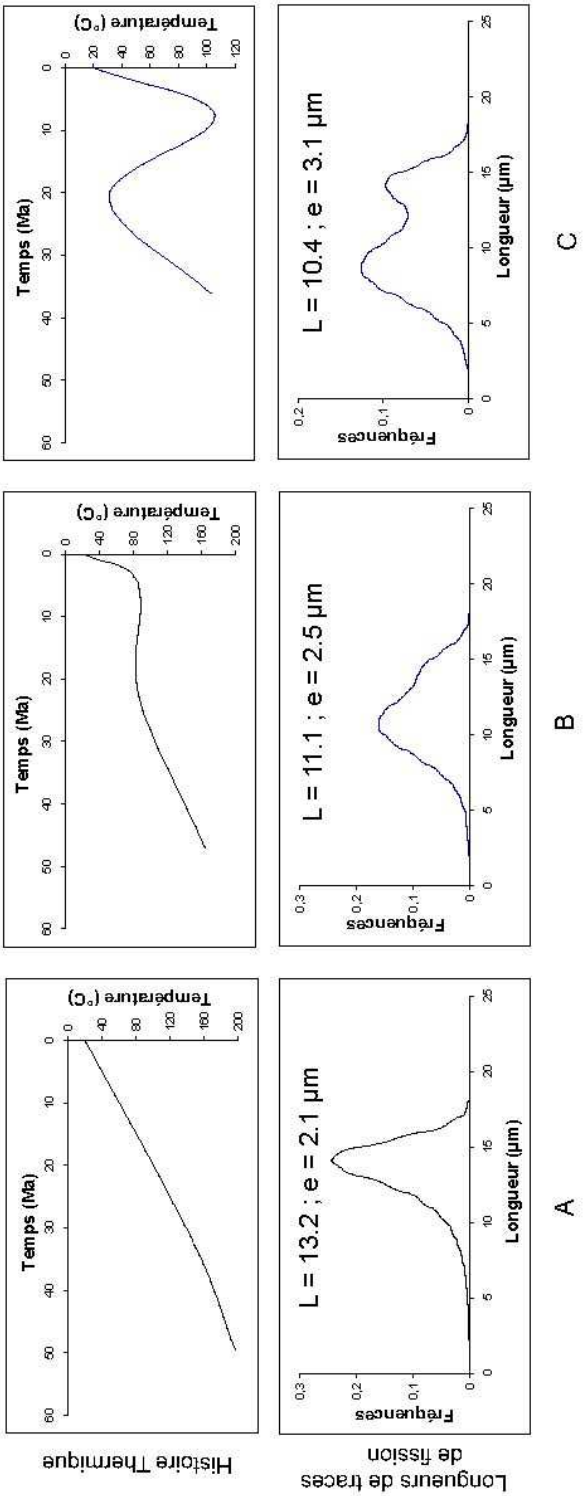

FIG. 2.6 – *Trois histoires thermiques avec les distributions de longueurs de traces associées, pour un âge thermochronologique identique (*20 *Ma) (L est la longueur moyenne, et e l'écart-type) : A. Exhumation continue ; B. Exhumation discontinue ; C. Exhumation, puis enfouissement et re-exhumation (calcul de cas d'école par AFTSolve).*

2.2.5 Notion de datation thermochronologique sur une roche détritique

Par définition, une roche sédimentaire détritique est une roche composée de clastes qui ont subi une exhumation dans leur zone source, une érosion, un transport, un dépôt, puis une diagénèse plus ou moins importante. Les rivières drainant des bassins d'alimentation pouvant être importants, il est possible que les roches sédimentaires du bassin contiennent des clastes de provenance et de sources très différentes. Ces roches possèdent alors un mélange de signatures correspondant à chaque source.

Lors de l'exhumation dans la zone source, les thermochronomètres enregistrent le trajet de la roche, à partir de la profondeur correspondant à la limite inférieure de la zone de rétention partielle (PAZ), jusqu'à la surface. Cet enregistrement est conservé dans les processus jusqu'à l'enfouissement dans le bassin sédimentaire de la roche. Plusieurs cas se présentent alors ((Brandon et al. 1998), Fig. 2.7) :

1. Si l'enfouissement ne permet qu'une température faible, inférieure à la température minimale de la PAZ : il n'y a aucun recuit du thermochronomètre, et le seul signal enregistré correspond à l'historique de la source. Les âges AFT possèdent un âge supérieur à l'âge détritique, correspondant respectivement aux ages thermochronologiques des différentes zones sources.
2. Si l'enfouissement atteint une température supérieure à la température maximale de la PAZ : le thermomètre est réinitialisé, *id est* le signal de la source est effacé intégralement. Il en résulte que le signal enregistré ne traduira que l'histoire du refroidissement de la roche sédimentaire, et non de la source. L'échantillon est alors totalement recuit, et toutes les populations possèdent un âge inférieur à l'âge détritique.
3. Si l'enfouissement atteint une température maximale comprise dans la fourchette de température de la PAZ : le thermochronomètre n'est que partiellement réinitialisé. L'échantillon est alors partiellement recuit, ce qui se traduit par certaines populations d'âges inférieurs à l'âge détritique, et certaines d'âges supérieurs. Le signal enregistré sera donc la somme d'un signal ancien correspondant à l'histoire de la source, et d'un signal récent attaché à

l'histoire du refroidissement de la roche sédimentaire en question. Dans ce dernier cas, pour les modélisations, une aide non négligeable est l'étude des longueurs de traces de fission.

Dans ce cas, pour chaque échantillon, il est nécessaire d'augmenter le nombre de grains comptés pour déterminer un âge pour chacun des 40 à 50 grains et mettre en évidence par un traitement statistique à partir de calcul de densité de probabilités des âges significatifs, donnant des populations d'âges thermochronologiques (Brandon 1996, Stewart et Brandon 2004).

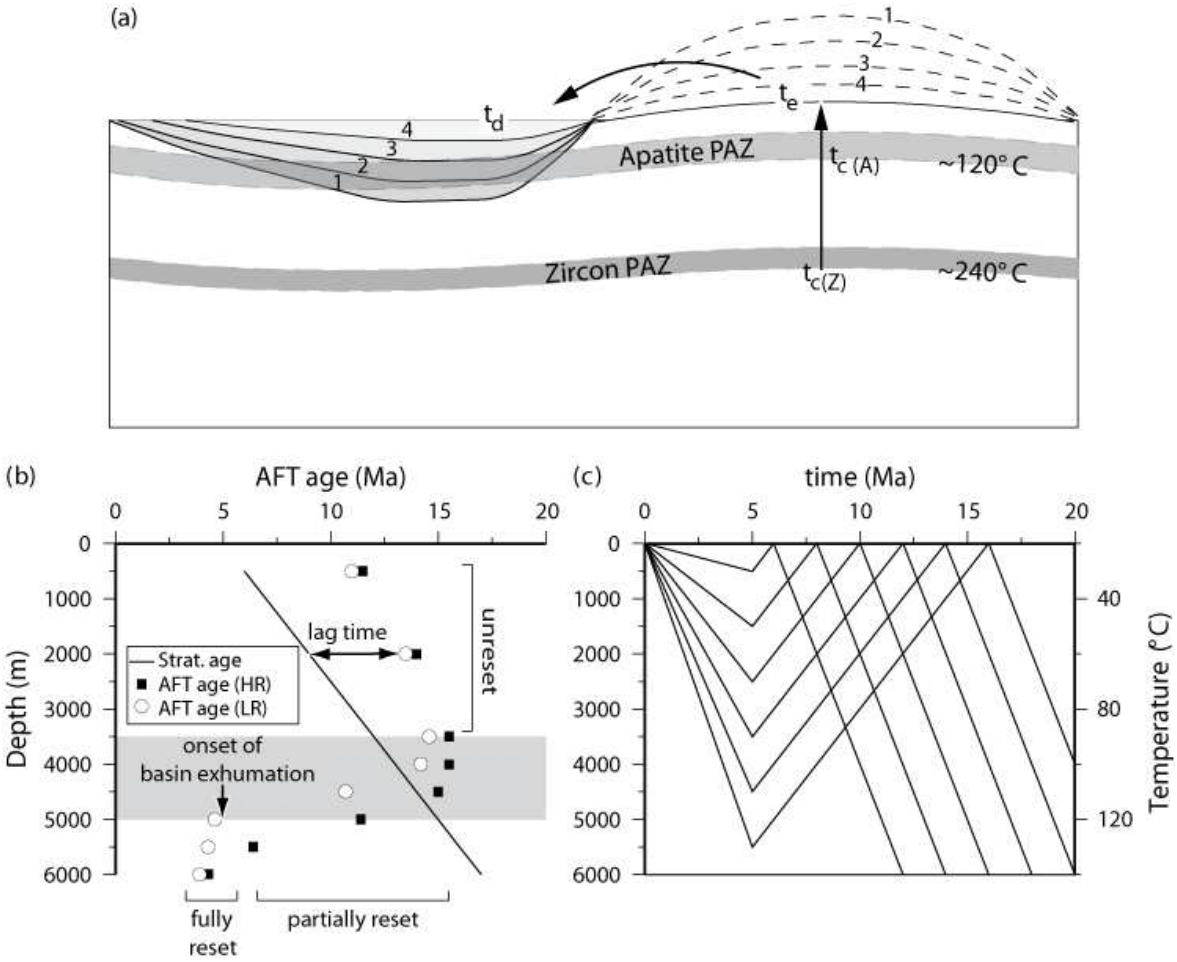

FIG. 2.7 – *Interprétation des différentes populations d'âges AFT d'une roche sédimentaire : concept de thermochronologie détritique. Les échantillons provenant d'horizons stratigraphiques 1 à 4 enregistrent le taux d'exhumation intégré entre leur passage à la température de fermeture du système (t_c) et leur arrivée à la surface (t_e). t_d est l'âge de dépôt qui est généralement considéré comme égal à t_e. Le Lag time est égal à $t_c - t_d$ ($= t_c - t_e$). (A) et (B) se réfèrent respectivement aux températures de fermeture des systèmes apatite et zircon ; la PAZ est la zone de rétention partielle. A cause de la faible température de fermeture du système apatite, les échantillons peuvent être partiellement ou totalement recuits dans le basin sédimentaire. Modifié de Garver et al. (1999). (b et c) Modèles synthétiques pour des échantillons provenant d'un bassin exhumé. Ces échantillons sont initialement exhumés dans la zone source, à un taux de 1 $km.Ma^{-1}$, érodés puis deposés dans un bassin depuis 16 Ma. Nous considérons une seule source avec un taux d'exhumation uniforme. De même, le taux de sédimentation est maintenu à 500 $m.Ma^{-1}$ entre 16 et 5 Ma. Ce bassin est ensuite exhumé à partir de 5 Ma. Pour simplifier, nous utilisons un géotherme constant de 20°$C.km^{-1}$ dans la zone source et dans le bassin sédimentaire. Les âges AFT prédits sont présentés en (b) en regard de l'âge stratigraphique associé à l'échantillon pour des apatites réagissant lentement (High Rententive, HR) et pour des apatites réagissant rapidement (Low Rententive, LR). Les âges AFT sont calculés en utilisant le modèle de Ketcham et al. (2000) prenant en compte les histoires thermiques décrites en (c) et les cinétiques de recuit caractérisées par des valeurs de Dpar entre 2.0 et 1.0 mm respectivement pour des apatites HR et LR (Carlson et al. 1999, Barbarand et al. 2003). La boite ombrée en (b) représente la PAZ pour les apatites. D'après van der Beek et al. (2006).*

2.2.6 Modélisation multi - cinétique de traces de fission dans l'apatite

La distibution des longueurs de traces confinées associée à l'âge trace de fission pour un échantillon donné permet la reconstitution de son histoire thermique au dessous de sa température de fermeture. Le principe de base des programmes de modélisation de données AFT est une calibration caractérisant le recuit des traces de fission en fonction du temps et de la température. Cette calibration s'effectue sur la base d'expériences de recuit en laboratoire (Green et al. 1985; 1989b).

Des modèles quantitatifs ont été proposés par Lutz et Omar (1991), Corrigan (1991), Crowley (1993), Gallagher (1995), Willett et al. (1997), Ketcham et al. (2000), Hadler et al. (2001) et Ketcham (2005). Ils permettent tous, un modèle théorique du raccourcissement des traces confinées, une intégration continue du modèle sur un trajet temps-température, un test statistique pour comparer les résultats des modèles avec les données mesurées et une détermination d'un modèle optimal basé sur cette comparaison.

Nous utilisons AFTsole (Ketcham et al. 2000) basé sur les cinétiques de recuit (Carlson et al. 1999, Barbarand et al. 2003). Il permet la prédiction de trajets temps-température comme un système multi-cinétique. La correction de l'influence de l'anisotropie de l'apatite sur la longueur des traces est effectuée, et pour chaque grain, l'ensemble des paramètres cinétiques mesurés est pris en compte.

2.3 Méthode de modélisation et d'inversions

Pour contraindre les différentes hypothèses présentées en partie 1, j'ai modélisé la cinétique du prisme himalayen. Ces modèles permettent de prédire le champ température associé à chaque modèle, et ainsi de calculer des âges thermochronologiques respectivement associés. Pour cela, j'utilise le code PECUBE (Braun 2003) modifié par Jean Braun et moi-même, ainsi qu'un algorythme d'inversion (NA, Sambridge (1999a)).

2.3.1 Modélisation thermique

Le code PECUBE (Braun 2003) est un code d'éléments finis permettant de prédire l'âge de fermeture des systèmes thermochronologiques utilisés, par résolution de l'équation de la chaleur dans un bloc crustal affecté par des mouvements verticaux, horizontaux et/ou de l'érosion :

$$\rho c(\frac{\partial T}{\partial t} + u\frac{\partial T}{\partial x} + v\frac{\partial T}{\partial y} + w\frac{\partial T}{\partial z}) = \frac{\partial}{\partial x}k\frac{\partial T}{\partial x} + \frac{\partial}{\partial y}k\frac{\partial T}{\partial y} + \frac{\partial}{\partial z}k\frac{\partial T}{\partial z} + \rho A$$

où $T(x, y, z, t)$ est la température, ρ la densité des roches, c la capacité thermique, u, v et w les coordonnées de la vitesse, k la conductivité et A la production de chaleur par radioactivité. Cette équation doit être résolue pour un champ de températures initial :

$$T_0 = T(x, y, z, t = 0),$$

un champ de vitesses donné dans le modèle tectonique :

$$\begin{cases} u \neq 0, \\ v \neq 0, \\ w \neq 0, \end{cases}$$

et un set de conditions aux limites :

$$\begin{cases} T(x, y, z = -H, t) = T_H, \\ T(x, y, z = S(x, y, t), T) = T_{MSL} + \beta S(x, y, t), \\ \frac{\partial T}{\partial n} = 0 \; le\ long\ des\ frontières\ du\ modèle, \end{cases}$$

où $z = -H$ représente la base du modèle, $S(x, y, t)$ la surface topographique à t, T_{MSL} est la température au niveau de la mer, T_H la température à la base du modèle, n le vecteur normal à la surface externe du modèle et β le gradient atmosphérique de température (lapse rate). Avec ce modèle, nous ne définissons pas un flux de chaleur à la base, mais une température basale. Ce choix a été fait pour simplifier les calculs thermiques.

Dans ces modélisations, nous négligerons aussi le transfert de chaleur par les fluides. Des travaux récents (Evans et al. 2004, Whipp et Ehlers 2007) suggèrent que le transfert de chaleur par circulation de fluides peut être significatif dans le Haut Himalaya. Mais son importance relative à l'advection verticale importante de

ce flux par l'exhumation des roches est inconnue (Ehlers 2005). Nous supposons donc que le transfert de chaleur par advection des roches et par conduction sont les mécanismes dominants du système thermique.

Nous utilisons un approche mixte Eulérienne - Lagrangienne demandant de fréquentes re-interpolations du champ de températures dans la direction verticale. Les chemins $T - t$ (température - temps) sont alors calculés, ce qui permet l'obtention des âges thermochronologiques pour les systèmes étudiés. Nous calculons les âges traces de fission sur apatites (AFT, $T_f = 110°C$), $(U + Th)/He$ sur apatites ($T_f = 70°C$) et $^{40}Ar/^{39}Ar$ sur muscovites ($T_f = 350°C$) par modélisation directe de l'accumulation des produits fils, et pas simplement en prenant l'âge de fermeture (Wolf et al. 1998). Pour les traces de fission sur apatites, nous utilisons le modèle de Laslett (1987), Lutz et Omar (1991) décrit dans van der Beek (1995), pour l'$(U + Th)/He$, les modèles de Wolf et al. (1998), Farley (2000), et le modèle de Rahn et al. (2004) pour les traces de fissions sur zircons.

2.3.2 Modélisation tectonique/cinématique

Nous utilisons ici un modèle cinématique de plats et de rampes avec chevauchement(s) et/ou réactivation hors-séquence développé pour l'occasion par Jean Braun. Ces différents processus peuvent avoir un rôle important dans la déformation du front de la chaîne. Ces différents processus sont décrits dans l'article de la partie 1.3.2. Dans ce modèle, nous définissons des failles qui délimitent des blocs dont les particules sont mobiles grâce à un champ de vitesse bien défini. Pour définir ces processus, il est necessaire de définir un repère fixe dans le modèle.

Détermination d'un repère fixe :

Décrire un champ de vitesses, définir des mouvements implique de définir un repère fixe dans lequel nous décrivons toutes les failles, leurs activités et leurs mouvements au cours du temps. Il y a plusieurs manières de déterminer un point fixe :

L'Asie-Tibet fixe : à ce moment, il n'y a pas de déformation du bloc du Tibet. Ce modèle est en contradiction avec les données de terrain. Nous ne l'utiliserons pas.

L'Inde fixe : Dans notre scénario, en 20 *Ma*, il y a environ 300 *km* de raccourcissement. L'Inde fixe engendre :

- La taille du modèle est démesurément grande, ce qui implique un temps de calcul démesurément long.
- La topographie himalayenne doit être advectée, ce qui implique une augmentation du temps de calcul.

Pour ces raisons, nous ne l'utiliserons pas.

La faille fixe : Prendre la faille fixe, implique deux interprétations. Une première interprétation est de considérer la faille fixée loin du modèle, comme sous le Tibet dans notre cas. Il en découle qu'avec ce modèle, il est possible de créer facilement un mécanisme de channel-flow en jouant sur les vitesses des blocs supérieurs. L'autre interprétation est de considérer que la faille est fixée à la topographie. Dans les deux cas, l'avantage est qu'il est possible de garder la topographie en steady state. La définition de plusieurs failles peut entraîner des problèmes. Il faut fixer le chevauchement le plus jeune, et translater les autres en fonction de la cinématique imposée.

Pour connaître la position de différentes failles dans le temps, nous calculons en remontant le temps, l'état initial du modèle. Nous sommes alors capables de reproduire le mouvement et la position des failles de l'état initial à l'état final (aujourd'hui).

Définition d'une faille :

Une faille est d'abord définie par la position de 2 points dans le plan horizontal à la surface du modèle (z_l) (Fig. 2.8). Les coordonnées de ces points sont données en latitude/longitude. L'ordre de définition de ces deux points détermine un système de coordonnées locales (r, s). L'axe r est défini pour le côté droit de cette ligne (du point 1 au point 2), l'axe s est vertical, et son origine est située n'importe où sur la ligne à $z = z_l$. Ceci implique que la géométrie de la faille est bi-dimensionnelle. La faille est ensuite implémentée en entrant n points caractéristiques dans le plan (r, s), et en les reliant par interpolations linéaires. La faille est alors défine dans le plan (r, s). L'ordre de ces points détermine le demi-espace qui bouge le long de la faille : c'est celui à droite de la faille. Sa vitesse v_o est imposée le long de la surface

de la faille, et son sens de mouvement est donné par son signe, dans le repère (r, s) (normal = signe positif, inverse = signe négatif).

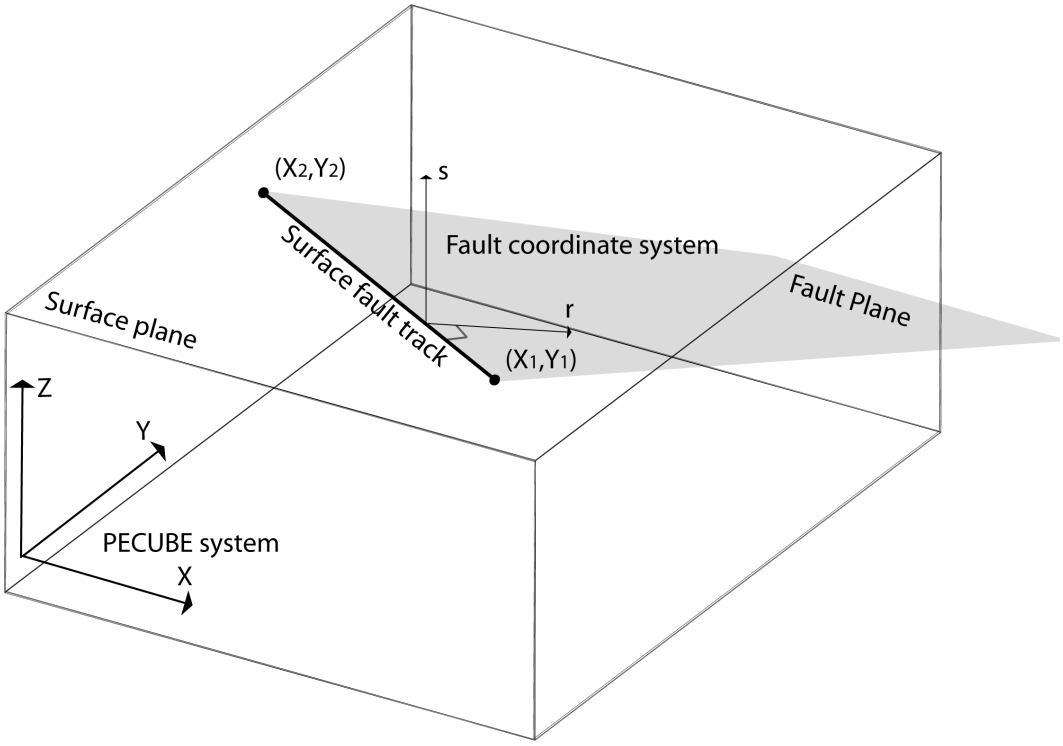

FIG. 2.8 – *Définition d'une faille dans le nouveau module de PECUBE dédié à l'utilisation de failles.*

Les failles sont définies pour l'état final du modèle, c'est à dire à l'actuel. Lors du run, la géométrie des failles est recalculée pour chaque pas de temps en fonction du champ de vitesses.

Définition du champ de déformation/vitesses :

Le champ de déformation est décrit par le champ de vitesses. Ce dernier est calculé en deux dimensions dans le plan (r, s) grâce à la méthode des kink-band et des plis-failles (Suppe 1983), et est translaté dans l'espace (x, y, z). Les vitesses sont calculées segment par segment. Dans les régions définies par un segment de faille unique et ses normales à chaque extrémité, la vitesse est imposée parallèle au segment de faille, avec v_o pour module. S'il y a plusieurs segments pour une même faille, conserver la masse implique (Fig. 2.9) :

Angle aigu : la direction de la vitesse de la région au-dessus est donnée par la moyenne des directions des deux segments (somme de deux vecteurs), et son

amplitude est donnée par $v'_o = v_o \frac{cos\alpha}{cos\frac{\alpha}{2}}$ avec α l'angle construit par les deux normales aux segments.

Angle obtu : la direction est obtenue de la même manière, mais le module est donné par $v'_o = v_o \frac{1}{cos\frac{\alpha}{2}}$

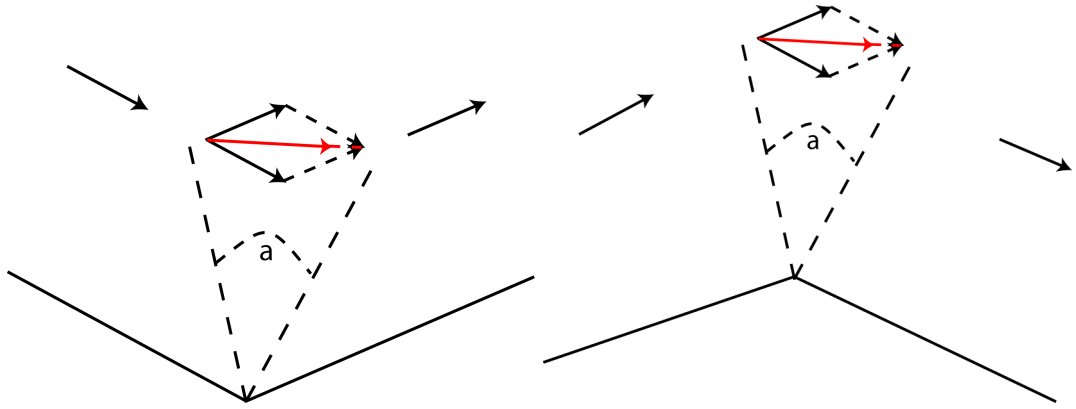

FIG. 2.9 – *Définition de la vitesse au niveau d'une rupture de pente du plan de faille.*

Pour implémenter plusieurs failles, il faut prendre en compte l'advection de la position et de la géométrie de la faille. Ici, les failles sont advectées en fonction de leurs positions, en déplaçant chacun des points les définissant par le vecteur déplacement correspondant. Le problème qui se pose est le passage d'une faille transportée au niveau d'un changement de pente (ex : plat $\Longrightarrow$ rampe ou vice versa). En effet, le champ de vitesses implique alors une déformation de la faille transportée. Par sa définition, il en résulte que pour une géométrie finale complexe, les failles transportées peuvent alors jouer pour des pas de temps intermédiaires, dans une géométrie qui n'est pas réaliste. Lors de cas litigieux, il est possible d'insérer un flag permettant de ne pas advecter les failles.

Cette définition des failles et du champ de vitesses interdit tout transfert de matière d'un bloc à l'autre.

2.3.3 Géométrie et cinématique utilisées

Un des aspects de cette modélisation est de comparer les résultats des modèles aux mesures de terrain. Pour cela, il faut choisir un transect qui se rapproche du transect d'échantillonnage. Plusieurs stratégies sont possibles :

- Suivre plus ou moins la ligne d'échantillonnage. Mais est-ce que cela n'introduit pas un biais dans le relief par le fait que la ligne d'échantillonnage ne suit pas un transect nord - sud, mais varie d'est en ouest ?
- Prendre une ligne droite perpendiculaire à la chaîne, qui passe par la zone étudiée, ce qui donne un modèle purement bidimensionnel. Les échantillons sont alors représentés par leur projection sur le transect. Le calcul ne prend alors pas en compte les effects topographiques.
- Utiliser un volume (3 dimensions) dont la surface supérieure représentant la topographie contient le transect échantillonné, ce qui nous permet de nous affranchir des effets liés au fait que la ligne d'échantillonnage n'est pas une doite. Cela permet de retrouver exactement nos points échantillonnés, à l'altitude correspondante.

Nous choisirons la dernière stratégie, qui est la plus simple à implémenter, et la plus réaliste dans le calcul des états thermiques (effets de la topographie, géométrie des failles non perpendiculaires au transect effectué). De plus, dans les orogènes actifs, le champ thermique est multidimentionel et étroitement lié à la topographie (Braun 2002a;b) et au trajet d'exhumation des roches qui possèdent des composantes significatives, à la fois verticales et horizontales (Stuwe et al. 1994, Manktelow et Grasemann 1997, Ehlers et al. 2001, Batt et Brandon 2002, Ehlers et al. 2003). La vue 3D restreinte de la zone étudiée est extraite à partir du modèle numérique de terrain (MNT) à 90 m du Népal (SRTM90), que j'ai dégradé à 1 km pour limiter les temps de calculs sous PECUBE.

Les âges de traces de fission sur apatites les plus vieux que nous avons sont de l'ordre de 10 Ma. Il en découle que notre modèle doit prendre en compte au moins cette période. Pour les coupes où il est nécessaire d'utiliser des données argon pour mieux contraindre le modèle, nous conservons la même date d'initiation du modèle, mais gardons uniquement les âges argon dans les zones où ils sont inférieurs ou égaux à 10 Ma, ce qui nous permet de nous affranchir du mouvement du MCT. D'après des données sédimentologiques et géochimiques datant l'exhumation du Bas Himalaya et le début de l'augmentation de son érosion, Huyghe et al. (2001) déduisent que le MBT s'est initié vers 8 Ma. Il faut donc le prendre en compte dans notre modélisation. En utilisant des données thermochronologiques recuites par-

tiellement, Robert (2005), van der Beek et al. (2006) montrent que le MFT s'est initié vers 2 *Ma*. Pour notre modèle, nous avons donc à prendre en compte, le MBT, le MFT, et la potentielle faille liée au front topographique. Il faut déterminer depuis quand cette dernière est en activité.

En revanche, nous ne considérons pas de glissement potentiel sur le STD pour la gamme d'âges thermochronologiques que nous utilisons. En effet, la quantité de déplacement ainsi que son timing sont peu contraints en comparaison avec l'activité du MFT ou du MCT (Hodges 2000).

La convergence totale étant de l'ordre de 14 et 21 $mm.an^{-1}$ sur la durée du modèle, il est nécessaire de partitionner les vitesses entre l'underthrusting et l'overthrusting de manière à ce que la somme des vitesses horizontales soit de l'ordre de 21 $mm.an^{-1}$.

A cette échelle de temps, nous considérons la topographie en steady state pour plusieurs raisons :

1. Nous n'avons pas de données suffisamment précises pour contraindre le changement de topographie au cours du temps pour des échelles de temps supérieures à 3 *Ma*.
2. Modéliser des processus de surface complexes entrainerait une modification importante de la base conceptuelle du PECUBE car il faudrait suivre les points de la surface à chaque pas de temps. En effet, ceci demanderait à ce que la surface soit modélisée par une grille dynamique qui serait découplée de la grille calculée pour le modèle 3D.
3. Diverses observations suggèrent que la position des systèmes fluviatiles a peu changé lors de ces 10 derniers millions d'années (Whipp et al. 2007). Nous retrouvons peu de paléo-rivières, le drainage de la marge sud du plateau tibétain ne semble pas avoir été modifié depuis plusieurs millions d'années. Si le relief change, cette position aurait dû varier de façon importante au cours du temps (Gabet et al. 2004).

2.3.4 Modélisation des processus de surface

Pour modéliser l'érosion/déformation, plusieurs stratégies sont possibles :

– Idéalement, l'implémentation d'un code de type Cascade (Braun et Sambridge 1997) permettrait une bonne approche de la modélisation des processus de surface. Plusieurs problèmes en découlent. Le premier est purement technique et concerne le couplage de PECUBE à Cascade car ils n'utilisent pas le même type de grille (grille dynamique *versus* grille statique), ce qui pose des problèmes quant au suivi des points pour le calcul de leur trajet temps - température. Il est peut être possible de le faire avec un coupleur du type PALM (LMC, Grenoble). Le second problème qui se pose est comment obtenir une topographie actuelle correspondant à la réalité, et donc comment comparer les âges calculés et les âges mesurés sur des échantillons actuellement situés en surface.
– Plus simplement, nous utilisons une routine supplémentaire sous PECUBE d'érosion sous forme de loi exponentielle. Sa limite est de créer un biais pour les hautes altitudes et pas de sédimentation dans le bassins d'avant-pays. Cette dernière, que nous avions développée pour l'étude du Dabie Shan (Braun et Robert 2005), est présente dans la version de PECUBE actuellement disponible.

2.3.5 Choix de la température basale

Dans PECUBE, il n'est actuellement pas possible de définir un flux de chaleur à la base du modèle. Pour des simplifications de calculs, il n'est possible que de définir une température fixe à la base du modèle.

Ce paramètre est aussi une valeur difficile à définir précisément. Pour cela, il est nécessaire de l'inclure en paramètre variable lors d'inversions.

Dans sa synthèse sur l'histoire cénozoïque de l'Himalaya, Yin (2006) utilise à plusieurs reprises un gradient géothermique de $30°C.km^{-1}$ en surface. Cette valeur correspond à une température à la base du modèle (60 km) de $1800°C$, si nous ne prenons en compte ni l'advection des roches, ni la production de chaleur par radioactivité. Cette température est probablement surestimée. En effet, à cette température, les roches devraient être en fusion. Nous devons donc implémenter une production de chaleur dans le modèle représentant la production de chaleur dans

la croûte par radioactivité principalement, afin de diminuer la valeur de la température basale.

2.3.6 Détermination de la production de chaleur

Théoriquement, le taux de production de chaleur (Q, production de chaleur volumique) est calculé à partir des constantes dans l'équation de la chaleur. C'est une énergie par unité de temps et par unité de volume ($[Q] = W.m^{-3}$). Or, dans PECUBE, nous devons entrer la valeur $[A] = K.Ma^{-1}$. La relation entre les 2 est liée à la capacité calorifique massique à pression constante Cp ($[Cp] = J.K^{-1}.kg^{-1}$) et à la masse volumique ρ ($[\rho] = kg.m^{-3}$) par la relation suivante :

$$[A] = [\frac{Q}{\rho.Cp}] \tag{2.7}$$

L'ordre de grandeur de Q pour la lithosphère est de 0.3 à 3 10^{-6} $W.m^{-3}$, ρ est de l'ordre de 2700 $kg.m^{-3}$, et Cp de l'ordre de 1000 $J.K^{-1}.kg^{-1}$ (valeurs issues de Jaboyedoff (1999)). A devrait donc être de l'ordre de 10^{-13} à 10^{-12} $K.s^{-1}$ soit 2.3 à 23 $°C.Ma^{-1}$.

Pour des raisons pratiques, ce paramètre est normalisé (A_N) dans PECUBE. La valeur réelle A est alors calculée par :

$$A = \frac{A_N.k}{Z_l^2.T_{max}} \tag{2.8}$$

où k est la diffusivité thermique, Z_l la profondeur du modèle et T_{max} la température à la base du modèle.

Le paramètre A_N est difficilement quantifiable. De plus, dans les modèles construits, nous imposons une production de chaleur A_N constante sur chaque modèle complet pour des raisons pratiques. Ce n'est pas complètement réaliste, mais couplé avec la notion de température basale, cela permet d'obtenir un champ de température réaliste. Il peut alors être utile de laisser A_N variable au cours d'inversions.

2.3.7 Méthode d'inversion et de recherche de paramètres via le Neighbourhood Algorithm (NA)

Grâce au package NA développé par Sambridge (1999a;b), il est possible d'effectuer une recherche multi-dimensionnelle directe de paramètres dans notre modèle pour des paramètres définis entre 2 bornes géologiquement et physiquement cohérentes. Cette méthode est applicable pour un grand nombre d'inversions non-linéaires, en particulier pour les problèmes où les relations entre les observables et les inconnues (paramètres) sont complexes.

Cette approche est divisée en deux étapes. La première étape, dite de recherche, échantillonne aléatoirement l'espace de paramètres (multi-dimensionnel) pour un nombre défini de combinaisons (modèles). L'espace de paramètres est alors découpé en cellules de Voronoy centrées autour de chaque modèle. Pour chaque modèle, un misfit est alors calculé. Dans le cas de l'approche thermo-cinématique que nous avons effectué, il est donné par :

$$misfit = \frac{\sqrt{\sum_{i=1}^{n_{obs}} \left(\frac{Age^i_{obs} - Age^i_{calc}}{error^i_{obs}} \right)^2}}{n_{obs}} \tag{2.9}$$

où Age^i_{calc} est l'âge i calculé correspondant à l'Age^i_{obs} mesuré avec l'erreur $error^i_{obs}$, i variant de 1 à n_{obs}, nombre total d'observables.

Une seconde étape affine la recherche de paramètres en tirant aléatoirement un nouveau set de paramètres dans les cellules de Voronoy avec le meilleur misfit. L'utilisateur définit le nombre de modèles initiaux, le nombre de cellules rééchantillonnées, et le nombre d'itérations. Cette méthode permet de limiter les effets des minima locaux, et d'en retenir qu'un seul d'entre-eux.

La structure du code NA (Fig. 2.10) permet l'intégration simple du modèle dans le code de recherche de paramètres, et surtout permet de définir et de configurer simplement les inversions. `forward` calcule le misfit de la fonction pour un modèle donné. Seule cette routine est appelée plusieurs fois (à chaque modèle dans chaque itération). `Na.in` permet le contrôle des options et de la recherche de paramètres. `na.sum` `na.nad` et `NA_results.txt` correspondent respectivement aux sorties écran de l'exécution de NA, et au fichier résultat de l'inversion. Ce dernier

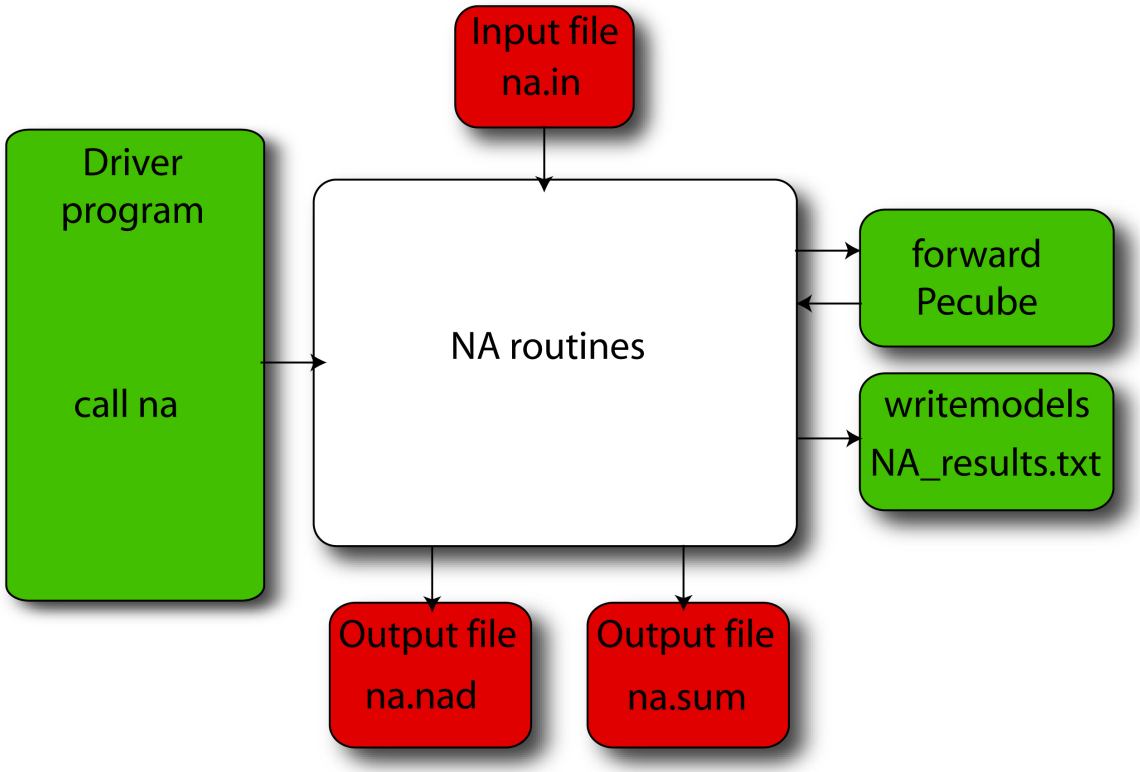

FIG. 2.10 – *Structure du code NA. Les routines vertes sont données et/ou modifiées par l'utilisateur. Les fichiers rouges sont les entrées - sorties utilisées par le programme (D'après Sambridge (1999a)).*

donne simplement pour chaque modèle testé la valeur du misfit et la valeur des paramètres associés.

Pour visualiser les résultats, il faut projeter dans des espaces à deux dimensions, où chaque axe correspond à un paramètre.

Transition

Cette méthodologie nous a permis d'acquérir 35 nouveaux âges AFT au Népal central, et de développer un modèle 3D rendant compte des âges thermochronologiques de basses températures à la fois dans la partie haute chaîne et dans la partie moyen pays. Ces données et ces modélisations nous permettent dans la partie suivante de démontrer le rôle prépondérant de la géométrie des failles crustales dans un prisme orogénique.

Cinématique récente et structure profonde du prisme himalayen

3

Sommaire

Dans ce chapitre, nous présentons les résultats analytiques et numériques obtenus au niveau de la transition topographique entre le Moyen Pays Himalayen et la Haute Chaîne. Nous les discutons par la suite en termes de variations latérales cinématiques, géométriques ou érosives.

This chapter presents analytical and numerical results from the physiographic transition in the Lesser Himalaya. We discuss them in terms of lateral variations of kinetics, geometry or denudation.

3.1 Présentation

Le travail sur la coupe nord - sud du Langtang (Népal central) est la base d'un article de synthèse soumis à Geology. Dans cet article, nous montrons à partir de modélisations directes et inverses que la géométrie des failles majeures du prisme himalayen contrôle majoritairement la distribution des âges thermochronologiques à la surface actuelle. La répartition des vitesses sur ces failles joue au second ordre. Les paragraphes suivants donnent quelques informations complémentaires non développées dans l'article.

Une partie importante du travail a été l'obtention des données traces de fission sur apatite le long de la coupe nord-sud du Langtang. Nous avons échantillonné des gneiss dans la zone du MCT, des quartzites et des grès dans le Lesser Himalaya. J'ai ensuite traité ces échantillons du broyage aux datations, ce qui m'a demandé un peu plus d'une année. La très grande majorité de ces échantillons ont pu être datés sans problème de matériel ou de concentration initiale en uranium trop faible. Les résultats bruts sont donnés dans l'annexe A.3.2, et la carte des résultats est dans l'article suivant. Les âges traces de fission sur apatite sont très jeunes dans la zone du MCT ($\leqslant 1\ Ma$), puis augmentent régulièrement vers le sud sans montrer de saut, ce qui est fortement compatible avec une cinématique sans méchanisme en hors-séquence.

Deux relations âge-altitude, une au sud de la coupe au niveau du granit de Palung, située au dessus du plat du MHT, et la seconde au niveau de la transition physiographique, dans le High Himalaya nous permettent d'estimer respectivement, des taux d'exhumations de 0.5 $km.My^{-1}$ et de 4.4 $km.My^{-1}$. Nous les interpretons en première approximation à partir de simples calculs angulaires pour obtenir un encadrement de la valeur des angles du pendage du MHT. Sous le granit de Palung, nous estimons le pendage du plat du MHT à $4 - 7°$. En revanche, le fort taux d'exhumation au niveau de la transition physiographique signe une rampe de pendage $26 - 60°$. Cette dernière est mal contrainte à cause d'une surestimation du taux d'exhumation à cause de la forte topographie (Braun 2002b). Si l'on corrige de cette topographie en utilisant l'approche de Stuwe et al. (1994) ou Manktelow et

Grasemann (1997), nous ramenons cette valeur de pendage de la ramp crustale du MHT à $\sim 30°$. Ces valeurs sont compatibles avec les données géophysiques.

La Fig. 3.1 donne un aperçu de la géométrie et des cinématiques implémentées dans le modèle du Langtang. Cette géométrie a été construite à partir des modèles établis précédement par Avouac (2003), Bollinger et al. (2006). La Fig. 3.1, dans laquelle la pente de la rampe émergeant à la surface est de 27°, et de celle se situant sous le front topographique de 18° représente un des géométries utilisées, et est représentative de la géométrie générale des modèles.

Dans ces modèles, nous définissons le champ de vitesses dans le repère du MHT fixe. La vitesse horizontale de convergence totale est de 20 à 21 $mm.an^{-1}$. Nous fixons la vitesse d'underthrusting à 15 $mm.an^{-1}$.

Les questions (liées) qui se posent sont :

1. Les chevauchements sont-ils réactivés ?
2. Quel est le raccourcissement sur chaque chevauchement ?
3. Quel paramètres thermiques utiliser ?

Pour mener à bien ces modélisations et afin de contraindre au mieux le champ de températures, nous utilisons deux systèmes thermochronologiques de basses températures distincts, à savoir, des données traces de fission sur apatites (cette étude et les données de Copeland, communication personnelle), et des données $^{40}Ar/^{39}Ar$ sur muscovites de Rai (1998) (Fig. 3.2).

En résumé, un modèle sans hors-séquence avec des paramètres thermiques raisonnables donnant un gradient de température moyen de $35°C.km^{-1}$ est bien corrélé avec les âges traces de fission sur apatites. Les âges traces de fission sur apatites sont très jeunes au nord du front topographique. Cela s'explique par la présence de la rampe. En effet, cette présence perturbe fortement les isothermes, en les remontant fortement vers la surface. Le rajout d'un chevauchement hors séquence modifie légèrement ce résultat, en augmentant la proportion d'âges très jeunes : la zone est plus étendue vers le nord du modèle. *Un chevauchement hors séquence n'est pas necessaire pour expliquer la transition dans les âges thermochronologiques observée au niveau de la transition topographique.*

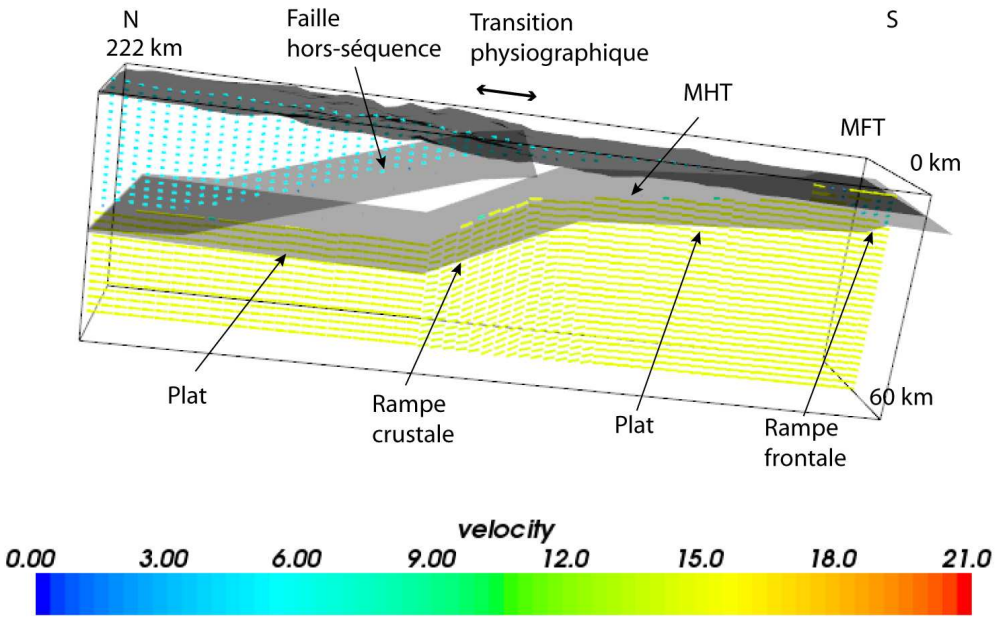

FIG. 3.1 – *Géométrie de failles (MFT, MHT et hors séquence) implémenté dans la modélisation, et champ de vitesses associées (en km.My*$^{-1}$*. Ici, la pente de la rampe du MHT est de* 17.8°.

Pour les données brutes, l'article se réfère à un Data Repository Item, qui est publié dans ce manuscrit dans l'annexe A.3.2.

3.2 Assessing quaternary reactivation of the Main Central Thrust Zone (central Nepal Himalaya) : New thermochronologic data and numerical modeling

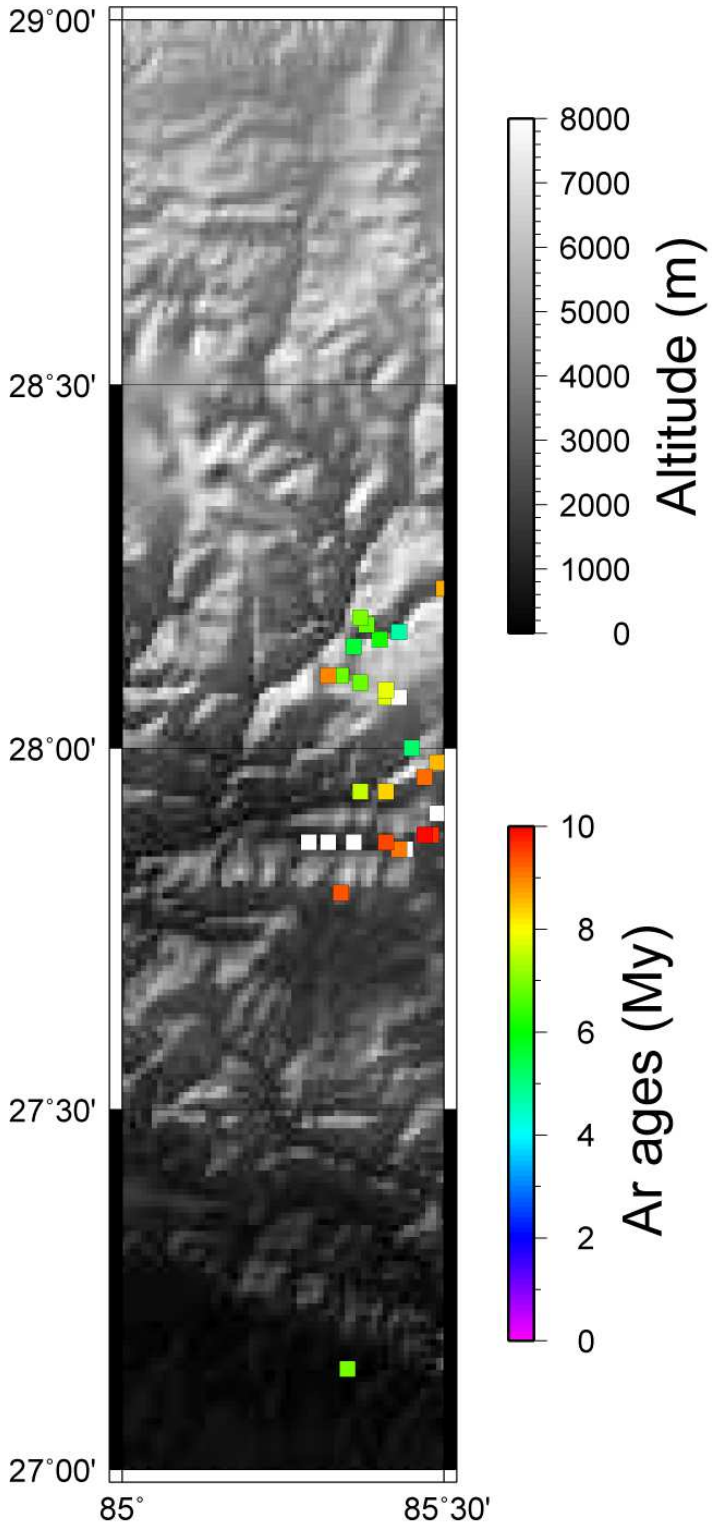

FIG. 3.2 – *Localisation des données $^{40}Ar/^{39}Ar$ de Rai (1998) sur le modèle numérique de terrain utilisé dans les modélisations avec PECUBE.*

Assessing Quaternary reactivation of the Main Central Thrust zone (central Nepal Himalaya): New thermochronologic data and numerical modeling

Xavier Robert[1], Peter van der Beek[1], Jean Braun[2], Claire Perry[1,2*], Mathieu Dubille[1] and Jean-Louis Mugnier[3]

1. Laboratoire de Géodynamique des Chaînes Alpines, Université Joseph Fourrier, Grenoble, France
2. Géosciences Rennes, Université de Rennes 1, Rennes, France
3. Laboratoire de Géodynamique des Chaînes Alpines, CNRS, Le Bourget-du-Lac, France

* Present address: GEOTOP, Université du Québec à Montréal, Montreal, Canada

To be submitted to Geology

ABSTRACT

We study the recent dynamics of the Himalayan orogen in central Nepal with the goal of quantifying the onset of activity and the deformation history recorded by the different major thrusts. Here, we focus on the possible reactivation of the footwall of the MCT, which is marked by a strong topographic transition. Different tectonic mechanisms, such as out-of-sequence thrusting or underplating over a major crustal ramp, have been suggested to explain the morphology and exhumation patterns in this area. We present 25 new apatite fission-track (AFT) ages collected in central Nepal

along a north – south transect from the Langtang Himal to the active deformation front, as well as two age-elevation profiles. Ages are consistently < 3 Ma in the MCT zone and increase continuously in age to 4 - 6 Ma in the south. The topographic transition does not correspond to a sharp jump in AFT ages. Apparent exhumation rates from the age-elevation relationships vary from $0.46^{+0.13}_{-0.09}$ km.My^{-1} in the Palung granite south of Kathmandu to $4.4^{+4.8}_{-1.5}$ km.My^{-1} in the MCT zone, although the latter rate is probably overestimated by a factor of two due to topographic effects. As shown by a new numerical model, these strongly varying exhumation rates can be explained by a model of overthrusting over a crustal ramp, which exerts a primary control on age patterns, and do not require out-of-sequence reactivation of thrusts in the MCT zone.

Keywords: Himalaya, Nepal, Main Central Thrust, Tectonics, Thermochronology, Numerical modeling.

INTRODUCTION

The Himalayan orogen is characterized by a north-dipping, southward-propagating, crustal-scale thrust sequence (Fig. 1). Major thrusts delimit three distinct units that are, from south to north: the Siwaliks foreland fold-and-thrust belt between the Main Frontal (MFT) and the Main Boundary (MBT) thrusts; the metasediments of the Lesser Himalaya between the MBT and the Main Central Thrust (MCT); the Greater Himalayan crystalline thrust sheet with overlying Tethyan sediments (Gansser, 1964; Le Fort, 1975). Geophysical and structural studies suggest that all major faults in the central Himalaya, including the MFT, MBT and MCT, branch at depth to a single major mid-crustal decollement, the Main Himalayan Thrust (MHT; Hirn and Sapin, 1984; Zhao et al., 1993; Makovsky et al., 1996; Schulte-Pelkum et al.,

2005). The MHT is characterized by a ramp-flat geometry, probably with two major ramps. One is shallow and corresponds to where the fault emerges with a dip angle of around 30° at the surface (MFT). The other is envisaged at mid-crustal depth beneath the sharp topographic front of the high range with a dip angle to the north of about 15-30° (Avouac, 2003; Berger et al., 2004). Ten to thirty kilometres south of the MCT in central Nepal, a sharp topographic transition separates a northern high-relief zone at a mean elevation >3000 m and a southern zone of more moderate relief at a mean elevation <1500 m (Lavé and Avouac, 2001; Duncan et al., 2003; Wobus et al., 2003).

Recently, two competing models have been proposed to describe the present-day kinematics of the Central Nepal Himalaya (Fig. 1). These differ principally in their predictions of which surface-breaking faults accommodate current shortening and what kinematics drive rapid exhumation in the topographic transition zone around the MCT. Avouac (2003) and Bollinger et al. (2004; 2006) argue that recent deformation is concentrated along the MHT and that rapid exhumation in the MCT zone results from underplating along the MHT ramp. In contrast, Hodges et al. (2004) suggest active out-of-sequence thrusting in the MCT zone, possibly driven by climatically-controlled and strongly localized exhumation in this area. A jump in detrital thermochronologic and cosmogenic ages across the topographic transition in central Nepal has been argued to support the latter model (Wobus et al., 2005; 2006).

The opposing models predict different upper-crustal exhumation paths for rocks in the Lesser Himalaya and the topographic transition zone, which should be recorded by low- and medium-temperature thermochronometers such as apatite fission-track (AFT) and mica Ar-Ar data (Fig. 1). In particular, the out-of-sequence model predicts a jump in ages in the MCT zone (Hodges et al., 2004; Wobus et al., 2006), whereas the underplating model would predict a gradual decrease in ages across the Lesser Himalaya from the MBT to the MCT (Bollinger

et al., 2004; 2006). However, due to unfavorable lithologies, little thermochronologic data has been collected until recently in the Lesser Himalaya, precluding a clear discrimination between the two models. Here, we present new apatite fission-track data from a transect across the central Nepal Himalaya and combine these with a forward numerical model in order to assess the different models.

THERMOCHRONOLOGICAL DATA

Samples were collected along a north-south transect from the Langtang Himal to the Ganga plain in central Nepal (Fig. 2). In this area, the MCT forms a large klippe of Greater Himalayan rocks, the Kathmandu klippe (Upreti, 1999). The central part of the klippe is intruded by the Ordovician Palung granite, which was a main target for our sampling. In the half-window of Lesser Himalayan sequences to the northwest of the Kathmandu klippe, we targeted quartzites and sandstones of the Lower Nawakot Group as well as the Ulleri gneiss (Upreti, 1999) for sampling. Two age-elevation profiles were collected; one within the topographic transition zone from the Trisuli River valley at Dunche up Gosainkund mountain, with sample elevations spanning 1780-4500 m; another in the Palung granite between 770 and 2500 m elevation.

Details on sample processing and the data reported in this paper are provided in the Data Repository[*]. An AFT-age transect shows a continuous trend (Fig. 2), with ages younging nearly linearly from the MBT to the MCT (with the exception of two young AFT ages at low elevations in the Palung granite south of Kathmandu). The northernmost samples from the MCT zone are consistently very young (<3 Ma) and comparable to data collected from further west (Blythe et al., 2007). This trend crosses the topographic transition and the MCT zone

[*] A data repository item, Apatite fission-track data from the central Nepal Himalaya, is submitted with this manuscript

without a significant jump in ages. Mica Ar–Ar data from the same region (Arita et al., 1997; Rai, 1998; Bollinger et al., 2004), although less spatially extensive as the AFT data reported here, show the same pattern (Fig. 2).

The two age-elevation profiles are shown in Fig. 3. In the Palung granite, ages vary from 2.1±1.0 Ma at 770 m to 6.5±0.6 Ma at 2360 m elevation. Weighted linear regression on these data suggests an exhumation rate of $0.46^{+0.13}_{-0.09}$ km.My^{-1}. In contrast, ages from the Gosainkund profile only vary between 1.2±0.4 and 2.6±0.5 Ma, suggesting an exhumation rate an order of magnitude higher, at $4.4^{+4.8}_{-1.5}$ km.My^{-1}. However, at such high rates of exhumation, topographic disturbance of the closure isotherm may lead to seriously overestimating exhumation rates from age-elevation relationships (Stüwe et al., 1994; Manktelow and Grasemann, 1997; Braun, 2002; Ehlers, 2005). This overestimate can be quantified as (Braun, 2002):

$$\frac{dh}{da} = \frac{\dot{e}}{(1-\alpha)}$$

Where *dh/da* is the apparent age-elevation relationship, $\dot{e}$ is the "real" exhumation rate, and α is the vertical deflection of the closure temperature isotherm relative to the amplitude of the surface topography; α varies from 0 (no deflection of the isotherm) to 1 (the isotherm follows the surface topography).

We have estimated α for the AFT closure isotherm of 110±10 °C using both the methods of Stüwe et al.(1994) and Manktelow and Grasemann (1997; cf. Braun et al., 2006 for a review), using topographic wavelengths (~30 km) and amplitudes (~3 km) that characterize the Gosainkund (Langtang Himal) sampling area. In both cases, we find that $\alpha \approx 0.5$, so that we should expect to overestimate exhumation rates by approximately 100%; "real" exhumation rates for the Gosainkund profile are thus probably in the order of 2.0-2.5 km.My^{-1}.

We use a simple geometric model (Fig. 3) to test whether these large differences in exhumation rate are compatible with overthrusting on a crustal ramp. We assume a ramp and flat geometry for the MHT and estimate the angles of the flat and ramp that are required to explain these differences. Previous thermo-kinematic models (Bollinger et al., 2006; Brewer and Burbank, 2006; Wobus et al., 2006; Whipp et al., 2007) have shown that, in order to explain the AFT and mica Ar-Ar ages observed in the MCT zone, the ~21 km.My^{-1} convergence rate accommodated by the central Himalaya (Lavé and Avouac, 2000; Mugnier et al., 2004) should be partitioned into 5-6 km.My^{-1} of Himalayan overthrusting over the MHT and ~15 km.My^{-1} of underthrusting of the Indian plate (see also Robert et al., submitted). The rate of overthrusting (v) can be simply linked to the exhumation rate through the detachment angle (ϕ): $\tan \phi = \dot{e}/v$ (Fig. 3). Applying this approach to the exhumation rate inferred for the Palung granite suggests a detachment dip below the Lesser Himalaya and Kathmandu klippe of 5.2±1.6°, in good agreement with earlier estimates from elastic dislocation modelling of the present-day displacement field (Larson et al., 1999; Berger et al., 2004). When taking the exhumation rate of $4.4^{+4.8}_{-1.5}$ km.My^{-1} from the Gosainkund profile at face value, this would imply a ramp angle of 44±18°, only just overlapping with the highest estimates from geophysical and geodetic data (Avouac, 2003; Berger et al., 2004). However, when taking into account their probable 100% overestimation, the exhumation rate recorded by the Gosainkund profile is compatible with a ramp angle of ~22°, exactly within the range (15-30°) of allowable ramp angles from the geophysical and geodetic data. We thus conclude that the spatial pattern of thermochronologic ages and inferred exhumation rates do not require out-of-sequence thrusting in the MCT zone but can be explained by a model of overthrusting on a crustal ramp.

NUMERICAL MODEL

The topographic perturbation taken into account in the above analysis assumes vertical exhumation whereas the geometric model we use implies highly oblique particle trajectories, which may strongly affect inferred exhumation rates from age-elevation profiles (e.g., Huntington et al., 2007). Although the effect should be limited in the Palung profile because of relatively low exhumation rates and limited relief, and in the Gosainkund profile because it was sampled orthogonal to the tectonic transport direction (Huntington et al., 2007), we use a numerical model to study the relationship between structure, kinematics and exhumation rate more quantitatively.

We use a modified version of PECUBE (Braun, 2003), a finite-element code that predicts the thermal structure in a crustal block affected by vertical and/or horizontal advection. New features in the code include the incorporation of faults and associated kinematics, assuming vertical shear. Thermochronological ages are predicted by combining predicted cooling paths of rocks currently at the surface and a forward model of AFT annealing (Stephenson et al., 2006), assuming steady-state topography for the models presented here. Thermal parameters are described in Table 1. The input geometry for the numerical model is based on the crustal-scale cross-section proposed by Avouac (2003; Fig. 3). The model is run for 10 My in order to predict AFT ages up to this age. The MBT is active from 10 to 3 Ma and the MFT from 3 Ma to the present. The total overthrusting and underthrusting velocity on the MHT are 6 km.My^{-1} and 15 km.My^{-1} respectively (Fig. 4).

The model predicts a region of very young (<2 Ma) AFT ages overlying the MHT ramp (Fig. 4), where the vertical component of motion reaches 2.2 km.My^{-1}. Ages increase both to the north and the south of this zone, until reaching non-reset zones at both edges of the model.

Model exhumation rates above the southern flat are 0.5 km.My^{-1}. The AFT ages predicted by the model compare very favorably with observed ages, both when comparing the spatial pattern in a north-south transect across the central Himalaya, and when comparing the two age-elevation profiles.

CONCLUSIONS

An AFT-age transect through central Nepal shows a continuous younging trend from the Lesser Himalaya through the topographic transition and the MCT zone, and therefore no direct evidence for out-of-sequence thrusting in the latter area. Two age-elevation profiles, one from the topographic transition zone of high-relief above the MHT ramp and the other from the Kathmandu klippe above the southern flat of the MHT, show apparent exhumation rates that vary by an order of magnitude. However, when taking topographic perturbation of isotherms into account, these exhumation rates are consistent with overthrusting at a constant rate of 5-6 km.My^{-1} over a ~20° dipping crustal ramp and a ~5° detachment respectively, in accord with independent geophysical and geodetic data constraining the geometry of the MHT. A numerical thermo-kinematic model shows that both the spatial pattern of AFT ages and the age-elevation relationships are well fitted by such a scenario. Therefore, the new thermochronologic dataset that we sampled throughout the Lesser Himalaya with the specific objective to test the various kinematic models proposed for the central Nepal Himalaya, do not require out-of-sequence reactivation of a thrust in the MCT zone. This does not, however, mean that they are incompatible with it. In a separate contribution, we will use a formal inversion approach together with our numerical model in order to address this question further.

ACKNOWLEDGEMENTS

We thank Rodolphe Cattin, Frédéric Hermann and Jean-Philippe Avouac for helpful discussions and ideas. This study was supported by the *Institut National des Sciences de l'Univers* through the *Reliefs de la Terre* programme. We thank Ananta Gajurel of Tribuvhan University, Kathmandu, for assistance during field work

REFERENCES CITED

Arita, K., Dallmeyer, R.D., and Takasu, A., 1997, Tectonothermal evolution of the Lesser Himalaya, Nepal: Constraints from $^{40}Ar/^{39}Ar$ ages from the Kathmandu Nappe: The Island Arc, v. 6, p. 372-385.

Avouac, J.P., 2003, Mountain building, erosion and the seismic cycle in the Nepal Himalaya: Advances in Geophysics, v. 46, p. 1-79.

Berger, A., Jouanne, F., Hassani, R., and Mugnier, J.L., 2004, Modelling the spatial distribution of present-day deformation in Nepal: how cylindrical is the Main Himalayan Thrust in Nepal?: Geophysical Journal International, v. 156, p. 94-114.

Blythe, A., Burbank, D.W., Carter, A., Schmidt, K.L., and Putkonen, J., 2007, Plio-Quaternary exhumation history of the central Himalaya: 1. Apatite and zircon fission-track and apatite [U-Th]/He analyses: Tectonics, v. 26, TC3002, doi:10.1029/2006TC001990.

Bollinger, L., Avouac, J.-P., Catlos, E.J., Harrison, T.M., Grove, M., Beyssac, O., Goffé, B., and Sapkota, S., 2004, Thermal structure and exhumation history of the Lesser Himalaya in central Nepal: Tectonics, v. 23, p. TC5015, doi:10.1029/2003TC001564.

Bollinger, L., Henry, P., and Avouac, J.P., 2006, Mountain building in the Nepal Himalaya: Thermal and kinematic model: Earth and Planetary Science Letters, v. 244, p. 58-71.

Braun, J., 2002, Quantifying the effect of recent relief changes on age-elevation relationships: Earth and Planetary Science Letters, v. 200, p. 331-343.

—, 2003, Pecube: A new finite element code to solve the heat transport equation in three dimensions in the Earth's crust including the effects of a time-varying, finite amplitude surface topography: Computers and Geosciences, v. 29, p. 787–794.

Braun, J., van der Beek, P., and Batt, G., 2006, Quantitative Thermochronology: Numerical Methods for the Interpretation of Thermochronological Data: Cambridge, New York, Cambridge University Press, 258 p.

Brewer, I.D., and Burbank, D.W., 2006, Thermal and kinematic modeling of bedrock and detrital cooling ages in the central Himalaya: J. Geophys. Res., v. 111, doi:10.1029/2004JB003304.

Duncan, C., Masek, J., and Fielding, E., 2003, How steep are the Himalaya? Characteristics and implications of along-strike topographic variations: Geology, v. 31, p. 75-78.

Ehlers, T.A., 2005, Crustal thermal processes and thermochronometer interpretation, *in* Reiners, P.W., and Ehlers, T.A., eds., Low-temperature Thermochronology: Techniques, Interpretations, and Applications, 58: Chantilly, Virginia, Mineralogical Society of America/Geochemical Society Reviews in Mineralogy and Geochemistry, p. 315-350.

Gansser, A., 1964, Geology of the Himalayas: London, John Wiley and Sons Ltd., 289 p.

Hirn, A., and Sapin, M., 1984, The Himalayan zone of crustal interaction; suggestions from explosion seismology: Annales Geophysicae, v. 2, p. 123-130.

Hodges, K.V., Wobus, C.W., Ruhl, K., Schildgen, T., and Whipple, K.X., 2004, Quaternary deformation, river steepening, and heavy precipitation at the front of the Higher Himalayan ranges: Earth and Planetary Science Letters, v. 220, p. 379-389.

Huntington, K.W., Ehlers, T.A., Hodges, K.V., and Whipp Jr., D.M., 2007, Topography, exhumation pathway, age uncertainties, and the interpretation of thermochronometer data: Tectonics, v. 26, TC4012, doi:10.1029/2007TC002108.

Larson, K.M., Bürgmann, R., Bilham, R., and Freymueller, J.T., 1999, Kinematics of the India-Eurasia collision zone from GPS measurements: Journal of Geophysical Research, v. 104, p. 1077-1093.

Lavé, J., and Avouac, J.P., 2000, Active folding of fluvial terraces across the Siwaliks Hills (Himalayas of central Nepal): Journal of Geophysical Research, v. 105, p. 5735-5770.

—, 2001, Fluvial incision and tectonic uplift across the Himalayas of central Nepal: Journal of Geophysical Research, v. 106, p. 25561-25593.

Le Fort, P., 1975, Himalaya: the collided range. Present knowledge of the continental arc: American Journal of Science, v. 275, p. 1-44.

Makovsky, Y., Klemperer, S.L., Liyan, H., Deyuan, L., and Project INDEPTH Team, 1996, Structural elements of the southern Tethyan Himalaya crust from wide-angle seismic data: Tectonics, v. 15, p. 997-1005.

Manktelow, N.S., and Grasemann, B., 1997, Time-dependent effects of heat advection and topography on cooling histories during erosion: Tectonophysics, v. 270, p. 167-195.

Mugnier, J.L., Huyghe, P., Leturmy, P., and Jouanne, F., 2004, Episodicity and rates of thrust sheet motion in the Himalayas (western Nepal), *in* McClay, K.C., ed., Thrust Tectonics and Petroleum Systems, American Association of Petroleum Geologists Memoir 82, p. 1-24.

Rai, S.M., 1998, Les Nappes de Kathmandou et du Gosainkund, Himalaya du Népal central (Etude cartographique, structurale, métamorphique, géochimique et radiochronologique) [Ph.D. thesis]: Grenoble, Université Joseph Fourier.

Schulte-Pelkum, V., Monsalve, G., Sheehan, A., Pandey, M.R., Sapkota, S., Bilham, R., and Wu, F., 2005, Imaging the Indian subcontinent beneath the Himalaya: Nature, v. 435, p. 1222-1225.

Stephenson, J., Gallagher, K., and Holmes, C.C., 2006, A Bayesian approach to calibrating apatite fission track annealing models for laboratory and geological timescales Geochimica Cosmochimica Acta, v. 70, p. 5183–5200.

Stüwe, K., White, L., and Brown, R.W., 1994, The influence of eroding topography on steady-state isotherms. Application to fission track analysis: Earth and Planetary Science Letters, v. 124, p. 63-74.

Upreti, B.N., 1999, An overview of the stratigraphy and tectonics of the Nepal Himalaya: Journal of Asian Earth Sciences, v. 17, p. 577-606.

Whipp, D.M., Ehlers, T.A., Blythe, A., Huntington, K.W., Hodges, K.V., and Burbank, D.W., 2007, Plio-Quaternary exhumation history of the central Nepalese Himalaya: 2. Thermokinematic and thermochronometer age prediction model: Tectonics, v. 26, TC3003, doi:10.1029/2006TC001991.

Williamson, J.H., 1968, Least squares fitting of a straight line Canadian Journal of Physics, v. 46, p. 1845-1847.

Wobus, C.W., Hodges, K.V., and Whipple, K.X., 2003, Has focused denudation sustained active thrusting at the Himalayan topographic front?: Geology, v. 31, p. 861-864.

Wobus, C.W., Heimsath, A., Whipple, K.X., and Hodges, K.V., 2005, Active out-of-sequence thrust faulting in the central Nepalese Himalaya: Nature, v. 434, p. 1008-1011.

Wobus, C.W., Whipple, K.X., and Hodges, K.V., 2006, Neotectonics of the central Nepalese Himalaya: Constraints from geomorphology, detrital $^{40}Ar/^{39}Ar$ thermochronology, and thermal modeling: Tectonics, v. 25, doi:10.1029/2005TC001935.

Zhao, W., Nelson, K.D., and Project INDEPTH Team, 1993, Deep seismic reflection evidence for continental underthrusting beneath southern Tibet: Nature, v. 366, p. 557-559.

TABLE AND FIGURE CAPTIONS

Table 1. Thermal parameters assumed for the numerical model. These values lead to a 32 °C.km^{-1} stable geothermal gradient.

Figure 1. Two schematic scenarios suggested for the central Himalaya (modified from Hodges et al., 2004) with the expected thermochronological age trends. A: In the model of Avouac (2003), shortening is concentrated on the Main Himalayan Thrust (MHT), which includes a crustal ramp below the High Himalaya. Expected high- and low-temperature thermochronologic age trends should show continuous younging toward the MCT zone and the topographic transition. B: In the model of Hodges and co-workers (e.g., Hodges et al., 2004), out-of-sequence faulting occurs in the MCT zone. Both high- and low-temperature thermochronologic age trends should present a jump at the topographic transition / the MCT zone.

Figure 2. A: Location of samples collected along a north-south transect along the Trisuli River and across the Mahabarat Range, from the Langtang Himal to the Ganga plain in Central Nepal. Apatite fission-track (AFT) ages are indicated. B: AFT (squares: this study; circles: data from P. Copeland reported by Bollinger et al., 2006) and mica Ar/Ar (Arita et al., 1997; Rai, 1998; Bollinger et al., 2004) age transects, plotted as a function of latitude. The

relationship to the major structures of the central Himalaya is indicated by the crustal-scale cross-section (modified from Bollinger et al., 2004).

Figure 3. Palung and Gosainkund age-elevation profiles placed in their kinematic context. Straight line is weighted linear regression using the method of Williamson (1968); envelopes show 95% confidence limits on age-elevation relationship. AER: apparent exhumation rate. Lower plot shows inferred kinematics and how we determine detachment slope from these data; v is the overthrusting velocity, ϕ the detachment angle (η for the frontal flat; θ for the ramp) and $\dot{e}$ the erosion rate. Value for ramp dip in parentheses takes the apparent exhumation rate from the Gosainkund profile without correcting for topographic effects.

Figure 4. (A) Forward-model geometry showing the modeled MHT, model kinematics and predicted thermal structure and thermochronological age pattern at the surface. B: Comparison between measured and predicted AFT ages, plotted as a function of latitude. C: comparison between observed and predicted age-elevation relationships for the Palung and the Gosainkund profiles.

Parameter	Value
Basal temperature	850 °C
Heat production	7.5 °C.My^{-2}
Thermal diffusivity	25 km^{2}.My^{-1}
Temperature at z = 0	20 °C
Atmospheric lapse rate	6 °C.km^{-1}

Table 1, *Robert et al.* Geology.

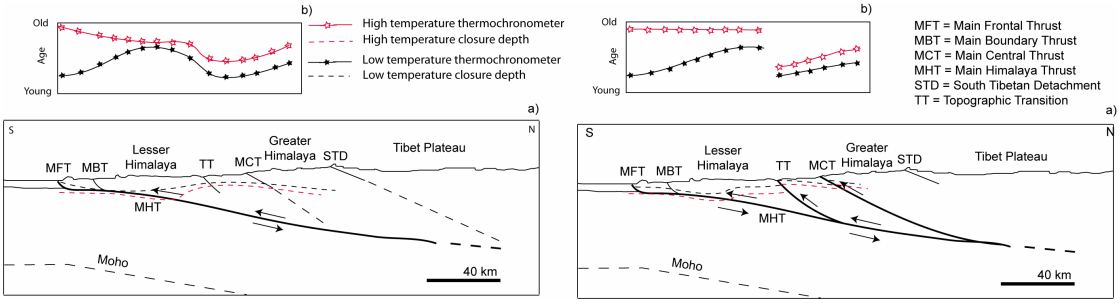

Fig.1. *Robert et al.* Geology.

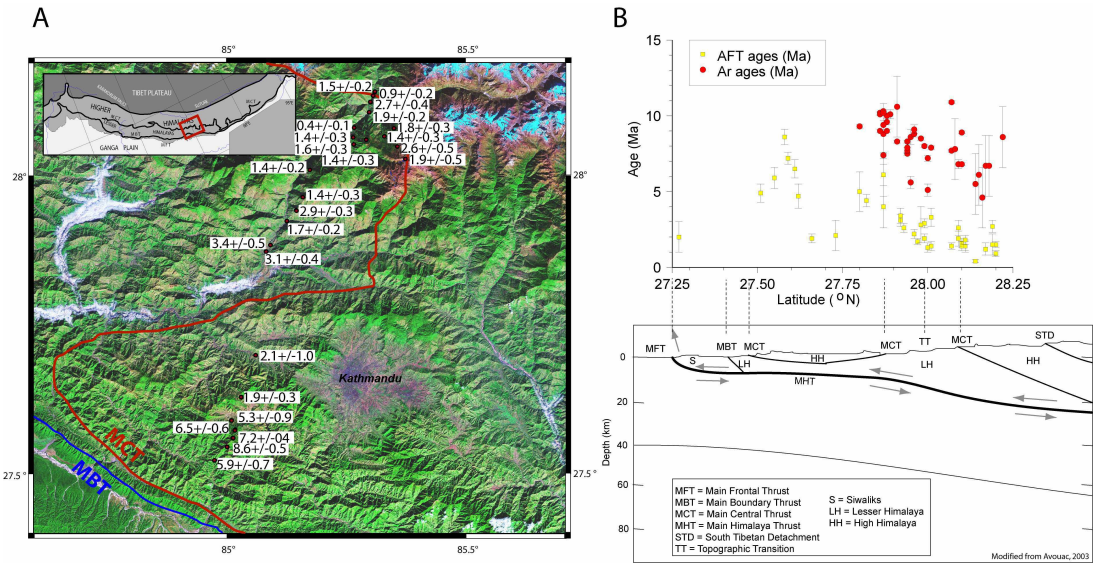

Fig.2, *Robert et al.* Geology.

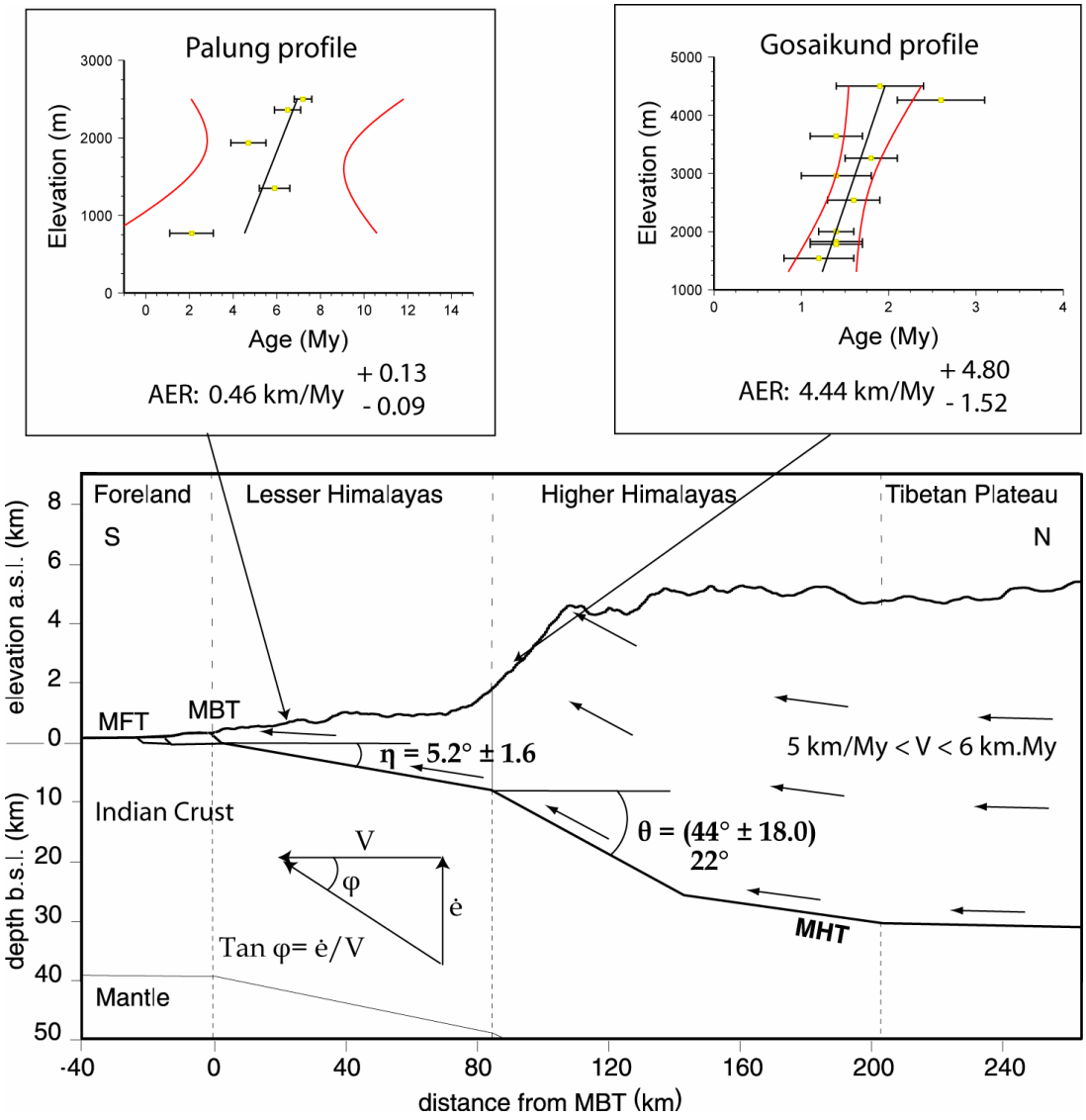

Fig.3, *Robert et al.* Geology.

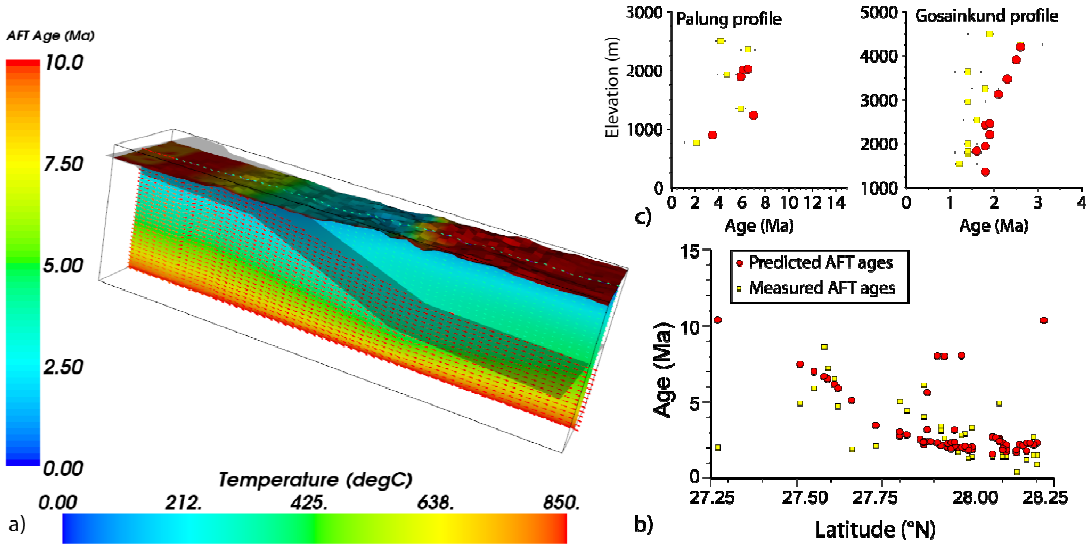

Fig.4, *Robert et al.* Geology.

Transition

Cette méthodologie (thermochronologie de basses températures couplée à des modèles numériques) permet d'appuyer des modèles cinématiques cohérents sur des orogènes. Nous avons travaillé ici sur des données issues de roches plutoniques ou sédimentaires fortement métamorphisées. L'histoire thermique et donc cinématique de ces objets ne peut être contrainte que pour la dernière phase de leur histoire.

Nous avons montré qu'un des éléments majeurs pour expliquer la répartition des âges thermochronologiques à la surface actuelle est la géométrie des failles crustales du prisme himalayen. Les résultats que nous obtenons est ici pour le Népal central. Or, si nous mettons en vis à vis nos données avec d'autres données himalayennes, mais soit plus à l'ouest, soit plus à l'est, nous observons une variation latérale significative. Dans la partie suivante, nous démontrons que nous pouvons les interpréter en terme de variations latérales géométriques.

4 Variations latérales de la géométrie du Main Himalayan Thrust

Sommaire

Dans ce chapitre, nous présentons les résultats analytiques et numériques latéralement le long de la chaîne himalayenne, ce que nous discuterons en termes de variations latérales cinématiques et géométriques du Main Himalayan Thrust. Nous comparerons ces résultats aux variations connues climatiques et érosives.

This chapter presents analytical and numerical results along strike of the Himalayan range in terms of lateral variations of kinetics and geometry of the Main Himalayan Thrust. We compare the results to the known variations in climate and erosion.

4.1 Variabilité le long de la chaîne himalayenne

Des études topographiques (Duncan et al. 2003), climatiques (Bookhagen et al. 2005, Bookhagen et Burbank 2006), géologiques et géophysiques (Hauck et al. 1998) mettent en évidence une variation conséquente de ces observables d'est en ouest. En effet, Duncan et al. (2003) montrent que le saut topographique dans le moyen pays au Népal central est inexistant en Himalaya de l'est. De plus, la distribution des précipitations varie d'est en ouest. Parallèlement, la proportion de Lesser Himalaya à l'affleurement est plus importante à l'ouest qu'à l'est, ce qui est inverse au cas de l'affleurement des séquences du High Himalaya. Hauck et al. (1998) mettent en évidence par des techniques d'imagerie sismique que la rampe située au Népal central n'est pas localisée au même endroit en Himalaya de l'est, et qu'elle est bien moins prononcée.

Nous avons montré au chapitre précédent par l'étude de la géométrie et de la cinématique du Népal central, le rôle important des marqueurs thermochronologiques de basses températures dans la contrainte de ces paramètres. C'est pourquoi, en parallèle aux données de la coupe du Langtang, nous avons aussi effectué un profil nord - sud, du High Himalaya aux Siwaliks, au niveau des Annapurnas au Népal. Nous avons choisi cette coupe car aucune donnée n'existait dans la partie sud de la vallée de la Kali Gandaki, alors qu'une base de données conséquente a été publiée dans le Haut Himalaya de la Marsyandi (Burbank et al. 2003, Blythe et al. 2007). J'ai traité ces échantillons grâce à la méthode du chapitre 2. De nombreux échantillons possèdent soit des apatites opaques en microscopie (impossibilité de compter le nombre de traces spontannées), soit des apatites très pauvres en uranium (densité de traces induites extrèmement faible). Les lithologies concernées sont principalement des quartzites très blanches et homogènes. Il en résulte que seulement 4 échantillons sur 30 ont pu être datés.

L'acquisition de ces données et la comparaison avec les données bibliographiques du Népal central (Arita et al. (1997), Rai (1998), Burbank et al. (2003), Blythe et al. (2007) Fig. 3.2 et Fig. 4.1) et à en Himalaya de l'est (Grujic et al. (2006) et Fig. 4.2) nous permet de discuter de la cylindricité de la chaîne himalayenne actuellement, et des variations latérales de sa tectonique récente, ce qui

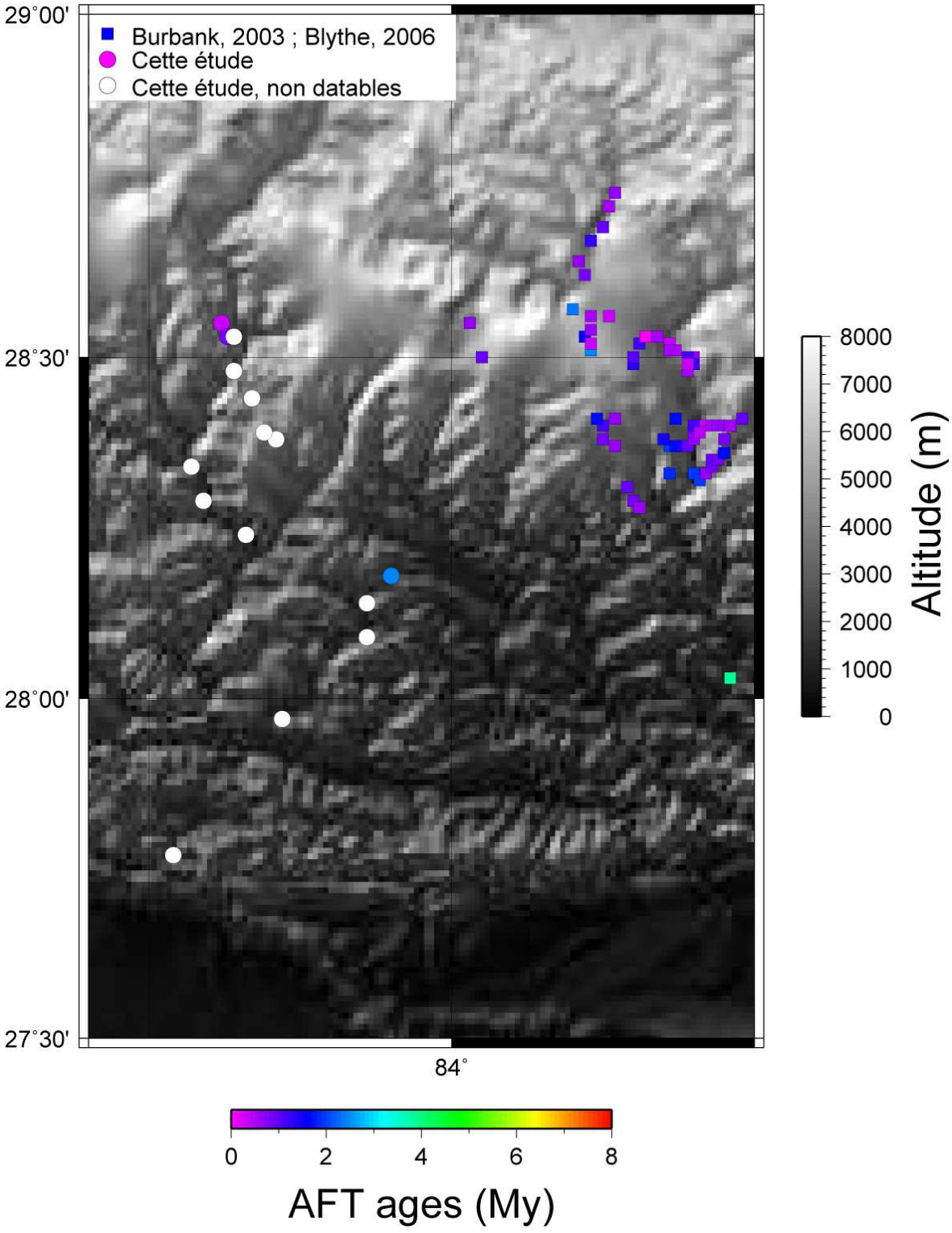

FIG. 4.1 – *Localisation des données AFT de Burbank et al. (2003) et de Blythe et al. (2007) sur le modèle numérique de terrain utilisé dans les modélisations sur les Annapurnas avec PECUBE. Les datations effectuées au cours de la thèse sont aussi positionnées, ainsi que les échantillons qu'il a été impossible de dater.*

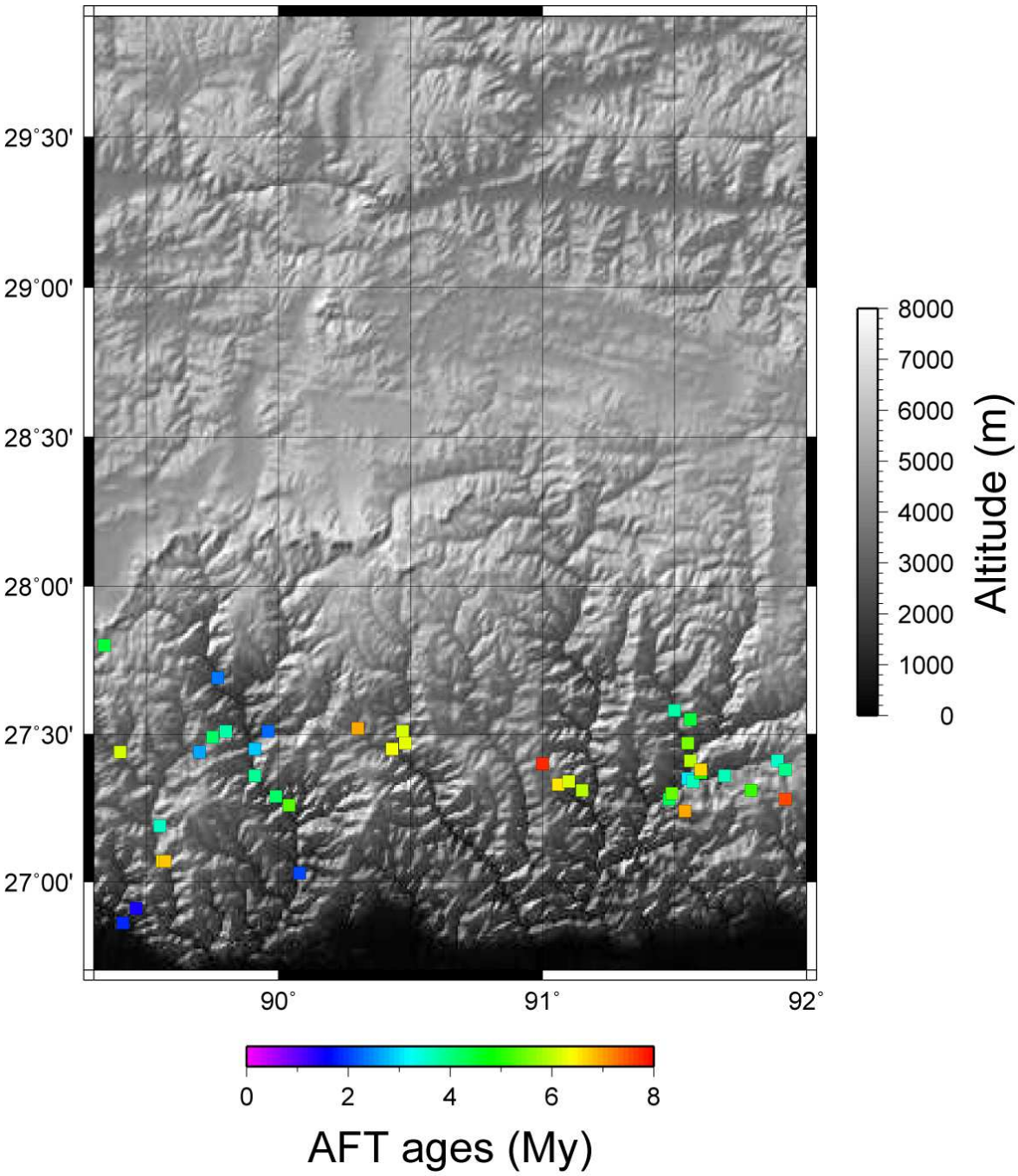

FIG. 4.2 – *Localisation des données AFT de Grujic et al. (2006) sur le modèle numérique de terrain utilisé dans les modélisations au Bhoutan avec PECUBE.*

est la problématique de l'article qui suit en partie 4.2. De manière à comparer les différentes coupes, il est necessaire de projeter les âges thermochronologiques de chaque zone étudiée sur un profil fictif perpendiculaire au MFT, respectivement proche des points analysés.

Des modélisations inverses ont aussi été effectuées en suivant la méthode présentée dans la partie 2 sur la zone des Annapurnas/Kali Gandaki, et sur la zone du Bhoutan. Dans ces modélisations, j'ai limité la recherche de paramètres sur la géométrie du MHT dans chaque zone. Les paramètres recherchés sont les paramètres thermiques (Production de chaleur et température à la base du modèle), et les positions (latérale et verticale) de points définissant la géométrie de la rampe profonde du MHT. Pour les trois zones, la valeur des paramètres thermiques sont proches, alors que la valeur des angles varient d'ouest en est. La géométrie du MHT trouvée par les inversions des données thermochronologiques est, pour chaque modèle, du même ordre de grandeur avec les interprétations des données de terrain.

4.2 How cylindrical is the Main Himalayan Thrust? Insights into the controls on lateral variations in exhumation rates from low-temperature thermochronology and numerical modeling

How cylindrical is the Himalaya? Insights into the controls on lateral variations in exhumation rates from low – temperature thermochronology and numerical modeling

Xavier Robert[1], Peter van der Beek[1], Jean Braun[2], Claire Perry[1,2*], Jean-Louis Mugnier[3]

1. Laboratoire de Géodynamique des Chaînes Alpines, Université Joseph Fourrier, Grenoble, France
2. Géosciences Rennes, Université de Rennes 1, France
3. Laboratoire de Géodynamique des Chaînes Alpines, CNRS, Le Bourget-du-Lac, France

* Present adress: GEOTOP, Université du Québec à Montréal, Montreal, Canada

To be submitted to Journal of Geophysical Research.

word count (10/23/2008): Main text – 8185 words

Abstract

The Himalayan range is commonly presented as a cylindrical structure from west to east. However, geological structure, topography, precipitation rate, convergence rates and low – temperature thermochronological ages all vary significantly along strike. Here, we focus on the interpretation of thermochronological datasets in terms of cylindricity in geometry and kinematics of the MHT along the Himalayan range. We report new apatite fission-track (AFT) ages collected along north-south transects in western- and eastern-central Nepal (at the latitudes of the Annapurna and Langtang massifs, respectively). AFT ages are consistently young (< 3 Ma) along both N-S transects in the MCT zone and increase (4 to 6 Ma) toward the south in the Lesser Himalaya. We compare our new data to published low-temperature thermochronological datasets for Nepal and the Bhutan Himalaya. We use these data to perform both forward and inverse thermal-kinematic modeling with a modified version of the *Pecube* code, in order to constrain potential along-strike variations in the kinematics of the Himalayan range. Our results show that lateral variations in geometry of the MHT (in particular the presence or absence of a major ramp) strongly control the kinematics and exhumation history of the orogen.

Keywords: Himalaya, Nepal, Bhutan, Main Himalayan Thrust, Reactivation, Tectonics, Thermochronology, Numerical modeling.

1. Introduction

The high elevation of active convergent mountain belts is driven by a balance between the tectonic processes that create topography and surface processes that erase it. The system is dynamic, with feedbacks that tend to drive orogenic systems toward steady state [*Adams*,

1980; *Jamieson and Beaumont*, 1988; *Willett and Brandon*, 2002]. Because of its rapid convergence and exhumation rates, the Himalayan orogen provides an excellent natural laboratory to study evolving orogenic systems and mountain building processes. Numerous balanced cross-sections have been constructed to infer the geological structure of the Himalaya and to develop scenarios for its kinematic development [e.g., *Schelling and Arita*, 1991; *DeCelles et al.*, 2001; *Yin*, 2006] and its deep structure is known through several geophysical experiments [e.g., *Hirn and Sapin*, 1984; *Zhao et al.*, 1993; *Schulte-Pelkum et al.*, 2005]. During the last twenty years, thermochronological datasets have been published that constrain exhumation rates and pathways along several transects across the range [e.g., *Copeland et al.*, 1991; *Catlos et al.*, 2001; *Bollinger et al.*, 2004; *Thiede et al.*, 2004; *Vannay et al.*, 2004; *Grujic et al.*, 2006].

The Himalayan orogen (Figure 1) is classically considered as a cylindrical structure from west to east [e.g., *Gansser*, 1964; *Le Fort*, 1975; *Yin and Harrison*, 2000; c.f. *Yin*, 2006 for a recent review]. Its structure commonly described as a north-dipping, southward-propagating, crustal-scale thrust sequence [*Gansser*, 1964; *Le Fort*, 1975; *Yin and Harrison*, 2000]. Recently, emphasis has been laid on potential out-of-sequence reactivation of the more internal part of the belt [*Hodges et al.*, 2004; *Wobus et al.*, 2005], possibly controlled by rapid recent erosion rates [*Thiede et al.*, 2004] and linked to crustal "channel flow" [*Beaumont et al.*, 2001; *Hodges et al.*, 2001; *Grujic et al.*, 2002].

In contrast to the general two-dimensional view of the Himalaya, topography and relief [*Duncan et al.*, 2003; *Bookhagen and Burbank*, 2006], precipitation rates and patterns [*Bookhagen et al.*, 2005; *Bookhagen and Burbank*, 2006; *Grujic et al.*, 2006], orogen structure [*Yin*, 2006] and convergence rates [*Larson et al.*, 1999; *Paul et al.*, 2001] all vary

significantly from west to east, showing that the Himalayan range is not cylindrical when studied in a minimum of detail. Whether climatic parameters, tectonic forcing or pre-existing structures control these lateral variations remains a question, which is not easy to answer due to the coupled nature of these potential forcing parameters. Topography drives variations in climate and erosion rates [*Montgomery and Brandon*, 2002; *Roe*, 2005], and tectonics drives topography. Erosion rate depends on relief, elevation and rainfall [e.g., *Summerfield and Hulton*, 1994; *Hovius*, 1998; *Burbank*, 2002] and directly influences topography and tectonics [*Willett*, 1999; *Stolar et al.*, 2007]. A better understanding of the lateral spatial variations in kinematics and exhumation rates is thus required to resolve the fundamental controls on topography and erosion in the Himalaya, and may also provide more general insight into the coupling mechanisms between crustal-scale geometry, orogen tectonics, climate and erosion.

To address this question, we employ both forward and inverse numerical modeling, using a newly developed thermo-kinematic model, in order to explain observed patterns of low-temperature thermochronological ages (mainly apatite fission-track; AFT) along three transects across western-central Nepal, eastern-central Nepal and Bhutan. The upper crustal thermal structure is strongly affected by orogen kinematics, fault geometry, surface processes and topography [e.g., *Ehlers*, 2005; *Braun et al.*, 2006; *Reiners and Brandon*, 2006]; these processes are thus recorded by the time – temperature – depth history of exhumed rocks. In optimal conditions, low-temperature thermochronometry allows constraining the temperature field and rock exhumation paths through its record of the time-temperature history. However, in a highly complex and dynamic system such as the Himalayan orogen, characterized by spatially and temporally variable and non-vertical particle paths and a strong influence of topography on the upper crustal thermal structure, numerical models are essential in order to extract meaningful information from thermochronologic data [*Braun et al.*, 2006].

In the following, we first review the geologic structure, kinematics, topography and climate of the central and eastern Himalaya, focusing on both recent controversies and lateral variations. We then present the AFT data, combining our own data with published datasets, and the numerical model that forms the basis for this study. We show inverse model results that constrain the crustal geometry and kinematics along the three studied transects.

We show that, for the transect in central Nepal, where the recent kinematics of the belt have been strongly disputed in recent years [*Avouac*, 2003; *Bollinger et al.*, 2004; *Hodges et al.*, 2004; *Jamieson et al.*, 2004; *Bollinger et al.*, 2006; *Wobus et al.*, 2006], the low-temperature thermochronology data do not have sufficient resolution to discriminate between different kinematic models for the Quaternary evolution of the belt. However, they do constrain very well the geometry of the Main Himalayan Thrust [the crustal-scale detachment underlying the orogen; *Hirn and Sapin*, 1984; *Zhao et al.*, 1993; *Makovsky et al.*, 1996; *Schulte-Pelkum et al.*, 2005]. The results from the other two transects highlight important along-strike variations in this geometry, which is shown to exert a first-order control on exhumation rates. Our synthesis of exhumation in the Himalayan orogen allows us to propose a geometric and kinematic model for its recent evolution.

2. Tectonic and Morphologic Setting

2.1. Geological Structure of the Himalaya

The Himalayan orogen is characterized by a series of north-dipping crustal-scale faults that delimit four distinct tectonic units [*Le Fort*, 1975; *Hodges*, 2000; *Yin and Harrison*, 2000], which can be followed along its 2500 km length (Figure 1). The northernmost Tethyan

Himalayan zone consists of Cambrian to Eocene sedimentary to low-grade metamorphic rocks. It is separated from the structurally underlying Higher (or Greater) Himalaya by the extensional Southern Tibetan Detachment System [STDS; *Burchfiel et al.*, 1992]. The Higher Himalaya crystalline thrust sheet consists of high-grade metamorphic rocks, with abundant evidence for partial melting, and overthrusts the underlying Lesser Himalaya along the Main Central Thrust (MCT). Precise dating of the activity of the STDS and MCT has shown that they were active simultaneously during the Early Miocene [around 22 – 18 Ma; *Burchfiel et al.*, 1992; *Hodges et al.*, 1996], giving rise to the "channel-flow" model of extrusion of partially molten Higher Himalayan middle crust from under the overthickened Tibetan Plateau [*Beaumont et al.*, 2001; *Hodges et al.*, 2001; *Grujic et al.*, 2002].

The Lesser Himalaya forms a complex structural duplex with several major internal thrusts [*Schelling and Arita*, 1991; *DeCelles et al.*, 2001]. In Nepal, these indicate a forward-propagating sequence that initiated after cessation of activity on the MCT. Thrusts in the internal Lesser Himalayas of western Nepal are active between ~12 and 15 Ma [*DeCelles et al.*, 2001; *Robinson et al.*, 2006] and the Lesser Himalayan duplex was built since ~10 Ma [*DeCelles et al.*, 2001; *Huyghe et al.*, 2005; *Robinson et al.*, 2006]. The Lesser Himalaya varies strongly in width along strike, due to the presence or absence of a lid of Higher Himalayan rocks that have overthrusted the Lesser Himalaya up to 150 km southward of the general trace of the MCT and that form a series of prominent klippen in Nepal [*Schelling and Arita*, 1991; *Upreti and Le Fort*, 1999; *DeCelles et al.*, 2001; *Grujic et al.*, 2002; *Yin*, 2006]. In the eastern Himalaya, Lesser Himalayan tectonic structures are similar, but the unit has been reduced to a narrow width and has been strongly deformed in the Bhutan Himalaya [*Gansser*, 1983; *Bhargava*, 1995].

The Lesser Himalaya overthrusts the Sub-Himalaya or Siwalik thrust belt, composed of Mio-Pliocene syn-tectonic clastic deposits, along the Main Boundary Thrust (MBT). In the western and central Himalaya, the MBT was active around 5 Ma [*Meigs et al.*, 1995; *DeCelles et al.*, 2001; *Huyghe et al.*, 2001]. The Siwaliks form a wide and structurally complex zone in the western Himalaya [e.g., *Powers et al.*, 1998; *Mugnier et al.*, 1999], but are composed of a single discontinuous thrust sheet of narrow width in Bhutan [*Gansser*, 1983; *Lakshminarayana and Singh*, 1995]. The Siwaliks overthrust the Ganges plain along the currently active Main Frontal Thrust (MFT).

Geophysical and structural studies suggest that all the major thrusts in the Himalaya, including the MFT, MBT and MCT, branch at depth on a single major shear zone and mid-crustal décollement, the Main Himalayan Thrust [MHT; *Hirn and Sapin*, 1984; *Zhao et al.*, 1993; *Makovsky et al.*, 1996; *Avouac*, 2003; *Schulte-Pelkum et al.*, 2005]. In Nepal, where it is best studied, geophysical and structural data show that the MHT is characterized by a ramp and flat geometry with two major ramps. The frontal ramp is shallow and corresponds to where the fault emerges with a dip angle around 30° at the surface (MFT). The other is envisaged at mid-crustal depth beneath the sharp topographic front of the high range [*Avouac*, 2003]. Geophysical data from central Nepal [*Lemonnier et al.*, 1999; *Pandey et al.*, 1999] suggest a dip angle of ~15° for the mid-crustal ramp; mechanical modelling based on the present-day displacement field measured by GPS surveys [*Berger et al.*, 2004] suggests a somewhat higher dip of ~30°.

From a detailed analysis of GPS data, *Berger et al.* [2004] have proposed that the detachment is segmented and the crustal ramp more pronounced in central Nepal than in western Nepal, in accord with balanced structural cross-sections based on surface geology

[*DeCelles et al.*, 2001; *Mugnier et al.*, 2004]. Similarly, drainage patterns [*van der Beek et al.*, 2002] and present-day displacement rates [*Larson et al.*, 1999] suggest that the southern, shallow flat segment is steeper in western Nepal than in Central Nepal. In Bhutan, the deep fault structure is poorly known because of a lack of geophysical studies. *Hauck et al.* [1998] present a crustal transect from deep reflection-seismic profiling of the Himalayan orogen at ~90 °E. Combined with published geological cross-sections they suggest a major lateral change in geometry to occur along the "Yadong cross-structure" [*Burchfiel et al.*, 1992], which underlies a major left-lateral offset in the main Himalayan structures and topography roughly along the Sikkim-Bhutan border. To the west of this structure, the MHT shows a crustal ramp underlying the MCT zone, similar to central Nepal, whereas to the east, the MHT appears to dip more shallowly and contains a crustal ramp much further to the north, underneath the Tethyan Himalayan zone.

2.2. Topographic and Climatic Variability

The topography of the Himalaya varies strongly along strike [*Duncan et al.*, 2003; *Bookhagen and Burbank*, 2006]. Figure 2 presents a digital elevation model (DEM) and elevation profiles through Nepal and Bhutan perpendicular to the major structures, constructed from Shuttle Radar Topography Mission (SRTM) data. In both Nepal and Bhutan, the distance from the deformation front (MFT), with elevations near sea level, to the range crest, with elevations >7000 m, is 130-150 km. Topographic profiles in central Nepal are strongly concave; the mean topography in the Lesser Himalaya rises to only 2000 m at ~100 km north of the MFT, before rising to close to 7000 m in the next 30-50 km. There thus exists a sharp physiographic transition 10 to 30 kilometers south of the MCT in central Nepal [*Seeber and Gornitz*, 1983; *Lavé and Avouac*, 2001; *Duncan et al.*, 2003; *Wobus et al.*, 2003], which is situated above the deep crustal ramp of the MHT. This physiographic transition has

been interpreted in different ways, related to the kinematic models proposed for the central Himalaya [*Lavé and Avouac*, 2001; *Avouac*, 2003; *Wobus et al.*, 2003; *Bollinger et al.*, 2004; *Hodges et al.*, 2004; *Wobus et al.*, 2005; see discussion below].

As previously shown by *Duncan et al.* [2003] and *Bookhagen and Burbank* [2006], the morphology is very different in the eastern (Bhutan) Himalaya. There, the topography shows an almost straight to slightly convex taper. Consequently, the topography rises more steeply from the deformation front and the 2000-m elevation contour is reached within 50 km from the front, whereas the rise to the high peaks is much more gradual than in Nepal.

Bookhagen and Burbank [2006] combine their topographic analysis with satellite precipitation data to show two distinct precipitation maxima along strike in the Himalaya. An outer, continuous band occurs along the southern edge of the Lesser Himalaya, where elevations reach ~1000 m. A second band occurs where a strong physiographic transition from the Lesser to the Higher Himalaya exists and is thus discontinuous in strike, disappearing to the east. Previous studies have revealed two more general Himalayan precipitation gradients: a strong orographic gradient across the belt, with precipitation decreasing from over 3000 $mm.y^{-1}$ (and locally up to 10,000 $mm.y^{-1}$) on the southern flank to <200 $mm.y^{-1}$ on the Tibetan Plateau [*Roe*, 2005; *Anders et al.*, 2006], as well as an east-west overall decrease in precipitation [*Bookhagen et al.*, 2005], due to the fact that the major moisture source for monsoon precipitation, the Bay of Bengal, lies to the southeast of the Himalayan belt.

2.3. Kinematics of the Himalaya

GPS measurements [*Bilham et al.*, 1997; *Larson et al.*, 1999; *Jouanne et al.*, 2004] constrain present-day convergence rates across the Himalaya at 18±3 mm.y^{-1}. They show a west-to-east increase in convergence rate, qualitatively consistent with the location of the India-Eurasia rotation pole to the west of the collision zone [*Larson et al.*, 1999; *Paul et al.*, 2001]. The present-day rates are similar to Holocene shortening rates across the MFT in Nepal of 14-21 km.My^{-1} from folded and uplifted river terraces [*Lavé and Avouac*, 2000; *Mugnier et al.*, 2004], as well as to Quaternary shortening rate across Siwaliks [~19 km.My^{-1}; *Mugnier et al.*, 2004] and Mio-Pliocene shortening rates across the Lesser Himalaya [19-22 km.My^{-1}; *DeCelles et al.*, 2001]. The similarity of rates on different timescales suggests that the Himalayan orogen has absorbed India-Eurasia convergence and propagated toward the Indian continent at steady rates since mid-Miocene times [*Mugnier and Huyghe*, 2006].

In a reference frame attached to the MHT, this convergence is partitioned into underthrusting of the Indian plate and overthrusting of the Himalayan orogen [cf. *Robert et al.*, "Kinematic models of the central Himalaya: A critical evaluation", manuscript submitted to *Earth and Planetary Science Letters*, hereafter referred to as "*Robert et al.*, submitted (a)" for a more detailed discussion]. Several authors [*Bollinger et al.*, 2006; *Brewer and Burbank*, 2006; *Whipp et al.*, 2007] have shown that available thermochronological data for central Nepal limit overthrusting velocities to 5-6 km.My^{-1} since ~10 Ma, implying underthrusting of India (or underplating and forward propagation of the Himalayan thrust wedge) at a rate of ~15 km.My^{-1} since that time.

Recently, two competing models have been proposed to describe the present-day kinematics of the central Nepal Himalaya (Figure 3) and explain the sharp physiographic

transition. These differ principally in their predictions of which surface-breaking faults accommodate current shortening and what kinematics drive rapid exhumation in the topographic transition zone around the MCT. *Avouac* [2003] and *Bollinger et al.* [2004; 2006] argue that recent deformation is concentrated along the MHT, generating major (M >8) earthquakes on this thrust, and that rapid exhumation in the MCT zone results from combined underplating and overthrusting along the MHT ramp. In contrast, *Wobus et al.* [2003] and *Hodges et al.* [2004] suggest active Quaternary out-of-sequence thrusting in the MCT zone, possibly driven by strongly localized climatically-controlled exhumation in this area. A jump in detrital thermochronologic and cosmogenic ages across the topographic transition in central Nepal has been argued to support the latter model [*Wobus et al.*, 2005; 2006]. A link between such reactivation and crustal-scale channel flow has been suggested [*Hodges et al.*, 2001; 2004] but the exact mechanism envisaged remains unclear [cf. *Robert et al*., submitted (a)].

3. Thermochronologic Data

3.1. Existing Datasets and Sampling Strategy

We use new apatite fission-track (AFT) data and existing AFT and mica Ar-Ar ages, together with numerical modeling to constrain the geometry and kinematics of major faults along three north-south transects through the central and eastern Himalaya. A major obstacle to obtaining thermochronologic datasets across the entire Himalayan orogen is formed by the unfavorable lithologies of the Lesser Himalaya, which consists mainly of fine-grained pelitic rocks with low degrees of metamorphism. We have chosen three areas where it is either possible to obtain AFT data or where extensive low-temperature thermochronologic data already exist. These are, from west to east (Figure 1a): the Annapurna region in west-central Nepal, the Langtang-Kathmandu region in east-central Nepal and the Bhutan Himalaya.

We have collected samples for AFT thermochronometry along two transects across the range: in west-central Nepal from the MCT zone along the Kali Gandaki valley (Annapurna massif) to the MBT at Buthwal; and in east-central Nepal from the MCT zone along the Trisuli River (Langtang Himal) across the Kathmandu klippe to the MBT at Hetauda. We concentrated our sampling on the Lesser Himalaya for the reasons outlined above. Our sampling strategy consisted of trying to obtain a transect from the MBT northward to and across the MCT zone, as well as local age-elevation profiles sampled orthogonally to the tectonic transport direction in order to limit complications due to non-vertical particle paths [e.g., *Huntington et al.*, 2007]. We targeted quartzites of the Kusma, Kunshna and Naurpul formations [Proterozoic Nawakot Group; *Upreti*, 1999] as well as the ~1830 Ma [*DeCelles et al.*, 2000] Ulleri gneiss and the Oligocene [*DeCelles et al.*, 1998] Dumri formation in the Lesser Himalaya. In the Langtang transect, we exploit the fact that the transect crosses the Higher Himalayan crystalline Kathmandu klippe to sample the Ordovician [*Gehrels et al.*, 2006] Palung granite intruded into it.

Twenty-seven new AFT ages from the Langtang-Hetauda transect, including two age-elevation profiles at Mount Gosainkund in the MCT zone (Langtang Himal) and through the Palung granite, are reported by *Robert et al.* ["Assessing Quaternary reactivation of the Main Central Thrust zone (central Nepal Himalaya): New thermochronologic data and numerical modeling", manuscript submitted to *Geology*, hereafter referred to as *Robert et al.*, submitted (b)]. We sampled and processed sixteen further samples along the Annapurna-Buthwal transect, including an age-elevation profile at Ghorepani Hill (Lesser Himalaya in the topographic transition zone just south of the Annapurna massif). However, twelve of these samples, mostly from the Lesser Himalaya, could not be dated. The majority of undatable samples are white quartzites from the Nawakot Group, which either do not contain sufficient

apatite, or apatite that is so poor in Uranium that no spontaneous or induced fission tracks were recorded. For completeness, all samples are reported in Table 1.

We complete our database for the Annapurna-Buthwal transect with extensive AFT data from the Marsyandi valley ~50 km to the east [*Burbank et al.*, 2003; *Blythe et al.*, 2007]. This database contains 82 AFT ages and several age-elevation profiles, which were, however, exclusively sampled in Higher Himalayan crystalline rocks. For the Langtang-Hetauda transect, we complete our AFT data with mica Ar-Ar data from *Arita et al.* [1997], *Rai* [1998] and *Bollinger et al.* [2004], as well as a few unpublished AFT ages obtained by P. Copeland and reported in *Bollinger et al.* [2006]. Finally, we include an extensive AFT dataset from Bhutan [*Grujic et al.*, 2006] comprising 45 AFT ages, again all from the Higher Himalayan crystalline series, in our analysis. The different north-south transects through the Himalayan range are compared by projecting each transect on a profile normal to the MFT (Figure 4).

3.2. AFT age patterns

The most continuous age trend has been obtained for the Langtang-Hetauda transect. AFT ages plotted as a function of distance to the MFT shows a continuous trend, in which ages young continuously and nearly linearly from the MBT to the MCT. The northernmost samples, from the MCT zone in Langtang, are very young (<3 Ma), indicating strong local exhumation. This trend crosses the topographic transition and the MCT zone without a significant jump in ages. In *Robert et* al. [submitted (b)], we discuss the interpretation of the data from this transect, including two age-elevation profiles, in detail. An age-elevation profile from the Palung granite (Kathmandu klippe in the Lesser Himalaya) shows an exhumation rate of 0.5±0.1 km.My^{-1}. In contrast, an age-elevation profile from the MCT zone (Gosainkund Mountain) suggests an apparent exhumation rate an order of magnitude higher,

at $4.4^{+4.8}_{-1.5}$ km.My^{-1}, comparable with strike-parallel age-elevation relationships observed in the Marsyandi area [*Blythe et al.*, 2007]. However, at such high rates of exhumation, topographic disturbance of the closure isotherm may lead to seriously overestimating exhumation rates from age-elevation relationships [*Stüwe et al.*, 1994; *Manktelow and Grasemann*, 1997; *Braun*, 2002; *Ehlers*, 2005]; we estimate "real" exhumation rates for the Gosainkund profile to be in the order of 2.0-2.5 km.My^{-1} [*Robert et al*., submitted (b)]. These exhumation rates are consistent with overthrusting at a rate of 5-6 km.My^{-1} over a ~20° dipping crustal ramp in the MCT zone and a ~5° dipping flat for the Palung granite. Thus, the data from the Langtang transect do not appear to require active out-of-sequence thrusting in the MCT zone or the topographic transition and are compatible with the ramp-flat geometry of the MHT as constrained by independent geophysical and geodetic data as described in Section 2.1. We will assess this assertion by numerical modeling in Section 4.2.

The age pattern for the Annapurna-Buthwal transect is less well constrained than that for the Langtang transect because of a lack of data in the Lesser Himalaya, in spite of our efforts to sample this region. However, the comparison of the projection of the AFT ages along a line perpendicular to the MFT shows a similar trend for both transects (Figure 4): ages from the MCT zone are similar (if possibly slightly younger in the Annapurnas compared to Langtang) and there also appears to be a similar increase in ages toward the south in the Lesser Himalaya. They thus appear, to a first order, compatible with a similar geometry and kinematic of the MHT as for the Langtang transect.

A projection of *Grujic et al.*'s [2006] AFT data from Bhutan does not show a very regular trend, even if we use separate projections for the data from western and eastern Bhutan (Figure 2). As already noted by *Grujic et al.* [2006], AFT ages are generally older

than in central Nepal. Moreover, the pattern appears to be opposite to that observed for Nepal: AFT ages increase from south to north in Bhutan, whereas they decrease in Nepal. This first-order observation suggests that rocks from the orogenic front in Bhutan are exhumed more rapidly than rocks from the region of highest topography. No AFT-age inflexion is observed in this region. The AFT age pattern observed in Bhutan appears to imply that (1) there is no reactivation of the MCT, (2) the MHT does not comprise a crustal ramp below the region of highest topography, and (3) the overall dip of the MHT is lower than in Nepal. The Bhutan Himalaya has served as the type area where geological evidence for the "channel-flow" model has been collected [*Grujic et al.*, 2002]. We note, however, that currently active channel flow in the Bhutan Himalaya should be marked by very young AFT ages in the MCT zone and in the Higher Himalaya and appears excluded by the data. The data are compatible, however, with channel flow operating before 12-10 My ago, as proposed by *Hollister and Grujic* [2006].

4. Thermo-kinematic Model

4.1. Model Description

In order to assess the above inference more quantitatively, we develop both forward and inverse numerical models. We employ a modified version of *Pecube* [*Braun*, 2003], a finite-element code that predicts thermochronological ages by solving the 3-dimensional heat transport equation in a crustal/lithospheric block affected by vertical and/or horizontal advection and characterized by an evolving surface topography. New features in the code include the incorporation of faults and associated kinematics. Faults define different blocks and no matter can be advected through any fault. Faults are defined in the model by their surface trace and a number of points that define their (laterally constant) profile. The velocity field is calculated by conserving the mass equation, using a kink-band model originally

developed by *Braun et al.* [1994]. As in other thermo-kinematic models for the Himalaya [*Bollinger et al.*, 2006; *Brewer and Burbank*, 2006; *Wobus et al.*, 2006; *Whipp et al.*, 2007; cf. Robert et al., submitted(a) for a review], we use a reference frame fixed to the MHT. If other faults are present, these are advected and deformed along with the block they occur in due to motion on the MHT.

In order to capture the topographic effect on thermochronological age variability, we couple the essentially 2D kinematic model to a planform surface topography, derived from the Shuttle Radar Topography Mission (SRTM) 90-m digital elevation models of the zones of interest (downgraded to the model resolution of 1 km), and assumed to be in steady state in the models presented here. Models are run for 10 My, as we concentrate on predicting the AFT age pattern and all AFT ages are <10 Ma. We start from a steady-state thermal structure for the kinematics defined at 10 Ma and then predict the transient thermal structure through the model run. Particle paths are tracked through time for rocks that end up at the surface at the end of the model run; the resultant time-temperature paths are used to predict AFT ages using the fission-track annealing model of *Green et al.* [1989] with the modified annealing parameters of *Stephenson et al.* [2006].

The initial model geometry is based on the inferred structure of the MHT in central Nepal [*Cattin and Avouac*, 2000; *Avouac*, 2003]; i.e., a flat-ramp-flat geometry with the location of the mid-crustal ramp located below the topographic transition between the Lesser and the High Himalaya (Figure 5a). The MHT is active throughout the model run. Due to the proximity of the MBT and the MFT, we consider these as a single fault in order to simplify the models. Previous thermo-kinematic models for the central Nepal Himalaya have shown that, for a reference frame fixed to the MHT, observed thermochronological ages require

overthrusting velocities of 5-6 km.My^{-1} [*Bollinger et al.*, 2006; *Brewer and Burbank*, 2006; *Whipp et al.*, 2007; cf. Robert et al., submitted(a) for a review], implying underthrusting of the Indian plate at a velocity of 15 km.My^{-1} in order to obtain a total convergence rate of 20-21 km.My^{-1}. Here we will use over- and underthrusting velocities of 6 and 15 km.My^{-1}, respectively, although we present model runs with a different partitioning in order to study its effect on predicted age patterns. The geometry of the MHT is allowed to vary between different models (see below) and, for the east-central Nepal models, we include a separate fault that breaks to the surface at the front of the topographic transition in order to simulate out-of-sequence thrusting (Figure 5b).

Note that, because no material is allowed to cross the MHT in our models, and both the MHT and the topography are fixed, we cannot include underplating of Indian plate material as modeled by *Bollinger et al.* [2006] and *Wobus et al.* [2006]. However, although either underplating of out-of-sequence thrusting is required to explain the well-known inverse metamorphic gradient observed in the Lesser Himalaya south of the MCT [*Bollinger et al.*, 2006; *Wobus et al.*, 2006], a simple overthrusting model as developed here permits to explain both low- (AFT) and intermediate (mica Ar-Ar) temperature thermochronology data just as well as the more elaborate models [*Brewer and Burbank*, 2006; *Whipp et al.*, 2007]. This is because the upper-crustal kinematics are similar for models with or without underplating [cf. *Robert et al*., submitted(a) for a more detailed review].

The thermochronologic age predictions depend on the fault geometry and kinematics as well as the thermal structure of the modeled crustal block. In order to explore this complex multidimensional parameter space, we couple *Pecube* with the Neighborhood Algorithm (NA) inversion routine [*Sambridge*, 1999], using the approach developed by *Braun and*

Robert [2005]. The NA inversion scheme allows both to find an optimum set of parameters to explain the data and to evaluate the sensitivity of the model predictions to the values of the input parameters. NA performs an intelligent search to find the set of parameter values of a given model that will minimize the difference between model predictions and measured ages. We define a misfit function that is defined as the L_2-norm of the weighted difference between the observation vector, O, and the prediction vector, P:

$$misfit = \frac{1}{n}\sqrt{\sum_{i}^{n}\left(\frac{O_i - P_i}{\Delta O_i}\right)^2}$$

where n is the number of measured ages and ΔO_i are the observational errors, taken here as the 1σ-errors on the AFT ages. This search necessitates that a large number of model runs be performed to sample a wide range of parameter values. Using a high-performance cluster, we were able to perform a large number of forward model runs in a reasonable amount of time.

We have run a series of inversions for the different transects, in which we search the thermal, geometric and kinematic parameter space for optimal parameter combinations. In an initial inversion, we allowed to vary the basal temperature (T_0) and normalized heat production (Q), but this led the model to zoom in on a geologically unrealistic set of parameters (see below). The MHT geometry is modified by allowing variations in the x and y positions (i.e., the distance from the MFT and the depth) of both the top and the base of the mid-crustal ramp within the bounds set by the geophysical data. Finally, in models including an out-of-sequence thrust, we allow partitioning of the overthrusting velocity (V_o) between motion on the out-of-sequence thrust (V_{TF}) and the MHT (V_o - V_{TF}).

4.2. Geometry of MHT and Importance of Out-of-Sequence Thrusting

Figure 5 shows forward model geometries and predicted AFT ages for a simple overthrusting model, as well as models including out-of-sequence thrusting at different velocities, applied to the Langtang transect. In these models, overthrusting takes place along the MHT for the first 8 My of the model run and is subsequently partitioned between the MHT and the out-of-sequence thrust for the last 2 My, in order to simulate Quaternary reactivation of the MCT zone [e.g., *Hodges et al.*, 2004]. As expected (cf. Figure 3), AFT ages in the Lesser Himalaya become older with increasing activity of the out-of-sequence thrust; for $V_{TF} \geq 4$ km.My^{-1}, AFT ages in the southern part of the Lesser Himalaya are unreset since 10 Ma. However, except for these extreme models, where nearly all overthrusting is taken up on the out-of-sequence thrust, the models do not predict a clear age jump at the topographic transition zone. This is because out-of-sequence thrusting, and associated slowing down of the overthrusting velocity for the Lesser Himalaya, has not been going on for long enough in these models to influence the AFT ages in the Lesser Himalaya, which are mostly around 5 Ma. Surprisingly, the models including the most rapid overthrusting also predict older ages within the hangingwall of the out-of-sequence thrust. This is because the hangingwall of the out-of-sequence thrust is much thinner in the MCT zone than the hangingwall of the MHT, so that the thermal perturbation associated with overthrusting is much smaller, and the near-surface thermal gradient consequently lower, when a significant part of the overthrusting velocity is taken up by the out-of-sequence thrust (compare Figures 5a and b). None of these forward models fit the observed AFT age pattern particularly well, probably because we can improve on the model geometry and thermal parameters.

In order to search for the best-fitting combination of thermal, geometric and kinematic parameters, we ran an initial inversion in which we allowed the basal temperature to vary

between 500 and 1500 °C and the "normalized heat production" (a non-dimensional parameter that scales the crustal heat production to the model thickness, the thermal diffusivity and the basal temperature) between 1 and 5 (corresponding to minimum and maximum depth-averaged heat production rates of 0.25 and 3.80 $\mu W.m^{-3}$, respectively). We search for the optimum partitioning between frontal and out-of-sequence thrusting by letting V_{TF} vary between 0 and 5 $km.My^{-1}$ and we allow the MHT geometry to vary as described above. We ran 100 generations of 100 models each for this inversion, giving a total of 10,100 models (including an initial "seed" of 100 models). The model is fit to the set of AFT ages shown in Figure 4, as well as 45 mica Ar-Ar ages reported by *Arita et al.* [1997], *Rai* [1998] and *Bollinger et al.* [2004]. However, since the spatial distribution of the latter is not optimal, they do not constrain the models much more than the AFT data.

The results of this initial inversion are presented in Figure 6 and the parameter combination for the best-fit model is reported in Table 2 (model TF1). This initial inversion leads to optimal solutions in which a significant amount of overthrusting is taken up by the out-of-sequence thrust since 2 Ma (V_{TF} = 4.2 $km.My^{-1}$ for the best-fit model) and a poorly expressed mid-crustal ramp (ramp dip of 9° versus a shallow detachment dip of 6°). However, optimal solutions also lead to an unrealistically "hot" crust, with a best-fit basal temperature of 1100 °C at 65 km depth and a stable (in the absence of heat advection) near-surface geothermal gradient of 63 $°C.km^{-1}$. Although there is a clear tradeoff between basal temperature and heat production in these models, all optimal solutions are characterized by unrealistically high geothermal gradients.

We therefore proceeded to run a set of less general inversions, in which we fixed the thermal parameters at T_0 = 850 °C and Q = 1.5 (corresponding to a depth-averaged heat

production rate of 0.65 $\mu W.m^{-3}$), in order to predict a stable near-surface geothermal gradient of 35 $°C.km^{-1}$. We ran a smaller amount of models for these inversions (i.e. 50 generations of 50 models each, for a total of 2550 models) because they appear to "zoom in" to an optimal solution relatively rapidly. The geometric and kinematic parameters were allowed to vary as before. The results for this inversion (TF2; shown in Figure 7a and reported in Table 2) are opposite to the initial ones in that optimal models have practically no out-of-sequence thrusting (V_{TF} = 0.2 $km.My^{-1}$ for the best-fit model). Optimal models fit the data somewhat better than in for the first inversion (minimum misfit value of 0.7 versus 1.0). The geometry of the MHT (shallow flat dip of 6° and ramp dip of 20°) is in good agreement with what is known from geophysical and geodetic data.

In a third inversion (TF3), we explore the influence of changing the partitioning between over- and underthrusting on the MHT by running an inversion where the total overthrusting velocity is fixed at 8 $km.My^{-1}$ (with a corresponding underthrusting velocity of 13 $km.My^{-1}$). All other parameters (both fixed and free) are similar to the previous models. Somewhat surprisingly, this model again favors solutions with significant to near total out-of-sequence thrusting (V_{TF} = 7.8 $km.My^{-1}$ for the best-fit model) and a purely linear MHT, with both flat and ramp dips of 11°. A possible explanation for this puzzling behavior is that the higher overthrusting (and thus exhumation) rates need to be offset by a smaller thermal perturbation in the MCT zone, as predicted by the out-of-sequence model (see above). Another possibility is that the AFT data simply lack the resolution to record reactivation of the MCT zone in the last 2 My.

A final inversion run (TF4) was designed to test the latter assertion, as well as the possible effect of the timing of onset of out-of-sequence thrusting. This timing is not very

well constrained by the proponents of recent reactivation in the MCT zone. For instance, although *Hodges et al*. [2004] speak of "Quaternary" faulting, they also relate it to possible increased precipitation and denudation since mid-Pliocene (i.e. 3-4 Ma) times. We thus ran a final inversion in which the onset of possible out-of-sequence thrusting is pushed back to 4 Ma, while maintaining a total overthrusting velocity of 8 km.My^{-1}. This final inversion leads again to completely opposite results, namely a total absence of out-of-sequence thrusting (V_{TF} = 0 for the best-fit model) and a ramp dip of 19°, very close to that inferred from inversion TF2. The predicted dip of the shallow detachment is very low (1°) in this model, in contrast, in order to accommodate the relatively low exhumation rates recorded by the AFT data in the Lesser Himalaya with the higher overthrusting velocity.

We conclude from the above inversion results that the AFT data in the Langtang transect lack the resolution to formally rule out recent (i.e., Quaternary) reactivation of an out-of-sequence thrust below the topographic transition zone. However, such a model requires either unrealistically high crustal temperatures or high total overthrusting velocities. Moreover, significant out-of-sequence thrusting is incompatible with the presence of a mid-crustal ramp in the MHT, although such a ramp is inferred from a wealth of structural, geophysical and geodetic data (cf. Section 2.1.). In contrast, the data do constrain the geometry of the MHT very well, and best-fit models without significant out-of-sequence thrusting (in particular the results of inversion TF2) predict a flat-ramp geometry that is in quantitative agreement with available geophysical and geodetic data. In the next set of model runs, we will thus use this model as a template and study what lateral variation in MHT geometry are required by the data from the transects to the west and east of the Langtang transect.

4.3. Lateral variations in MHT geometry

We ran two model inversions for the Annapurna-Buthwal transect (west-central Nepal). Inversion GEO1 searches exactly the same parameter space as TF2 and leads to similar best-fit kinematics without out-of-sequence thrusting (V_{TF} = 0 for the best-fit model; Figure 8; Table 2). The predicted MHT ramp dip is higher, however (34° instead of 20°), as required by the in general somewhat younger ages reported by *Blythe et al*. [2007] from the Marsyandi valley (with a majority of AFT ages < 1 Ma) as compared to our data from Langtang. Since the ramp and flat dips are coupled through the location of the top of the ramp (point 4 defining the geometry of the MHT), this also implies a very low dip (<1°) of the southern detachment.

In a second inversion (GEO2), we simplified the kinematics by removing the potential out-of-sequence thrust, but again allowed the thermal structure to vary within the same bounds as for model TF1, in order to test whether these young ages can also be explained by a higher geothermal gradient. The optimal model from this inversion indeed shows a ramp dip that is closer to that inferred for the Langtang transect (21°) and a consequently somewhat higher (2°) detachment dip. However, this inversion favors a thermal structure that is even more extreme than that of TF1, with a best-fit basal temperature of 1300 °C depth and a stable near-surface geothermal gradient of 70 °C.km^{-1}. We therefore favor the result of GEO1.

Both inversions, however, show a MHT geometry for the Annapurna transect that is grossly similar to that of Langtang. Best fits impose the presence of a ramp below the MCT and physiographic transition. This ramp appears to be even more expressed in west-central Nepal than in east-central Nepal.

We use a similar inversion scheme to analyze the data from Bhutan (inversion Bhu1), with the final depth of the MHT at the northern boundary of the model as an additional free parameter. We choose to provide the inversion with this additional degree of freedom because there is no data to constrain the depth and geometry of the MHT in the Bhutan Himalaya. As expected from the very different pattern of AFT ages in Bhutan as compared to Nepal, the inversion results are completely different. In terms of thermal parameters, the inversion favors a relatively cool basal boundary condition (T_0 = 716 °C) but a relatively high crustal heat production (Q = 3.9, corresponding to a depth-averaged heat production rate of 1.4 $\mu W.m^{-3}$), leading to a stable near-surface geothermal gradient of 52 $°C.km^{-1}$. The contrast is even stronger for the MHT geometry, as the optimal models favor a practically linear MHT, with a constant detachment dip of 5-7° from below the mountain front to the north edge of the model, where the MHT reaches ~42 km depth.

These inversions thus clearly corroborate our initial qualitative interpretation of the different AFT age patterns: only subtle differences exist in the MHT geometry between western and eastern central Nepal, but a major difference exists between Nepal and Bhutan. In particular, the mid-crustal ramp disappears toward the east and the MHT becomes a planar detachment dipping at 5-7° to the north.

5. Discussion

Inversion results for the Langtang transect aimed at testing the importance of recent out-of-sequence thrusting in the MCT zone are somewhat inconclusive. Sets of parameters can be found that allow both kinematic models to predict the data. However, we show that active

out-of-sequence thrusting at the physiographic transition requires either unrealistically high geothermal gradients or relatively rapid total overthrusting rates. Moreover, out-of-sequence thrusting is incompatible with the existence of a mid-crustal ramp in the MHT. In contrast, models without Quaternary out-of-sequence thrusting require such a crustal ramp with a ~20° dip below this area. This latter geometry seems more compatible with the available reflection seismic profiles [*Hirn and Sapin*, 1984; *Zhao et al.*, 1993; *Makovsky et al.*, 1996; *Schulte-Pelkum et al.*, 2005; *Hetényi*, 2007], as well as with seismicity data [*Pandey et al.*, 1999] and geo-electric soundings [*Lemonnier et al.*, 1999]. If out-of-sequence thrusting is active only during Quaternary times, the available AFT data from the Lesser Himalaya (where the greatest difference is predicted to occur; cf. Figures 3 and 5) does not have sufficient resolution to either corroborate or contradict it, because most AFT ages are ~5 Ma. As argued before, the younger AFT ages from the MCT zone cannot constrain the problem because the kinematic differences between the two models are subtle in the hangingwall of the proposed out-of-sequence thrust [e.g., *Whipp et al.*, 2007; see Figure 5]. Thus, the only possibility we envisage to obtain a clear answer to this question would be to obtain data permitting to resolve the temperature history below the AFT closure temperature for the Lesser Himalaya, i.e. apatite fission-track length distributions and/or (U-Th)/He data. Given our limited success in obtaining AFT ages from Lesser Himalayan rocks, the large amount of material required for meaningful length measurements in young samples and the quality criteria associated with apatite (U-Th)/He dating, we are pessimistic about the chances of success of such an undertaking.

The data do, however, constrain the geometry of the MHT and its lateral variations very well. Along-strike variations in thermochronological ages in the Himalaya are linked to along-strike variations in topography (Figures 2 and 4). Since the convergence velocity only

varies by <10% along strike and increases to the east, whereas exhumation rates decrease, these variations should be controlled by changes in kinematics associated with the geometry of the MHT. Where the MHT contains a mid-crustal ramp, as in central Nepal, because of mass conservation, it is necessary to accommodate the flow of rocks by creating high relief over the ramp with high exhumation and erosion rates. The topographic profile will thus obtain a concave form. This is not necessary if the dip of the detachment is continuous, leading to a linear to convex topographic surface and more constant exhumation rates along strike, leading to a less pronounced trend in thermochronological ages.

The Annapurna and Langtang transects show similar patterns in topography (Figure 2) and AFT ages (Figure 4), suggesting that both regions should be characterized by a similar MHT geometry and kinematics. Our numerical models confirm this but show that the dip of the crustal ramp is somewhat steeper in the Annapurna area than in the Langtang area. Such a lateral variation of ramp dip is compatible with the conclusions of *Berger et al.* [2004], who inferred lateral variations in the geometry of the MHT in Nepal from the analysis of present-day (GPS-derived) displacement rates. They propose the existence of lateral ramps to permit the transition between areas with different crustal ramp dips. In particular, they show that in westernmost Nepal, the mid-crustal ramp should be much less well expressed and the shallow detachment dip more important than in central Nepal, in agreement with inferences from drainage patterns [*van der Beek et al.*, 2002]. The topographic transition between the Lesser and High Himalaya also becomes less well expressed in western Nepal [*Berger et al.*, 2004]. Sampling a thermochronological age transect across western Nepal would allow to test our model, which predicts that minimum AFT ages in the MCT zone should be older than in central Nepal and the increase in ages toward the south less pronounced, if existent at all.

AFT data show that exhumation rates in the MCT zone and the topographically highest part of the range are lower in the eastern Himalaya. This is consistent with observations of the regional geology of the Himalaya. In the eastern Himalaya, the Higher Himalaya is much more widespread than in central Nepal, to the expense of the Lesser Himalaya. As clearly shown by the Higher Himalayan klippen in Nepal, the Higher Himalayan sequence has overthrusted the Lesser Himalaya on a nearly horizontal detachment [e.g., *Schelling and Arita*, 1991; *Upreti and Le Fort*, 1999; *DeCelles et al.*, 2001]. We can thus interpret the regional variation in surface geology as a consequence of a variation in the depth of erosion between the central and eastern Himalaya. This is highly compatible with a change in crustal fault geometry. As GPS measurements show a somewhat higher convergence rate in the eastern Himalaya compared to the western Himalaya, the sole solution to allow coexistent higher convergence rates and lower exhumation rates is to reduce angle of the MHT detachment.

Our interpretation and numerical modeling of the lateral variations in AFT age patterns permit us to present a conceptual 3D view of the MHT below Nepal and Bhutan (Figure 9). The MHT is clearly not cylindrical. In western Nepal, the southern shallow flat of the MHT is steeper than in central Nepal [*Larson et al.*, 1999; *van der Beek et al.*, 2002], but the dip angle of the mid-crustal MHT ramp is steeper in central Nepal than in western Nepal [*Berger et al.*, 2004]. Within central Nepal, more subtle variations appear to exist between the Annapurna and Langtang regions, as implied by our inversions, but we cannot definitely state at this stage whether these differences are real or beyond the resolution of our model. In Bhutan, the MHT appears as a continuously shallow dipping detachment without a ramp below our model domain. If a mid-crustal ramp exists below the eastern Himalaya it should be located more to the north, possibly associated with exhumation of the Kangmar dome in southern Tibet, as

suggested by *Hauck et al*. [1998]. This interpretation implies important and fairly rapid changes of geometry between each zone (western Nepal central Nepal and Bhutan), most easily explained by the presence of lateral crustal ramps within the underthrusting Indian crust. *Hauck et* al. [1998] suggest that the Yadong Cross structure in westernmost Bhutan represents one of these lateral ramps and controls the transition zone between the Bhutan and Nepal Himalaya [see also *Duncan et al.*, 2003].

Our analysis thus poses the question of what is the fundamental control on topography in the Himalaya and in collisional mountain belts in general. *Bookhagen et al.* [2005], *Bookhagen and Burbank* [2006] and *Grujic et al.* [2006] have argued for a strong climatic control on laterally varying topographic trends, due to the lateral variations in precipitation rates and patterns observed in the Himalaya. We show, however, that lateral variations in topography and exhumation rates should be correlated to variation in the geometry of the MHT and associated crustal kinematics. Our study underlines the strong influence of the geometry of deep tectonic structures on the topography. Increasing relief in mountain belts will lead to enhanced erosion through the relief dependence of major erosional mechanisms [e.g., *Montgomery and Brandon*, 2002]. Increasing elevation also leads to higher erosion rates by orographically enhancing precipitation rates [e.g., *Roe*, 2005]. Thus, our study highlights the complex couplings in the system but emphasizes the potentially important role of pre-existing structure, which may have been somewhat overlooked in recent years.

6. Conclusions

In this study we have discussed the influence of the geometry of major crustal faults on exhumation patterns and show its importance in controlling surface observations.

Low-temperature thermochronology data from the Lesser Himalaya in central Nepal currently lack the resolution to asses the importance of Quaternary out-of-sequence faulting at the physiographic transition. But the geometry of the MHT required by a model in which overthrusting in concentrated on the MHT and the frontal thrust is more in accord with available geophysical data than that for models with significant out-of-sequence thrusting. Out-of-sequence thrusting thus appears to be a secondary mechanism at best for explaining the observed pattern of thermochronological ages in comparison to the geometry of main crustal faults.

The tectonic structure and geomorphology of the Himalayan range clearly show it is not a cylindrical structure. We link the along-strike variations in topography, erosion and geometry of the crustal faults. The crustal faults and associated kinematics drive the topography through the exhumation pathways of rocks that can differ drastically. The presence of a mid-crustal ramp in central Nepal induces the formation of a sharp topographic transition. Both the mid-crustal ramp and the topographic transition are absent in the Eastern Himalaya. The formation of relief strongly influences precipitation and erosion rates, and explains the gradient of denudation from west to east, underlined by variations in map view of the outcrop pattern of the Higher and Lesser Himalaya.

Acknowledgments

We thank Rodolphe Cattin, Frédéric Hermann, Jean-Philippe Avouac and Christoph Glotzbach for helpful discussions and ideas. Most of the computations presented in this paper were performed at the *Service Commun de Calcul Intensif de l'Observatoire de Grenoble* (SCCI), additional model runs were performed on the *Géocalc* cluster at *Géoscience Rennes.* This study was supported by the *Institut National des Sciences de l'Univers* through the

Reliefs de la Terre programme and by a *Chaire d'Excellence* of the *Agence Nationale de la Recherche* to JB. We thank Ananta Gajurel of Tribuvhan University, Kathmandu, for assistance during field work.

References cited

Adams, J. (1980), Contemporary uplift and erosion of the Southern Alps, New Zealand, *Geol. Soc. Am. Bull.*, *91*, 1-114.

Anders, A. M., G. H. Roe, B. Hallet, D. R. Montgomery, N. J. Finnegan, and J. Putkonen (2006), Spatial patterns of precipitation and topography in the Himalaya, in *Tectonics, Climate, and Landscape Evolution*, edited by S. D. Willett et al., pp. 39-53, Geological Society of America, Special Paper 398.

Arita, K., R. D. Dallmeyer, and A. Takasu (1997), Tectonothermal evolution of the Lesser Himalaya, Nepal: Constraints from $^{40}Ar/^{39}Ar$ ages from the Kathmandu Nappe, *Isl. Arc*, *6*, 372-385.

Avouac, J. P. (2003), Mountain building, erosion and the seismic cycle in the Nepal Himalaya, *Adv. Geophys.*, *46*, 1-79.

Beaumont, C., R. A. Jamieson, M. H. Nguyen, and B. Lee (2001), Himalayan tectonics explained by extrusion of a low-viscosity channel coupled to focused surface denudation, *Nature*, *414*, 738-742.

Berger, A., F. Jouanne, R. Hassani, and J. L. Mugnier (2004), Modelling the spatial distribution of present-day deformation in Nepal: how cylindrical is the Main Himalayan Thrust in Nepal?, *Geophys. J. Int.*, *156*, 94-114.

Bhargava, O. N. (1995), Geology of Bhutan - A synoptic view, in *The Bhutan Himalaya: A Geological Account*, edited by O. N. Bhargava, pp. 13-17, Geological Society of India, Special Publication, 39.

Bilham, R., K. Larson, J. Freymueller, and Project IDYLHIM Members (1997), GPS measurements of present-day convergence across the Nepal Himalaya, *Nature*, *386*, 61-64.

Blythe, A., D. W. Burbank, A. Carter, K. L. Schmidt, and J. Putkonen (2007), Plio-Quaternary exhumation history of the central Himalaya: 1. Apatite and zircon fission-track and apatite [U-Th]/He analyses, *Tectonics*, *26*, TC3002, doi:10.1029/2006TC001990.

Bollinger, L., J.-P. Avouac, E. J. Catlos, T. M. Harrison, M. Grove, O. Beyssac, B. Goffé, and S. Sapkota (2004), Thermal structure and exhumation history of the Lesser Himalaya in central Nepal, *Tectonics*, *23*, TC5015, doi:5010.1029/2003TC001564.

Bollinger, L., P. Henry, and J. P. Avouac (2006), Mountain building in the Nepal Himalaya: Thermal and kinematic model, *Earth Planet. Sci. Lett.*, *244*, 58-71.

Bookhagen, B., and D. W. Burbank (2006), Topography, relief, and TRMM-derived rainfall variations along the Himalaya, *Geophys. Res. Lett.*, *33*, doi:10.1029/2006GL026037.

Bookhagen, B., R. C. Thiede, and M. R. Strecker (2005), Abnormal monsoon years and their control on erosion and sediment flux in the high, arid northwest Himalaya, *Earth Planet. Sci. Lett.*, *231*, 131-146.

Braun, J. (2002), Quantifying the effect of recent relief changes on age-elevation relationships, *Earth Planet. Sci. Lett.*, *200*, 331-343.

Braun, J. (2003), Pecube: A new finite element code to solve the heat transport equation in three dimensions in the Earth's crust including the effects of a time-varying, finite amplitude surface topography, *Comp. Geosci.*, *29*, 787–794.

Braun, J., G. E. Batt, D. L. Scott, H. McQueen, and A. R. Beasley (1994), A simple kinematic model for crustal deformation along two- and three-dimensional listric normal faults derived from scaled laboratory experiments, *J. Struct. Geol.*, *16*, 1477-1490.

Braun, J., and X. Robert (2005), Constraints on the rate of post-orogenic erosional decay from low-temperature thermochronological data: application to the Dabie Shan, China, *Earth Surf. Proc. Landf., 30*, 1203-1225.

Braun, J., P. van der Beek, and G. Batt (2006), *Quantitative Thermochronology: Numerical Methods for the Interpretation of Thermochronological Data*, 258 pp., Cambridge University Press, Cambridge, New York.

Brewer, I. D., and D. W. Burbank (2006), Thermal and kinematic modeling of bedrock and detrital cooling ages in the central Himalaya, *J. Geophys. Res.*, *111*, doi:10.1029/2004JB003304.

Burbank, D. W. (2002), Rates of erosion and their implications for denudation, *Mineral. Mag.*, *66*, 25-52.

Burbank, D. W., A. E. Blythe, J. K. Putkonen, B. A. Pratt-Sitaula, E. J. Gabet, M. E. Oskin, A. P. Barros, and T. P. Ojha (2003), Decoupling of erosion and precipitation in the Himalaya, *Nature*, *426*, 652-655.

Burchfiel, B. C., C. Zhiliang, K. V. Hodges, L. Yuping, L. H. Royden, D. Changrong, and X. Jiene (1992), *The South Tibetan detachment system, Himalayan orogen: Extension contemporaneous with and parallel to shortening in a collisional mountain belt*, Geological Society of America Special Paper, 269, 41 pp., Boulder.

Catlos, E. J., T. M. Harrison, M. J. Kohn, M. Grove, F. J. Ryerson, C. E. Manning, and B. N. Upreti (2001), Geochronologic and barometric constraints on the evolution of the Main Central Thrust, central Nepal Himalaya, *J. Geophys. Res.*, *106*, 16177-16204.

Cattin, E., and J. P. Avouac (2000), Modeling mountain building and the seismic cycle in the Himalaya of Nepal, *J. Geophys. Res.*, *105*, 13389-13408.

Copeland, P., T. M. Harisson, K. V. Hodges, P. Maruejol, P. Le Fort, and A. Pêcher (1991), An Early Pliocene thermal disturbance of the Main Central Thrust, central Nepal: Implications for Himalayan tectonics, *J. Geophys. Res.*, *96*, 8475-8500.

DeCelles, P. G., G. E. Gehrels, J. Quade, B. LaReau, and M. Spurlin (2000), Tectonic implications of U-Pb zircon ages of the Himalayan orogenic belt in Nepal, *Science*, *288*, 497-499.

DeCelles, P. G., G. E. Gehrels, J. Quade, T. P. Ojha, P. A. Kapp, and B. N. Upreti (1998), Neogene foreland basin deposits, erosional unroofing, and the kinematic history of the Himalayan fold-thrust belt, western Nepal, *Geol. Soc. Am. Bull.*, *110*, 2-21.

DeCelles, P. G., D. M. Robinson, J. Quade, T. P. Ojha, C. N. Garzione, P. Copeland, and B. N. Upreti (2001), Stratigraphy, structure, and tectonic evolution of the Himalayan fold-thrust belt in western Nepal, *Tectonics*, *20*, 487-509.

Duncan, C., J. Masek, and E. Fielding (2003), How steep are the Himalaya? Characteristics and implications of along-strike topographic variations, *Geology*, *31*, 75-78.

Ehlers, T. A. (2005), Crustal thermal processes and thermochronometer interpretation, in *Low-temperature Thermochronology: Techniques, Interpretations, and Applications*, edited by P. W. Reiners and T. A. Ehlers, pp. 315-350, Mineralogical Society of America/Geochemical Society Reviews in Mineralogy and Geochemistry, Chantilly, Virginia, 58.

Galbraith, R. F., and G. M. Laslett (1993), Statistical models for mixed fission track ages, *Nucl. Tracks Radiat. Meas.*, *21*, 459-470.

Galy, A. (1999), Etude géochimique de l'érosion actuelle de la chaîne himalayenne, Ph.D. thesis, 433 pp, Institut National Polytechnique de Lorraine, Nancy.

Gansser, A. (1964), *Geology of the Himalayas*, 289 pp., John Wiley and Sons Ltd., London.

Gansser, A. (1983), *Geology of the Bhutan Himalaya*, 181 pp., Birkhaeuser Verlag, Basel.

Gehrels, G. E., P. G. DeCelles, T. P. Ojha, and B. N. Upreti (2006), Geologic and U-Th-Pb geochronologic evidence for early Paleozoic tectonism in the Kathmandu thrust sheet, central Nepal Himalaya, *Geol. Soc. Am. Bull.*, *118*, 185-198.

Green, P. F., I. R. Duddy, G. M. Laslett, K. A. Hegarty, A. J. W. Gleadow, and J. F. Lovering (1989), Thermal annealing of fission tracks in apatite 4. Quantitative modelling techniques and extension to geological timescales, *Chem. Geol. (Isot. Geosci. Sect.)*, *79*, 155-182.

Grujic, D., I. Coutand, B. Bookhagen, S. Bonnet, A. Blythe, and C. Duncan (2006), Climatic forcing of erosion, landscape, and tectonics in the Bhutan Himalayas, *Geology*, *34*, 801-804.

Grujic, D., L. S. Hollister, and R. R. Parrish (2002), Himalayan metamorphic sequence as an orogenic channel: insight from Bhutan, *Earth Planet. Sci. Lett.*, *198*, 177-191.

Hauck, M. L., K. D. Nelson, L. D. Brown, W. Zhao, and A. R. Ross (1998), Crustal structure of the Himalayan orogen at ~90° east longitude from Project INDEPTH deep reflection profiles, *Tectonics*, *17*, 481-500.

Hetényi, G. (2007), Evolution of deformation of the Himalayan prism: from imaging to modelling, Ph.D. thesis, 400 pp, Ecole Nationale Supérieure, Paris.

Hirn, A., and M. Sapin (1984), The Himalayan zone of crustal interaction; suggestions from explosion seismology, *Ann. Geophys.*, *2*, 123-130.

Hodges, K. V. (2000), Tectonics of the Himalaya and southern Tibet from two perspectives, *Geol. Soc. Am. Bull.*, *112*, 324-350.

Hodges, K. V., J. M. Hurtado, and K. X. Whipple (2001), Southward extrusion of Tibetan crust and its effect on Himalayan tectonics, *Tectonics*, *20*, 799-809.

Hodges, K. V., R. R. Parrish, and M. P. Searle (1996), Tectonic evolution of the central Annapurna Range, Nepalese Himalayas, *Tectonics*, *15*, 1264-1291.

Hodges, K. V., C. W. Wobus, K. Ruhl, T. Schildgen, and K. X. Whipple (2004), Quaternary deformation, river steepening, and heavy precipitation at the front of the Higher Himalayan ranges, *Earth Planet. Sci. Lett.*, *220*, 379-389.

Hollister, L. S., and D. Grujic (2006), Pulsed channel flow in Bhutan, in *Channel Flow, Ductile Extrusion and Exhumation in Continental Collision Zones*, edited by R. D. Law et al., pp. 415–423, Geological Society, London, Special Publication, 268.

Hovius, N. (1998), Controls on sediment supply by large rivers, in *Relative Role of Eustacy, Climate and Tectonics in Continental Rocks*, edited by K. W. Shanley and P. J. McCabe, pp. 3-16, Society of Economic Paleontologists and Mineralogists, Special Publication, 59.

Huntington, K. W., T. A. Ehlers, K. V. Hodges, and D. M. Whipp Jr. (2007), Topography, exhumation pathway, age uncertainties, and the interpretation of thermochronometer data, *Tectonics*, *26*, TC4012, doi:10.1029/2007TC002108.

Huyghe, P., A. Galy, J. L. Mugnier, and C. France-Lanord (2001), Propagation of the thrust system and erosion in the Lesser Himalaya: Geochemical and sedimentological evidence, *Geology*, *29*, 1007–1010.

Huyghe, P., J. L. Mugnier, A. P. Gajurel, and B. Delcaillau (2005), Tectonic and climatic control of the changes in the sedimentary record of the Karnali River section (Siwaliks of Western Nepal), *Isl. Arc*, *14*, 311-327.

Jamieson, R. A., and C. Beaumont (1988), Orogeny and metamorphism: A model for deformation and Pressure-Temperature-time paths with applications to the central and southern Appalachians, *Tectonics*, *7*, 417–445.

Jamieson, R. A., C. Beaumont, S. Medvedev, and M. H. Nguyen (2004), Crustal channel flows: 2. Numerical models with implications for metamorphism in the Himalayan-Tibetan orogen, *J. Geophys. Res.*, *109*, B06407, doi:06410.01029/02003JB002811.

Jouanne, F., J. L. Mugnier, J. F. Gamond, P. Le Fort, M. R. Pandey, L. Bollinger, M. Flouzat, and J. P. Avouac (2004), Current shortening across the Himalayas of Nepal, *Geophys. J. Int.*, *157*, 11-14.

Lakshminarayana, G., and B. Singh (1995), Siwalik Group, in *The Bhutan Himalaya: A Geological Account*, edited by O. N. Bhargava, pp. 22-28, Geological Society of India, Special Publication, 39.

Larson, K. M., R. Bürgmann, R. Bilham, and J. T. Freymueller (1999), Kinematics of the India-Eurasia collision zone from GPS measurements, *J. Geophys. Res.*, *104*, 1077-1093.

Lavé, J., and J. P. Avouac (2000), Active folding of fluvial terraces across the Siwaliks Hills (Himalayas of central Nepal), *J. Geophys. Res.*, *105*, 5735-5770.

Lavé, J., and J. P. Avouac (2001), Fluvial incision and tectonic uplift across the Himalayas of central Nepal, *J. Geophys. Res.*, *106*, 25561-25593.

Le Fort, P. (1975), Himalaya: the collided range. Present knowledge of the continental arc, *Am. J. Sci.*, *275*, 1-44.

Lemonnier, C., G. Marquis, F. Perrier, J.-P. Avouac, G. Chitrakar, B. Kafle, S. Sapkota, U. Gautam, D. Tiwari, and M. Bano (1999), Electrical structure of the Himalaya of central Nepal: High conductivity around the mid-crustal ramp along the MHT, *Geophys. Res. Lett.*, *26*, 3261–3264.

Makovsky, Y., S. L. Klemperer, H. Liyan, L. Deyuan, and Project INDEPTH Team (1996), Structural elements of the southern Tethyan Himalaya crust from wide-angle seismic data, *Tectonics*, *15*, 997-1005.

Manktelow, N. S., and B. Grasemann (1997), Time-dependent effects of heat advection and topography on cooling histories during erosion, *Tectonophysics*, *270*, 167-195.

Meigs, A. J., D. W. Burbank, and R. A. Beck (1995), Middle-Late Miocene (> 10 Ma) formation of the Main Boundary Thrust in the western Himalaya, *Geology*, *23*, 423-426.

Montgomery, D. R., and M. T. Brandon (2002), Topographic controls on erosion rates in tectonically active mountain ranges, *Earth Planet. Sci. Lett.*, *201*, 481-489.

Mugnier, J.-L., and P. Huyghe (2006), Ganges basin geometry records a pre-15 Ma isostatic rebound of Himalaya, *Geology*, *34*, 445-448.

Mugnier, J. L., P. Huyghe, P. Leturmy, and F. Jouanne (2004), Episodicity and rates of thrust sheet motion in the Himalayas (western Nepal), in *Thrust Tectonics and Petroleum Systems*, edited by K. C. McClay, pp. 1-24, American Association of Petroleum Geologists Memoir 82.

Mugnier, J. L., P. Leturmy, G. Mascle, P. Huyghe, E. Chalaron, G. Vidal, L. Husson, and B. Delcaillau (1999), The Siwaliks of western Nepal: I - Geometry and kinematics, *J. Asian Earth Sci.*, *17*, 629-642.

Pandey, M. R., R. P. Tandukar, J. P. Avouac, J. Vergne, and T. Héritier (1999), Seismotectonics of the Nepal Himalaya from a local seismic network, *J. As. Earth Sci.*, *17*, 703-712.

Paul, J., R. Bürgmann, V. K. Gaur, R. Bilham, K. M. Larson, M. B. Ananda, S. Jade, M. Mukal, T. S. Anupama, G. Satyal, and D. Kumar (2001), The motion and active deformation of India, *Geophys. Res. Lett.*, *28*, 647-650.

Powers, P. M., R. J. Lillie, and R. S. Yeats (1998), Structure and shortening of the Kangra and Dehra Dun reentrants, Sub-Himalaya, India, *Geol. Soc. Am. Bull.*, *110*, 1010-1027.

Rai, S. M. (1998), Les Nappes de Kathmandou et du Gosainkund, Himalaya du Népal central (Etude cartographique, structurale, métamorphique, géochimique et radiochronologique), Ph.D. thesis, 150 pp, Université Joseph Fourier, Grenoble.

Reiners, P. W., and M. T. Brandon (2006), Using thermochronology to understand orogenic erosion, *Ann. Rev. Earth Planet. Sci.*, *34*, 419-466, doi:10.1146/annurev.earth.34.031405.125202.

Robinson, D. M., P. G. DeCelles, and P. Copeland (2006), Tectonic evolution of the Himalayan thrust belt in western Nepal: Implications for channel flow models, *Geol. Soc. Am. Bull.*, *118*, 865-885.

Roe, G. H. (2005), Orographic precipitation, *Ann. Rev. Earth Planet. Sci.*, *33*, 645-671.

Sambridge, M. (1999), Geophysical inversion with a neighbourhood algorithm - I. Searching a parameter space, *Geophys. J. Int.*, *138*, 479-494.

Schelling, D., and K. Arita (1991), Thrust tectonics, crustal shortening, and the structure of the far eastern Nepal Himalaya, *Tectonics*, *10*, 851-862.

Schulte-Pelkum, V., G. Monsalve, A. Sheehan, M. R. Pandey, S. Sapkota, R. Bilham, and F. Wu (2005), Imaging the Indian subcontinent beneath the Himalaya, *Nature*, *435*, 1222-1225.

Seeber, L., and V. Gornitz (1983), River profiles along the Himalayan arc as indicators of active tectonics, *Tectonophysics*, *92*, 335-367.

Stephenson, J., K. Gallagher, and C. C. Holmes (2006), A Bayesian approach to calibrating apatite fission track annealing models for laboratory and geological timescales *Geochim. Cosmochim. Act.*, *70*, 5183–5200.

Stolar, D. B., G. H. Roe, and S. D. Willett (2007), Controls on the patterns of topography and erosion rate in a critical orogen, *J. Geophys. Res.*, *112*, F04002, doi:10.1029/2006JF000713.

Stüwe, K., L. White, and R. W. Brown (1994), The influence of eroding topography on steady-state isotherms. Application to fission track analysis, *Earth Planet. Sci. Lett.*, *124*, 63-74.

Summerfield, M. A., and N. J. Hulton (1994), Natural controls of fluvial denudation rates in major world drainage basins, *J. Geophys. Res.*, *99*, 13871-13883.

Thiede, R. C., B. Bookhagen, J. R. Arrowsmith, E. R. Sobel, and M. R. Strecker (2004), Climatic control on rapid exhumation along the Southern Himalayan Front, *Earth Planet. Sci. Lett.*, *222*, 791-806.

Upreti, B. N. (1999), An overview of the stratigraphy and tectonics of the Nepal Himalaya, *J. Asian Earth Sci.*, *17*, 577-606.

Upreti, B. N., and P. Le Fort (1999), Lesser Himalayan crystalline nappes of Nepal: Problems of their origin, in *Himalaya and Tibet: Mountain Roots to Mountain Tops*, edited by A. MacFarlane et al., pp. 225-238, Geological Society of America, Boulder, CO, Special Paper 328.

van der Beek, P. A., B. Champel, and J. L. Mugnier (2002), Control of detachment dip on drainage development in regions of active fault-propagation folding, *Geology*, *30*, 471-474.

van der Beek, P. A., X. Robert, J. L. Mugnier, M. Bernet, P. Huyghe, and E. Labrin (2006), Late Miocene – Recent exhumation of the central Himalaya and recycling in the foreland basin assessed by apatite fission-track thermochronology of Siwalik sediments, Nepal, *Basin Res.*, *18*, 413–434, doi: 10.1111/j.1365-2117.2006.00305.x.

Vannay, J.-C., B. Grasemann, M. Rahn, W. Frank, A. Carter, V. Baudraz, and M. Cosca (2004), Miocene to Holocene exhumation of metamorphic crustal wedges in the NW Himalaya: Evidence for tectonic extrusion coupled to fluvial erosion, *Tectonics*, *23*, TC1014, doi:1010.1029/2002TC001429.

Whipp, D. M., T. A. Ehlers, A. Blythe, K. W. Huntington, K. V. Hodges, and D. W. Burbank (2007), Plio-Quaternary exhumation history of the central Nepalese Himalaya: 2. Thermokinematic and thermochronometer age prediction model, *Tectonics*, *26*, TC3003, doi:10.1029/2006TC001991.

Willett, S. D. (1999), Orogeny and orography: The effects of erosion on the structure of mountain belts, *J. Geophys. Res.*, *104*, 28957-28981.

Willett, S. D., and M. T. Brandon (2002), On steady state in mountain belts, *Geology*, *30*, 175-178.

Wobus, C. W., A. Heimsath, K. X. Whipple, and K. V. Hodges (2005), Active out-of-sequence thrust faulting in the central Nepalese Himalaya, *Nature*, *434*, 1008-1011.

Wobus, C. W., K. V. Hodges, and K. X. Whipple (2003), Has focused denudation sustained active thrusting at the Himalayan topographic front?, *Geology*, *31*, 861-864.

Wobus, C. W., K. X. Whipple, and K. V. Hodges (2006), Neotectonics of the central Nepalese Himalaya: Constraints from geomorphology, detrital $^{40}Ar/^{39}Ar$ thermochronology, and thermal modeling, *Tectonics*, *25*, doi:10.1029/2005TC001935.

Yin, A. (2006), Cenozoic tectonic evolution of the Himalayan orogen as constrained by along-strike variation of structural geometry, exhumation history, and foreland sedimentation, *Earth-Sci. Rev.*, *76*, 1-131.

Yin, A., and T. M. Harrison (2000), Geologic Evolution of the Himalayan-Tibetan Orogen, *Ann. Rev. Earth Planet. Sci.*, *28*, 211-280.

Zhao, W., K. D. Nelson, and Project INDEPTH Team (1993), Deep seismic reflection evidence for continental underthrusting beneath southern Tibet, *Nature*, *366*, 557-559.

Figure and Table captions

Figure 1. a) Simplified geological map of the Himalaya showing the major structural units and the major thrusts [modified from *Galy*, 1999]; lines indicate locations of three structural cross-sections shown in (c). b) Schematic representation of the relative widths of the High Himalayan crystalline, Lesser Himalaya and Siwaliks along strike of the Himalayan range. c) Structural cross-sections across (A) western Nepal [original cross-section from *DeCelles et al.*, 2001; modified from *Yin*, 2006], (B) central Nepal [modified from *Avouac*, 2003] and (C) the Bhutan Himalaya [modified from *Yin*, 2006]. Colour scheme in cross-sections is same as in map.

Figure 2. a) DEM of the central and eastern Himalaya showing the location of studied transects and thermochronological data used in this study. Transect A corresponds to the Annapurna-Buthwal region; transect B to the Langtang-Hetauda region; transect C and D to the Western and Eastern Bhutan Himalaya, respectively. B) Swath elevation profiles for each transect. Black solid line corresponds to the mean elevation calculated in the corresponding 20 km wide box; outer grey lines correspond to the maximum and minimum elevations, and the red fill to the probability-density of elevation within the envelope.

Figure 3. Sketch of the two kinematic scenarios envisaged for the central Himalaya [modified from *Hodges et al.*, 2004] and expected thermochronological age trends for both. a) In the model of Avouac and co-workers [e.g., *Avouac*, 2003; *Bollinger et al.*, 2004; 2006], shortening is concentrated on the Main Himalayan Thrust (MHT), which includes a crustal ramp below the High Himalaya where Indian plate material is accreted to the overriding plate. Both low- and high-temperature thermochronologic age trends should show continuous

younging from the MBT to the topographic transition and MCT zone. b) In the model of Hodges and co-workers [e.g., *Wobus et al.*, 2003; *Hodges et al.*, 2004; *Wobus et al.*, 2005], out-of-sequence faulting occurs in the MCT zone on the topographic transition (TT). The sharp topographic transition and a jump in both detrital thermochronology and cosmogenic ages have been used to support such a model. Both low- and high-temperature thermochronologic age trends should present a jump in the topographic transition and/or in the MCT zone.

Figure 4. AFT datasets projected onto profiles perpendicular to the MFT. Locations of samples are indicated in Figure 2. Upper panel: Annapurna-Buthwal transect; data principally from *Blythe et al.* [2007] augmented by four new AFT ages from the Kali Gandaki valley and the Lesser Himalaya. Middle panel: Langtang-Hetauda transect; data from *Robert et al.* [submitted (b)] augmented by a few ages obtained by P. Copeland and reported in *Bollinger et al.* [2006]. Lower panel: Bhutan Himalaya; data from *Grujic et al.* [2006].

Figure 5. a) Forward-model geometry for the Langtang transect showing the modeled MHT, model kinematics and predicted thermal structure and AFT age pattern at the surface for a model of overthrusting on the MHT (V_0 = 6 km.My^{-1}). b) Same as (a) but for a model including out-of-sequence thrusting on a fault breaking the surface at the front of the topographic transition (V_{TF} = 5 km.My^{-1}). c) Comparison of observed and predicted AFT age patterns for the Langtang transect, as a function of out-of-sequence thrusting velocity (V_{TF}); the overthrusting velocity on the MHT is equal to ($6 - V_{TF}$) km.My^{-1} in these models.

Figure 6. Initial inversion results for the Langtang transect. Results are shown as two-dimensional sections through the parameter space, in which each model (parameter

combination) is represented by a dot, colored according to the misfit between predicted and observed data. Star shows location of best-fit model reported in Table 2.

Figure 7: Results of model inversions TF1 and TF2 for the Langtang transect. The central sketch explains the significance of the free parameters (*X4,Y4, X5, Y5,* V_{TF}) controlling the geometry and kinematics. For each inversion, the comparison of predicted and observed AFT ages is shown. a) Inversion TF2 with thermal parameters which lead to a geothermal gradient of 35°C.km^{-1} (T_0=850°C and A=1.5). Best fit is for a model without significant out-of-sequence thrusting and with a 20° dipping crustal ramp; b) Inversion with free thermal parameters, leading to a strong geothermal gradient of 63°C.km^{-1} (T_0=1100°C and A=2.5). Best fit is for a model with significant out-of-sequence and without a well-expressed crustal ramp. Lower panels show comparisons between predicted and observed AFT age patterns for both cases, by plotting the ages predicted for all sampling locations where we have data.

Figure 8. Comparison of the inversion results constraining the MHT geometry for the Annapurna transect the Langtang transect, and the Bhutan Himalaya. The sketch explains significance of the free parameters controlling the geometry. For each inversion, the comparison of predicted and observed AFT ages is shown. a) Inversion GEO1 with thermal parameters that lead to a thermal gradient of 35 °C.km^{-1} (T_O=850°C and A=1.5) for the Annapurnas area. Best fit is for a model with a 34° dipping crustal ramp. b) Inversion TF2 for the Langtang area. Best fit is for a model with a 20° dipping crustal ramp; c) Inversion Bhu1 with thermal parameters that lead to a thermal gradient of 52°C.km^{-1} (T_O=714°C and A=3.9) for the Bhutan area. Best fit is for a model with a planar MHT (no crustal ramp) dipping at 5-7°.

Figure 9. Schematic drawing showing 3D view of MHT geometry and kinematic of the Himalaya from Nepal to Bhutan. Geometries of the best fit models from NA inversions are shown for comparison.

Table 1. Apatite fission-track data from Annapurna-Buthwal (west-central Nepal) and Langtang-Hetauda (east-central Nepal) transects. For completeness, all analyzed samples are reported here, including those that did not contain sufficient apatite or Uranium to provide meaningful ages and those reported in *Robert et* al. [submitted (b)]. N: number of individual grains dated; ρ_s, spontaneous track density; Ns, spontaneous track counted; ρ_i, induced track density in external detector (muscovite); Ni, number of induced track counted; ρ_d, induced track density in external detector attached to dosimeter glass; Nd, number of track counted in determining ρ_d; P(χ^2), chi-square probability; D: age dispersion. All reported ages are central ages [*Galbraith and Laslett*, 1993] ± 1 standard deviation. Note that zero-track grains were abundant and included in the age determinations. Sample preparation followed standard methods [cf. *van der Beek et al.*, 2006]. All ages were determined by XR using a zeta-calibration factor of 350±7.

Table 2. Parameters used for the different inversions and best fit results for each inversion. Numbers in bold italic represent the values of the free parameters for the best-fit model, others are kept constant. The stable near-surface geothermal gradient (grad(T)) in the absence of heat advection, and the dips of the MHT ramp and southern (shallow) flat have been computed for each model in order to compare parameter values to observables. O.o.S. timing = timing of onset of out-of-sequence thrusting.

Annapurna - Butwal Section

Ghorepani Vertical South Section

Sample	Struct. Unit	Elevation (m)	Roks	Long °	Long min	Long s	Lat °	Lat min	Lat s	Locality	N	ρs (x10^6 cm^{-2})	Ns	ρi (x10^6 cm^{-2})	Ni	ρd (x10^6 cm^{-2})	Nd	P(χ2) %
NP05.34	Lesser Himal.	2510	quartzite	83	42	39.1	28	23	2.4	Nangethanti	-	-	-	-	-	5.62	11971	-
NP05.36	Lesser Himal.	3190	quartzite	83	41	21.1	28	23	58.2	Poon Hill	-	-	-	-	-	5.62	11971	-
NP05.38	Lesser Himal.	2050	gneiss	83	40	27.9	28	26	11.8	Sikha	-	-	-	-	-	5.62	11971	-
NP05.40	Lesser Himal.	1200	Amphibolites	83	38	55.6	28	29	7.2	Tatopani Bridg	-	-	-	-	-	5.62	11971	-

High Kali Gandaki Section

Sample	Struct. Unit	Elevation (m)	Roks	Long °	Long min	Long s	Lat °	Lat min	Lat s	Locality	N	ρs (x10^6 cm^{-2})	Ns	ρi (x10^6 cm^{-2})	Ni	ρd (x10^6 cm^{-2})	Nd	P(χ2) %
NP05.41	High Himal.	1550	gneiss	83	37	57.5	28	33	21.5	Kabre Bridge	25	0.47	11	151.49	3559	5.62	11971	95
NP05.42	High Himal.	1450	gneiss	83	38	40.6	28	32	53.9	Titre	25	0.87	20	92.9	2137	5.62	11971	96.53
NP05.43	Lesser Himal.	1480	quartzite	83	38	54.1	28	32	6.0	Suke Bagar	-	-	-	-	-	5.62	11971	-
NP05.44	Lesser Himal.	1130	quartzite	83	38	1.98	28	28	14.68	Mahabir	27	1.19	26	137.19	3002	5.62	11971	94.25
NP05.47	Lesser Himal.	840	sandstone	83	34	1.1	28	20	23.9	Beni	-	-	-	-	-	5.62	11971	-
NP05.48	Lesser Himal.	1170	quartzite	83	35	10.2	28	17	53.6	Baglung	-	-	-	-	-	5.62	11971	-
NP05.49	Lesser Himal.	800	Amphibolites	83	39	35.2	28	14	31.9	Lampata	-	-	-	-	-	5.62	11971	-

Lower Kali Gandaki Section

Sample	Struct. Unit	Elevation (m)	Roks	Long °	Long min	Long s	Lat °	Lat min	Lat s	Locality	N	ρs (x10^6 cm^{-2})	Ns	ρi (x10^6 cm^{-2})	Ni	ρd (x10^6 cm^{-2})	Nd	P(χ2) %
NP05.50	Lesser Himal.	1140	sandstone	83	54	12.7	28	11	16.3		18	4.04	45	157.99	1758	5.62	11971	97.95
NP05.51	Lesser Himal.	1010	quartzites	83	51	34.8	28	8	23.4		-	-	-	-	-	5.62	11971	-
NP05.52	Lesser Himal.	850	sandstone	83	51	56.2	28	5	41.2		-	-	-	-	-	5.62	11971	-
NP05.53	Lesser Himal.	740	sandstone	83	43	8.1	27	58	27.5	Andhi Khola	-	-	-	-	-	5.62	11971	-
NP05.61	Lesser Himal.	434	sandstone	83	32	20.4	27	46	4.9	hola / Top MB	-	-	-	-	-	5.62	11971	-

Langtang - Amlekhganj Section

Kakani Vertical Profil

Sample	Struct. Unit	Elevation (m)	Rocks	Long °	Long min	Long s	Lat °	Lat min	Lat s	Locality	N	ρs (x10⁶ cm⁻²)	Ns	ρi (x10⁶ cm⁻²)	Ni	ρd (x10⁶ cm⁻²)	Nd	P(χ2) %	D %	Age Ma	±1σ
NP05.06	Lesser Himal.	650	quartzite	85	8	50	27	55	12.1	Bidur	21	3.35	60	112.63	2015	6.00	9956	97.33	0	3.1	0.4
NP05.07	Lesser Himal.	674	sandstone	85	9	17	27	55	45.6	Simwutar	15	6.87	45	190	1244	5.62	11971	95.52	0	3.4	0.5
NP05.08	Lesser Himal.	739	sandstone	85	11	3.5	27	58	29.6	Betrawati	22	0.3	49	1.56	2884	6.00	9956	65.23	1	1.7	0.2
NP05.09	Lesser Himal.	1540	sandstone	85	20	39	28	10	3.6	Syabru Besi	21	0.58	12	49.6	1019	6.00	9956	90.16	1	1.2	0.4
NP05.10	Lesser Himal.	1621	gneiss	85	20	48	28	11	7.8	Wangal	23	1.86	42	71.67	1314	6.00	9956	79.62	2	2.7	0.4
NP05.11	High Himal.	1582	sandstone	85	21	15	28	12	11.8	Kagdinma	24	2.69	63	182.3	4265	6.00	9956	40.24	12	1.5	0.2
NP05.12	High Himal.	1600	quartzite	85	21	6.6	28	11	49	Lingling	25	1.59	39	190.27	4676	6.00	9956	0.26	76	0.9	0.2
NP05.13	High Himal.	1600	quartzite	85	20	54	28	11	23.6	Lingling	16	0.32	5	21.55	339	6.00	9956	14.86	1	1.5	0.7
NP05.14	Lesser Himal.	1833	quartzite	85	18	59	28	8	24.1	Thulo Barkhu	30	0.71	21	209.9	6190	6.00	9956	15.13	49	0.4	0.1
NP05.15	Lesser Himal.	1180	quartzite	85	12	10	27	59	33.5	Kalikasthan	21	3.92	81	140	2890	6.00	9956	80.74	0	2.9	0.3

Palung Section

Sample	Struct. Unit	Elevation (m)	Rocks	Long °	Long min	Long s	Lat °	Lat min	Lat s	Locality	N	ρs (x10⁶ cm⁻²)	Ns	ρi (x10⁶ cm⁻²)	Ni	ρd (x10⁶ cm⁻²)	Nd	P(χ2) %	D %	Age Ma	±1σ
NP05.17	Lesser Himal.	770	quartzite	85	7	38	27	44	8.1	Amarkhu	11	1.36	11	60.11	221	6.62	11971	95.04	0	2.1	1
NP05.18	Lesser Himal.	2027	sandstone	85	5	57	27	39	46.2	Tistung	18	3.17	43	172.47	2343	6.00	9956	99.89	0	1.9	0.3
NP05.20	Lesser Himal.	1935	granite	85	4	50	27	37	19.1	Palung	9	4.57	37	90.25	731	6.00	9956	90.3	0	4.7	0.8
NP05.21	Lesser Himal.	2360	granite	85	5	19	27	36	19.2	Daman	17	8.83	138	143.19	2238	6.00	9956	72.34	0	6.5	0.6
NP05.22	Lesser Himal.	2500	granite	85	5	3.8	27	35	27.6	Simbhanjang	22	19.73	419	287.15	6097	6.00	9956	84.13	0	7.2	0.4
NP05.23	Lesser Himal.	2190	granite	85	4	23	27	34	31.3		18	21.88	385	264.55	4655	6.00	9956	47.03	7	8.6	0.5
NP05.24	Lesser Himal.	1350	gneiss	85	2	54	27	33	4.4	Lamindanda	22	11.3	78	201.29	1389	6.00	9956	81.44	1	5.9	0.7
NP05.25	Lesser Himal.	611	diorite	85	2	37	27	29	30.7		-	-	-	-	-	6.00	9956	-	-	NON datable	
NP05.26	Lesser Himal.	530	schistes	85	2	31	27	28	34.4	Hetauda	-	-	-	-	-	6.00	9956	-	-	NON datable	

Hetauda Section (Detrital thermochronology)

Sample	Struct. Unit	Elevation (m)	Rocks	Long °	Long min	Long s	Lat °	Lat min	Lat s	Locality	N	ρs (x10⁶ cm⁻²)	Ns	ρi (x10⁶ cm⁻²)	Ni	ρd (x10⁶ cm⁻²)	Nd	P(χ2) %	D %	Age Ma	±1σ
NP05.27	Siwalik	510	sandstone	85	1	34	27	23	41.5		-	-	-	-	-	6.00	9956	-	-	NON datable	
NP05.28	Siwalik	330	sandstone	84	59	55	27	16	56.2	Amlekhganj	90	5.51	362	95.7	6284	5.62	11971	4.48	24	5.4	0.4

Gosaikung vertical section

Sample	Struct. Unit	Elevation (m)	Rocks	Long °	Long min	Long s	Lat °	Lat min	Lat s	Locality	N	ρs (x10⁶ cm⁻²)	Ns	ρi (x10⁶ cm⁻²)	Ni	ρd (x10⁶ cm⁻²)	Nd	P(χ2) %	D %	Age Ma	±1σ
T6	Lesser Himal.	1825	quartzite	85	12	32	28	0	47.3	Bhaleydanda	16	1.78	25	125.63	1766	5.93	12513	94.6	0	1.4	0.3
T7	Lesser Himal.	2000		85	13	25	28	3	57.5	Grang	19	2.22	37	158.79	2641	5.93	12513	96.65	0	1.4	0.2
T9	Lesser Himal.	1780	quartzite	85	18	50	28	6	34.7	Dunche	16	1.73	17	124.87	1225	5.93	12513	95.43	0	1.4	0.3
T10	Lesser Himal.	2540	schiste	85	19	35	28	6	11.2	Deurali	17	2.21	29	131.56	1729	5.93	12513	84.35	0	1.6	0.3
T11	Lesser Himal.	2960	gneiss	85	19	53	28	6	26.4	Dimsa	14	1.02	12	71.97	849	5.93	12513	95.92	0	1.4	0.4
T13	High Himal.	3640	gneiss	85	20	53	28	6	27.4	Cholangpati	18	1.74	29	117.4	1955	5.67	12016	97.05	0	1.4	0.3
T14	High Himal.	4500	gneiss	85	24	33	28	5	4.4	Gosaikund	21	1.03	19	49.57	916	5.67	12016	92.02	0	1.9	0.5
T15	High Himal.	4260	gneiss	85	23	47	28	5	7.5	holangpati Dac	18	1.58	26	57.57	945	5.67	12016	67.01	0	2.6	0.5
T17	High Himal.	3260	gneiss	85	22	16	28	6	29.1	Cholangpati	16	2.11	33	109.28	1708	5.67	12016	98.45	0	1.8	0.3

Table 1.

Inversion	TF1	TF2	TF3	TF4	GEO1	GEO2	Bhu01
Area	Langtang	Langtang	Langtang	Langtang	Annapurnas	Annapurnas	Bhutan
No of models	10100	2550	2550	2550	2050	410	328
Best misfit	1	0.7	0.7	0.7	0..7	0.6	0.6
***T_0* (°C)**	***1100***	850	850	850	850	***1300***	***714***
Q	***2.5***	1.5	1.5	1.5	1.5	***2.6***	***3.9***
grad(T) (°C/km)	63	35	35	35	35	70	52
***V_0* (km/My)**	-6	-6	-8	-8	-6	-6	-6
O.o.S. timing	2 - 0	2 - 0	2 - 0	4 - 0	/	/	/
***V_{TF}* (km/My)**	***-4.2***	***-0.2***	***-7.8***	***0***	***0***	/	/
***X4* (km)**	***80***	***80***	***85***	***80***	***110***	***97***	***117***
***Y4* (km)**	***-9***	***-9***	***-14***	***-3.5***	***-3***	***-5***	***-7***
***X5* (km)**	***129***	***150***	***150***	***150***	***150***	***140***	***147***
***Y5* (km)**	***-17***	***-28***	***-27***	***-27***	***-30***	***-23***	***-17***
Flat dip (°)	***6.2***	***6.2***	***11.0***	***1.0***	***0.3***	***2.0***	***5***
Ramp dip (°)	***9***	***20***	***11***	***19***	***34***	***21***	***7***

Table 2.

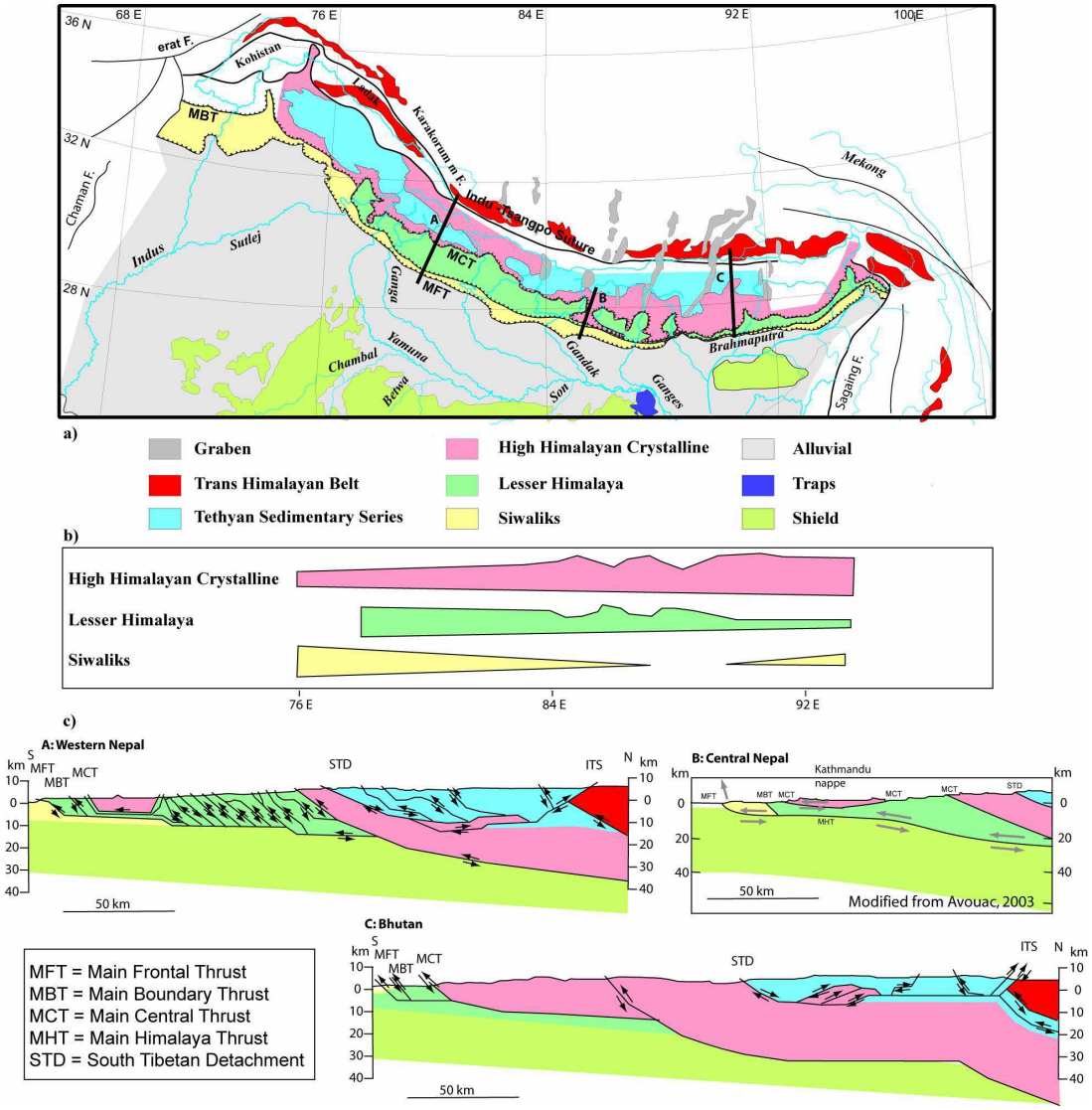
36 N
68 E
76 E
84 E
92 E
100E
32 N
28 N
erat F.
Kohistan
Ladakh
Karakoram m F.
Indus-Tsangpo Suture
MBT
Chaman F.
Indus
Sutlej
Ganga
MCT
MFT
A
B
C
Mekong
Brahmaputra
Yamuna
Chambal
Betwa
Son
Gandak
Ganges
Sagaing F.
a)
Graben
Trans Himalayan Belt
Tethyan Sedimentary Series
High Himalayan Crystalline
Lesser Himalaya
Siwaliks
Alluvial
Traps
Shield
b)
High Himalayan Crystalline
Lesser Himalaya
Siwaliks
76 E
84 E
92 E
c)
A: Western Nepal
S
MFT
MBT
MCT
STD
ITS
N
km
50 km
B: Central Nepal
Kathmandu
nappe
MFT
MBT
MCT
MHT
STD
Modified from Avouac, 2003
C: Bhutan
MFT = Main Frontal Thrust
MBT = Main Boundary Thrust
MCT = Main Central Thrust
MHT = Main Himalaya Thrust
STD = South Tibetan Detachment

Figure 1.

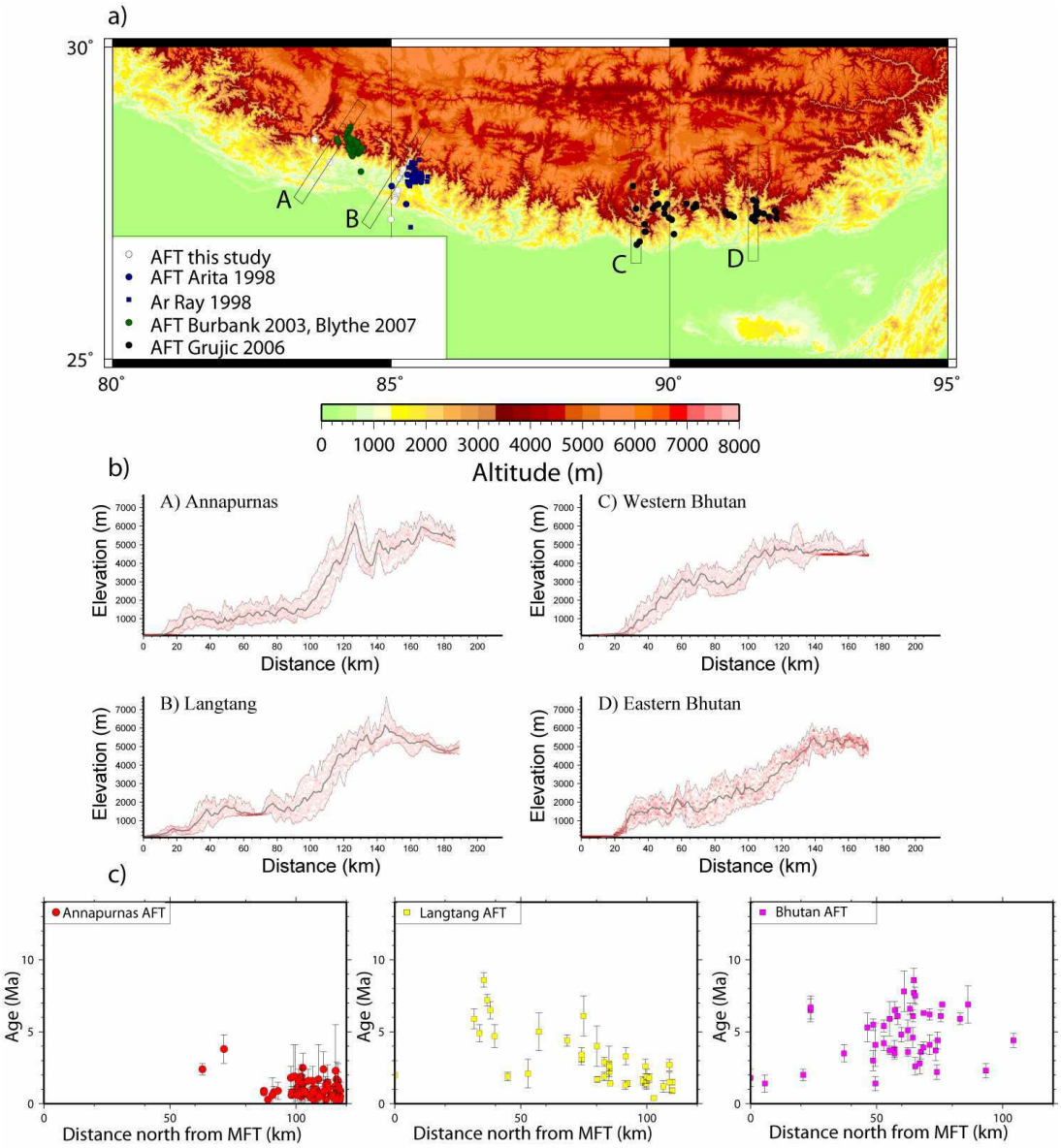
a)
30°
25°
80°
85°
90°
95°
A
B
C
D
AFT this study
AFT Arita 1998
Ar Ray 1998
AFT Burbank 2003, Blythe 2007
AFT Grujic 2006
0 1000 2000 3000 4000 5000 6000 7000 8000
Altitude (m)
b)
A) Annapurnas
C) Western Bhutan
B) Langtang
D) Eastern Bhutan
Elevation (m)
Distance (km)
c)
Annapurnas AFT
Langtang AFT
Bhutan AFT
Age (Ma)
Distance north from MFT (km)

Figure 2.

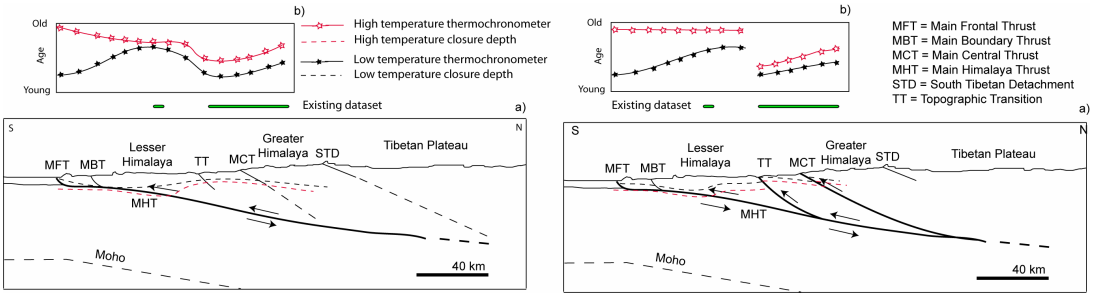
b)
Old
Age
Young
High temperature thermochronometer
High temperature closure depth
Low temperature thermochronometer
Low temperature closure depth
Existing dataset
a)
S
N
MFT
MBT
Lesser Himalaya
TT
MCT
Greater Himalaya
STD
Tibetan Plateau
MHT
Moho
40 km
MFT = Main Frontal Thrust
MBT = Main Boundary Thrust
MCT = Main Central Thrust
MHT = Main Himalaya Thrust
STD = South Tibetan Detachment
TT = Topographic Transition

Figure 3.

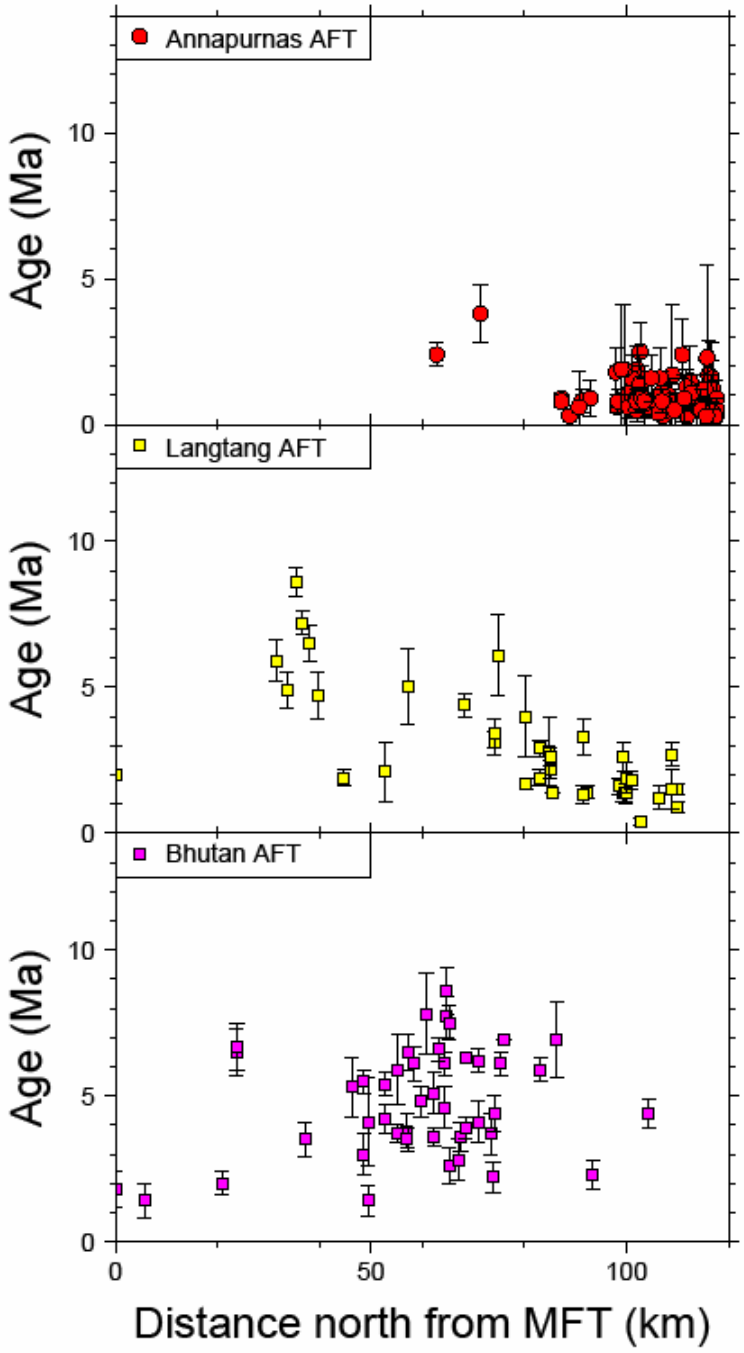
Annapurnas AFT
Langtang AFT
Bhutan AFT
Age (Ma)
Age (Ma)
Age (Ma)
0
5
10
0
50
100
Distance north from MFT (km)

Figure 4.

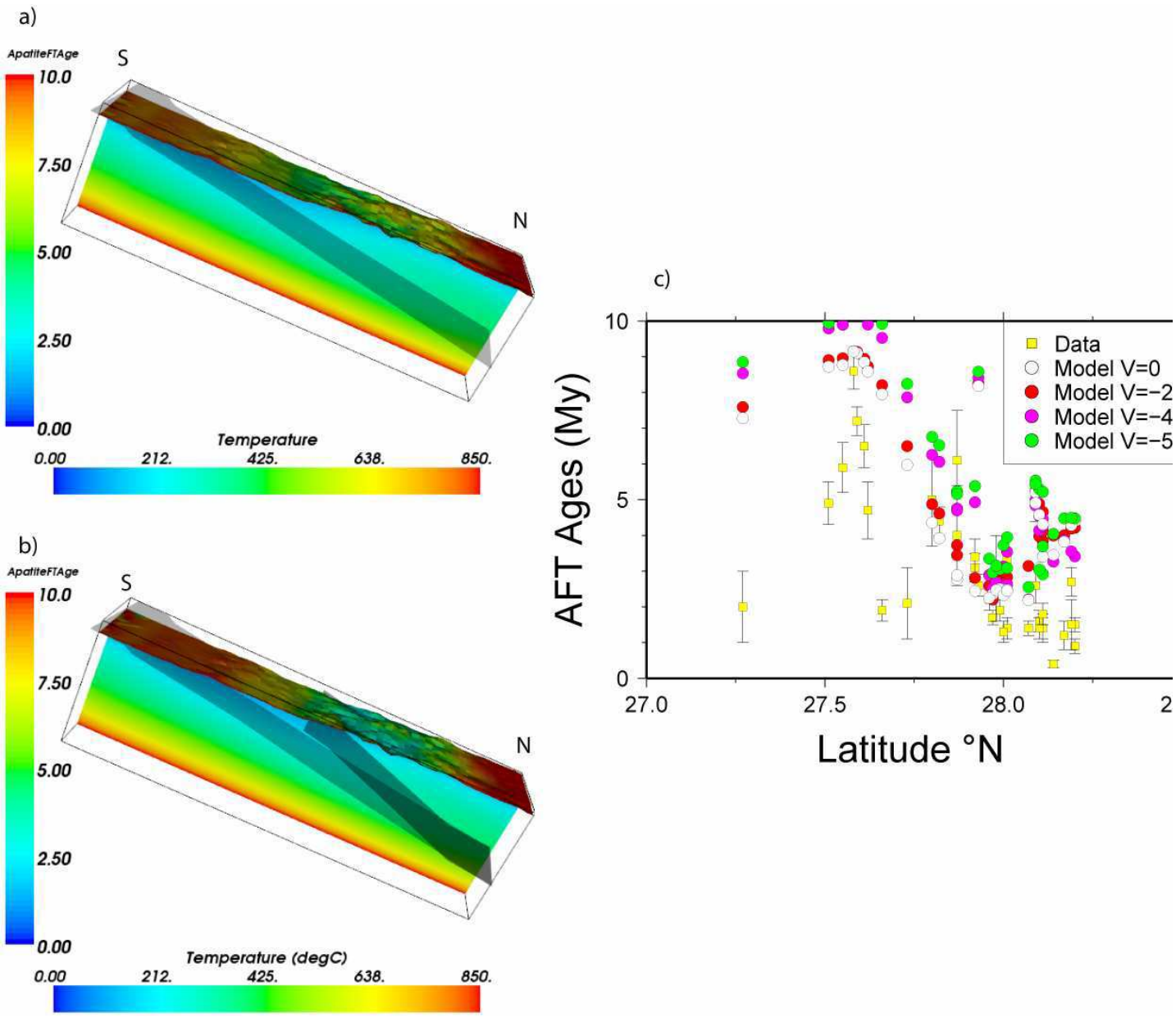
a)
ApatiteFTAge
10.0
7.50
5.00
2.50
0.00
S
N
Temperature
0.00
212.
425.
638.
850.
b)
ApatiteFTAge
10.0
7.50
5.00
2.50
0.00
S
N
Temperature (degC)
0.00
212.
425.
638.
850.
c)
AFT Ages (My)
10
5
0
27.0
27.5
28.0
Latitude °N
Data
Model V=0
Model V=−2
Model V=−4
Model V=−5

Figure 5.

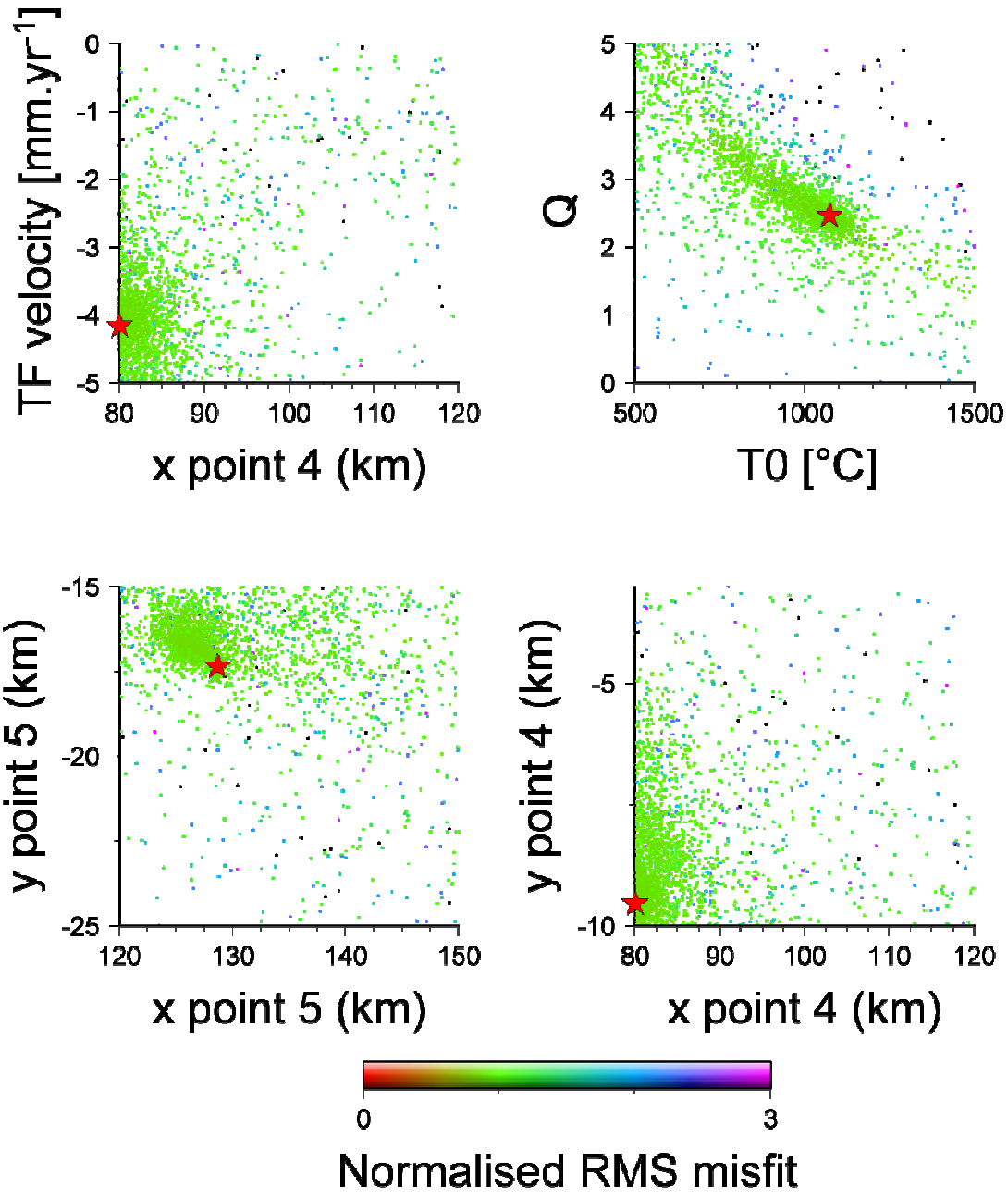
TF velocity [mm.yr-1]
0
-1
-2
-3
-4
-5
80
90
100
110
120
x point 4 (km)
Q
5
4
3
2
1
0
500
1000
1500
T0 [°C]
y point 5 (km)
-15
-20
-25
120
130
140
150
x point 5 (km)
y point 4 (km)
-5
-10
80
90
100
110
120
x point 4 (km)
0
3
Normalised RMS misfit

Figure 6.

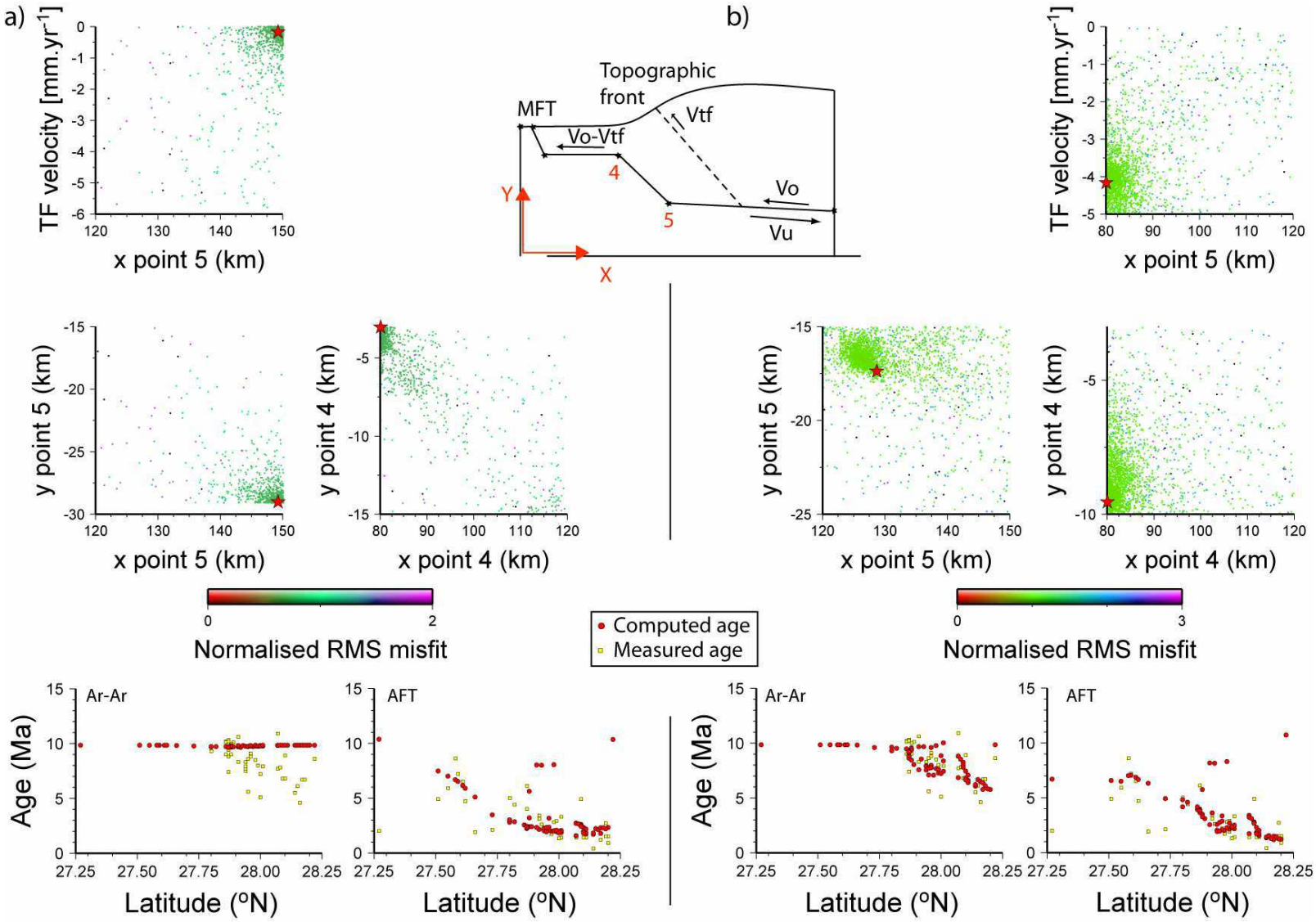
a)
b)
TF velocity [mm.yr-1]
x point 5 (km)
Topographic front
MFT
Vtf
Vo-Vtf
4
5
Vo
Vu
Y
X
y point 5 (km)
y point 4 (km)
x point 4 (km)
Normalised RMS misfit
Computed age
Measured age
Ar-Ar
AFT
Age (Ma)
Latitude (°N)

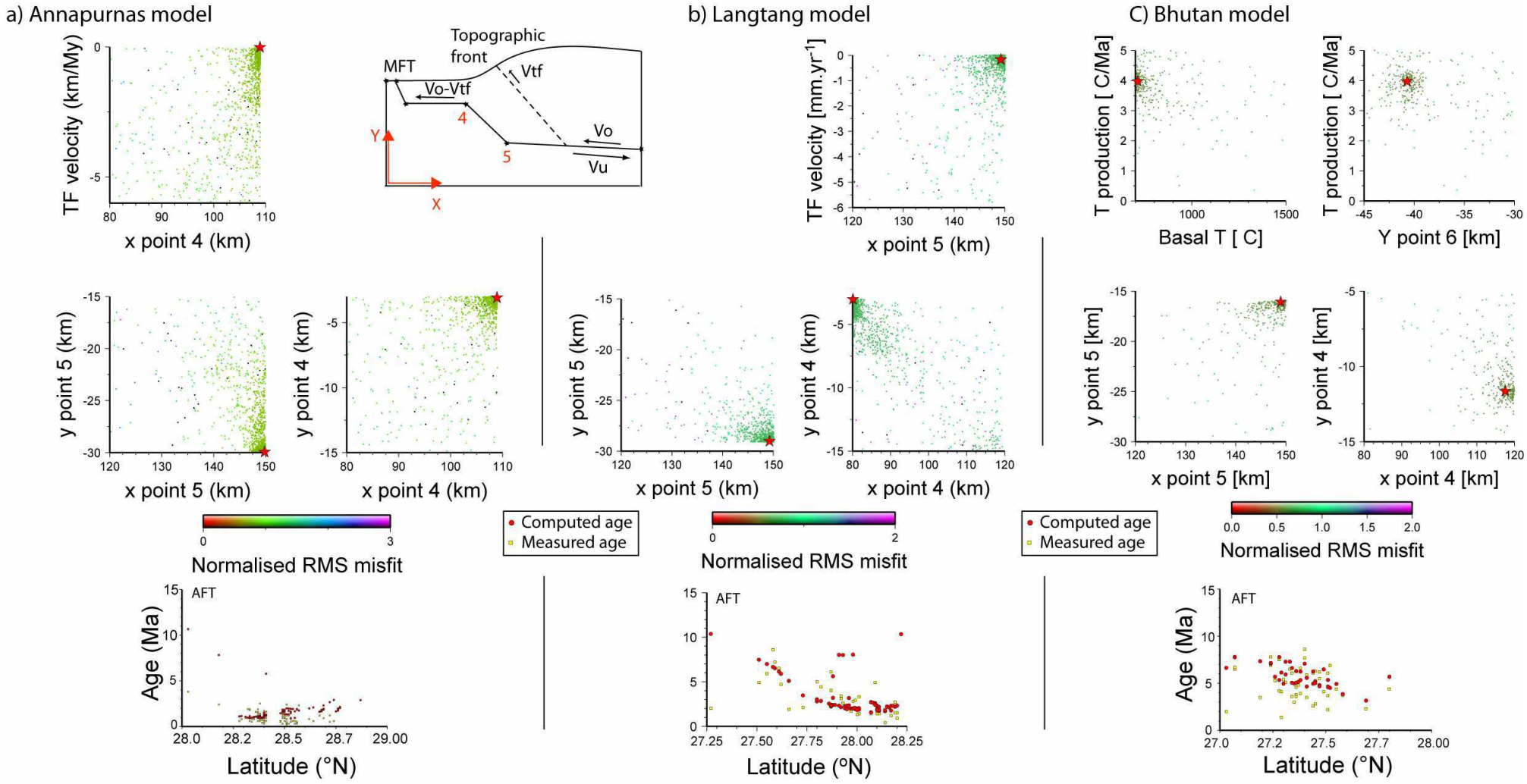
a) Annapurnas model
b) Langtang model
C) Bhutan model
TF velocity (km/My)
x point 4 (km)
Topographic front
MFT
Vtf
Vo-Vtf
Vo
Vu
4
5
Y
X
TF velocity [mm.yr-1]
x point 5 (km)
T production [C/Ma]
Basal T [C]
Y point 6 [km]
y point 5 (km)
x point 5 (km)
y point 4 (km)
x point 4 (km)
y point 5 [km]
x point 5 [km]
y point 4 [km]
x point 4 [km]
Computed age
Measured age
Normalised RMS misfit
AFT
Age (Ma)
Latitude (°N)
West
Est

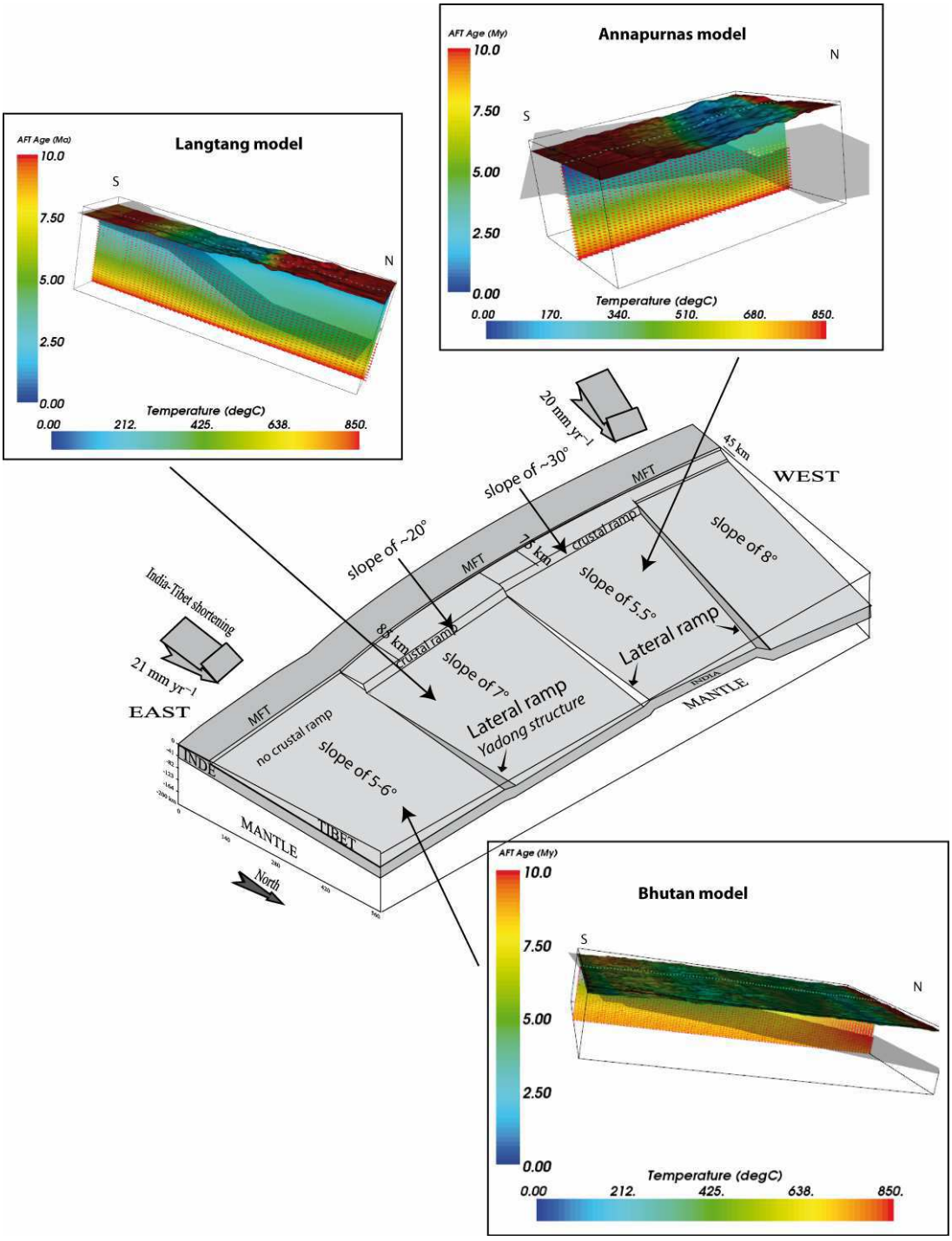
Annapurnas model
AFT Age (My)
10.0
7.50
5.00
2.50
0.00
S
N
Temperature (degC)
0.00
170.
340.
510.
680.
850.
Langtang model
AFT Age (Ma)
10.0
7.50
5.00
2.50
0.00
S
N
Temperature (degC)
0.00
212.
425.
638.
850.
20 mm yr⁻¹
slope of ~30°
45 km
WEST
MFT
slope of ~20°
MFT
26 km
crustal ramp
slope of 8°
slope of 5.5°
Lateral ramp
India-Tibet shortening
21 mm yr⁻¹
EAST
85 km
crustal ramp
slope of 7°
Lateral ramp
Yadong structure
MFT
no crustal ramp
slope of 5-6°
INDIA
MANTLE
MANTLE
TIBET
North
Bhutan model
AFT Age (My)
10.0
7.50
5.00
2.50
0.00
S
N
Temperature (degC)
0.00
212.
425.
638.
850.

Figure 9.

Transition

Cette méthodologie (thermochronologie de basses températures couplée à des modèles numériques) permet d'appuyer des modèles cinématiques cohérents sur l'ensemble de l'orogène. Nous avons travaillé ici sur des données issues de roches plutoniques ou sédimentaires métamorphisées. Comme pour la partie précédente, l'histoire thermique et donc cinématique de ces objets ne peut être contrainte que pour la dernière phase de leur histoire. Mais ils permettent de montrer la variation latérale de la géométrie des failles crustales en Himalaya, et d'expliquer de nombreuses observations et/ou résultats thermochronologiques, climatiques, érosifs et topographiques.

En revanche, la mise en œuvre de cette technique diffère si l'on travaille sur des roches sédimentaires non recuites totalement. C'est le cas des grès des Siwaliks, situés entre le MFT et le MDT. Ces données permettent d'obtenir des informations à la fois sur l'histoire de la source et sur l'histoire récente des chevauchements frontaux en Himalaya.

Cinématique récente du Main Frontal Thrust et variations latérales

5

Sommaire

Dans ce chapitre, nous présentons les résultats analytiques et numériques sur le front de la chaîne (MFT et prisme des Siwaliks) que nous discuterons en termes de variations latérales cinématiques, géométriques ou érosives pour la période la plus récente.

This chapter presents analytical and numerical results from the front of the orogen (MFT and Siwaliks prism). We discuss these in terms of lateral variations of kinetics, geometry or erosion for the most recent history of the orogen.

5.1 Méthodologie

En Himalaya, les études précédentes sur les Siwaliks et le MFT ont principalement été effectuées au Népal de l'ouest (Mugnier et al. 1999; 2004, Huyghe et al. 2005, van der Beek et al. 2006). Dans le chapître 1, nous avons montré que le MFT est branché sur le MHT. Nous avons mis en évidence les variations de structure du MHT le long de la chaîne dans le chapître 4. Peut-on reporter ces variations latérales à la structure et au fonctionnement du MFT ?

Cette étude, en partie publiée dans van der Beek et al. (2006) a été effectuée pour étudier :

1. l'histoire tectonique - érosive - climatique des sources des sédiments Siwaliks du Népal de l'ouest,
2. dater puis reconstruire l'initiation du MFT ainsi que son activité.

Pour cela, plusieurs coupes ont été effectuées au Népal dans les séries Siwaliks. Les coupes échantillonnées au Népal sont celles de la Tinau Khola, de la Surai Khola, et de la Karnali River (Fig. 5.1), à partir du MFT jusqu'au chevauchement intra-siwaliks, le Main Dun Thrust (MDT) (Fig. 5.2). Les échantillons ont été prélevés dans les bancs gréseux avec un pas de temps de 1 *Ma* dans la section sédimentaire. Ces prélèvements ont été étroitement calés par rapport à des études magnétostratigraphiques antérieures (Appel et al. (1991), Gautam et Rösler (1999) et De Celles et (inpress) pour Tinau et la Surai Khola, et Gautam et Fujiwara (2000) pour la Karnali River) en échantillonnant à proximité de trous référencés pour la magnétostratigraphie. Au cours de la mission 2005, nous avons aussi prélevé quelques échantillons dans les grès des Siwaliks inférieurs et moyens au sud d'Hetauda au Népal que j'ai traités au cours de ma thèse. Malheureusement, pour des raisons de qualité médiocre des minéraux et d'une quantité d'apatite insuffisante, une seule datation (NP05.28) a pu être menée à terme (Tab. 5.1).

Dans la suite, nous utilisons comme référence commune de profondeurs, la profondeur stratigraphique. Comme aucune des séquences sédimentaires n'est continue jusqu'à aujourd'hui, la profondeur maximale atteinte par chaque échantillon est assez mal contrainte. Les sédiments les plus jeunes des Siwaliks supérieurs de la Surai Khola sont estimés à 1.0 ± 0.5 *Ma* et sont recouverts par quelques centaines de

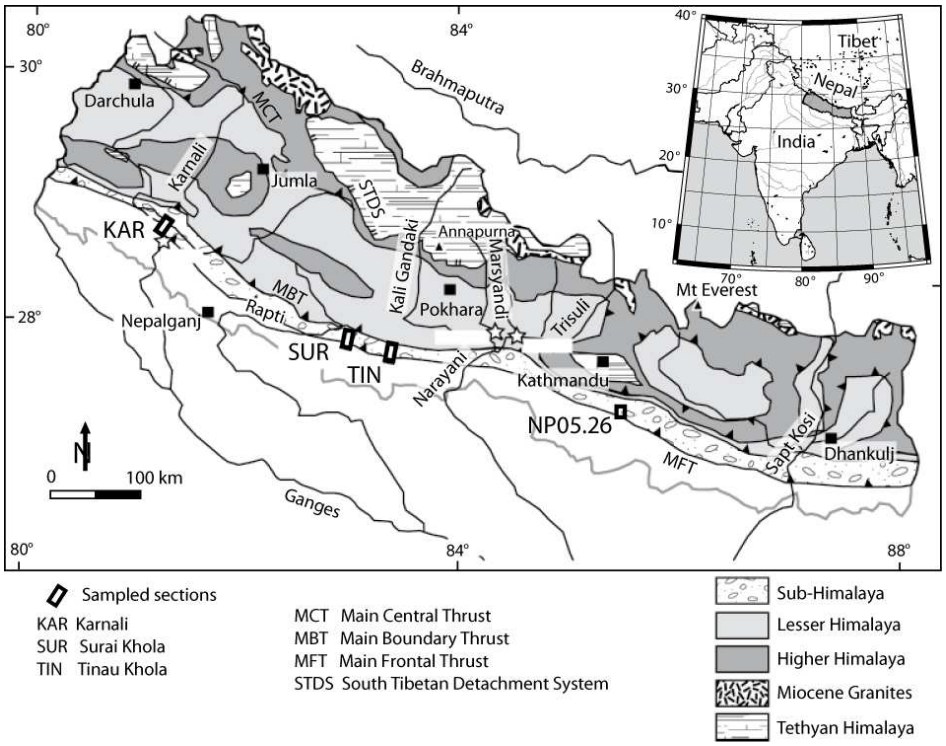

FIG. 5.1 – *Localisation sur une carte géologique simplifiée du Népal des coupes et des données AFT obtenues dans les Siwaliks au Népal. Les données utilisées proviennent des mesures effectuées au Laboratoire de Géodynamique des Chaînes Alpines, publiées en grande partie dans van der Beek et al. (2006) ; modifié d'après van der Beek et al. (2006).*

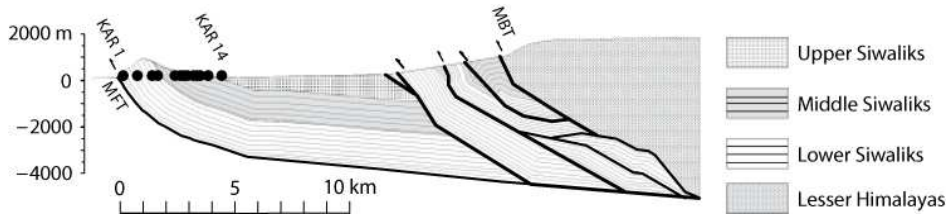

FIG. 5.2 – *Coupe équilibrée de la Karnali River montrant la localisation des échantillons et la relation avec la structure tectonique locale ; modifié d'après Mugnier et al. (1999), van der Beek et al. (2006).*

Echantillon	Age s. (Ma)	prof. s. (m)	N	Age central ($Ma \pm 2\sigma$)	P1 $\pm 2\sigma$ (Ma)	P2 $\pm 2\sigma$ (Ma)	P3 $\pm 2\sigma$ (Ma)
				Karnali River			
KAR14	2.8 ± 0.3	925	41	6.0 ± 1.0	5.0 ± 1.1 (74)	8.2 ± 4.3 (22)	14.1 ± 14.1 (4)
KA30	4.3 ± 0.2	1420	41	7.4 ± 1.2	5.9 ± 1.3 (65)	10.2 ± 2.3 (35)	
KAR13	5.2 ± 0.1	1720	16	9.0 ± 2.2	7.1 ± 1.7 (76)	14.4 ± 4.5 (24)	
KAR12	6.0 ± 0.1	1950	44	8.9 ± 1.2	7.9 ± 1.3 (79)	13.3 ± 6.0 (21)	
KA34	6.4 ± 0.1	2070	63	9.5 ± 1.0	3.6 ± 2.2 (9)	9.6 ± 1.7 (81)	13.9 ± 19.5 (10)
KAR10	8.1 ± 0.1	2630	59	6.9 ± 0.8	6.5 ± 0.8 (98)	23.8 ± 29.0 (2)	
KAR9	9.0 ± 0.1	2915	49	10.1 ± 1.2	9.9 ± 1.0 (97)	21.6 ± 36.8 (3)	
KAR7	10.9 ± 0.1	3710	56	8.5 ± 1.0	5.1 ± 2.6 (20)	9.3 ± 1.3 (80)	
KAR6	12.1 ± 0.1	3980	48	8.2 ± 1.4	$\mathbf{2.1 \pm 1.8}$ (13)	9.0 ± 1.3 (87)	
KAR3	14.1 ± 0.1	4650	51	4.0 ± 1.0	$\mathbf{1.8 \pm 1.3}$ (43)	5.2 ± 1.8 (54)	17.2 ± 24.2 (3)
KA441	15.9 ± 0.1	5265	44	4.0 ± 1.0	$\mathbf{2.4 \pm 0.4}$ (82)	11.8 ± 2.0 (18)	
KAR1	15.9 ± 0.1	5280	81	5.7 ± 2.2	$\mathbf{2.4} \pm 0.4$ (58)	11.0 ± 6.9 (38)	25.8 ± 71.8 (4)
KA441+KAR1	15.9 ± 0.1	5280	81		$\mathbf{2.4 \pm 0.4}$ (75)	12.0 ± 2.1 (23)	19.2 ± 57.5 (2)
				Tinau Khola			
TIN8	7.2 ± 0.2	2504	54	11.2 ± 1.8	10.5 ± 1.8 (92)	19.3 ± 9.5 (8)	
BUT4	9.1 ± 0.1	2811	29	6.5 ± 0.8	2.3 ± 1.2 (6)	7.0 ± 0.7 (94)	
BUT3	10.3 ± 0.2	3343	29	6.0 ± 1.2	5.5 ± 0.6 (96)	34.9 ± 31.5 (4)	32.3 ± 32.3 (2)
BUT3+TIN5	10.3 ± 0.2	3343	77		3.4 ± 1.2 (32)	6.9 ± 1.2 (67)	
TA181	11.0 ± 0.1	3694	39	6.1 ± 1.6	6.3 ± 1.5 (92)	14.7 ± 6.3 (8)	
TA17	11.3 ± 0.2	3810	34	6.0 ± 1.0	5.4 ± 1.2 (83)	9.0 ± 5.9 (17)	
BUT1	12.0 ± 0.3	3976	9	4.5 ± 1.6	3.5 ± 1.1 (88)	13.4 ± 21.5 (12)	
BUT1+TIN1	12.0 ± 0.3	3976	33	9.1 ± 2.8	$\mathbf{2.5 \pm 0.7}$ (13)	6.9 ± 2.0 (83)	31.6 ± 29.7 (4)
				Hetauda			
NP05.28	$\sim 11 - 12$	~ 2900	90	5.4 ± 0.4	$\mathbf{2.0 \pm 1}$ (8)	5.5 ± 0.5 (90)	20.2 ± 6.5 (2)

TAB. 5.1 – *Datations AFT pour les échantillons des Siwaliks, et résultats de la décomposition en différentes populations d'âges ; Age S., âge stratigraphique ; Prof. s., profondeur stratigraphique ; N, nombre de grains comptés ; populations d'âges P1-P3 : les nombres entre parenthèses donnent la pourcentage de grains pour chaque pic ; Toutes les datations sauf l'échantillon NP05.28 ont été effectuées par E. Labrin au Laboratoire de Géodynamique des Chaînes Alpines et sont publiées dans van der Beek et al. (2006) ; J'ai daté l'échantillon NP05.28.*

mètres de conglomérats. Dans la coupe de la Karnali, l'épaisseur minimale estimée des sédiments des séries moyennes et supérieures recouvrant la coupe datée par magnétostratigraphie est de l'ordre de 1500 m. Mais dans les deux cas, les Siwaliks supérieurs sont clairement syntectoniques (Mugnier et al. 2004, Huyghe et al. 2005) et leur épaisseur varie fortement latéralement. Comme la coupe de la Tinau Khola se termine contre un chevauchement interne, il n'est pas possible d'estimer l'épaisseur des sédiments sus-jacents. van der Beek et al. (2006) estiment la profondeur stratigraphique maximale en extrapolant le taux de sédimentation calculé à partir des données magnétostratigraphiques (Fig. 5.3). Cette approche tend à surestimer la profondeur maximale atteinte par les échantillons en minimisant l'âge de l'arrêt de la sédimentation au niveau des coupes effectuées. En revanche, les courbes âges stratigraphiques / profondeurs obtenues sont cohérentes entre elles.

L'ensemble des données thermochronologiques concernant les Siwaliks sont des données portant sur des roches sédimentaires. Il est donc nécessaire de bien discriminer les informations des sources et celles concernant la cinématique du MFT, en mettant en évidence différentes populations d'âges (voir chapître 2). Pour augmenter la résolution des inversions effectuées à partir d'AFTsolve (Ketcham et al. 2000), j'ai mesuré les longueurs et les largeurs des traces de différents échantillons de la Karnali River (Tab. 5.2, Fig. 5.4 et Robert (2005)).

5.2 Initiation et cinématique du Main Frontal Thrust

5.2.1 Initiation du MFT au Népal de l'Ouest

Les âges centraux de la Karnali River, de la Surai Khola et de la Tinau Khola sont présentés en Fig. 5.3. La combinaison des trois coupes montrent une cohérence dans la transition de non-recuit à recuit des échantillons, qui se situe entre 2500 et 2800 m de profondeur. Cettte transition correpond à l'entrée des échantillons dans la zone de recuit partiel (PAZ). Ces températures sont cohérentes avec les valeurs de réflectance de la vitrinite provenant d'un nombre limité d'échantillons de la partie supérieure de la Karnali River (L. Martinez, communication personnelle, 2003) qui suggèrent une température de 62 et 75°C à une profondeur entre 1700 et 2600 m. Mugnier et al. (1995) publient des valeurs de réflectance de la vitrinite de $0.3 - 0.5$ %

Echantillon	MTL $\pm 1\sigma$ (μm)	S. d. (μm)	N	D_{par} (μm)	S. d. (μm)
Karnali River					
KAR14	11.7 ± 0.3	2.0	84	1.7	0.4
KAR13				1.7	0.3
KAR12	11.0 ± 0.3	2.9	75	1.6	0.3
KAR11	11.3 ± 0.3	2.6	78	1.6	0.3
KAR10	12.1 ± 0.2	2.0	68	1.8	0.3
KAR9	11.2 ± 0.3	2.5	54	1.3	0.4
KAR7	10.7 ± 0.2	2.1	80	1.6	0.4
KAR6	9.4 ± 0.3	1.9	51	1.2	0.3
KAR3	9.5 ± 0.3	1.9	36	1.5	0.4
Tinau Khola					
TIN8	10.9 ± 0.2	1.6	100		

TAB. 5.2 – *Mesures de longueurs et de D_{par} sur les échantillons des sédiments Siwaliks ; MTL, longueur moyenne des traces ; N, nombre de traces confinées horizontales utilisées pour la mesure de longueurs ; S. d., écart type (standard deviation) ; D_{par}, largeurs des traces parallèles à l'axe C ; pour chaque échantillon, 100 mesures de largeurs ont été effectuées ; j'ai effectué ces mesures, publiées dans van der Beek et al. (2006).*

pour les Siwaliks moyens et de $0.6 - 1.0\%$ pour les Siwaliks inférieurs du Népal de l'ouest, ce qui correspond respectivement à des températures d'enfouissement de $60 - 90°C$ et $\geq 100°C$. Huyghe et al. (2005) donnent aussi une estimation de la température d'enfouissement dans la coupe de la Karnali à partir de la cristallinité de l'illite de $70 - 95°C$ pour les profondeurs $\geq 2100\ m$. Ces différentes estimations indiquent un gradient thermique de $18 - 24°C.km^{-1}$, en prenant une température moyenne à la surface de $20°C$, ce qui est en accord avec les mesures de température en forage dans les Siwaliks de l'ouest de l'Inde (Agarwal et al. 1994). Nos extrapolations à partir des estimations de profondeurs stratigraphiques apparaissent donc raisonnables.

Les échantillons profonds, partiellement recuits, ont enregistré le recuit sédimentaire et l'histoire de l'exhumation des Siwaliks, directement liée à la cinématique du front de déformation actuel himalayen. Les âges AFT minima des quatre plus profonds échantillons de la Karnali (KAR6, KAR3, KAR441, KAR1), les deux âges les plus profonds de la Tinau Khola (BUT1, TIN1) sont tous proches

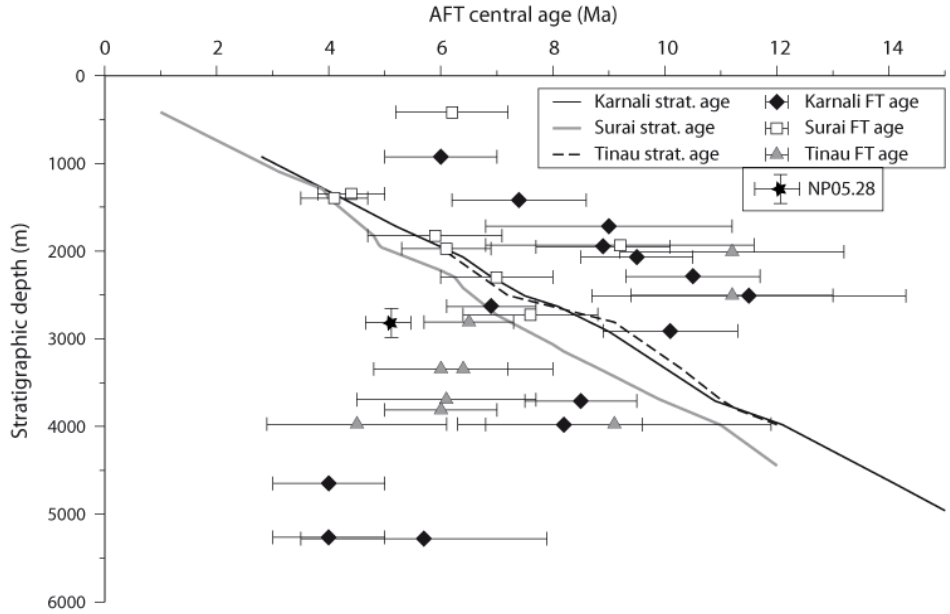

FIG. 5.3 – *Ages centraux AFT $\pm 2\sigma$ en fonction de la profondeur des échantillons pour les coupes de la Karnali River, de la Surai Khola et de la Tinau Khola. Les âges stratigraphiques des trois coupes proviennent de Gautam et Fujiwara (2000) pour la Karnali et de T.P. Ohja (communication personnelle, 2003) pour les deux autres ; d'après van der Beek et al. (2006).*

de 2.1 ± 0.4 *Ma* (voir Tab. 5.1 et Fig. 5.4), ce qui suggère une exhumation liée à l'activité du MFT aux alentours de cette date.

De manière à mieux contraindre l'histoire de l'exhumation, nous (van der Beek et al. 2006) avons inversé les données longueurs de traces de fission de la Karnali River en utilisant le code AFTsolve (Ketcham et al. 2000). Nous devons considérer les résultats des inversions en terme d'histoires thermiques avec précaution. En effet, la relative courte longueur des traces des échantillons non-recuits indiquent que l'histoire de l'exhumation au niveau de la source est relativement complexe (Tab 5.1 ou Fig. 5.4) et qu'elle doit être prise en compte pour la modélisation de l'histoire post-dépôt de l'échantillon (Carter et Gallagher 2004). Ensuite, le nombre de traces dont il est possible de mesurer la longueur dans chaque échantillon est faible, ce qui diminue le niveau de résolution pour contraindre la prédiction de l'histoire thermique. Et dernièrement, nous avons étudié des échantillons partiellement recuits caractérisés par une gamme de longueurs de traces importante, qui signent une histoire pré-dépôt, ou une résistance au recuit variables.

Dans l'approche de Ketcham et al. (2000), il est possible de définir des populations multicinétiques. De plus, pour des échantillons détritiques, les modélisations

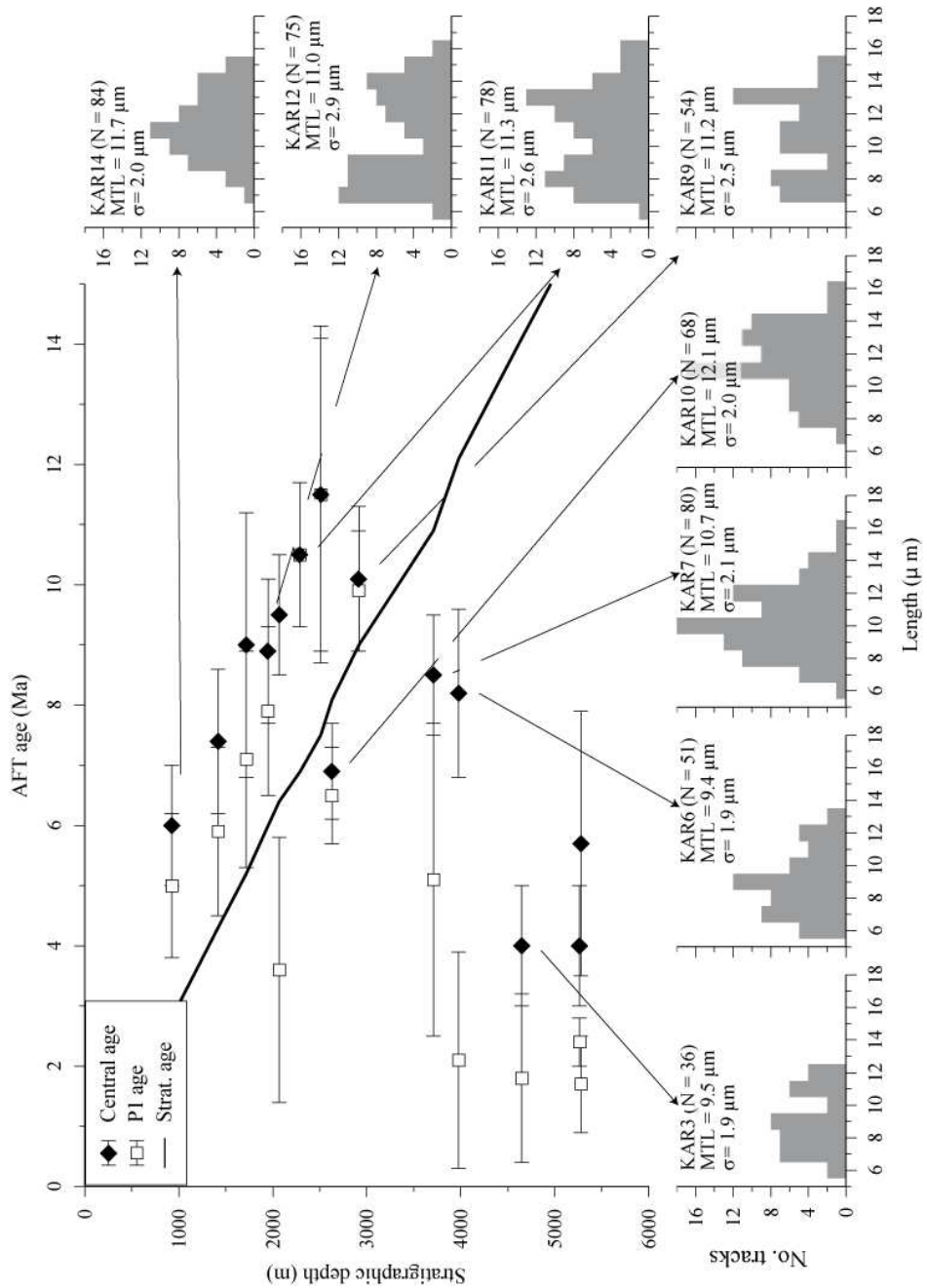

FIG. 5.4 – *Ages AFT (âges centraux et âges de la population la plus jeune, P1) en fonction de la profondeur et associés aux histogrammes de longueurs de traces respectifs (N, nombre de longueurs mesurées ; MTL, longueur de trace moyenne ; σ, standard déviation) pour la coupe de la Karnali River ; d'après van der Beek et al. (2006).*

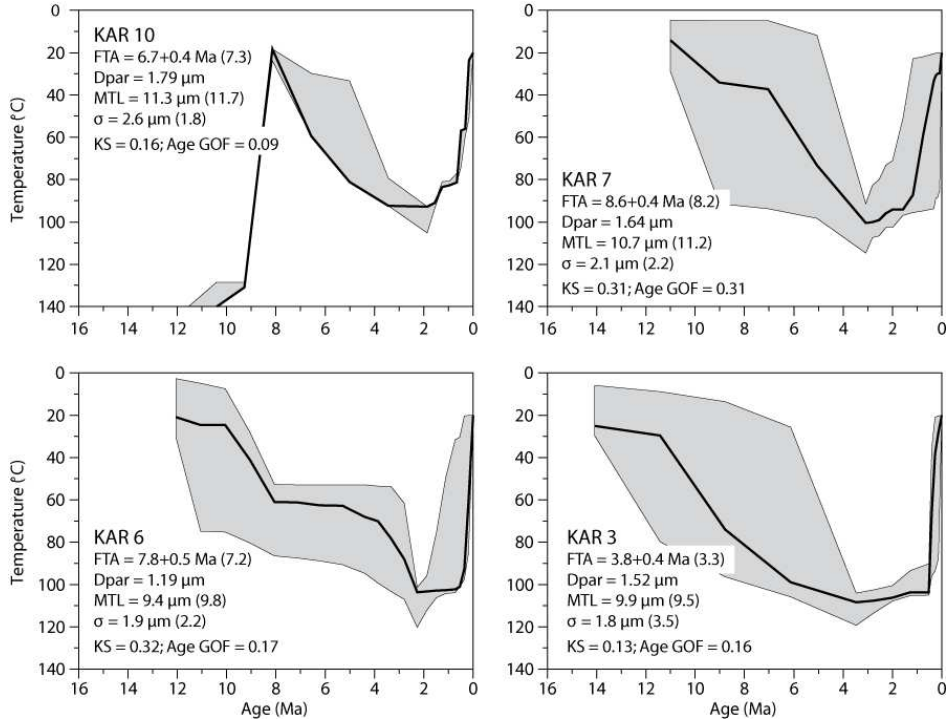

FIG. 5.5 – *Histoires thermiques représentatives des échantillons partiellement recuits de la coupe de la Karnali River. La ligne noire en train plein représente le meilleur modèle, et l'aire grisée correspond à l'ensemble des modèles acceptables. Pour chaque échantillon, la légende donne l'âge AFT mesuré, les longueurs de traces mesurées (MTL), la déviation standard de la distribution des longueurs de traces (σ), comparés avec les valeurs calculées associées pour le meilleur modèle entre parenthèses, ainsi que la valeur de D_{par} utilisée. Chaque inversion est basée sur un tirage aléatoire de 10 000 modèles sur une plage de valeurs contraintes (Ketcham et al. 2000). Le test statistique KS permet la comparaison des distributions observées et calculées, le GOF (Goodness Of Fit) analogue au test KS donne un indice de comparaison entre l'âge AFT calculé et mesuré. Pour des raisons de clarté, les chemins temps - températures pre-dépôt des échantillons KAR3, KAR6 et KAR7 n'ont pas été représentés ; d'après van der Beek et al. (2006).*

thermiques devraient être idéalement effectuées sur une seule population pour caractériser une et une seule phase de l'histoire thermique (Carrapa et al. 2006). Mais comme nous travaillons avec peu de mesures de longueurs de traces, nous nous abstenons de séparer nos mesures en fonction des groupes d'âges. En revanche, nous avons mesuré la résistance au recuit grâce aux valeurs de D_{par}, qui varient pour chaque échantillon pris séparément, et entre les différents échantillons.

Pour modéliser les histoires thermiques, nous considérons comme contrainte principale, que les échantillons étaient à la surface au moment du dépôt. Nous implémentons aussi les histoires thermiques de la source données par les échantillons peu recuits, pour appréhender l'historique pré-dépôt des échantillons profonds fortement recuits. A cause de la complexité discutée ci-dessus, aucune des histoires

thermiques correspond parfaitement aux informations des données thermochronologiques, ce qu'indiquent les valeurs assez faibles des indicateurs statistiques. Pourtant, les différentes histoires thermiques tirées indépendamment de chaque échantillon sont remarquablement cohérentes entre-elles. Elles indiquent toutes un réchauffement entre l'âge de dépôt et $\sim 2\ Ma$, suivi d'une phase stable ou d'un refroidissement lent puis d'un refroidissement final très rapide à partir de $\sim 0.3\ Ma$. L'exhumation finale est principalement contrainte par l'échantillon le plus profond et le plus recuit (KAR3). La température maximale atteinte par les échantillons est de $104°C$ pour KAR11 (2290 m de profondeur) à $106 - 115°C$ pour KAR3 (profondeur de 4650 m)

Nous n'avons pas utilisé des inversions combinées (Gallagher et al. 2005), car ceci implique un gradient géothermal constant à priori. La Fig. 5.6 montre les paléotempératures maximales prédites en fonction de la profondeur. Bien que ces palétotempératures maximales soient cohérentes entre elles, elles suggèrent un gradient thermique très faible entre $\sim$ 2300 et 4650 m ($7.3°C.km^{-1}$), et impliquent un gradient de $30°C.km^{-1}$ pour les 2 km du haut de la série (Fig. 5.6). Les pics de températures prédisent que les trois échantillons les plus profonds sont cohérents avec un géotherme de $20°C.km^{-1}$ déduit précédemment à partir de la transition recuit/non-recuit. Mais les paléotempératures maximales prédites des deux échantillons les plus hauts de la série sont $15 - 25°C$ plus élevés que celles attendues. Si ces prédictions sont valides, alors, le géotherme dans le bassin des Siwaliks est fortement non-linéaire, ce qui suggère un mécanisme de transport de la température convectif dans le bassin associé, par exemple, à des mouvements de fluides. Bien que des marqueurs indépendants de la paléotempérature puissent être utilisés pour valider ces prédictions, les données de réflectance de la vitrinite et de la cristallinité de l'illite actuellement disponible (Huyghe et al. 2005) ne permettent pas de discriminer un géoterme linéaire d'un géoterme non-linéaire (Fig. 5.6).

Ces histoires thermiques peuvent être expliquées par la tectonique de la chaîne frontale des Siwaliks. Le réchauffement post-dépôt est clairement lié à l'enfoncement du bassin et à la diagénèse. Son arrêt à $\sim 2\ Ma$ indiquerait l'initiation du MFT et l'exhumation des roches des Siwaliks le long du MFT. Cette datation est cohérente avec les âges AFT minima obtenus indépendamment pour les échantillons les

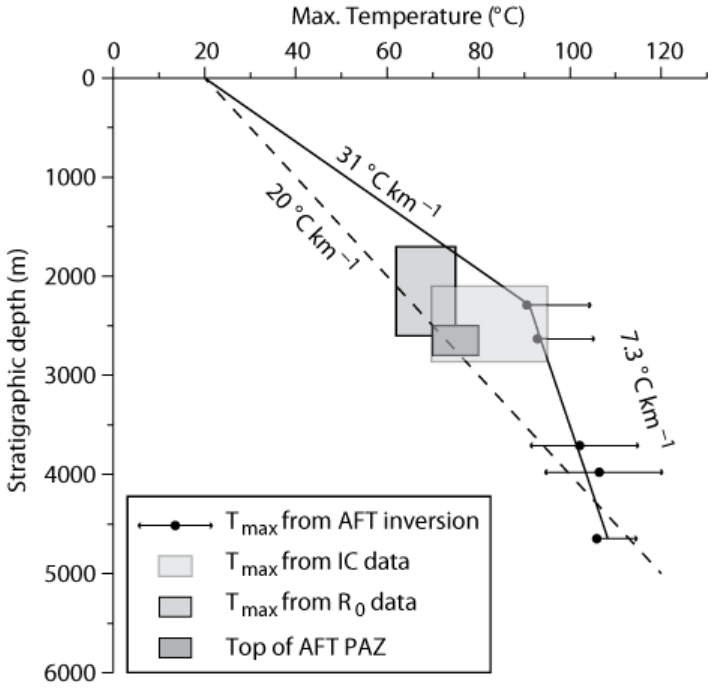

FIG. 5.6 – *Paléotempératures maximales atteintes par les échantillons partiellement recuits prédites par les inversions d'AFTsolve en fonction de la profondeur stratigraphique. Les points représentés correspondent au meilleur modèle lié à chaque échantillon, et la barre d'erreur au maximum et au minimum autorisé pour les modèles acceptables. Pour comparaison, le champ de paléotempératures maximales issu des valeurs de réflectance de la vitrinite (R_0 ; L. Martinez, communication personnelle, 2003) et de cristallinité de l'illite (IC ; Huyghe et al. (2005)) est respectivement représenté ; d'après van der Beek et al. (2006).*

plus profonds, ainsi qu'avec les observations de terrain de Mugnier et al. (2004) qui observent une discordance progressive datée au début du Quaternaire et liée aux mouvements sur le MFT. L'accélération du refroidissement à 0.3 Ma est cohérente avec le passage des roches durant l'exhumation du décollement basal du MFT à sa rampe frontale. Cette transition s'effectue à $\sim$ 3500 m de profondeur dans la Karnali River (Fig. 5.2), le pendage de la rampe est de 30°, ce qui correspond à un taux d'exhumation de $\sim$ 12 $mm.an^{-1}$ et à un raccourcissement moyen de 20 $mm.an^{-1}$. Ces valeurs sont cohérentes avec les taux à court terme de raccourcissement et de soulèvement des études géomorphologiques (Lavé et Avouac 2000, Mugnier et al. 2004), ce qui suggère que le raccourcissement actuellement observé a été maintenu depuis au minimum 0.3 Ma.

Il serait tentant de proposer que ce raccourcissement de $\sim$ 20 $mm.an^{-1}$ sur le MFT est stable depuis 2 Ma, ce qui engendrerait un raccourcissement de $\sim$ 40 km le long du MFT. Mais un tel scénario impliquerait des profondeurs de recuit des échantillons à la base de la section non réalistes. En effet, le pendage du décollement au Népal de l'ouest de l'ordre de $6-8°C$ (Larson et al. 1999, Berger et al. 2004) associé au raccourcissement proposé pendant 1.7 Ma (avant l'exhumation rapide liée à la rampe) impliquerait pour l'échantillon le plus profond une profondeur maximale de $7.1-8.3$ km et donc une paléotempérature maximale de $162-187°C$ pour un gradient géothermal de $20°C.km^{-1}$. En conséquence, nos échantillons les plus profonds devraient être totalement recuits. Si nous considérons un gradient thermique perturbé, la température maximale atteinte par l'échantillon le plus profond serait de $126-135°C$, suffisante pour recuire totalement les apatites en regard de leur composition. Pourtant, aucun de nos échantillons n'est complètement recuit. Ces résultats impliquent donc, soit une activité du MFT intermittente dans le temps, soit une augmentation récente des taux de raccourcissement le long du MFT, soit un problème avec nos inversions thermiques. Nous reviendrons sur cette question au paragraphe 5.2.3.

5.2.2 Initiation du MFT au Népal central et en est-Himalaya (Bhoutan)

Actuellement, au Népal central, nous ne disposons que d'une seule datation, l'échantillon NP05.28 (Tab. 5.1 et Fig. 5.7). Cet échantillon est mal contraint en terme d'âge stratigraphique (base des middle Siwaliks) et en terme de profondeur stratigraphique. Nakayama et Ulak (1999) estiment cette profondeur entre 2700 et 3040 m. Géographiquement, il a été échantillonné au front même du MFT, au niveau où le dernier relief des Siwaliks laisse place à la plaine du Gange. Au Bhoutan, les données les plus méridionnales accessibles se situent à l'ouest du pays. A cet endroit, le MBT et le MCT sont très proches ($\sim$ 10 km), et ni les Siwaliks, ni le MFT ne sont présents (Grujic et al. 2006). Les deux échantillons proches du front de déformation se situent dans le Lesser Himalaya et à la base du High Himalaya. Aucune donnée n'a pu être extraite au front de la chaîne à l'est du Bhoutan [1].

Au Népal central et au Népal de l'ouest, les datations AFT sur des échantillons profonds dans la série des Siwaliks donnent des résultats similaires en terme d'âges centraux, et de populations d'âges (Tab. 5.1 et Fig. 5.4). En effet, la population P1 d'âge minimal est de l'ordre de 2 Ma dans chaque cas. Bien que ni l'âge, ni la profondeur stratigraphique précis de l'échantillon NP05.28 (Fig. 5.7) ne soient réellement connus, cette population d'âges P1 montrent que cet échantillon est partiellement recuit, et a enregistré une partie de l'histoire de l'enfouissement du bassin, ainsi que son exhumation au front de la rampe. Les mesures de longueurs et de D_{par} n'ont pas encore été effectuées pour l'échantillon au sud d'Hétauda. En conséquence, il n'est pas possible d'effectuer une inversion des données en utilisant AFTsolve (Ketcham et al. 2000). En revanche, par similarité avec les échantillons partiellement recuits de l'ouest Népal, nous pouvons en déduire que le MFT s'est mis en place à la même période au Népal de l'ouest et au Népal central.

Dans l'ouest du Bhoutan, l'âge de l'échantillon le plus au sud est de 1.8 Ma, ce qui est similaire aux données du front actif du Népal. A cette longitude au Bhoutan, le MFT n'est pas présent morphologiquement (Grujic et al. 2006), le chevauchement le plus au sud est le MBT qui met les roches du Lesser Himalaya directement sur

[1] Une mission au Bhoutan a été entreprise pour justement acquérir des données pour cette problématique. malheureusement, des complications administratives et politiques nous ont interdit de sortir les échantillons du pays.

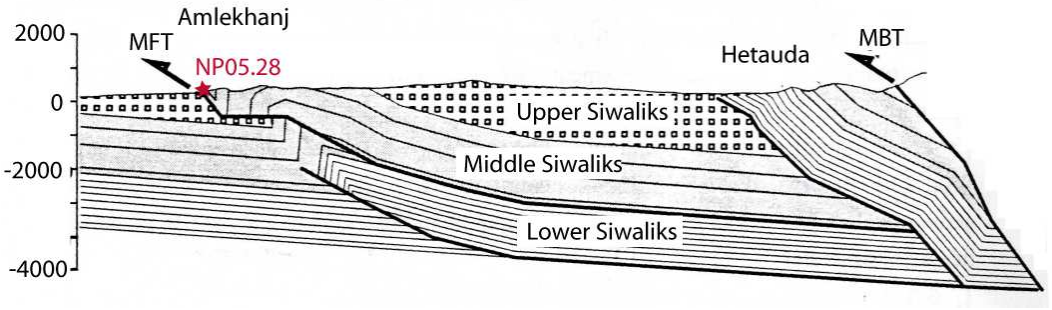

FIG. 5.7 – *Position de l'échantillon NP05.28 sur la coupe équilibrée Hetauda - Amlekhanj ; modifié d'après Leturmy (1997).*

le Quaternaire du bassin du Gange. Par similarité, nous pouvons donc proposer qu'actuellement, le front de déformation à l'ouest du Bhoutan est constitué par le MBT, qui est confondu localement avec le MFT.

D'un point de vue mise en place du MFT tout au long de l'Himalaya, ces données montrent que l'initiation du chevauchement actif actuel s'effectue extrêmement rapidement ($\leq 0.1 - 0.2$ Ma) à l'échelle des temps géologiques, et ce sur une longueur supérieure à 500 km. Si nous extrapolons tout le long du MFT, nous sommes obligés de ne pas prendre en compte l'est de la chaîne à cause de l'absence de MFT, et cette longueur est de l'ordre de $1700 - 1800$ km.

Ces résultats sont en accords avec les expériences de modélisation analogiques menées par F. Graveleau sur la croissance d'un prisme orogénique en liaison avec les précipitations (F. Graveleau, communication personnelle, 2008). Au cours de ses expériences, il observe l'initiation de chevauchements frontaux quasi-simultanément en diverses zones du modèle. Ces initiations croissent rapidement pour former un chevauchement majeur unique, ce qui peut exprimer une destabilisation quasi-uniforme du prisme.

5.2.3 Importance relative de l'overthrusting et de l'underthrusting

Les vitesses de convergence déduites des données AFT sédimentaires disponibles sur le front de la chaîne himalayenne sont cohérentes avec les estimations publiées précédement (Lavé et Avouac 2000, Mugnier et al. 2004), qui donnent une convergence de $20 - 21$ $km.Ma^{-1}$. Au front de la chaîne, elle est associée à la vitesse d'exhumation des roches Siwaliks, ce qui impliquerait que l'overthrusting est

bien plus important que l'underthrusting si l'on croit nos inversions d'histoires thermiques.

Or, dans la haute chaine, les vitesses d'overthrusting sont de $5-6$ $km.Ma^{-1}$ (Brewer et Burbank 2006, Bollinger et al. 2006, Whipp et Ehlers 2007). C'est la valeur utilisée dans nos modélisation dans les chapîtres 3 et 4, et la vitesse d'underthrusting est plus importante (15 $km.Ma^{-1}$). Pour tester l'importance de l'overthrusting et de l'underthrusting, j'ai effectué une inversion à partir des données et du modèle numérique de terrain du Langtang en utilisant le même code PECUBE et NA que dans les chapîtres 3 et 4. Pour cette inversion, j'ai couplé les vitesses d'underthrusting et d'overthrusting pour maintenir une vitesse totale de convergence de 21 $km.Ma^{-1}$. Un seul paramètre variable me permet de contrôler ces deux vitesses. De plus, je laisse la géométrie de la rampe du MHT libre, comme précédement. Je définis la température basale à $850°C$ et la production de chaleur normalisée à 1.5, ce qui induit un gradient de température moyen de $35°C.km^{-1}$ compatible avec les données de terrain. Les résultats de l'inversion sont présentés en Fig. 5.8 et Fig. 5.9.

Le résultat majeur de ces modélisations est de pointer que de l'underthrusting est necessaire pour expliquer les données thermochronologiques (Fig. 5.8, Fig. 5.9 et Tab. 5.3). La vitesse d'overthrusting est de l'ordre de 8 $km.Ma^{-1}$, ce qui induit une vitesse d'underthrusting de 13 $km.Ma^{-1}$, assez proche des valeurs utilisées dans les chapîtres précédents (6 et 15 $km.Ma^{-1}$ respectivement). La rampe crustale obtenue est de 16°, ce qui est légèrement inférieur à la valeur trouvée précédemment. Le meilleur modèle donne des âges qui représentent bien les âges AFT mesurés, mais moins bien les âges argon mesurés. Ceci montre que le modèle est un peu froid.

Ces valeurs ne correspondent pas à celles trouvées à partir de l'analyse des longueurs de traces pour les échantillons partiellement recuits de la Karnali River. En revanche, si nous ne considérons que l'âge de la population minimale des échantillons partiellement recuits, que la rampe frontale est de 30°, et que la transition rampe frontale / plat est à 5 km de profondeur, alors, la vitesse d'overthrusting est de 5 $km.Ma^{-1}$.

Il se pose donc la question de la validité de nos interprétations. Nous pouvons penser qu'à cause de la qualité médiocre des échantillons recuits partiellement, les données sur les longueurs de traces de fission ne sont pas interprétables correcte-

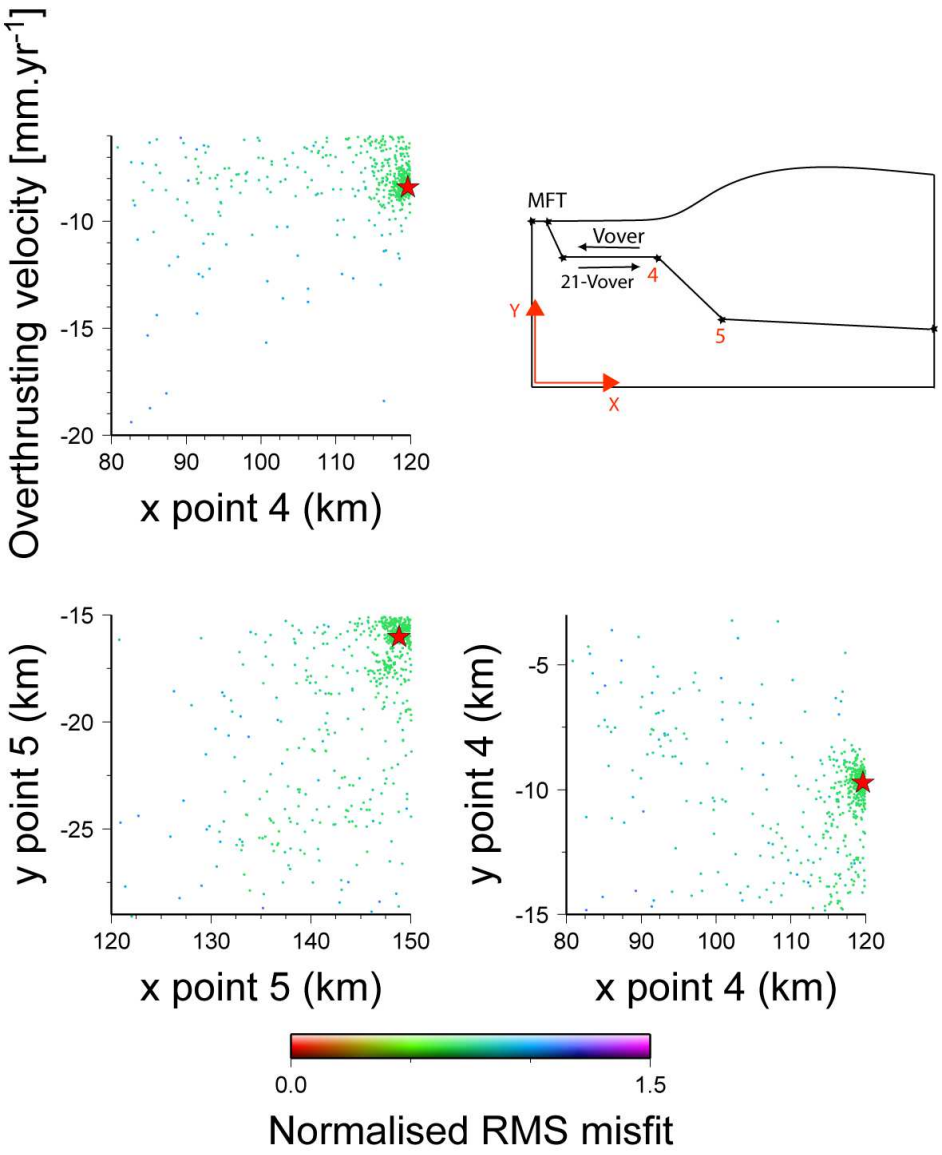

FIG. 5.8 – *Résultats de l'inversion avec NA sur la géométrie du MHT et le rapport de vitesses d'overthrusting/underthrusting.*

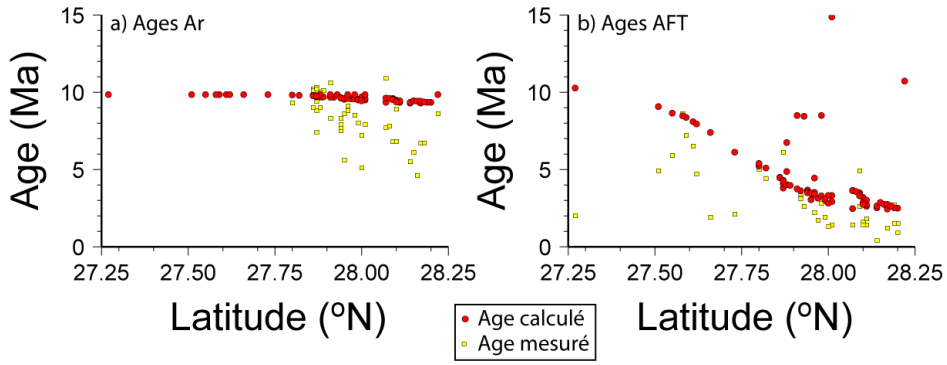

FIG. 5.9 – *Comparaison des données thermochronologiques calculées avec les données réelles pour le meilleur modèle donné par l'inversion. a) Comparaison des données argon ; b) Comparaison des données AFT.*

Model	OvsU1	OvsU2
Area	Langtang	Langtang
Nb of models	1020	1020
Misfit	0.7	0.7
T_{basal} ($^{\circ}C$)	1139	850
A_N	1.74	1.5
grad(T) ($^{\circ}C.km^{-1}$)	51	35
Overthrusting ($km.My^{-1}$)	**-8.5**	**-8.2**
V_{TF} ($km.My^{-1}$)	/	/
X4 (km)	**120**	**120**
Y4 (km	**-9**	**-9**
X5 (km)	**150**	**148**
Y5 (km	**-17**	**-16**
Ramp slope ($^{\circ}$)	16	16
Palung $e\cdot$ ($km.My^{-1}$)	/	$1.4^{+0.7}_{-164}$
Gosaikund $e\cdot$ ($km.My^{-1}$)	/	$3.2^{+0.7}_{-5.3}$

TAB. 5.3 – *Synthèse des meilleurs modèles donnés par les inversionssur le rapport overthrusting/underthrusting. Les points $(X,Y)_4$ et $(X,Y)_5$ représentent les point constituant la rampe crustale du MHT, et sont définis dans la Fig. 5.8. $e\cdot$ représente le taux d'exhumation calculé à partir des valeurs calculées respectivement par le meilleur modèle et correspondantes aux données.*

ment. D'un autre côté, les deux façons d'interpréter nos données sont compatibles avec des observations distinctes, et de plus, comment expliquer que nous avons 5 $km.Ma^{-1}$ d'overthrusting mesuré dans la haute chaîne, et 20 $km.Ma^{-1}$ au front de la chaîne ?

Deux solutions sont envisageables (Fig. 5.10) :

– Une explication plausible est de considérer que le front de la chaîne voit à la fois l'overthrusting et l'underthrusting. La présence d'un niveau de décollement (un plat "supérieur"), fixé au MFT, des Siwaliks sur l'Inde serait alors nécessaire (Fig.5.10b). Cette solution est peu crédible car elle n'est pas en accord avec les observations de terrain : la transition entre la plaine du Gange et les premières montagnes des Siwaliks est brutale et correspond à l'émergence du chevauchement. De plus, cette hypothèse impliquerait une déformation du footwall à la base de la rampe, ce qui n'a jamais été mis en évidence, notamment sur les profils sismiques. Il ne peut donc pas y avoir de niveau de décollement à ce niveau.

– Une autre explication possible est de se placer dans un repère Inde fixe et

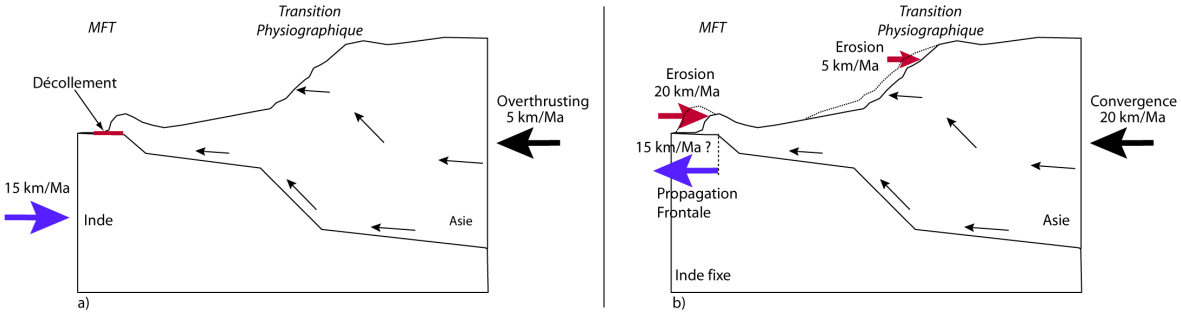

FIG. 5.10 – *Schéma conceptuel donnant deux explications indépendantes explicant le différentiel de vitesses observé entre la transition topographique et la zone du MFT. a) Décollement du front des Siwaliks sur l'Inde ; b) Interprétation de la vitesse d'overthrusting an terme d'érosion différentielle, dans un repère fixé sur l'Inde.*

de considérer que le front de la chaîne se propage vers le sud. Le MDT précède le MFT d'environ 0.8 *Ma*, et se situe actuellement à une dizaine de kilomètres au nord du MFT (Chalaron et al. 1995, Mugnier et al. 2003). En première approximation, ces observations donnent une vitesse de propagation de $\sim 13\ km.Ma^{-1}$ qui correspond à une valeur moyenne du déplacement de la position de la rampe frontale vers le sud. Si nous retirons cette valeur à la vitesse de chevauchement total estimée sur le terrain ($20\ km.Ma^{-1}$), alors, la répartition overthrusting/underthrusting est proche de celle de nos modélisations. Mais ce que nous mesurons est l'advection de la topographie himalayenne, dans un cadre de référence fixé à l'Inde, par la convergence totale moins la projection horizontale du taux d'érosion. Comme Brewer et Burbank (2006) le montrent, dans ce cas, ce taux est équivalent à la vitesse d'overthrusting. Nous pouvons expliquer la différence de vitesses observées par le fait que la partie sud (Siwaliks, composés d'alternances de grès et de conglomérats peu indurés) est relativement facile à éroder ($20\ km.Ma^{-1}$), et la partie nord (haute chaîne, composée en grande partie de quartzites et de gneiss) est plus difficile à éroder ($5\ km.Ma^{-1}$), ce qui induit une advection de la topographie de la haute chaîne de $\pm 15 km.Ma^{-1}$, équivalent à la propagation de la flexure du bassin du Ganges.

Cette deuxième alternative semble plus facilement acceptable, car l'émergence du MFT au front de la topographie des Siwaliks implique que l'érosion est en équilibre avec le raccourcissement sur cette structure. De plus, cela permet d'expliquer la disparition des Siwaliks vers l'est (Bhoutan), si les taux d'érosion frontaux,

contrôlés par une plus forte précipitation, y sont plus élevés que la convergence (comme déjà proposé par Champel et al. (2002)). En revanche, les deux modèles impliquent que les taux d'incision dans la haute chaîne, calculés par Lavé et Avouac (2001) à partir de calibration de l'érodabilité des roches, soient fortement surévalués (d'un facteur 4 environ).

Conclusion générale

6

Sommaire

Pour mener à bien cette étude, il a d'abord été nécessaire que j'effectue un état des lieux sur les données thermochronologiques de basses températures disponibles en Himalaya, et que je fasse une revue critique des différentes modélisations thermo-cinématiques récentes. Cela m'a permis de construire une banque de données thermochronologiques conséquente pour l'Himalaya. J'ai utilisé cette banque de données pour déterminer la stratégie d'échantillonnage sur le terrain afin de la compléter. J'ai ensuite mis en valeur cette base de données en la couplant à des modélisations numériques thermo-cinématiques sur les différentes zones étudiées. Au cours de cette étude, j'ai abordé l'histoire cinématique récente et la géométrie des chevauchements majeurs en Himalaya, puis étudié leurs variations latérales au travers le la chaîne de montagnes. Les conclusions pour chaque partie se retrouvent à la fin de chaque chapître ou des articles correspondants.

Les paragraphes suivants posent les limites de cette étude, leurs causes et des suggestions pour les repousser.

6.1 Une histoire cinématique de l'Himalaya central

J'ai montré que l'histoire cinématique du MHT est très fortement dépendante de sa géométrie, qui masque les processus susceptibles d'entrer en jeu dans la tectonique et la cinématique de la zone située au dessus de la rampe profonde du MHT. C'est pourquoi, malgré un échantillonnage comprenant et encadrant cette zone, il est difficile de quantifier exactement l'importance relative de différents scénarii tectoniques pour l'histoire la plus récente dans cette zone.

Au début, nous avions prévu de compléter l'étude cinématique du prisme himalayen en quantifiant l'activité du MBT au Népal central en utilisant la même méthode que celle mise en application pour le MFT. Pour cela, nous avons échantillonné le toit du MBT en deux endroits distincts, mais les lithologies (diorites ou schistes dits Benigar Slates de la formation Dalagan) ne nous ont permis aucune datation. Pour pouvoir mener à bien ces datations, il est indispensable de mieux définir les zones à échantillonner, et peut être de passer plus de temps sur le terrain

pour trouver des roches susceptibles de permettre des datations thermochronologiques.

En revanche, les données du front de la chaîne contraignent relativement bien l'histoire récente du MFT. Pour l'étude de cette partie de la chaîne, la difficulté majeure est d'obtenir des données suffisamment propres. En effet, le chevauchement frontal coupe des sédiments synchrone de l'érosion de l'Himalaya. Il faut donc utiliser une technique statistique pour discriminer les données des sources, et les données liées à l'histoire du bassin sédimentaire. Pour les techniques que nous avons mises en oeuvre, il est nécessaire que l'échantillon contienne un nombre suffisamment important de grains d'apatites. Il faut donc échantillonner des grès en prélevant un échantillon assez important (5 à 7 kg). Au Népal central, nous avons actuellement une datation, sans mesures de longueurs de traces ni de D_{par}. Ces mesures vont être effectuées pour corroborer ou infirmer mon interprétation calquée par similarité sur l'interprétation des données du Népal de l'ouest. De plus, une vingtaine de kilomètres à l'est de l'échantillon daté du Népal central, nous avons prélevé une coupe pour datations thermochronologiques dans les gorges de la Bakaia, dans laquelle une étude magnétostratigraphique a aussi été menée (Harrison et al. 1993). Cette coupe permettrait entre autre de corroborer ou d'infirmer mon interprétation.

6.2 Une variation latérale des structures en Himalaya

L'utilisation de données bibliographiques (Arita et al. 1997, Rai 1998, Burbank et al. 2003, Grujic et al. 2006, Blythe et al. 2007) m'a permis de montrer que le MHT n'est pas réellement cylindrique tout le long de la chaîne himalayenne, et qu'à l'est, il n'y a pas de rampe profonde. Ces conclusions sont basées sur des données provenant principalement du High Himalaya. Il serait fortement bénéfique de compléter ce jeu de données par des transects sud-nord prenant en compte le Lesser Himalaya. Cette tâche ne sera pas facile à cause des problèmes liés à la lithologie qui peuvent être comparables à ceux que nous avons rencontré pour la coupe au niveau des Annapurnas et de la Kali-Gandaki.

De plus, nos conclusions sur l'activité du MFT tout le long de la chaîne pêchent par le manque de données provenant du front de déformation actif en Himalaya

de l'est. Comme le MFT n'est pas continu en Himalaya de l'est et est probablement relayé sur le MBT, il faut choisir une région comprenant des sédiments Siwaliks, les plus épais possible de manière à obtenir des échantillons partiellement recuits. Il faudrait effectuer une coupe en échantillonnant régulièrement dans ces rivières. Ce travail a été commencé au Bhoutan, où, à cause de problèmes politiques, nous n'avons pas pu rapatrier les échantillons. Pour pallier ce problème, il serait possible de transférer cet échantillonnage dans la partie indienne à l'est du Bhoutan (Arunachal Pradesh).

6.3 Et la place de l'underplating ?

Au cours de nos modélisations, nous n'avons pris en compte aucun mécanisme d'underplating. Ce mécanisme est un des deux mécanismes nécessaires pour expliquer le gradient inverse de métamorphisme observé dans le Lesser Himalaya. Ayant eu des difficultés pour mener à terme les inversions sur des modèles plus simples, je n'ai pas tenté cette implémentation. Il est à noter que nos modèles sans underplating ne reproduisent pas réellement le gradient inverse de métamorphisme, mais reproduisent fidèlement les données thermochronologiques. Numériquement, l'implémentation de ce mécanisme ajoute une complexité. Il y a plusieurs moyens de le progammer :

1. Créer comme Wobus et al. (2006) ou Bollinger et al. (2006) une fenètre à travers laquelle nous faisons passer de la matière en continue. Ce processus serait difficile à implémenter dans la version actuelle de Pecube à cause de la définition même des failles, et de la difficulté à conserver une rampe avec ce processus.
2. Changer la morphologie de la faille au niveau de la rampe crustale pour un pas de temps donné. Ceci permettrait de modéliser un mécanisme discontinu dans le temps, compatible avec les conclusions de DeCelles et al. (2001), mais pose un problème de repère par rapport à la topographie (la transition physiographique est liée à la position de la rampe).

Il faut se poser la question de la continuité ou non du processus d'underplating. Si ce processus est continu, alors, il faut le modéliser comme décrit en 1, ou

comme en 2, mais avec un pas de temps très court à l'échelle de la modélisation. Or, d'après DeCelles et al. (2001), la propagation du duplex sous le Lesser Himalaya s'effecturait de manière épisodique : si l'on suppose que la taille des écailles du duplex est de l'ordre de 60 *km* (d'après la coupe de Lavé et Avouac (2000)) et que la création d'une nouvelle écaille de duplex est l'un des processus majeur qui absorbe l'underthrusting, la création d'une écaille se produirait tous les 4 *Ma*. Pour l'implémenter, il faut donc utiliser la technique du point 2. Or, cette durée est supérieure à la majorité des âges thermochronologiques de la plupart des échantillons du High Himalaya et de la partie nord du Lesser Himalaya. Il est donc fortement probable que ce processus affecte peu les résultats des modélisations.

6.4 Apports de cette étude

Malgré les difficultés et les points à perfectionnés évoqués ci-dessus, cette étude a tout de même apporté les éléments suivants, nécessaires à notre compréhension du fonctionnement du prisme himalayen :

1. J'ai effectué un tri dans les précédents modèles publiés sur l'Himalaya, et j'ai éclairci les différents scénarios cinématiques potentiellement impliqués.
2. J'ai apporté de nouvelles données contraignant la cinématique récente de l'Himalaya.
3. J'ai démontré par l'analyse des données de terrain et par des modélisations numériques qu'il est peu probable qu'un mécanisme de chevauchement hors-séquence soit actif actuellement au niveau de la transition physiographique du Népal central.
4. J'explique que la géométrie du MHT possède un rôle prépondérant et montre qu'elle varie latéralement.
5. Je montre que l'initiation du MFT est récente et rapide tout le long de la chaîne himalayenne.

Bibliographie

J. Achache, V. Courtillot, et Y. Xiu. Paleogeographic and tectonic evolution of southern Tibet since middle Cretaceous time : New paleomagnetic data and synthesis. *Journal Of Geophysical Research*, 89 :10.311–10.339, 1984. (Cité page 17.)

S.K. Acharaya et K.K. Ray. Guide to excursion No. 4. Chapitre Geology of the Darjeeling-Sikkim Himalaya, page 25 pp. Fourth International Gondwana Symposium, 1977. (Cité pages 24 et 331.)

R.p. Agarwal, D.n. Prasad, U. Sumanta, C.m. Berry, et J. Sharma. Hydrocarbon potential of Siwalik basin. *Himalayan Geology*, 15 :301–320, 1994. (Cité page 203.)

E. Appel, W. Rösler, et G. Corvinus. Magnetostratigraphy of the Miocene-Pleistocene Surai Khola Siwaliks in West Nepal. *Geophysical Journal International*, 105 :191–198, 1991. (Cité page 199.)

K. Arita, R. D. Dallmeyer, et A. Takasu. Tectonothermal evolution of the Lesser Himalaya, Nepal : Constraints from $^{40}Ar/^{39}Ar$ ages from the Kathmandu Nappe. *Island Arc*, 6 :372–385, 1997. (Cité pages 27, 76, 135 et 220.)

J.-P. Avouac. Mountain building, erosion, and the seismic cycle in the Nepal Himalaya. *Advences in Geophysics*, 46 :–, 2003. (Cité pages 20, 21, 25, 75, 110, 331 et 332.)

J.P. Avouac et E.B. Burov. Erosion as a driving mechanism of intracontinental mountain growth. *Journal of Geophysical Research*, 101 :17747–17769, 1996. (Cité page 4.)

P. Banerjee et R. Burgmann. Convergence across the northwest Himalaya from GPS measurements. *Geophys. Res. Lett.*, 29 :31–34, 2002. (Cité page 17.)

J. Barbarand, A. Carter, I. Wood, et A. Hurford. Compositional and structural control of fission-track annealing in apatite. *Computers and Geosciences*, 198 :107–137, 2003. (Cité pages 87, 91, 92 et 333.)

J. Barbarand, A. Carter, I. Wood, et A. Hurford. Compositional and structural control of fission-track annealing in apatite. *Computers and Geosciences*, 198 :107–137, 2003b. (Cité page 80.)

J. Barbarand et M. Pagel. Contrôle de la cinétique de cicatrisation des traces de fission dans les cristaux d'apatites : Le rôle de la composition chimique. *Comptes rendus de l'Académie des Sciences*, 332 :259–265, 2001. (Cité page 87.)

G.E. Batt et M.T. Brandon. Lateral thin : 2-D interpretation of thermochronology cinvergent orogenic settings. *Tectonophysics*, 349 :185–201, 2002. (Cité page 98.)

C. Beaumont, P. Fullsack, et J. Hamilton. Erosional control of active compressional orogens. Dans *Thrust Tectonics*, pages 1–18, New York, 1992. (Cité page 4.)

C. Beaumont, P. Fullsack, et J. Hamilton. Styles of crustal deformation in compressional orogens caused by subduction of the underlying lithosphere. *Tectonophysics*, 232 :119–132, 1994. (Cité page 4.)

C. Beaumont, R. A. Jamieson, M. H. Nguyen, et B. Lee. Himalayan tectonics explained by extrusion of a low-viscosity crustal channel coupled to focused surface denudation. *Nature*, 414 :738–742, 2001. (Cité pages 4, 16 et 27.)

C. Beaumont, R. A. Jamieson, M. H. Nguyen, et S. Medvedev. Crustal channel flow : 1. Numerical models with applications to the tectonics of the Himalayan-Tibetan orogen. *Journal of Geophysical Research*, 109 :B06406, 2004. (Cité page 27.)

C. Beaumont, H. Kooi, et S. Willett. Coupled tectonic-surface process models with applications to rifted margins and collisional orogens. Dans *Geomorphology and Global Tectonics*, pages 29–55, New York, 1999. (Cité page 4.)

A. Berger, F. Jouanne, R. Hassani, et J.-L. Mugnier. Modelling the spatial distribution of present-day deformation in Nepal : How cylindrical is the Main Himalayan Thrust in Nepal ? *Geophys. J. Int.*, 156 :94–114, 2004. (Cité pages 20, 23, 209 et 331.)

M. Bernet, P. Van der Beek, R. Pik, P. Huyghe, et A. Mugnier, J.-L. ans Sculc. Miocene to Recent exhumation of the central Himalaya determined from combined

detrital zircon fission-track and U/Pb analysis of Siwalik sediments, western Nepal. *Basin Research*, 18 :393–412, 2006. (Cité page 79.)

J. Besse et V. Courtillot. Paleogeographic maps of the continents bordering the Indian Ocean since the Early Jurassic. *Journal Of Geophysical Research*, 93 :11.791–11.808, 1988. (Cité page 17.)

J. Besse et V. Courtillot. Revised and synthetic aparent polar wander paths of the African, Eurasian, North American and Indian Plates, and true polar wander since 200 Ma. *Journal Of Geophysical Research*, 96 :4029–4050, 1991. (Cité page 17.)

O. Beyssac, L. Bollinger, J.-P. Avouac, et B. Goffe. Thermal metamorphism in the Lesser Himalaya of Nepal determine from Raman spectroscopie of cabonaceous material. *Earth And Planetary Science Letters*, 225 :233–241, 2004. (Cité page 11.)

A. E. Blythe, D. W. Burbank, A. Carter, F. Schmidt, et J. Putkonen. Plio-Quaternary exhumation history of the central Himalaya : 1. Apatite and zircon fission-track and apatite [U-Th]/He analyses. *Tectonics*, 26 :–, 2007. (Cité pages 76, 77, 135, 136, 220 et 334.)

L. Bollinger, J. P. Avouac, O. Beyssac, E. J. Catlos, T. M. Harrison, M. Grove, B. Goffé, et S. Sapkota. Thermal structure and exhumation history of the Lesser Himalaya in central Nepal. *Tectonics*, 23 :1–19, 2004. (Cité pages 16, 25, 27 et 75.)

L. Bollinger, P. Henry, et J. P. Avouac. Moutain building in the Nepal Himalaya : Thermal and kinematic model. *EPSL*, 244 :58–71, 2006. (Cité pages 25, 27, 75, 76, 110, 212 et 221.)

B. Bookhagen et D. Burbank. Topography, relief, and TRMN-derived rainfall variations along the Himalaya. *Geophys. Res. Lett.*, 33 :L08405, 2006. (Cité pages 5, 7, 8, 19, 135, 329 et 331.)

B. Bookhagen, R. Thiede, et M.R. Strecker. Late Quaternary intensified monsoon phases control landscape evolution in the NW Himalaya. *Geology*, 33 :149–, 2005. (Cité page 135.)

M. T. Brandon. Probability density plot for fission-track-age samples. *Nuclear Tracks Radiation Measurements*, 26 :663–676, 1996. (Cité page 90.)

M. T. Brandon, M. K. Roden-Tice, et J. I. Garver. Late Cenozoic exhumation of the Cascadia accretionary wedge in the Olympic Mountains, Northwest Washington State. *Geol Soc Am Bull*, 110(8) :985–1009, Août 1998. (Cité pages 76 et 89.)

J. Braun. Estimating exhumation rate and relief evolution by spectral analysis of age-elevation datasets. *Terra Nova*, 14 :210–214, 2002a. (Cité page 98.)

J. Braun. Quantifying the effect of recent relief changes on age-elevation relationships. *Earth and Planetary Sciences Letters*, 200 :331–343, 2002b. (Cité pages 98 et 109.)

J. Braun. Pecube : A new finite element code to solve the heat transport equation in three Dimensions in the Earth's crust Including the effects of a time-varying, finite amplitude surface topography. *Computers and Geosciences*, 29 :787–794, 2003. (Cité pages 78, 92 et 93.)

J. Braun et X. Robert. Constraints on the rate of post-orogenic erosional decay from low temperature thermochronological data : application to the Dabie Shan, China. *Earth Surface Processes and Landforms*, 30 :1203–1225, 2005. (Cité pages 100 et 249.)

J. Braun et M. Sambridge. Modelling landscape evolution on geological time scales : a new method based on irregular spatial discretization. *Basin Research*, 9 :27–52, 1997. (Cité page 100.)

I. D. Brewer et D. W. Burbank. Thermal and kinematic modeling of bedrock and detrital cooling ages in the central Himalaya. *Journal of Geophysical Research*, 11 : –, 2006. (Cité pages 27, 76, 212 et 215.)

L.D. Brown, W. Zhao, K.D. Nelson, D. Hauck, D. Alsdorf, A. Ross, M. Cogna, M. Clark, X. Liu, et J. Che. INDEPTH deep seismic reflection observation of a regionally extensive high-amplitude basement reflector, and associated "bright spot" beneath the northern Yadong-Gulu rift, Tibert. *Science*, 274 :1688–1690, 1996. (Cité pages 20, 21 et 331.)

N. Brozovic, D.W. Burbank, et A.J. Meigs. Limits on landscape development in the northwestern Himalaya. *Science*, 276 :571–574, 1997. (Cité page 4.)

M. Brunel. Ductile thrusting in the Himalayas ; shear sense criteria and stretching lineations. *Tectonics*, 5 :247–265, 1986. (Cité page 12.)

D. Burbank. Causes of recent Himalayan uplift from deposited pattern in the Ganges basin. *Nature*, 357 :680–683, 1992. (Cité page 4.)

D. W. Burbank. Bedrock incision, rock uplift, and threshold hillslopes in the northwestern Himalaya. *Nature*, 379 :505–510, 1996. (Cité page 10.)

D. W. Burbank, A. E. Blythe, J. Putkonen, B. Pratt-Sitaula, E. Gabet, M. Oskin, A. Barros, et T. P. Ojha. Decoupling of erosion and precipitation in the Himalayas. *Nature*, 426(6967) :652–655, Décembre 2003. ISSN 0028-0836. (Cité pages 77, 135, 136, 220 et 334.)

B. C. Burchfiel, C. Zhiliang, K.V. Hodges, L. Yuping, L.H. Royden, D. Changrong, et X. Jiene. The South Tibetan detachment system, Himalayan orogen : Extension contemporaneous with and parallel to shortening in a collisional mountain belt. *Geological Society of America Special Paper*, 269 :41pp, 1992. (Cité page 16.)

R.L. Burtner, A. Nigrini, et R.A Donelick. Thermochronology of lower Cretaceous source rocks in the Idaho-Wyoming Thrust Blelts. *Bull. Am. Assoc. Petrol. Geol.*, 78 :1613–1636, 1994. (Cité page 80.)

W. D. Carlson. Mechanisms and kinetics of apatite fission-track annealing. *American Mineralogist*, 75 :1120–1139, 1990. (Cité page 80.)

W. D. Carlson, R. A. Donelick, et R. A. Ketcham. Variability of apatite fission-track annealing kinetics : I. Experimental results. *American Mineralogist*, 84 :1213–1223, 1999. (Cité pages 80, 91, 92 et 333.)

B. Carrapa, M.R. Strecker, et E. Sobel. Sedimentary, tectonic and thermochronologic evolution of the southernmost end of the Puna Plateau (NW Argentina). *Earth Planet. Sci. Lett.*, 247 :82–, 2006. (Cité page 206.)

A. Carter. Present status and future avenues of source region discrimination and characterisation using fission-track analysis. *Sediment. Geol.*, 124 :31–45, 1999. (Cité page 79.)

A. Carter et K. Gallagher. Characterizing the significance of provenance on the influence of thermal history models from apatite fission-track data - A synthetic data study. *Geological Society of America*, Special Paper 378 :7–23, 2004. (Cité pages 85 et 204.)

E. Chalaron, J. L. Mugnier, et G. Mascle. Control on thrust tectonics in the Himalayan foothills : a view from a numerical model. *tectonophysics*, *** :139–163, 1995. (Cité pages 10 et 215.)

B. Champel, P. Van der Beek, J.-L. Mugnier, et P. Leturmy. Growth and lateral propagation of fault-related folds in the siwaliks of western nepal : Rates, mechanisms, and geomorphic signature. *Journal Of Geophysical Research*, 107 :–, 2002. (Cité page 216.)

M. E. Coleman et K. V. Hodges. Contrasting Oligocene and Miocene thermal histories from the hanging wall and footwall of the South Tibetan detachment in the central Himalaya from $^{40}Ar/^{39}Ar$ thermochronology, Marsyandi Valley, central Nepal. *Tectonics*, 17 :726–740, 1998. (Cité pages 16 et 75.)

P. Copeland, T.M. Harisson, K.V. Hodges, P. Maruejol, P Le Fort, et A Pecher. An Early Pliocene Thermal Disturbance of th Main Central Thrust, Central Nepal : Implications for Himalayan Tectonics. *Journal of Geophysical Research*, 96 :8475–8500, 1991. (Cité page 16.)

P. Copeland, P. Le Fort, P. Henry, S. Man Rai, D. Foster, et R. Parrish. Neogene tectonothermal development of the Himalayan thrust system in the kathmandu region, Nepal. *Geological Society of American Bulletin*, ? ? : ? ?, 2000. (Cité page 76.)

J. Corrigan. Inversion of apatite fission track data for thermal history information. *Journal of Geophysical Research*, 96 :10347–10360, 1991. (Cité page 92.)

C. Crouzet, I. Dunkl, L. Paudel, P. Arkai, T.M. Rainer, K. Balogh, et E. Appel. Temperature and age constraints on the metamorphism of the Tethyan Himalaya in Central Nepal : A multidisciplinary approach. *Journal of Asian Earth Sciences*, 30 : 113–130, 2007. (Cité pages 11 et 76.)

K. D. Crowley, M. Cameron, et R. L. Schaefer. Experimental studies of annealing of etched fission tracks in fluorapatite. *Geochimica et Cosmochimica Acta*, 89 :1449–1465, 1991. (Cité page 80.)

K.D. Crowley. Lenmodel : a forward model for calculating length distributions and fission-track ages in apatite. *Computers and Geosciences*, 19 :187–194, 1993. (Cité page 92.)

Angie Dazé, James K. W. Lee, et Mike Villeneuve. An intercalibration study of the Fish Canyon sanidine and biotite 40Ar/39Ar standards and some comments on the age of the Fish Canyon Tuff. *Chemical Geology*, 199(1-2) :111–127, Août 2003. (Cité page 84.)

P. De Celles et . –. *Basin Research*, inpress. (Cité page 199.)

J. De Sigoyer, V. Chavagnac, J. Blichert-toft, I. Villa, B. Luais, S ; Guillot, M. Cosca, et G. Mascle. Dating the Indian Continental subduction and collisional thickening in the northwestern Himalaya : multichronology of the Tso Morari eclogites. *Geology*, 28 :487–490, 2000. (Cité page 13.)

P. G. DeCelles, D. M. Robinson, J. Quade, T. P. Ojha, C. N. Garzione, P. Copeland, et B. N. Upreti. Stratigraphy, structure, and tectonic evolution of the Himalayan fold-thrust belt in western Nepal. *Tectonics*, 20 :487–509, 2001. (Cité pages 17, 18, 20, 221, 222 et 330.)

B. Delcaillau. *Les fronts de chaînes actives. Génèse des reliefs et relations tectoniques - érosion - sédimentation*. Mém. Habil. Dir. Rech, Caen, 1997. (Cité pages 16 et 17.)

J. Dercourt, L.E. Ricou, et B.E. Vrielynck. Atlas Tethys, Palaeoenvironmental Maps. Rapport technique, 307, 1993. (Cité page 12.)

R. A. Donelick. Crystallographic orientation dependence of mean etchable track length in apatite : a physical model and experimental observations. *American Mineralogist*, 76 :83–91, 1991. (Cité page 87.)

R. A. Donelick, R. A. Ketcham, et W. Carlson. Variability of apatite fission-track annealing kinetics : II. Crystallographic orientation effects. *American Mineralogist*, 84 :1224–1234, 1999. (Cité pages 80 et 87.)

R.A. Donelick. A method of fission track analysis utilising bulk chemical etching of apatite. Rapport technique, Patent 5267274, 1993. (Cité page 80.)

R.A. Donelick. A method of fission track analysis utilising chemical etching of apatite. Rapport technique, Patent 658800, 1995. (Cité page 80.)

C. Duncan, J. Masek, et E. Fielding. How steep are the Himalaya ? Characteristics and implications of along-strike topographic variations. *Geology*, 31 :75–78, 2003. (Cité pages 5, 7, 9, 135 et 330.)

T. A. Ehlers, P.A. Armstrong, et D.S. Chapman. Normal fault thermal regimes and the interpretation of low-temperature thermochronometers. *Phys. Earth Planet. Inter.*, 126 :179–194, 2001. (Cité page 98.)

T.A. Ehlers. Low-Temperature Thermochronology : Techniques, Interpretations, and Applications, Rev. Mineral. Geochem. Chapitre Computational tools for low-temperature thermochronometer interpretation, pages 589–622. Mineral. Soc. of Am., 2005. (Cité page 94.)

T.A. Ehlers, S. Willet, P.A. Armstrong, et D.S. Chapman. Exhumation of the Central Wasatch Mountains, Utah : 2. Thermo-kinematics of exhumation and thermochronometer interpretation. *J. Geophys. Res.*, 108 :2173, 2003. (Cité page 98.)

M.J. Evans, L.A. Derry, et C. France-Lanord. Geothermal fluxes of alkalinity in the Narayani river system of central Nepal. *Geochem. Geophys. Geosyst.*, 5 :Q08011, 2004. (Cité page 93.)

K. A. Farley. (U-Th)/He dating : Techniques, Calibrations, and Applications. *Journal of Geophysical Research*, xxx :X–X, 2000. (Cité pages 76 et 94.)

E. Fielding, B. Isaks, M. Barazangi, et C. Duncan. How flat is Tibet ? *Geology*, 22 : 163–167, 1994. (Cité pages 4 et 10.)

D.P. Finlayson, D.R. Montgomery, et B. Hallet. Spatial conicidence of rapid inferred erosion with young metamorphic massifs in the Himalayas. *Geology*, 30 :219–222, 2002. (Cité pages 4 et 5.)

P. Fitzgerald, R. Sorkhabi, T. Redfield, et E. Stump. Uplift and denudation of the central Alaska Range : a case study in the use of apatite fission track thermochronology to determine absolute uplift parameters. *Journal of Geophysical Research*, 100 :20175–20191, 1995. (Cité page 79.)

P. G. Fitzgerald et A. J. W. Gleadow. New approaches in fission track geochronology as a tectonic tool : Examples from the transantartic mountains. International Journal of Radiation Applications and Instrumentation. *Nuclear Tracks Rad. Meas.*, 17 :351–357, 1990. (Cité page 80.)

R. L. Fleischer et P. B. Price. Charged particle tracks in glass. *J. Appl. Phys.*, 64 : 2903–2904, 1963a. (Cité page 81.)

R. L. Fleischer et P. B. Price. Tracks of cherged particles in high polymers. *Science*, 140 :1221–1222, 1963b. (Cité pages 81 et 82.)

R. L. Fleischer, P. B. Price, et R. M. Walker. *Nuclear tracks in solids - principles and applications*. University of California Press, Los Angeles, 1975. (Cité page 79.)

R.L. Fleischer, P. B. Price, et R. M. Walker. Effects of temperature, pressure and ionisation on the formation and stability of fission tracks in minerals and glasses. *Journal of Geophysical Research*, 70 :1497–1502, 1965. (Cité page 81.)

E.J. Gabet, B.A. Pratt-Sitaula, et D.W. Burbank. Climatic controls on hillslope angle and relief in the Himalayas. *Geology*, 32 :629–632, 2004. (Cité page 99.)

K. Gallagher. Evolving temperature histories from apatite fission track data. *Earth and Planetary Sciences Letters*, 136 :421–435, 1995. (Cité pages 80 et 92.)

K. Gallagher, R. Brown, et C. Johnson. Fission track analysis and its applications to geological problems. *Annual Review of Earth and Planetary Sciences*, 26 :519–572, 1998. (Cité pages 78, 79, 80, 82, 83, 84, 86 et 332.)

K. Gallagher, C Hawkesworth, et M. Mantovni. The denudation history of the onshore continental margin of SE Brazil inferred from fission track data. *J. Geol. Sac. London*, 154 :451–457, 1994. (Cité page 79.)

K. Gallagher, J. Stephenson, R. Brown, C. Holmes, et P. Fitzgerald. Low temperature thermochronology and modeling strategies for multiple samples 1 : vertical profiles. *Earth And Planetary Science Letters*, 237 :193–208, 2005. (Cité page 207.)

A. Galy. *Etude géochimique de l'érosion actuelle de la chaîne himalayenne*. PhD thesis, Institut National Polytechnique de Lorraine, Nancy, 1999. (Cité pages 12 et 330.)

A. Gansser. *Geology of the Himalayas*. Wiley-Interscience, New York, 1964. (Cité pages 10, 24 et 331.)

A. Gansser. *Geology of the Bhutan Himalaya*. Birkauser Verlag, 1983. (Cité page 11.)

J.I. Garver, M.T. Brandon, M. Roden-Tice, et P.J.J. Kamp. Exhumation Processes : Noraml Faulting, Ductile Flow and Erosion. Chapitre Exhumation history of orogenic highlands determined by detrical fission-track thermochronology, pages 283–304. Geological Society, 1999. (Cité pages 79, 91 et 333.)

E. Garzanti et M. Pagni Frette. Stratigraphic succession of the Thakkhola region (Central Nepal) : Comparison with the Northwestern Tethys Himalaya. *Revista italiana di Paleontologia e Stratigraphia*, 97 :3–26, 1991. (Cité page 11.)

P. Gautam et Y. Fujiwara. Magnetic polarity stratigraphy of Siwalik Group sediments of Karnali River section in Western Nepal. *Geophysical Journal International*, 142 :812–824, 2000. (Cité pages 199, 204 et 334.)

P. Gautam et W. Rösler. Depositional chronology and fabric of Siwaliks group sediments in Central Nepal from magnetostratigraphy and magnetic anisotropy. *Journal of Asian Earth Sciences*, 17 :659–682, 1999. (Cité page 199.)

A. J. W. Gleadow et I. R. Duddy. A natural long-term track annealing experiment for apatite. *Nuclear Tracks and Radiation Measurements*, 5 :169–174, 1981. (Cité page 87.)

A. J. W. Gleadow, I. R. Duddy, P. F. Green, et J. F. Lovering. Confined fission track lengths in apatite : a diagnostic tool for thermal history analysis. *Contributions to Mineralogy and Petrology*, 94 :405–415, 1986. (Cité pages 80 et 85.)

L. Godin. Structural evolution of the Tethyan sedimentary sequence in the Annapurna area, central Nepal Himalaya. *Journal of Asian Earth Sciences*, 22 :307–328, 2003. (Cité page 11.)

L. Godin, K. Hodges, R. Parrish, et R. Brown. Timing of thermal events in the Upper Kali Gandaki valley of central Nepal Himalaya. Dans *13th Himalayan Karakorum Tibet Workshop, Geological Bulletin, University of Peshawar, Special issue 31*, 1998. (Cité page 11.)

L. Godin, R. r. Parrish, R. l. Brown, et K. v. Hodges. Crustal thickening leading to exhumation of the Himalayan Metamorphic core of central Nepal : Insight from U-Pb Geochronology and $^{40}Ar/^{39}Ar$ Thermochronology. *Tectonics*, 20 :729–747, 2001. (Cité pages 16 et 76.)

P. F. Green, I. R. Duddy, A. J. W. Gleadow, et J. F. Lovering. Thermal History of Sedimentray Basins - Methods and Cas Histories. Chapitre Apatite fission track analysis as a paleotemperature indicator for hydrocarbon exploration, pages 181–195. Naeser, N.D. and Mcculloh, T., 1989a. (Cité page 80.)

P. F. Green, I. R. Duddy, A. J. W. Gleadow, G. P. R. Tingate, et M. Laslett. Fission-track annealing in apatite : Track length measurements and the form of the Arrhenius plot. *Nuclear Tracks Rad. Meas.*, 10 :323–328, 1985. (Cité pages 80 et 92.)

P. F. Green, I. R. Duddy, G. M. Laslett, K. A. Hegarty, A. J. W. Gleadow, et J. F. Lovering. Thermal annealing of fission tracks in apatite 4. Quantitative modelling techniques and extension to geological timescales. *Chemical Geology*, 79 :155–182, 1989b. (Cité pages 80 et 92.)

D. Grujic, I. Contand, B. Bookhagen, S. Bonnet, A. Blythe, et C. Duncan. Climatic forcing of erosion, landscape and tectonics in the Bhutan Himalayas. *Geology*, 34 : 801–804, 2006. (Cité pages 135, 137, 210, 220 et 334.)

S. Guillot, E. Garzanti, D. Baratoux, D. MArquer, G. MAhéo, et J de Sigoyer. The total shortenning history of the NW Himalaya. *Geochem. Geophys. Geosyst.*, 4 :1064 : –, 2003. (Cité page 13.)

J.C. Hadler, S.R. Paulo, P.J. Iunes, C.A.S. Tello, M.L. Balestrieri, G. Bigazzi, E.A.C. Curvo, et P.A. Hackspacher. PC compatible Brazilian software for obtaining thermal histories using apatite fission track analysis. *Radiation Measurements*, 34 : 149–154, 2001. (Cité page 92.)

W.E. Hames et S.A. Bowring. An empirical evaluation of the argon diffusion geometry in muscovite. *Earth And Planetary Science Letters*, 124 :161–67, 1994. (Cité page 76.)

T. M. Harrison, P. Copeland, S. A. Hall, J. Quade, S. Burner, T. P. Ojha, et W. S. F. Kidd. Isotopic preservation of Himalayan/Tibetan uplift, denudation, and climatic histories of two molasse deposits. *Journal of Geology*, 101 :157–175, 1993. (Cité page 220.)

M. L. Hauck, K. D. Nelson, L. D. Brown, W. Zhao, et A. R. Ross. Crustal structure of the Himalayan orogen at $\approx 90^{\circ}$ east longitude from Project INDEPTH deep reflection profiles. *Tectonics*, 17 :481–500, 1998. (Cité pages 23, 24, 135 et 331.)

A. Heim et A. Gansser. *Central Himalaya Geological Observation of Swiss*. -, 1939. (Cité pages 10 et 12.)

G. Hetenyi, R. Cattin, F. Brunet, L. Bollinger, J. Vergne, J. L. Nabelek, et M. Diament. Density distribution of the India plate beneath the Tibetan plateau : Geophysical and petrological constraints on the kinetics of lower-crustal eclogitization. *Earth and Planetary Science Letters*, 264 :226–244, 2007. (Cité page 20.)

K. V. Hodges, R. R. Parrish, T. B. Housh, D. R. Lux, B. C. Burchfiel, L. H. Royden, et Z. Chen. Simultaneous Miocene Extension and Shortening in the Himalayan Orogen. *Science*, 258(5087) :1466–1470, Novembre 1992. (Cité pages 16 et 75.)

K. V. Hodges, C. Wobus, K. Ruhk, T Schildgen, et K. Whipple. Quaternary deformation, river steepening, and heavy precipitation at the front of the Higher Himalayan ranges. *Earth and Planetary Sciences Letters*, 220 :379–389, 2004. (Cité pages 25, 26, 75 et 332.)

K.V. Hodges. Tectonics of the HImalaya and southern Tibet from two perspectives. *Geol. Soc. Am. Bul.*, 112 :324–350, 2000. (Cité page 99.)

K.V. Hodges, R.R. Parrish, et M. P. Searle. Tectonic evolution of the central Annapurna Range, Nepalese Hiamalayas. *Tectonics*, 15 :1264–1291, 1996. (Cité page 16.)

M. S. Hubbard. Thermobarometric constraint on the thermal history of the Main Central Thrust zone and Tibetan slab, eastern Himalaya. *Journal of Metamorphic Geology*, 7 :19–30, 1989. (Cité pages 12, 16 et 75.)

A. Hurford et K. Hammerschmidt. $^{40}Ar/^{39}Ar$ and K/Ar dating of the Bishop and Fish Canyon Tuffs : Calibration ages for fission track dating standards. *Chemical Geology*, 58 :23–32, 1985. (Cité page 84.)

P Huyghe, A Galy, J. L. Mugnier, et C. France-Lanord. Propagation of the thrust system and erosion in the Lesser Himalaya : Geochemical and sedimentological evidence. *Geology*, 29 :1007–1010, 2001. (Cité pages 16 et 98.)

P Huyghe, J. L. Mugnier, et B. Gajurel, A.p.and Delcaillau. Tectonic and climatic control of the changes in the sedimentary record of the Karnali River section (Siwaliks of western Nepal). *The Island Arc*, 14 :311–327, 2005. (Cité pages 199, 202, 203, 207, 208 et 335.)

M. Jaboyedoff. Modèles thermiques simples de la croûte terrestre : un regard sur les Alpes. *Bull. Soc. Vaud. Sc. Nat.*, 340(ISSN 0037-9603) :229–271, 1999. (Cité page 101.)

R.A. Jamieson, C. Beaumont, S. Medvedev, et M.H. Nguyen. Crustal Channel flow : 2. Numerical model with implications for metamorphism in the Himalayan-Tibetan orogen. *Journal of Geophysical Research*, 109 :B06407, 2004. (Cité page 27.)

F. Jouanne, J. L. Mugnier, J. F. Gamond, P. Le Fort, M. R. Pandey, L. Bollinger, M. Flouzat, et J. P. Avouac. Current shortening across the Himalayas of Nepal. *Geophysical Journal International*, 157(1) :1–14, 2004. (Cité pages 17, 22, 23 et 331.)

R. A. Ketcham. Forward and inverse modelling of low-temperature thermochronology data. *Rev. Mineral. Geoch.*, 84 :1235–1255, 2005. (Cité pages 80 et 92.)

R. A. Ketcham, R. A. Donelick, et W. D. Carlson. Variability of apatite fission-track annealing kinetics : III. Extrapolation to geological time scales. *American Mineralogist*, 84 :1235–1255, 1999. (Cité pages 76 et 80.)

R. A. Ketcham, R. A. Donelick, et M. B. Donelick. AFTSolve : A program for multi-kinetic modeling of apatite fission-track data. *Geological Materials Research*, 2 : 1–32, 2000. (Cité pages 80, 91, 92, 202, 204, 206, 210, 333 et 335.)

E. Konstantinovskaia et J. Mallavieille. Erosion and exhumation in accretionary orogens : Experimental and geological approaches. *G3*, 6 :Q02006, doi :10.1029/2004GC000794–Q02006, doi :10.1029/2004GC000794, 2005. (Cité page 4.)

P.O. Koons. The topographic evolution of collisional mountain belts : a numerical look at the Southern Alps, New Zealand. *Am. J. Sci.*, 289 :1041–, 1989. (Cité page 4.)

M.J. Kunk, F.F. Sutter, et C.W. Naeser. High precision ages of sannidine, biotite, hornblende and plagioclase from Fish Canyon Tuff, San Juan volcanic field, South Central Colorado. *Society of Amerci Abstract Program*, 17 :6–36, 1985. (Cité page 84.)

R. Lacassin, H. Maluski, P. Hervé Leloup, P. Tapponnier, C. Hinthong, K. Siribhakdi, S. Chuaviroj, et A. Charoenravat. Tertiary diachronic extrusion and deformation of western Indochina : Structural and $^{40}Ar/^{39}Ar$ evidence from NW Thailand. *Journal Of Geophysical Research*, 102 :10.013–10.037, 1997. (Cité pages 13, 15 et 330.)

K. Larson, R. Burgmann, R. Bilham, et J. Freymueller. Kinematics of the India-Eurasia collision zone from GPS measurements. *J. Geophys. Res.*, 104 :1077–1093, 1999. (Cité page 209.)

G. M. Laslett. Thermal annealing of fission tracks in apatite 2. A quantitative analysis. *Chemical Geology*, 65 :1–13, 1987. (Cité page 94.)

J. Lavé et J. P. Avouac. Active folding of fluvial terraces across the Siwalik hills, Himalayas of central Nepal. *Journal of Geophysical Research*, 105 :5735–5770, 2000. (Cité pages 7, 17, 25, 209, 211 et 222.)

J. Lavé et J.P. Avouac. Fluvial incision and tectonic uplift across the himalayas of Central Nepal. *J. Geophys. Res.*, 106 :26,561–26,592, 2001. (Cité pages 25, 26, 216 et 332.)

P. Le Fort. Himalaya : the collided range : Present knowledge of the continental arc. *Am. J. Sci.*, 275A :1–44, 1975. (Cité pages 10 et 12.)

P. Le Fort. The Tectonics of Asia. Chapitre Evolution of the Himalaya, pages 95–106. Cambridge University Press, 1996. (Cité page 10.)

X. Le Pichon, M. Fournier, et L. Jolivet. Kinematics, topography, shortening, and extrusion in the India-Asia collision. *Tectonics*, 11 :1085–1098, 1992. (Cité page 17.)

C. Lemonnier, G. Marquis, F. Perrier, J.-P. Avouac, G. Chitrakar, B. Kafle, S. Sapkota, U. Gautam, D. Tiwari, et M. Bano. Electrical structure of the Himalaya of Central Nepal : High conductivity around the mid-crustal ramp along the MHT. *Geophysical Research Letter*, 26 :3261–3264, 1999. (Cité pages 20, 21 et 331.)

P. Leturmy. *Sédiments et reliefs du front des systèmes chevauchants : Modélisations et exemples du front andin et des Siwaliks (Himalaya) à l'Holocène*. PhD thesis, Université Joseph Fourier, Grenoble, France, 1997. (Cité pages 211 et 335.)

P. Leturmy, P. Huyghe, J. L. Mugnier, et B. Delcaillau. An intermediate displacement scale between earthquake slip and finite geometry of thrust systems deduced from a comparison of Quaternary, Holocene and instantaneous rates of shortening in the frontal thrust belt of Himalaya (Western Nepal). *Extended abstract in Active Subduction and Collision in SE Asia : data and models, Montpellier*, 14 : 103–106, 1999. (Cité page 11.)

T. M. Lutz et G. I. Omar. An inverse method of modeling thermal histories from apatite fission-track data. *Earth and Planetary Sciences Letters*, 104 :181–195, 1991. (Cité pages 92 et 94.)

H. Lyon-Caen et P. Molnar. Gravity anomalies, flexure of the Indian plate, and the structure, support and evolution of the Himalaya and Ganga Basin. *Tectonics*, 4 : 513–538, 1985. (Cité page 20.)

N. S. Manktelow et B. Grasemann. Time-dependent effects of heat advection and topography on cooling histories during erosion. *Earth and Planetary Sciences Letters*, 270 :167–195, 1997. (Cité pages 98 et 109.)

J.G. Masek, B.L. Isacks, T.L. Gubbels, et E.J. Fielding. Erosion and tectonics at the margins of continental plateaus. *Journal Of Geophysical Research*, 99 :13941–13956, 1994. (Cité page 4.)

F. W. McDowell, W. C. McIntosh, et K. A. Farley. A precise $^{40}Ar - ^{39}Ar$ reference age for the Durango apatite $(U-Th)/He$ and fission-track dating standard. *Chemical Geology*, 214(3-4) :249–263, Janvier 2005. (Cité page 84.)

A. M. Mcfarlane. An evaluation of the inverted metamorphism gradient at Langtang National Park, Central Nepal Himalaya. *Journal of Metamorphic Geology*, 13 : 595–612, 1995. (Cité page 11.)

R. P. Metcalfe. Gondwanaland dispersion, Asian accretion and evolution of Eastern Thethys. *Australian Journal Of Earth Sciences*, 43 :605–623, 1996. (Cité page 12.)

P. Molnar et P. England. Late Cenozoic uplift of mountain ranges and global climate change : chicken and egg ? *Nature*, 346 :29–34, 1990. (Cité page 4.)

D. R. Montgomery, G. Balco, et S. D. Willett. Climate, tectonics, and the morphology of the Andes. *Geology*, 29 :579–582, 2001. (Cité page 4.)

J. L. Mugnier, E. Chalaron, G. Mascle, B. Pradier, et G. Herail. Structural and thermal evolution of the Siwaliks of western Nepal. *Journal of Nepal Geological Society*, 11 :171–178, 1995. (Cité page 202.)

J. L. Mugnier, P. Huyghe, P. Leturmy, et F. Jouanne. Thrust Tectonics and Hydrocarbon Systems. Chapitre Episodicity and rates of thrust sheet motion in Himalaya (Western Nepal), pages 1–25. AAPG Memoir 82, 2003. (Cité page 215.)

J. L. Mugnier, P. Huyghe, P. Leturmy, et F. Jouanne. Episodicity and rates of thrust-sheet motion in the Himalayas (Western Nepal). Dans *Thrust tectonic and Hydrocarbon systems : AAPG Memoires*, pages 1–24, X, 2004. (Cité pages 5, 11, 17, 199, 202, 209 et 211.)

J. L. Mugnier, P. Leturmy, P. Huyghe, E. Chalaron, G. Vidal, L. Husson, et B. Delcaillau. The Siwaliks of western Nepal : I. Geometry and kinematics. *Journal of Asian Earth Sciences*, 17 :629–642, 1999. (Cité pages 199, 200 et 334.)

C.W. Naeser et R.L. Fleischer. Age of the apatite at Cerro de Mercado, Mexico : A problem for fission track annealing correction. *Geaophisical Research Letters*, 1 : 67–70, 1975. (Cité page 84.)

Y. Najman, A. Carter, G. Olivers, et E. Garzanti. Provenance of Escene foreland basin sediments, Nepal : Constraints to the timing and diachroneity of early Himalayan orogenesis. *Geological Society of America*, 33-4 :309–312, 2005. (Cité page 79.)

Y. M. R. Najman, M. S. Pringle, M. R. W. Johnson, A. H. F. Robertson, et J. R. Wijbrans. Laser $^{40}Ar/^{39}Ar$ dating of single detrital muscovite grains from early foreland-basin sedimentary deposits in India : Implications for early Himalayan evolution. *Geology*, 25-6 :535–538, 1997. (Cité page 13.)

K. Nakayama et P. D. Ulak. Evolution of fluvial style in the Siwalik Group in the foothills of the Nepal Himalaya. *Sedimentary Geology*, 125(3-4) :205–224, Mai 1999. (Cité page 210.)

K. D. Nelson. Partially molten middle crust beneath southern Tibet : synthesis of project INDEPTH results. *Science*, 274 :1684–1687, 1996. (Cité pages 20, 21 et 331.)

M. R. Pandey, R. P. Tandukar, J. P. Avouac, J. Vergne, et Th. Heritier. Seismotectonics of the Nepal Himalaya from a local seismic network. *Journal of Asian Earth Sciences*, 17(5-6) :703–712, 1999. (Cité pages 21 et 331.)

R. P. Parrish et K. V. Hodges. Isotopic constrints on the age and provenance of the Lesser and Greater Himalayan sequences, Nepales Himalaya. *Geological Society of America Bulletin*, 108 :904–911, 1996. (Cité pages 16 et 75.)

P. Patriat et J. Achache. India-Eurasia collision chronology has implications for crustal shortening and driving mechanism of plates. *Nature*, 311(5987) :615–621, Octobre 1984. (Cité page 17.)

A. Patzelt, H. Li, J. Wang, et E. Appel. Paleomagnetism of Cretaceous to Tertiary sediments from southern Tibet : Evidence for the extent of the northern margin of India prior to the collision with Eurasia. *Tectonophysics*, 259 :259–284, 1996. (Cité page 17.)

A. Pecher. The metamorphism in the central Himalaya. *Journal of Metamorphic Geology*, 7 :31–41, 1989. (Cité page 12.)

A. Pecher et P. Le Fort. The metamorphism in central Himalaya : its relation with thrust tesctonic. *Sciences de la Terre, v. Mémoire*, 47 :285–309, 1986. (Cité page 11.)

M. K. Rahn, M. T. Brandon, G. E. Batt, et J. I. Garver. A zero-damage model for fission-track annealing in zircon. *American Mineralogist*, 89(4) :473–484, Avril 2004. (Cité page 94.)

S. M. Rai. *Les nappes de Katmandou et du Gosainkund, Himalaya du Népal central (étude cartographique, structurale, métamorphique, géochimique et radiochronologique)*. PhD thesis, Université Joseph Fourrier, 1998. (Cité pages 27, 76, 110, 112, 135, 220 et 334.)

L. Ratschbacher, W. Frisch, G. Liu, et C. Chen. Distributed deformation in southern and western Tibet during and after the India-Asia collision. *Journal Of Geophysical Research*, 99 :19817–19945, 1994. (Cité page 16.)

P. W. Reiners et M. T. Brandon. Using Thermochronology to Understand Orogenic Erosion. *Annual Review of Earth and Planetary Sciences*, 34(1) :419–466, 2006. (Cité pages 76, 77 et 332.)

T.L. Reiners, P.W. Spell, S. Nicolescu, et K.A. Zanetti. Zircon $(U-Th)/He$ thermochronometry : He diffusion and comparisons with $^{40}Ar/^{39}Ar$ dating. *Geochim. Cosmochim. Acta*, 68 :1857–87, 2004. (Cité page 76.)

G.A. Robbins. Radiogenic argon diffusion in muscuvite under hydrothermal conditions. Master's thesis, Brown University, Providence, RI, 1972. (Cité page 76.)

X Robert. Analyse thermochronologique des sédiments Siwalicks : implications pour la séquence d'activité des failles et la mécanique du prisme frontal de l'Himalaya. Master's thesis, OSUG, Université Joseph Fourrier, Grenoble 1, France, 2005. (Cité pages 99 et 202.)

D. B. Rowley. Age of initiation of collision between India and Asia : a review of stratigraphic data. *Earth And Planetary Science Letters*, 145 :1–13, 1996. (Cité page 12.)

J.-Y. Royer et P. Patriat. Himalaya - Tibet, le choc des continents. Chapitre L'inde part à la dérive, pages 25–31. Avouac, J.-P. and De Wever, P., 2002. (Cité pages 14 et 330.)

M. Sambridge. Geophysical Inversion with a Neighbourhood Algorithm -I. Searching a parameter space. *Geophysical Journal International*, 138 :479–494, 1999a. (Cité pages 78, 92, 102, 103 et 334.)

M. Sambridge. Geophysical Inversion with a Neighbourhood Algorithm -II. Appraising the ensemble. *Geophysical Journal International*, 138 :727–746, 1999b. (Cité pages 78 et 102.)

U. Scharer et C.J. Allegre. The Palung granite (Himalaya ; high resolution U-Pb systematics in zircon and monazite. *Earth And Planetary Science Letters*, 63 :423–432, 1983. (Cité page 23.)

D. Schelling. The tectonostratigraphy and structure of the eastern Nepal Himalaya. *Tectonics*, 11 :925–943, 1992. (Cité page 20.)

D. Schelling et K. Arita. Thrust tectonics, crustal shortening, and the structure of the far eastern Nepal, Himalaya. *Tectonics*, 10 :851–862, 1991. (Cité page 20.)

V. Schulte-Pelkum, G. Monsalve, A. Sheehan, M. R. Pandey, S. Sapkota, R. Bilham, et F. Wu. Imaging the Indian subcontinent beneath the Himalaya. *Nature*, 435 : 1222–1225, 2005. ISSN 0028-0836. (Cité page 20.)

M. Searle, R.I. Corfield, B. Stephenson, et J. McCarron. Structure of the North Indian continental margin in the Ladakh-Zanskar Himalayas : implications for the timing of obduction of the Spontang ophiolite, India-Asia collision and deformation events in the Himalaya. *Geol. Mag.*, 134 :297–316, 1997. (Cité page 13.)

T.A. Steven, H.H. Mehnert, et J.D. Obradovich. Age of volcanic activity in the San Juan Mountains, Colorado. *U.S. geological Survey professional paper*, 575-D :47–55, 1967. (Cité page 84.)

R. J. Stewart et M. T. Brandon. Detrical-zircon fission-track ages for the Hoh Formation : Implications for late Cenozoic evolution of the Cascadia subduction wedge. *Geological Society of America Bulletin*, 116 :60–75, 2004. (Cité page 90.)

J. Stocklin. Geology of Nepal and its regional frame. *Journal of Geological Society*, 137 :1–34, 1980. (Cité pages 11, 22 et 23.)

D. Stolar, S. Willet, et G. Roe. Climate and tectonic forcing of a critical orogen. *Geological Society of America Special Paper*, 398 :241–250, 2006. (Cité pages 3 et 329.)

K. Stuwe, L. White, et R. Brown. The influence of eroding topography on steady–state isotherms. Application to fission track analysis. *Earth and Planetary Sciences Letters*, 124 :63–74, 1994. (Cité pages 98 et 109.)

J. Suppe. Geometry and kinematics of fault-bend faulding. *Am. J. Sci.*, 283 :684–721, 1983. (Cité page 96.)

T. Tagami. Low-temperature Thermochronology. Chapitre Zircon fission track and applications to fault studies, pages 411–448. Rev. Mineral. Geoch., 2005. (Cité page 80.)

R. Tapponnier, G. Peltzer, A. Y. Le Dain, Rolando Armijo, et P. Cobbold. Propagating extrusion tectonics in Asia ; new insights from simple experiments with plasticine. *Geology*, 10(12) :611–616, Décembre 1982. (Cité page 13.)

R. C. Thiede, J. R. Arrowsmith, B. Bookhagen, M. O. Mcwilliams, E. R. Sobel, et M. S. Strecker. From tectonically to erosionally controller developement of the Himalayan orogen. *Geology*, 33/8 :689–692, 2005. (Cité page 5.)

R. C. Thiede, B. Bookhagen, J. R. Arrowsmith, E. R. Sobel, et M. S. Strecker. Climatic control on rapid exhumation along the Southern Himalayan Front. *Earth and Planetary Sciences Letters*, 222 :791–806, 2004. (Cité page 5.)

D. L. Turcotte et G. Schubert. *Geodynamics : Applications of Continuum Physics to Geological Problems*. 1982. (Cité page 3.)

P. van der Beek. *Tectonic evolution of continental rifts*. PhD thesis, Faculty of Earth Sciences, Free University, Amsterdam, 1995. (Cité page 94.)

P. van der Beek, X. Robert, J.-L. Mugnier, M. Bernet, P. Huyghe, et E. Labrin. Late Miocene - Recent denudation of the central Himalaya and recycling in the foreland basiin assessed by detrital apatite fission-track thermochronology of Siwalik

sediment, Nepal. *Basin Research*, 18 :413–434, 2006. (Cité pages 17, 79, 91, 99, 199, 200, 201, 202, 203, 204, 205, 206, 208, 273, 333, 334 et 335.)

J.-C. Vannay et K.D. Hodges. Tectonometamorphic evolution of the Himalayan metamorphic core between Annapurna and Dhaulagiri, central Nepal. *Journal of Metamorphic Geology*, 14 :635–656, 1996. (Cité page 11.)

G. A. Wagner et P. Van Den Haute. *Fission Track Dating*. Elsevier, Amsterdam, 1992. (Cité page 80.)

D. M. Jr. Whipp, T. A. Ehlers, A. Blythe, K. W. Huntington, K. Hodges, et D. Burbank. Plio-quaternary exhumation history of the central Nepalese Himalaya : 2. Thermokinematic and thermochronometer age prediction model. *Tectonics*, 26 : 1–23, 2007. (Cité pages 27, 75, 76 et 99.)

D.M. Whipp et T. A. Ehlers. Influence of groundwater flow on thermochronometer-derived exhumation rates in the central Nepalese Himalaya. *Geology*, 35 :851–854, 2007. (Cité pages 93 et 212.)

S. D. Willett. Orogeny and orography : the effects of erosion on the structure of mountain belts. *Journal of Geophysical Research*, 104 :28,957–28,981, 1999. (Cité page 4.)

S. D. Willett, D. Issler, C. Beaumont, R. A. Donelick, et A. Grist. Inverse modeling of annealing of fission tracks in apatite 2 ; Application to the thermal history of the Western Canada Sedimentary Basin. *American Journal of Science*, 297 :970–1011, 1997. (Cité page 92.)

C. Wobus, K. Whipple, et K. Hodges. Neotectonics of the central Nepalese Himalaya : Constraints from geomorphology, detrital $^{40}Ar/^{39}Ar$ thermochronology, and thermal modeling. *Tectonics*, 25(7036) :–, Avril 2006. ISSN 0028-0836. (Cité pages 7, 27 et 221.)

R. A. Wolf, K. A. Farley, et D. M. Kass. Modeling of the temperature sensitivity of the apatite (U-Th)/He thermochronometer. *Chemical Geology*, 148 :105–114, 1998. (Cité page 94.)

An Yin. Cenozoic tectonic evolution of the Himalayan orogen as constrained by along-strike variation of structural geometry, exhumation history, and foreland sedimentation. *Earth-Science Reviews*, 76(1-2) :1–131, Mai 2006. (Cité pages 5, 13, 16 et 100.)

P.K. Zeitler, A.Z. Meltzer, P.O. Koons, D. Craw, et B. Hallet. Erosion, Himalayan geodynamics, and the geomorphology of metamorphism. *GSA Today*, 11 :4–, 2001. (Cité page 4.)

W. Zhao et K. D. Nelson. Project INDEPTH Team. Deep seismic reflection evidence for continental underthrusting beneath Southern Tibet. *Nature*, 366 :557–559, 1993. (Cité pages 20, 21 et 331.)

M.L. Zoback. First and second order patterns of stress in the lithosphere : the World Stress Map Project. *Journal Of Geophysical Research*, 97 :11703–11728, 1992. (Cité page 3.)

Notations

MFT	Main Frontal Thrust
MDT	Main Dun Thrust
MBT	Main Boundary Thrust
MCT	Main Central Thrust
STD	South Tibetan Detachment
LH	Lesser Himalaya
HHC	High Himalaya
TSS	Tethyan Sedimentary Series
AFT	Trace de Fission sur Apatite
ZFT	Trace de Fission sur Zircon
PAZ	Partial Annealing Zone
NA	Neighbourhood Algorythm

Annexes

A

Sommaire

A.1 Méthodologie d'inversion

La méthodologie des inversions effectuée a été décrite dans Braun et Robert (2005), lors d'une étude pré-thèse sur le massif du Dabie Shan, en Chine.

Earth Surface Processes and Landforms
Earth Surf. Process. Landforms **30**, 1203–1225 (2005)
Published online in Wiley InterScience (www.interscience.wiley.com). **DOI:** 10.1002/esp.1271

Constraints on the rate of post-orogenic erosional decay from low-temperature thermochronological data: application to the Dabie Shan, China

Jean Braun[1]* and Xavier Robert[2]

[1] *Research School of Earth Sciences, The Australian National University, Canberra ACT 0200, Australia. Now at Géosciences Rennes, Université de Rennes 1, Rennes, France*

[2] *Département de Géologie, Ecole Normale Supérieure, Lyon, France. Now at Laboratoire de Géodynamique des Chaînes Alpines, Université Joseph Fourier, Grenoble, France*

**Correspondence to: J. Braun, Géosciences Rennes, Université de Rennes 1, Av. Gl Lectere, Rennes 35042, France. E-mail: Jean.Braun@univ-rennes1.fr*

Received 1 September 2004;
Revised 1 March 2005;
Accepted 17 March 2005

Abstract

We have investigated whether low temperature thermochronological datasets can be used to constrain the rate of surface evolution during the post-orogenic phase of a mountain belt. We use a numerical method to solve the heat transport equation in the Earth's crust, including the effects of a changing, finite-amplitude topography and the resulting flexural isostatic rebound. We demonstrate that accurate estimates of the amount of relief loss can be obtained by applying a recently developed spectral method that is based on estimates of the relationship between age and surface elevation as a function of topographic wavelength. We also show that the rate at which topography decays with time following cessation of tectonic activity can be constrained from estimates of exhumation rate derived from the slope of age–elevation profiles collected across short wavelength topography. Using the Neighbourhood Algorithm to perform a thorough search through parameter space, we are able to find a tectonomorphic scenario that predicts age distributions compatible with a thermochronological dataset collected in the Dabie Shan of eastern China by Reiners *et al.* (*American Journal of Science* 2003, vol. 303, pp. 489–518). We demonstrate that, in the Dabie Shan, the mean topographic relief has decreased by a factor of 2·5 to 4·5 during the last 60–80 Ma, while the mountain belt experienced a mean exhumation rate of 0·01 to 0·04 km Ma^{-1}. We confirm the conclusions of Reiners *et al.* that there is no need to invoke a discrete Cenozoic tectonic event to explain the observed age distribution. The thermochronological dataset can also be used to put constraints on the effective elastic thickness of the lithosphere underlying the orogen (10 to 30 km). There is, however, a trade-off between elastic thickness, mean exhumation rate and amount of topographic relief loss. The most likely scenario also predicts that the topography has decreased at a constant rate since the end of orogenic activity about 100 Ma ago.

Keywords: thermochronology; erosion; Dabie Shan; flexure

Introduction

It is well known that the rate at which landscapes evolve with time is strongly dependent on the local tectonic forcing (Kooi and Beaumont, 1996). The classical concepts of dynamic equilibrium landforms (Hack, 1960), phases of growth and decay of relief (Penck, 1924), and relaxation of landforms (Davis, 1899) can be understood as different aspects of the behaviour of the coupled tectonic–erosion system (Kooi and Beaumont, 1996). This is because, at the scale of an orogen, erosional processes can be characterized by a typical timescale (or rate at which they take place), the 'erosional response time' (Kooi and Beaumont, 1996). The erosional response time of an orogen depends on its geometry, i.e. its height, extent and overal shape, but also on the local climate and on the nature of the dominant process(es) for erosion (fluvial, glacial or hillsope processes, for example) (Kooi and Beaumont, 1996; Lague *et al.*, 2003; Whipple and Tucker, 1999).

In areas of slow tectonic forcing, erosion processes are usually capable of rapidly achieving a steady state in which the tectonic flux, i.e. the rate of mass input into an orogenic area, is perfectly compensated by the erosional flux, i.e. the removal of mass by erosion and transport (Kooi and Beaumont, 1996). In cases where the tectonic forcing takes place over a timescale that is similar to the erosional response time of the system, the erosional flux is always out of phase with respect to the tectonic flux (Kooi and Beaumont, 1996). However, when an orogen is subjected to a very rapid or discrete tectonic event, the erosional response takes the form of an exponential decay at a rate directly determined by the erosional response time (Kooi and Beaumont, 1996). Consequently, the erosional decay of a mountain belt that follows cessation of tectonic activity, usually in response to a discrete event of plate reorganization, provides us with an opportunity to determine the erosional response time of orogenic systems.

Erosion causes rocks to be advected towards the surface and cool. The timing of this cooling can be well constrained by thermochronology. In essence, for a given thermochronological system, the 'age' of a rock corresponds to the time at which it cooled through a so-called 'closure temperature' (Dodson, 1973). Dating rocks should therefore provide us with good estimates on the rate at which rocks are brought to the surface and, consequently, with good constraints on the rate at which surface erosion takes place. The purpose of the work described here is to demonstrate whether one can extract useful information from thermochronological datasets about the evolution of surface topography during the post-orogenic phase of a mountain belt.

It is, however, important to realize that surface erosion and transport in a 'tectonically quiet' area causes the underlying lithosphere to 'rebound' by isostasy (Molnar and England, 1990; Montgomery, 1994) at a scale that is determined by the flexural strength of the underlying lithosphere. This orogen-wide uplift causes further surface erosion. Thus, to use thermochronological data to quantify the rate of surface erosion and, from it, derive an estimate of the rate of relief evolution, one needs to incorporate the effect of isostasy.

In this paper, we first discuss the isostatic rebound associated with the evolution of surface topography by erosional processes. We consider the importance of the lithosphere flexural strength on the isostatic response of the system to erosion. Using a numerical method to solve the heat transport equation in three dimensions, we show how a synthetic age distribution can be computed and how it is affected by our assumption about the isostatic response of the lithosphere to surface unloading. We then investigate whether the age distribution is sensitive to the assumed erosional response time. Finally we use an inversion method to extract information on the rate of surface relief evolution in the Dabie Shan, from a thermochronological dataset collected by Reiners *et al*. (2003) in the area.

Local Isostasy

The post-orogenic phase of most mountain belts is characterized by a gradual erosion of the relief/topography created during the active tectonic phase. This erosion results in unloading of the underlying lithosphere and subsequent isostatic adjustment. The principle of isostasy states that there is a region beneath the lithosphere where rocks are so weak that they cannot sustain any horizontal stress gradient over geological times (i.e. greater than a few tens of thousands of years). This implies that, at isostatic equilibrium, the weight of adjacent lithospheric columns must be equal. Erosion of surface topography results in a reduction of the weight of the underlying lithospheric column and must therefore be compensated by vertical uplift.

As shown in Figure 1, surface erosion by an amount E_0 (panel b) of a reference lithospheric column (panel a) of crustal thickness h and total thickness $h + L$ results in an isostatic surface uplift by an amount u (panel c) such that the weights of the two columns (a and c) down to the compensation depth $h + L + d$ are identical. This leads to the following relationship:

$$h\rho_c + L\rho_m + d\rho_a = (h - E_0)\rho_c + L\rho_m + (d + u)\rho_a \tag{1}$$

where ρ_c, ρ_m and ρ_a are the mean densities of the crust, mantle lithosphere and asthenosphere, respectively, from which an expression for the isostatic uplift u as a function of the erosion, E_0, can be derived:

$$u = E_0 \frac{\rho_c}{\rho_a} \tag{2}$$

From this relationship, one can also derive the expression for the amount of erosion, E, needed to reduce topography by an amount Δh:

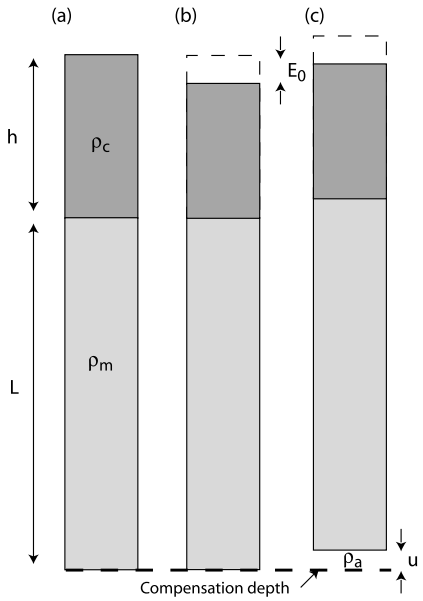

Figure 1. Erosion at the surface of a reference lithospheric column (a) by an amount E_0 (b) leads to isostatic uplift of the column by an amount u (c). For typical density and crustal thickness values, $u = 4$ to $5 \times E_0$.

$$E = \frac{\Delta h}{1 - \frac{\rho_c}{\rho_a}} \tag{3}$$

which, for average values of upper crustal and asthenospheric densities of 2600 and 3200 kg m^{-3}, respectively, leads to an isostatic amplification factor of approximately 5·3. This means that for every kilometre of surface topography reduction, one needs to erode approximately 5·3 km of crustal rocks. This also means that during the post-orogenic phase of a mountain belt, erosion of the topography may lead to tens of kilometres of exhumation, rock cooling and the subsequent closure of thermochronological systems, especially those characterized by a low closure temperature, such as apatite (U-Th)/He dating or apatite fission track dating. Consequently, for those thermochronological systems, ages observed at the surface of an ancient mountain belt are more likely to provide information about the rate of erosion and surface relief evolution during the post-orogenic phase of the mountain belt than about the rate of tectonic uplift and exhumation during its constructive (or orogenic) phase.

Flexural Isostasy

The concept of an 'isostatic compensation depth' leads to a vertically integrated mass balance only if one neglects the lateral strength of the lithosphere. This is usually true for very wide load, i.e. loads that are much wider than the thickness of the lithosphere. However, the load associated with erosional processes at the scale of a single valley or mountain range (1 to 100 km) is typically narrower than the thickness of the continental lithosphere (typically ranging from a few kilometres to several hundred kilometres).

The lateral strength of the continental lithosphere is usually taken into account by parameterizing its isostatic response as that of a thin, yet strong, elastic plate 'floating' on the underlying inviscid asthenosphere (Turcotte, 1979). Under the assumption that the surface deflection of the lithosphere, w, is small in comparison to its thickness, one can derive the following partial differential equation that relates w to an applied distributed vertical surface load, $q(x)$:

$$D\frac{\partial^4 w}{\partial x^4} + (\rho_a - \rho_s)gw = q(x) \tag{4}$$

where x is the horizontal spatial coordinate, D is the flexural rigidity of the plate, ρ_a and ρ_s are the densities of the asthenosphere and sediment/crust/air, respectively, and g is gravitational acceleration (Turcotte, 1979). What ρ_s represents depends on the assumption made on the evolution of the surface following its deflection by elastic rebound: if subsidence is accompanied by sedimentation, ρ_s is sediment density; if no sedimentation takes place, ρ_s is water density; where the surface is uplifted but no erosion takes place, ρ_s should be upper crustal rock density; where the surface is uplifted and erosion is very efficient, ρ_s should be zero.

The flexural rigidity can be expressed in terms of the elastic constants, Y_m and ν (Young's modulus and Poisson's ratio), and the assumed elastic thickness of the plate, L_e (Turcotte, 1979):

$$D = \frac{Y_m L_e^3}{12(1-\nu^2)} \tag{5}$$

Periodic Loading

The flexural isostatic response of the lithosphere to a periodic surface load (resulting, for example, from a periodic surface topography of amplitude h_0 and wavelength λ) can be obtained from the solution of Equation 4 in which:

$$q(x) = \rho_c g h_0 \sin\frac{2\pi x}{\lambda} \tag{6}$$

The solution is in phase with the load:

$$w = w_0 \sin\frac{2\pi x}{\lambda} \tag{7}$$

and its amplitude, w_0, is given by:

$$w_0 = \frac{h_0}{\frac{\rho_a}{\rho_c} - 1 + \frac{D}{\rho_c g}\left(\frac{2\pi}{\lambda}\right)^4} \tag{8}$$

The amplitude of the deformation depends on the wavelength of the load, λ, compared to the flexural wavelength, x_α, given by:

$$x_a = \left(\frac{D}{\rho_c g}\right)^{\frac{1}{4}} \tag{9}$$

Two end-member cases exist. First, when the wavelength of the topography is small in comparison to the flexural wavelength

$$\lambda << x_\alpha \tag{10}$$

the deflection of the plate, and thus the isostatic response of the lithosphere, becomes neglegible in comparison to the amplitude of the surface topography:

$$w_0 << h_0 \tag{11}$$

This means that the load of the topography is small enough to be fully compensated by the flexural strength of the lithosphere. Second, in cases where the wavelength of the topography is much greater than the flexural wavelength

$$\lambda >> x_\alpha \tag{12}$$

the flexural strength of the lithosphere becomes negligible and the topography is in local isostatic equilibrium:

$$w_0 = \frac{\rho_c h_0}{\rho_a - \rho_c} = w_0^e \tag{13}$$

The degree of isostatic compensation, C, of a topographic load of wavelength λ is defined as the ratio of the deflection of the lithosphere (Equation 13) to its maximum local isostatic (or hydrostatic) deflection (Equation 8):

$$C = \frac{w_0}{w_0^e} = C = \frac{\rho_a - \rho_c}{\rho_a - \rho_c + \frac{D}{g}\left(\frac{2\pi}{\lambda}\right)^4} \tag{14}$$

For small wavelength topography ($\lambda << x_\alpha$), C tends towards 0; for long wavelength topography ($\lambda >> x_\alpha$), C tends towards 1.

Isostatic Response to Relief Reduction

Whether topography is in isostatic equilibrium or fully compensated by the lateral strength of the lithosphere will affect the amount of isostatic amplification associated with post-orogenic relief reduction by erosion. To follow the convention of Braun (2002a), we will assume that today's topographic amplitude is β times what it was at the end of the orogenic phase (i.e. before the post-orogenic decay started). The change in surface topography is given by:

$$\Delta h = \left(\frac{1}{\beta} - 1\right) h_0 \tag{15}$$

where h_0 is the initial topography. Using Equation 8, Equation 3 can be generalized to obtain the total erosion, E, necessary to achieve a change in topography, Δh, at a wavelength λ, taking into account the flexural response of the lithosphere:

$$\begin{aligned} E &= \left(\frac{1}{\beta} - 1\right) h_0 + \left(\frac{1}{\beta} - 1\right) h_0 \frac{\rho_c}{\rho_a - \rho_c} C \\ &= \left(\frac{1}{\beta} - 1\right) h_0 \left(1 + \frac{\rho_c}{\rho_a - \rho_c} C\right) \end{aligned} \tag{16}$$

E tends towards the local isostatic solution (Equation 3) when C tends towards 1 (long wavelength topographic change); E tends towards the change in surface topography, Δh, when C tends towards 0 (short wavelength topographic change).

Topography Spectral Content and Age–Elevation Gain Function

Surface topography in active orogenic belts is typically characterized by a range of wavelengths, from small-scale relief at the valley scale to large-scale relief at the mountain belt scale (Huang and Turcotte, 1989). As suggested by (Braun, 2002a), this relatively wide spectrum of surface topography amplitude can be used to extract meaningful information about mean exhumation rate and the rate of surface topography change from thermochronological datasets. Indeed, the penetration depth of the thermal perturbation caused by finite amplitude surface topography decays exponentially with the wavelength of the topography (Turcotte and Schubert, 1982). Isotherms thus tend to follow the shape of the long wavelength component of the topography, while they are unaffected by the short wavelength component. This, in turn, implies that age–elevation relationships measured along very steep topographic profile provide a good estimate of the mean exhumation rate, while age–elevation relationships measured over long distances (i.e. of the same order as the longest wavelength in the topographic signal) provide a good estimate of the rate of change of the amplitude of the topography (Braun, 2002a).

A spectral method can be used to extract this information from age profiles collected along linear transects that (a) sample the surface topography at a wide range of wavelengths and (b) are orientated in such a way that the mean exhumation rate is relatively constant along the transect (Braun, 2002a). Optimally, such transects should contain up to several tens of regularly spaced points, be located in the part of the mountain belt characterized by the highest topographic

relief and orientated in a way that the mean exhumation rate is uniform along the transect and that the transect is perpendicular to drainage direction (i.e. mean local slope). Age–elevation data collected along the transect can then be used to build a gain function, G, that describes the relationship between age and elevation as a function of the wavelength of the topography, λ. The gain function can be constructed following classical spectral analysis methods (Jenkins and Watts, 1968) from an input signal (here the topographic profile) and an output signal (here the age dataset):

$$G(\lambda) = \frac{\sqrt{C_{12}^2 + Q_{12}^2}}{C_{11}} \tag{17}$$

where C_{12} and Q_{12} are the real and imaginary parts of the cross-spectrum obtained from the real and imaginary parts of the smoothed spectral estimators of the input and output signals. These estimators are, in turn, obtained from the Fourier transforms of the windowed input (elevation, z) and output (age, a) signals, R_z, I_z and R_a, I_a (Jenkins and Watts, 1968):

$$\begin{aligned} C_{12} &= R_z R_a + I_z I_a \\ Q_{12} &= I_z R_a - R_z I_a \end{aligned} \tag{18}$$

C_{11} is the power spectrum of the input signal:

$$C_{11} = R_z^2 + I_z^2 \tag{19}$$

The smoothed spectral estimators are obtained by applying a triangular Bartlett window (see Jenkins and Watts, 1968, p. 244) to the elevation and age profiles prior to the calculation of the Fourier transforms. Confidence intervals can be calculated from the smooth spectral estimators (see Jenkins and Watts, 1968, p. 437).

At short wavelengths, gain estimates (G_S) are inversely proportional to the mean exhumation rate; at long wavelengths, gain estimates (G_L) contain information on the change in surface topography amplitude (relief), β, over a time equal to the mean value of the age dataset:

$$\beta = \frac{1}{1 - \dfrac{G_L}{G_S}} \tag{20}$$

The derivation of this important relationship as well as more information on the use of the spectral method to interpret age–elevation datasets can be found in Braun (2002a).

Here, we propose to determine whether the spectral method can be used to estimate the mean rate of exhumation and the rate of topographic change during the post-orogenic phase in the evolution of a mountain belt. In such a situation, the rate of change of the geometry of the surface by surface erosion is also controlling the mean exhumation rate of the area through isostatic compensation. Thus, the two signals that we are trying to deconvolve by spectral analysis, are, in fact, spatially correlated at a wavelength that is determined by the flexural properties of the underlying lithosphere.

Effect on Age Distribution

To demonstrate this point, we first use a numerical model solving the heat transfer equation to investigate the effect of erosion-driven isostatic rebound on the distribution of ages measured along the surface of an old orogenic belt. The model is a modified version of the Pecube software, developed by Braun (2003), in which we have incorporated a module to calculate the vertical surface deflection of a thin elastic plate due to an applied surface vertical load, using the spectral method described in Nunn and Aires (1988). Pecube is a finite element code solving the heat transport equation in three dimensions:

$$\frac{\partial T}{\partial t} + \dot{E}\frac{\partial T}{\partial z} = \kappa\frac{\partial^2 T}{\partial x^2} + \kappa\frac{\partial^2 T}{\partial y^2} + \kappa\frac{\partial^2 T}{\partial z^2} + \frac{H}{c} \tag{21}$$

including the effects of vertical heat advection due to erosion ($\dot{E}$), heat conduction and heat production. T is temperature, x, y and z are spatial coordinates, t is time, k is thermal diffusivity, H is the rate of heat production per unit mass

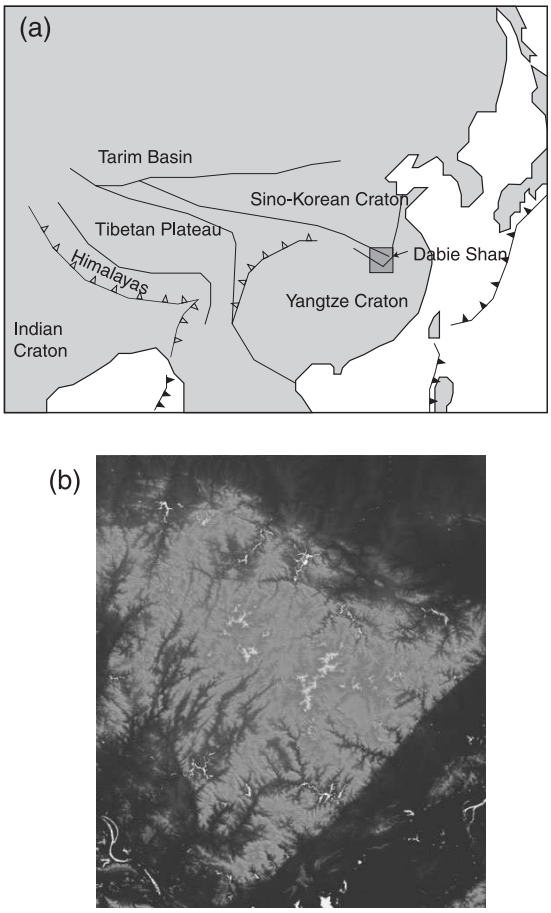

Figure 2. (a) Location of major tectonic elements surrounding the Dabie Shan and (b) topographic data used in this study.

and c is heat capacity. Pecube has been designed to accurately predict the effect of a finite amplitude, time-varying surface topography on the underlying temperature structure. More details on Pecube can be found in Braun (2003). Flexural isostasy has been included by computing at each time step, from the imposed change in surface topography, Δh, the resulting negative load, $\rho_c g \Delta h \times \Delta x \Delta y$, and the ensuing isostatic uplift. This uplift is then imposed as a velocity term in a system of reference that is fixed with respect to the base of the model.

Rather than using a synthetic topographic surface, we have used a topographic dataset from the Dabie Shan area in southeastern China (Figure 2a). The reason for this particular choice of natural topography is that we also have access to a rather extensive thermochronological dataset for this area (Reiners *et al*., 2003). This orogen developed between the northern edge of the Yantze craton and the southeastern corner of the Sino-Korean craton during a series of subduction-related episodes of crustal shortening, from the late Palaeozoic to the mid-Cretaceous (Schmid *et al*., 2001). There is debate on whether the orogen was reactivated during the ongoing Indo-Asian collision and whether some of the present-day topographic relief is the result of this Cenozoic reactivation (Grimmer *et al*., 2002). Alternatively, the topography is the erosional remnant of a much larger amplitude relief that was entirely formed in the Cretaceous (Reiners *et al*., 2003).

Later in this paper, we will make use of the thermochronological data to extract from them quantitative estimates of the amount of post-orogenic topographic decay and its timing. In a first step, however, we will use the topography of this area (a 190 by 220 km rectangular section extracted from the 30 arc second resolution DEM GTOPO30; Figure 2b) in a series of model runs in which we investigate the effect on low-T age distributions of the isostatic

rebound associated with a post-orogenic erosional phase. To perform this sensitivity analysis, we first impose that the topographic relief was arbitrarily four times larger 100 Ma ago than it is today and that it has decayed linearly since then, to reach its present-day value at the end of the model run. Changes in surface relief are imposed by changing the amplitude of the topography, not its shape. This is an approximation that is likely to be correct in a setting where horizontal tectonic advection is not important, such as during the post-orogenic phase of a mountain belt. In these situations, the potential for stream capture and reorganization of the drainage network is indeed small. It is, however, likely that the small-scale diffusive processes acting along hillslopes will decrease small-scale relief first and, in principle, one should assume a faster removal of the small-scale components of relief in comparison to its large-scale features. Hillslope processes are, however, active on a scale (tens to hundreds of metres) that is well below the horizontal scale of the topographic effects recorded by thermochronology.

We have first performed a series of five model runs to investigate how sensitive the predicted ages are to the assumed elastic plate thickness. The model runs differ by the assumed elastic plate thicknesses, 0, 1, 10, 20 and 40 km, which correspond to flexural wavelengths of 0, 4·1, 23, 39 and 66 km, respectively, if one assumes that $Y_m = 10^{11}$ Pa, $\nu = 0{\cdot}25$ and $\rho_c g = 3 \times 10^4$ Pa m^{-1}. The apatite He ages are computed from temperature–time histories derived from the results of the Pecube model using the method described by Wolf *et al.* (1998). We do not specify an *a priori* closure temperature for the (U-Th)/He system in apatite; the temperature range across which the system will 'close' is internally determined, including the effect of cooling rate and diffusion domain size. A temperature of 600 °C is imposed at the base of the model, 30 km beneath the surface. Note that, although there is a likely relationship between the effective elastic plate thickness and the thermal structure of the lithosphere, here we have assumed that these two parameters are independent. Heat diffusivity is set at 25 km^2 Ma^{-1}. Temperature at the surface, T_s, is imposed to be proportional to topographic height, h, according to:

$$T_s = T_{msl} + \gamma h \tag{22}$$

where T_{msl} is temperature at mean sea level ($z = 0$) and is taken to be 10 °C, and γ is the lapse rate (4 °C km^{-1}), i.e. the rate of decrease of temperature with elevation in the atmosphere. Heat production over heat capacity, H/c, is uniform throughout the crust and set at 8 °C Ma^{-1}. The initial temperature structure is assumed to be at equilibrium (steady state) with the imposed boundary conditions. We performed several model runs in which the initial temperature structure was first calculated assuming a mean exhumation rate of 1 km Ma^{-1} to represent the active tectonic phase preceding the post-orogenic decay phase of the orogen, but found that it did not affect the results in a significant way.

The results of five model experiments are shown in Figure 3 as five predicted apatite (U-Th)/He age distributions across the strike of the orogen, from the northwest to the southeast. In all model runs, ages are young near the centre of the orogen (Figure 3), i.e. they are smaller than the length of the model run (100 Ma). We have chosen the mean geothermal gradient (600/30 = 20 °C km^{-1}) and the amount of topographic relief reduction ($\beta^{-1} = 4$) such that, even in the absence of isostatic rebound, rocks that end up at the surface of the model have a starting temperature well above the apatite He closure temperature, typically in the range 55–75 °C, and see their age set during the post-orogenic exhumation. The minimum reset ages, found near the centre of the orogen, are inversely proportional to the assumed elastic plate thickness. Because we have assumed that the rate of decrease in surface topographic relief is constant through time, the larger the total erosion, the younger the ages. For low values of the elastic plate thickness (0–1 km), the system is at or near local isostatic equilibrium and the reduction in surface topographic relief over the last 100 Ma causes very large (up to 6 km) isostatic rebound and erosion. As the elastic plate thickness is increased, the amount of isostatic rebound decreases and the total amount of erosion necessary to reduce the surface topographic relief by a factor of 4 decreases.

Effect on Age–Elevation Distributions

A different way to look at these results is to state that, on the scale on the orogen, the ages are inversely proportional to (present-day) elevation, i.e. ages are younger near the centre of the orogen where topography is currently the largest. However, if one looks at the relationship between age and elevation at the scale of an individual valley (10 km in length), three behaviours are observed (Figure 3). In cases where the flexural wavelength is larger than the width of the valleys ($L_e = 10$, 20, 40 km), there is a strong positive correlation between age and elevation; in the case where the flexural wavelength is similar to the width of the smallest valleys ($L_e = 1$ km), there is little variation in age with elevation; in the case where the flexural wavelength is smaller than the valley width ($L_e = 0$ km), predicted age is inversely proportional to elevation.

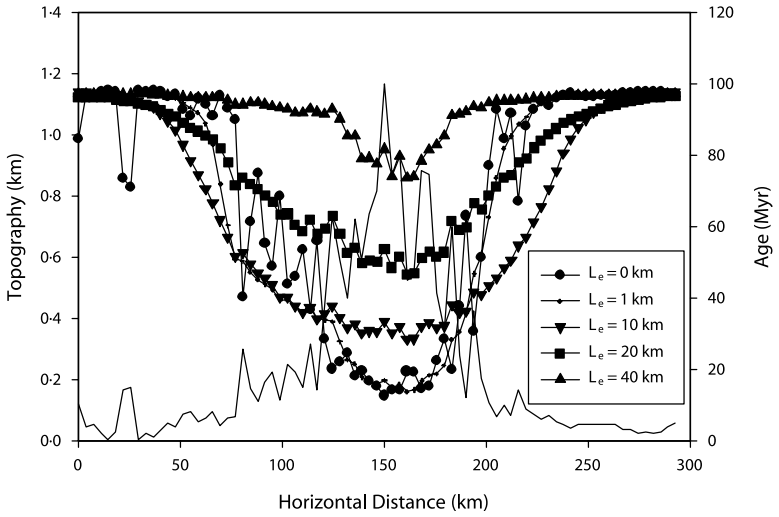

Figure 3. Topography and computed apatite He ages along a profile crossing the study area from the northwest to the southeast assuming different values for the elastic plate thickness.

This behaviour of the coupled erosional–isostatic system can be further documented by computing age–elevation profiles in two separate valleys, one near the centre of the orogen, the other half-way between the centre and one of its margins. Computed age–elevation profiles are shown in Figure 4. In both locations, the slope of the age–elevation relationship is negative when the flexural wavelength is very small and positive otherwise. When the elastic plate thickness is finite, the slope decreases with increasing elastic plate thickness. These synthetic transects are 'collected' across topographic features characterized by a wavelength (10 km) that is moderately larger than the critical wavelength, λ_c, given by the ratio of the closure temperature for the thermochronological system considered (55–75 °C) and geothermal gradient (20 °C km^{-1}) (Braun, 2002a). The perturbation caused by the valleys on the closure temperature isotherm is therefore moderate and the slope of the age–elevation profiles should provide a reasonable, yet overestimated measure of the local erosion rate (Braun, 2002a,b; Stüwe *et al*., 1994). In the case where the elastic thickness is large ($L_e = 20$ or 40 km) and isostatic rebound is negligible, total erosion is equal to the change in topographic amplitude (3 km near the centre of the orogen and 1·5 km near its margin) and the mean exhumation rate should be of the order of 0·03 or 0·015 km Ma^{-1}, respectively. The slope of the age–elevation relationship is 0·085 and 0·071 km Ma^{-1} near the centre of the orogen, for $L_e = 20$ and 40 km, respectively, and 0·041 and 0·087 km Ma^{-1} near the margin. When isostatic rebound becomes important (i.e. for smaller values of the assumed elastic plate thickness), the total erosion and, consequently, the mean erosion rate increase. This is why the model predicts that the apparent erosion rate derived from the slope of the age–elevation relationship measured along narrow valley profiles increases with decreasing elastic plate thickness.

Estimates of Relief Change Based on the Spectral Method

The results of these five model runs can also be used to determine under which circumstances the spectral method developed by Braun (2002a) can be used to estimate the amount of relief change experienced during the post-orogenic erosional decay of an ancient mountain belt. We first calculate the spectral content of the topographic profile along which age estimates will be used to determine the gain function. The results are shown in Figure 5 and demonstrate that the topographic profile is made of a long wavelength (approximately 150 km) component and a series of shorter wavelength components, the smallest above noise level is at approximately 12 km. We then estimate the value of the gain function between topography and age (G) at those two wavelengths and use them to compute the apparent change in topographic relief based on Equation 20.

To estimate the gain values G_L and G_S, we compute the power spectra of the topography and the predicted ages and combine their real and imaginary parts as detailed in Braun (2002a). We use two different methods to estimate

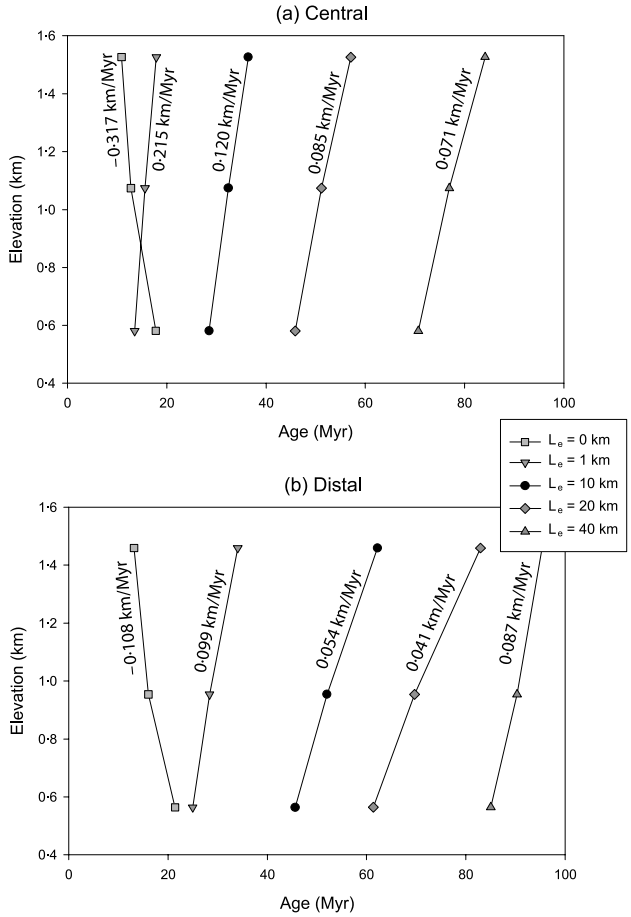

Figure 4. Computed apatite He age–elevation profiles along two 10-km-wide valleys, one near the centre of the orogen (a) and the other one half-way between the centre of the orogen and one of its margins (b). Each profile corresponds to a different value for the assumed elastic thickness, L_e.

the power spectra. The first method makes use of a Bartlett window, the second is based on multiple estimates of the spectrum from sub-samples of the topographic and age profiles which are then used to determine a mean value and standard deviation of the gain function at both wavelengths. The results are summarized in Table I. They demonstrate that the spectral method provides very good estimates of the topographic amplitude change when the plate thickness is of the order of 10 km or more. More generally, one can state that the spectral method can be used in situations where the degree of isostatic compensation, C, of the orogen is less than 0·5. For larger degrees of compensation (or smaller plate thicknesses), one of the main assumptions on which the spectral method is based is violated: the isostatic uplift and thus the mean erosion rate is not uniform across the orogen; in the case of local isostasy ($C = 1$), total erosion is directly proportional to topography and ages are inversely correlated to elevation, at all wavelengths.

Estimates of the elastic thickness of the continental lithosphere vary from a few to several hundred kilometres (Forsyth, 1985). In many cratonic areas, i.e. those which have not been subjected to a recent tectonic event, L_e estimates are consistently larger than 10 km (Bechtel *et al*., 1990; Maggi *et al*., 2000; Wang and Mareschal, 1999; Zuber *et al*., 1989). It is thus clear that the spectral method is likely to provide accurate estimates of topographic relief change associated with the erosional decay of ancient mountain belts.

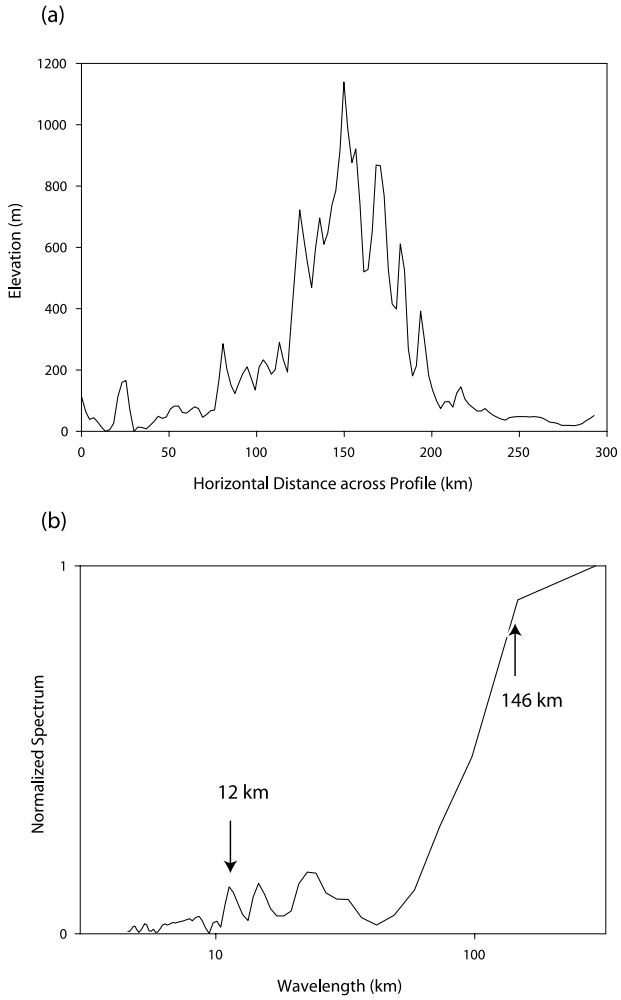

Figure 5. Topographic profile used to calculate the gain function (a) and its power spectrum (b). The arrows point to the components of the spectrum where the long wavelength gain value, G_L, and short wavelength gain value, G_S, are estimated to determine the amplitude of the relief loss (β^{-1}).

Table I. Computed gain values, G_L and G_S, and corresponding relief loss amplitude, β^{-1}, for five model runs characterized by different values of the elastic plate thickness, L_e. Method 1 is based on filtering of the age and elevation data by a Bartlett window. Method 2 is based on multiple computations of the gain function from sub-samples of the age and elevation datasets to derive error estimates

	Method 1			Method 2		
L_e (km)	G_L (Ma km^{-1})	G_S (Ma km^{-1})	β^{-1}	G_L (Ma km^{-1})	G_S (Ma km^{-1})	β^{-1}
0	–98	–27·1	–2·6	–106 ± 2	–58 ± 3	–0·83
1	–81	8·7	10·3	–94 ± 3	8·4 ± 4	12·2
10	–36	10·4	4·5	–51 ± 2	10·3 ± 3	5·9
20	–38	15·3	3·5	–45 ± 1	15·6 ± 2	3·9
40	–23	10·57	3·2	–23 ± 2	9·4 ± 1	3·4

Erosional Response Time

Now that we have established that, under most circumstances, the relief reduction accompanying the erosion decay of ancient mountain belts can be accurately derived from age–elevation datasets, we turn to the question of timing. Clearly, relief reduction estimates can be used to derive a minimum estimate for the rate of relief evolution, by assuming that the rate of erosion has been constant through time since the end of the orogenic phase. As most geomorphic laws imply that the rate of erosion should be somehow proportional to the height of the mountain belt (Whipple and Tucker, 1999), either through a slope or curvature dependence, it is most likely that relief evolution during a post-orogenic 'decay' phase obeys an exponential law of the form:

$$h = h_0 + h_0(\beta - 1)\frac{1 - e((t - t_e)/\tau)}{1 - e(-t_e/\tau)} \tag{23}$$

where t is time in the past, h_0 is today's relief amplitude, t_e is the time of the end of the orogenic phase and τ is the erosional response time. τ is the time it takes for relief to decrease by a factor e. If τ is short in comparison to t_e, most of the relief reduction takes place during the period following the end of the orogenic phase; if τ is much greater than t_e, relief has decayed quasi-linearly since the end of the orogenic phase.

Can we use thermochronological data and/or their relationship to elevation to put constraints on the value of the parameter τ characterizing the rate at which relief decreases during the post-orogenic phase of a mountain belt? To answer this question, we have performed another series of numerical experiments in which the value of the parameter τ was systematically varied. As in the previous set of experiments, we have taken $t_e = 100$ Ma and assumed values for τ of 10, 20, 40, 100 Ma and ∞. The elastic plate thickness is set at 40 km. All other parameters are given the same value as in the previous set of runs. The results are shown in Figure 6 as age distributions along the same profile for the apatite He system (Figure 6a) and apatite fission track (FT) system (Figure 6b). The fission track ages are calculated from predicted thermal histories using the method of van der Beek *et al.* (1995). We have also computed age–elevation relationships along a narrow transect near the centre of the orogen. They are shown in Figure 7. The gain estimates and the values of β derived from them are summarized in Table II.

The age distribution appears to be similar for all model runs (Figure 6) except for a younging of the ages with increasing value of τ. That the ages are older for small values of τ is consistent with a rapid phase of relief reduction following the orogenic phase (100 Ma ago) during which rocks are rapidly exhumed to the surface and cross the closure temperature isotherm. That the minimum age computed for $\tau = \infty$ is approximately 50 Ma is also consistent with a linear decrease in relief of approximately 3–4 km in 100 Ma. The fission track ages have a similar distribution but are all older, consistent with an approximate closure temperature of 110 °C.

The slope of age–elevation transects measured along the narrow valley in the centre of the orogen (Figure 7) is strongly dependent on the assumed value for the erosional response time, τ. For small values of τ, corresponding to a rapid decay of the topography following the orogen constructive phase, the apparent exhumation rate are very high, approximately five times larger than the value predicted for a linear, steady decrease in topography over the past 100 Ma. Comparing the apparent exhumation rates derived from the slope of the age–elevation profiles 'collected' in the central valley (Figure 7) for the apatite He and apatite FT ages, one notices that for large values of τ, i.e. quasi-linear decrease in relief, the exhumation rate derived from both thermochronometers is almost identical. For small values of τ, i.e. corresponding to a rapid relief decay following the end of the orogenic phase, the exhumation rate obtained from the apatite He chronometer is almost twice as large as that derived from the apatite FT ages. This is somewhat counterintuitive as it would lead to the conclusion that the rate of exhumation increased between 100 and

Table II. Computed gain values, G_L and G_S, and corresponding relief loss amplitude, β^{-1}, for five model runs characterized by different values of the erosional response time, τ. Method 1 and method 2 are as in Table I. Age is the mean of the reset ages

	Method 1			Method 2			
τ (Ma)	G_L (Ma km^{-1})	G_S (Ma km^{-1})	β^{-1}	G_L (Ma km^{-1})	G_S (Ma km^{-1})	β^{-1}	Age (Ma)
10	–7·8	2·9	3·7	–8·8 ± 0·2	2·9 ± 0·4	4	95
20	–13·4	5·6	3·4	–15·2 ± 0·3	5·5 ± 0·7	3·8	92
40	–22·0	9·8	3·2	–25·1 ± 0·5	9·7 ± 1·3	3·6	86
100	–31·5	13·7	3·3	–36·7 ± 0·8	13·7 ± 1·9	3·7	78
∞	–38·3	15·3	3·5	–45·5 ± 1·1	15·6 ± 2·4	3·9	73

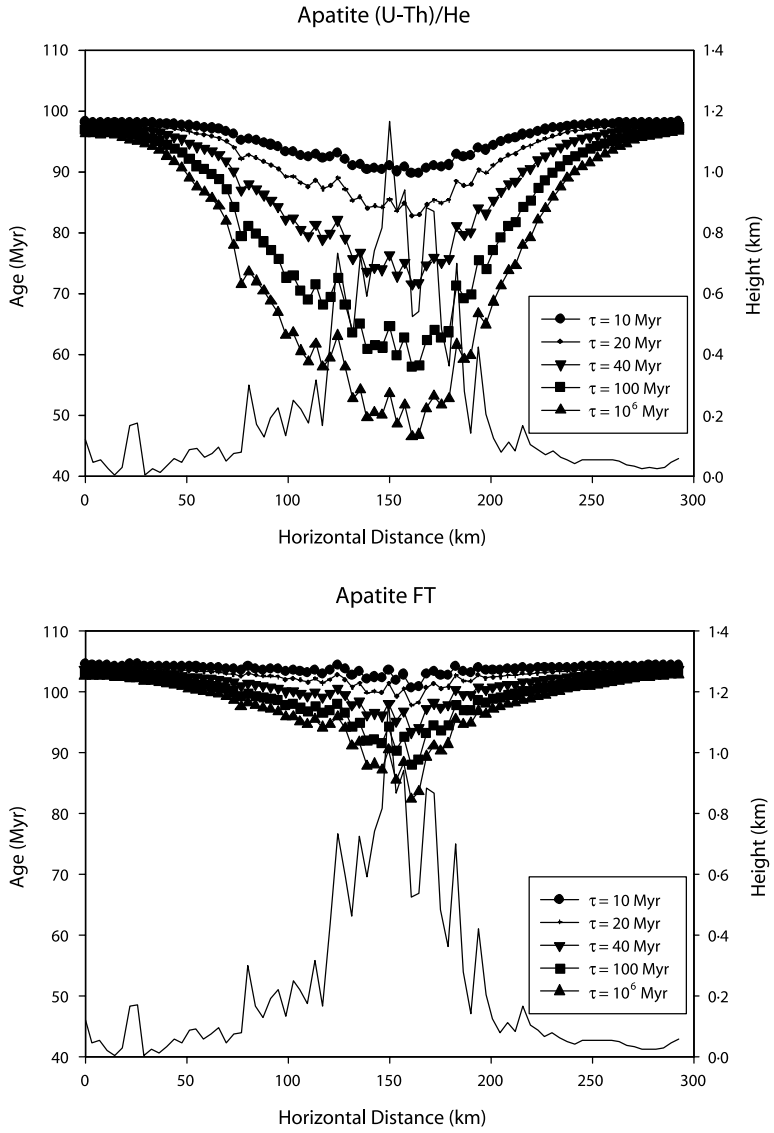

Figure 6. Topography and computed apatite He ages (a) and apatite FT ages (b) along a profile crossing the study area from the northwest to the southeast assuming different values for the erosional response time, τ.

90 Ma where, in fact, it decreased exponentially. This apparent increase in exhumation rate for the low temperature (and therefore younger) age estimates is a consequence of the rapid advection towards the surface which causes a greater perturbation to the closure temperature isotherm and generates higher apparent exhumation rates for the low temperature systems (Braun, 2002b).

Interestingly, the β-values derived from the gain estimates (Table II) are all consistent, regardless of the value of τ, indicating that the spectral method is very robust. Most estimates of β^{-1} are slightly smaller than the true value of 4. This is because by the time the rocks cools through the closure temperature for the apatite He system, the relief has already decrease by a small amount. The information contained in the age dataset can only provide us with information on the rate of relief change and/or mean exhumation rate since the time the rocks cooled through the closure temperature.

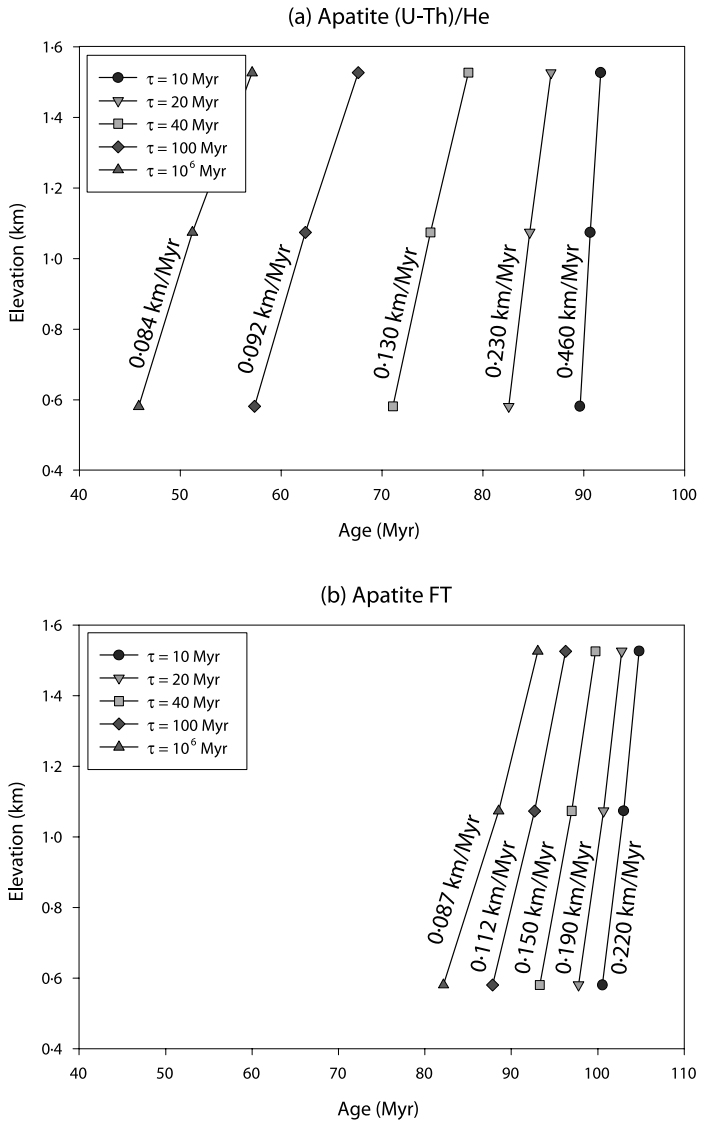

Figure 7. Computed apatite He age–elevation profiles from the centre of the orogen (Figure 4a). Each profile corresponds to a different value for the assumed erosional response time, τ. (a) (U-Th)/He system in apatite; (b) FT system in apatite.

In short, the slope of age–elevation profiles is sensitive to the rate at which erosional decay takes place during the post-orogenic phase of a mountain belt; estimates of the amount of relief/topographic change by the spectral method are not affected by the rate of decay, or whether it is linear or not.

Relief Evolution in the Dabie Shan

Spectral method

Having established that meaningful information about the rate of change of relief during the post-orogenic phase of mountain belt evolution can be extracted from thermochronological datasets, we turn our attention to the

data collected by Reiners *et al*. (2003) in the Dabie Shan (Figure 8). Our main purpose is to determine how the concepts illustrated by synthetic examples in the first part of this paper can be applied to a 'real' dataset. Rocks were collected across the orogen for (U-Th)/He and fission track dating in apatite and zircon (Reiners *et al*., 2003). Here we focus on the low temperature, apatite datasets (Figure 8). In both datasets, there is a general trend of younger ages near the core of the orogen and older ages around its rim. An age–elevation transect collected near the centre of the orogen yields well-defined age–elevation relationships for the He dates with a slope, or apparent exhumation rate, of approximately 0·064 km Ma^{-1} and, for the FT dates, a slope of 0·042 km Ma^{-1}. This could be interpreted as indicating an increase in exhumation rate between 60 and 35 Ma ago, i.e. the mean age of each datasets. However, as discussed by Reiners *et al*. (2003), it is more likely that this apparent increase in exhumation rate is, in fact, related to the deflection of the closure temperature isotherm (approximately 55–75 °C for apatite He and 100–120 °C for apatite FT) by the surface topography. The valley in which the vertical transect was collected is approximately 12 km wide (Reiners *et al*., 2003). It can be estimated that the deflection of the isotherm corresponding to the closure temperature for He in apatite caused by a 12-km-wide valley is sufficient to explain the difference in apparent exhumation rate. After correction, this yields a meaningful, orogen-wide exhumation rate of 0·06 km Ma^{-1} (Reiners *et al*., 2003). It was thus shown by Reiners *et al*. (2003) that the dataset is consistent with a scenario in which the mean exhumation rate has not changed since the end of the large mid-Cretaceous exhumation event (i.e. approximately 100 Ma ago).

This dataset has not been collected with the purpose of using the spectral method of Braun (2002a) to interpret its significance in terms of mean exhumation rate and rate of landform evolution. This would have required the collection of samples along a single transect crossing the orogen and at nearly equidistant locations. However, one can obtain a first-order estimate of the long wavelength gain value by restricting the dataset to the samples located in a narrow corridor as done by Reiners *et al*. (2003, figure 1B) and projecting and interpolating both the observed ages and elevations onto a southwest–northeast transect to estimate their Fourier components. Using the apatite He age, we obtain a value of approximately −50 Ma km^{-1} for the real part of the gain estimate at long wavelength. The negative value simply indicates that there is an anti-correlation between age and elevation, which, following the arguments developed in Braun (2002a,b), implies that the long wavelength relief has decreased in the recent geological past. Combining this with a value of 1/0·064 Ma km^{-1} for the short wavelength gain, i.e. the inverse of the slope age–elevation relationship observed in the narrow, central valley, yields a value of approximately 4 for the amount of relief reduction experienced by this orogen over the past 60–70 Ma, i.e. since the end of the orogenic phase. Considering that the present-day relief in the Dabie Shan is approximately 1·5 km, this implies that the mountain range was approximately 6 km high in the mid-Cretaceous.

Parameter search

More information can be extracted from this dataset. We have seen in the previous sections that the distribution of ages within the orogen (i.e. as a function of the distance to the orogen's centre) and the relationship between age and elevation vary significantly as the assumed elastic plate thickness or the erosional timescale is varied. The forward model Pecube can be used to search through parameter space for an 'optimal' set of parameters that result in age predictions that are similar to the observed ages (within measurement error), and also to evaluate the sensitivity of the model predictions to the value of the input parameters. In other words, we wish to 'invert' the thermochronological dataset to provide constraints on a range of Earth processes (surface erosion, lithospheric strength, temperature structure within the crust, timing of tectonic events, etc.) and/or, more importantly, to determine whether the dataset contains information on each of these processes.

To perform this inversion, we have used the Neighbourhood Algorithm (NA) of Sambridge (1999), a Monte-Carlo-type inversion method that does not require the calculation of the derivatives of the forward model with respect to the model parameters in its search for a minimum of the misfit function between observations and model predictions. Instead, the NA navigates through the parameter space to find this minimum by making use of the natural neighbour and Voronoi diagram concepts. The misfit function is defined as the L_2-norm of the weighted difference between the observation vector, O, and the prediction vector, P:

$$\text{misfit} = \frac{1}{n}\sqrt{\sum_{i}^{n}\left(\frac{O_i - P_i}{\Delta O_i}\right)^2} \tag{24}$$

where n is the number of measured ages (31 in our case) and ΔO_i are the observational errors. A detailed description of the NA can be found in Sambridge (1999). The important point to remember is that NA performs an intelligent

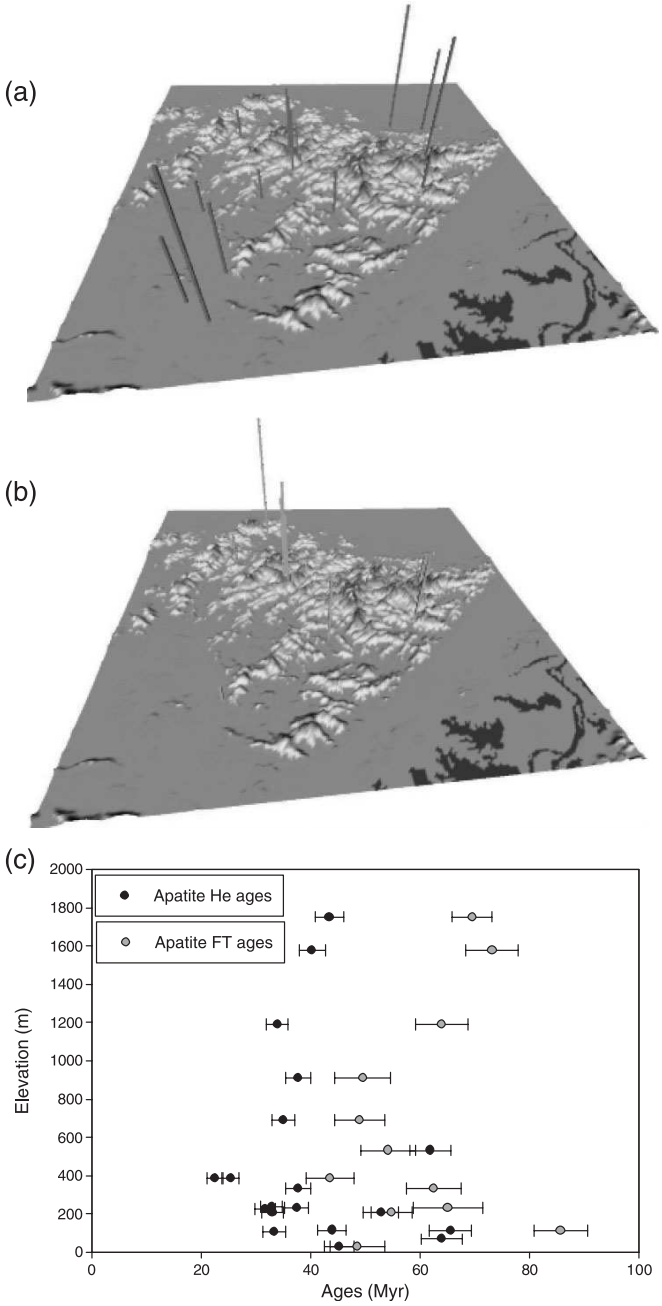

Figure 8. Relationship between age, topography and location for the apatite He dataset (a) and apatite FT dataset (b) collected by Reiners *et al.* (2003) in the Dabie Shan. Each bar corresponds to an age measurement. The location of the bar gives the location of the sample; the height of the bar is proportional to the measured age. Maximum age for apatite He is 65·5 Ma; maximum age for apatite FT is 85·7 Ma. (c) Age–elevation plot for apatite He and apatite FT ages. The relatively well-defined positive correlation between age and elevation among some of the data points corresponds to the vertical transect collected in the central part of the orogen; at the scale of the orogen, there is a negative correlation between age and elevation, with younger ages near the centre and older ages around the edges of the orogen.

search to find the set of parameter values of a given model (here Pecube) that will minimize the difference between model predictions (the synthetic ages) and observations (the measured ages). This search necessitates that a large number of model (Pecube) runs be performed to sample a wide range of parameter values.

In our application, the 'free' model parameters, i.e. those for which the inversion is performed, are the effective elastic plate thickness, L_e, the length of the model run, t_e, which can also be regarded as the time since the last major tectonic event at the end of which the erosional decay episode started, the erosional response time, τ, the basal temperature, T_1, the amplitude of the topography/relief decrease since the end of the orogenic phase, β^{-1}, and a mean exhumation rate, $\dot{E}$, i.e. uniform in space and constant in time.

Using a high performance cluster, we were able to perform a very large number of forward model runs (17 744 in total) in a reasonable amount of time. The results are shown in Figures 9 and 10 as scatter plots in parameter space. Each circle corresponds to a Pecube forward model run. The grey shade of the circles is proportional to the predicted misfit (dark shades correspond to low misfit, light shades correspond to high misfit). In Figure 9, all model runs are shown. In Figure 10, only the 50 best-fitting model runs are shown. Although the search was performed in a six-dimensional space (the space of the free parameters), we can only display the results as two-dimensional plots, by projecting the other four dimensions. We selected six combinations of pairs of parameters.

The results demonstrate that the thermochronological data contain information on: the timing of the end of the orogenic phase: 60 Ma $< t_e <$ 80 Ma; the effective elastic plate thickness: $L_e <$ 20 km; the amplitude of the relief loss: $2 < \beta^{-1} < 4$; the mean exhumation rate: 0·01 km Ma^{-1} $< \dot{E} <$ 0·04 km Ma^{-1}. The data do not contain information on the basal temperature, T_1, or the erosional response time, τ. The best-fitting forward model run (indicated on Figure 9 by a large white circle) is obtained with the following parameter values: $L_e = 9{\cdot}3$ km, $t_e = 72$ Ma, $\tau = 270$ Ma, $T_1 = 660$ °C, $\beta^{-1} = 2{\cdot}3$ and $\dot{E} = 0{\cdot}022$ km Ma^{-1}. The ages predicted from this best-fitting model run are shown and compared to the observed ages in Figure 11 as age–elevation distributions for the He and FT ages. The best forward model run is able to explain the steep, positive correlation between age and elevation near the centre of the orogen and the increase in age with distance from the centre of the orogen (and thus mean elevation). For the value of the 'best fit model' parameters, the total erosion in the centre of the orogen is approximatively 4 km, i.e. 1·6 km of uniform erosion, 2 km of relief loss and 0·4 km of associated isostatic rebound. That the data are better explained by a model in which a mean rock exhumation of 0·022 km Ma^{-1} is imposed indicates that areas where little surface topography exists today have undergone finite exhumation/erosion. We interpret this result as indicating that our approximation of relief evolution by simple amplification (or multiplication) is too simplisitic.

One should note, however, that the 'best' 50 model runs differ by less than 4 per cent in their misfit to the data but differ markedly by the value of the model parameters. The location in parameter space of these 50 best-fitting model runs is shown in Figure 10. Their distribution demonstrates that some of the model parameters are linearly dependent, i.e. that there is a trade-off between pairs of parameters: the data are equally explained by high relief loss or low mean exhumation rate (and vice versa) (see Figure 10c); the data are equally explained by high elastic thickness or high mean exhumation rate (and vice versa) (see Figure 10e); the data are consequently equally explained by high relief loss or high elastic plate thickness (and vice versa) (see Figure 10d). The timing of the end of the orogenic phase is independent of the other parameters.

The results of the inversion confirm the conclusions of Reiners *et al*. (2003) that, to explain the thermochronological data, there is no need to invoke a discrete tectonic event some 40–60 Ma ago as suggested by Grimmer *et al*. (2002). Slow exhumation related in part to the erosional decay of a relatively large surface topography and the subsequent isostatic uplift can explain the data. Surface topography/relief appears to have decreased by a factor of 2 to 4 since the beginning of the erosional decay phase. The data are better explained, however, if one assumes that the entire orogen (including the present-day low topography areas) has undergone, in addition to the isostatically driven exhumation, 1·6 km of uniform exhumation. Interestingly, the thermochronological data appear to provide better constraints on the effective elastic thickness of the underlying lithosphere than on the temperature structure (i.e. geothermal gradient) of the crust.

Finally, the results of the inversion (Figures 9 and 10) suggest that there is little information in the data to determine whether the relief loss occurred soon after the end of the orogenic event (small value of τ) or whether the topography has decayed at a constant rate since (large value of τ). However, most of the best-fitting model runs are characterized by relatively large values of τ, i.e. larger than 100 Ma, suggesting that a linear decrease in topographic height over the past 60–70 Ma is the most likely scenario. In Figure 12, we compare observations with predicted ages for a model run characterized by a small value of the erosional reponse time, $\tau = 16{\cdot}5$ Ma. Other parameters are $L_e = 12{\cdot}4$ km, $t_e = 73$ Ma, $T_1 = 600$ °C, $\beta^{-1} = 2{\cdot}5$ and $\dot{E} = 0{\cdot}028$ km Ma^{-1}. It is the sixth best-ranked model and is shown as a dark black circle in Figure 10. The predicted ages (Figure 12) have similar age–elevation slope to the observations but the He ages are clearly older than the observations, suggesting that a small value (i.e. smaller than 100 Ma) for τ is not compatible with the data.

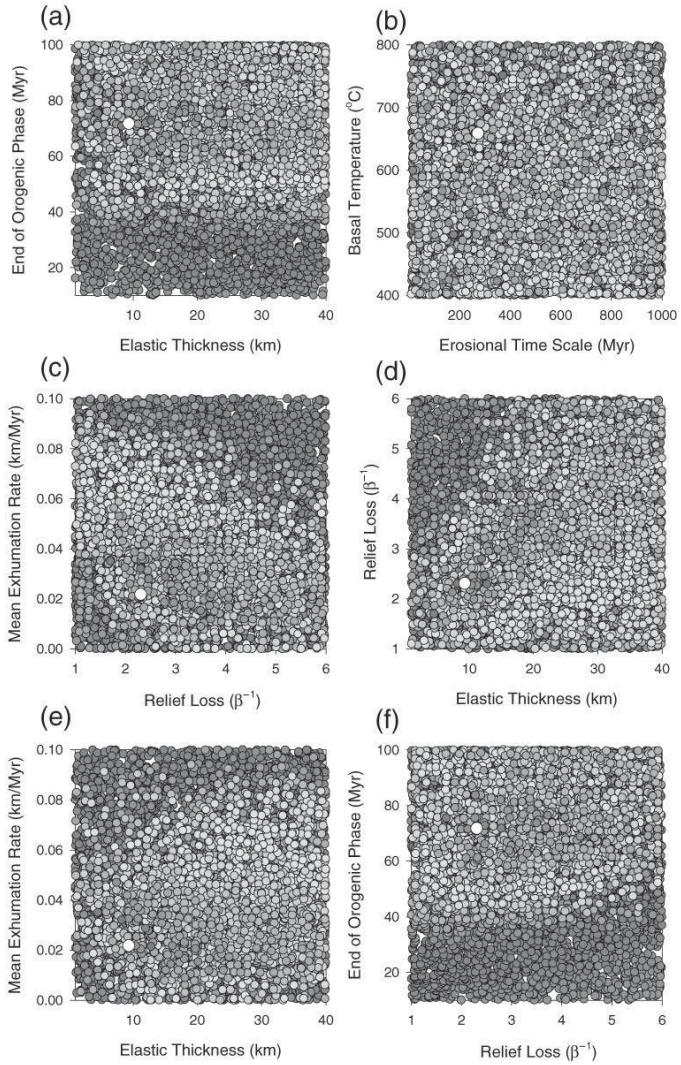

Figure 9. Results of the NA inversion as scatter diagrams of the misfit between observations and predictions. Each circle corresponds to a forward model run. The position of the circle is determined by the value of the model parameters. The grey shade of the circle is proportional to the value of the calculated misfit: dark shades correspond to low misfit values; light shades corresponds to high misfit values. The larger, white circle corresponds to the best-fit model run. Each diagram corresponds to a projection of all model runs onto a plane defined by two of the six parameters. Note that during the inversion procedure all model parameters are free to vary simultaneously. Only a small number (six) of all possible combinations of pairs of parameters are shown.

Conclusions and Discussion

Using a numerical model for the evolution of the temperature structure within the Earth's crust that includes the effect of a changing, finite-amplitude surface topography and isostatically driven exhumation, we have demonstrated that thermochronological data can be used to put constraints on the rate and amplitude of topographic decay during the post-orogenic phase of mountain belt evolution.

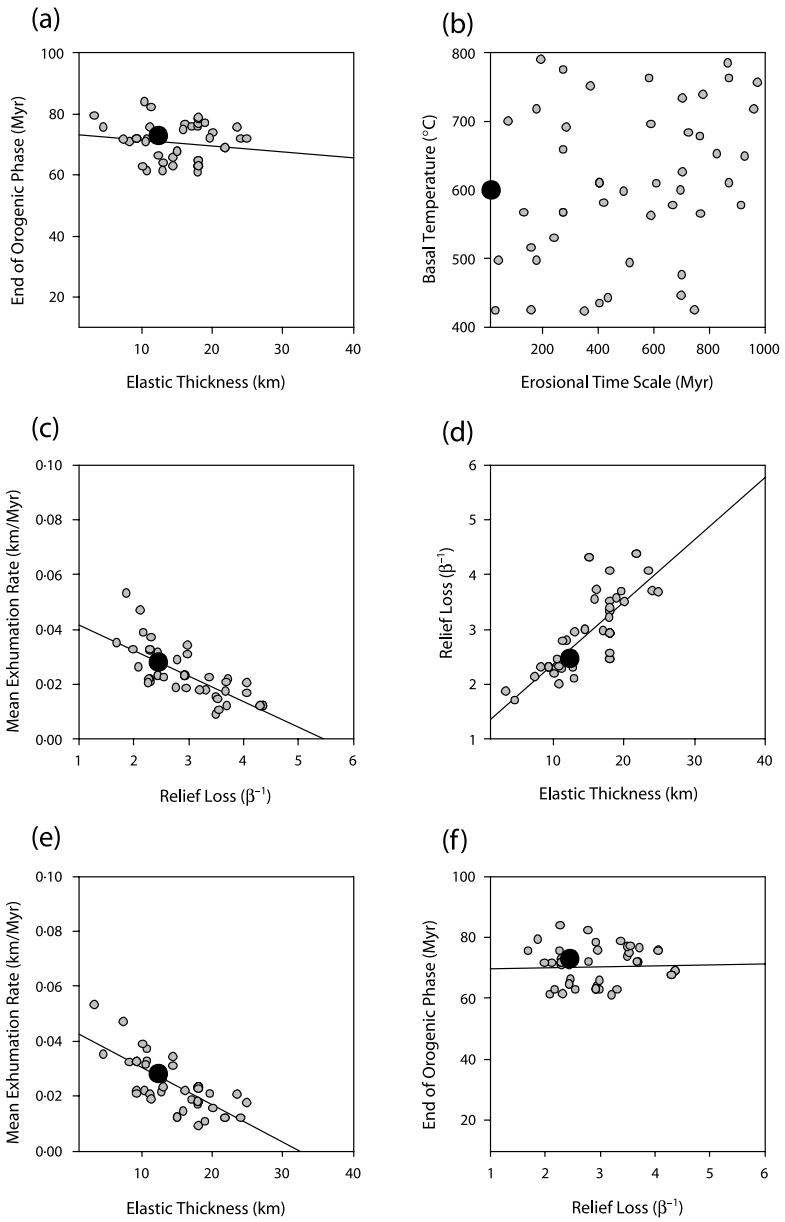

Figure 10. Same as Figure 9 but limited to the 'best' 50 model runs, i.e. those corresponding to the 50 smallest misfit values out of the 17 744 model runs performed during the inversion procedure with NA. The larger, black circle corresponds to the sixth best-fit model run, characterized by a small value of the parameter τ.

In particular, the spectral method developed by Braun (2002a) provides very good estimates of the mean exhumation rate and amplitude of relief loss even in cases when erosion is controlled by flexural isostasy; it is only in cases where lithospheric strength is so low and the effective elastic thickness is of the order of a few kilometres or less that the method overestimates the amount of relief loss.

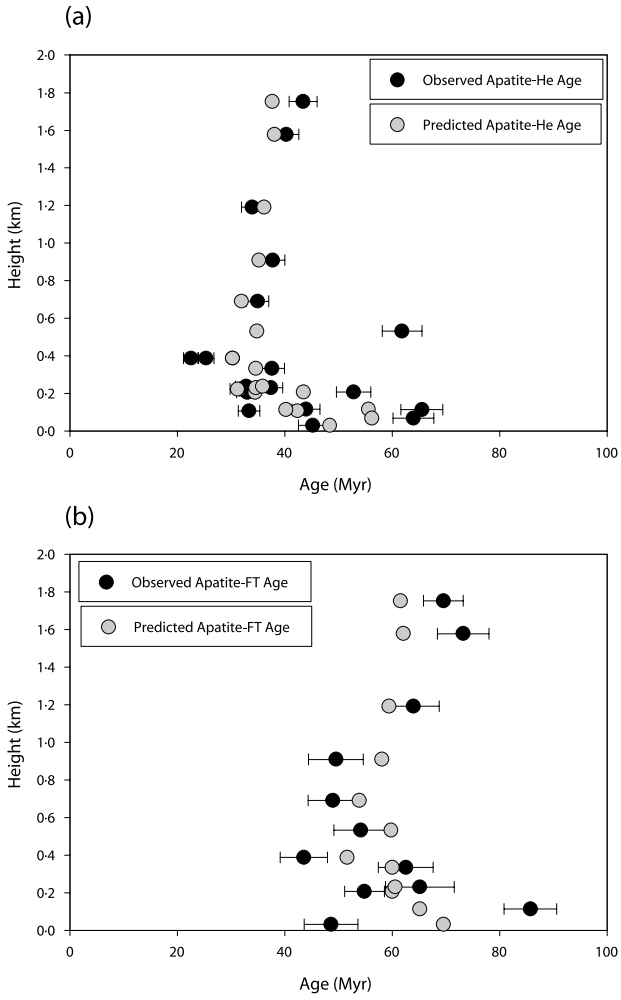

Figure 11. Comparison between observed and synthetic age–elevation relationships for apatite He ages (a) and apatite FT ages (b) estimated from the best-fitting model run.

The timescale, τ, over which relief decays once tectonic activity ceases can also be constrained by low-T thermochronological data; the slope of age–elevation profiles collected along short wavelength topography provides a good estimate of the mean rate of erosion which, in turn, is strongly dependent on the mean rate of topographic decay.

Applying the spectral method to a thermochronological dataset collected in the Dabie Shan of eastern China provides first-order estimates of the amount of relief reduction ($\beta^{-1} = 4$) since the end of tectonic activity (at least 70 Ma ago).

A thorough search through parameter space indicates that the Dabie Shan dataset is best explained if the underlying lithospheric thickness if of the order of 10 km, the relief has decreased by a factor of approximately 2·5 over the last 60 to 70 Ma, and if the area has been subjected, over the same period of time, to a mean exhumation rate of 0·02 km Ma^{-1}.

We have also demonstrated that these optimum parameter values should not be regarded as unique; the data suggest that there is a trade-off between mean exhumation rate and relief loss. For example a smaller mean exhumation rate of 0·01 km Ma^{-1} and a greater relief loss of 4·5 leads to a misfit to the data that is only a few per cent greater than that calculated for the optimum parameter set. There is also a trade-off between elastic thickness and relief loss with model

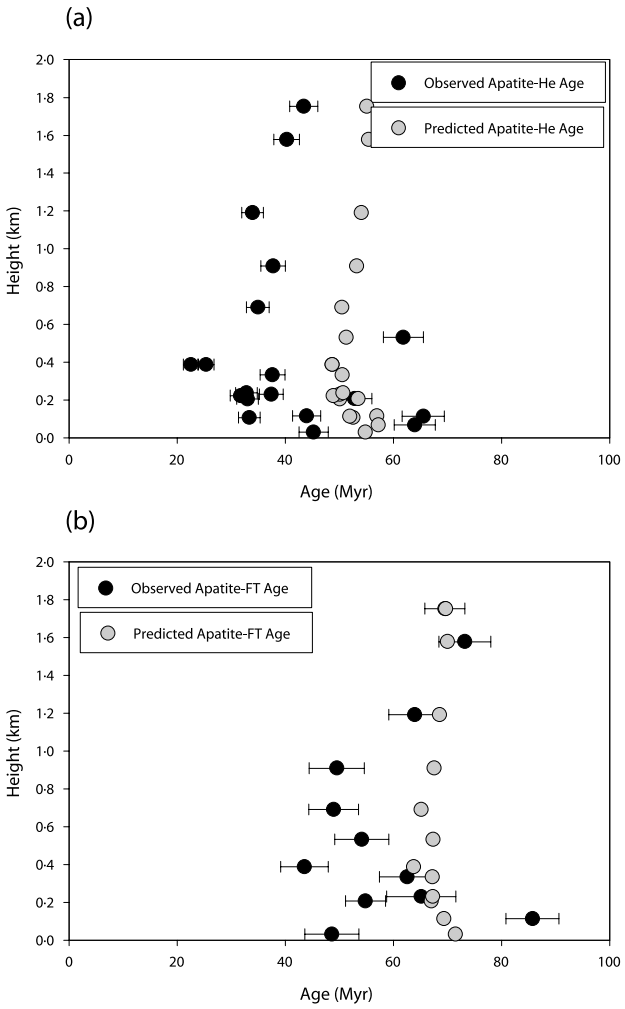

Figure 12. Comparison between observed and synthetic age–elevation relationships for apatite He ages (a) and apatite FT ages (b) estimated from the sixth best-fitting model run, characterized by a small erosional response time, $\tau = 16{\cdot}5$ Ma.

runs characterized by a larger elastic thickness (up to 30 km thick) and a greater topographic relief loss (up to 4·5) yielding similar misfit values.

We also found that surface topography in the Dabie Shan is likely to have decayed relatively linearly since the end of the orogenic event; the value for the parameter τ cannot be accurately derived from the thermochronological dataset but is likely to be relatively large, i.e. $\tau > 100$ Ma.

Finally, the misfit between model predictions and observations appears insensitive to the choice of geothermal gradient.

The most interesting result of our analysis of the Dabie Shan dataset is that it supports the conclusion of Reiners *et al*. (2003) that the rate of exhumation and thus the rate of change of surface topography has been more or less constant during the post-orogenic phase of the evolution of the mountain belt. The 'best-fit model' is not compatible with an exponential decrease in relief (and thus erosion rate) as predicted by most landscape evolution models that assume that the rate of erosion is proportional to relief amplitude (through the slope dependency of most erosional processes).

This result can be interpreted in several ways.

(1) The large-scale features of the landform do not evolve at a rate that is proportional to their relative height. This would imply that although the basic physical processes that drive the evolution of surface topography through time, such as stream incision or hill slope processes, have a strong dependency on local slope, this cannot later be time-averaged or spatially homogenized at the scale of an orogen and lead to a dependency of mean erosion rate on the slope measured along its major large-scale features. This would then imply that much of the recent work on the balance between tectonics and erosion that is based on an extrapolation of the stream power law to the overall shape of an orogen (Hilley and Strecker, 2004; Roe *et al*., 2005; Whipple and Meade, 2004) is not well posed.
(2) Other landforming processes, such as glacial erosion, may play a more important role than commonly assumed (Braun *et al*., 1999; Tomkin and Braun, 2002) and lead to a constant lowering rate, especially in mountainous regions that are in a post-orogenic erosional decay phase.
(3) Low-*T* thermochronological data are not sufficiently sensitive to changes in surface relief to provide constraint on the details of the temporal evolution of the relief. This does not seem to be supported by the results of our modelling (Figures 6 and 7) but could be due to the accuracy with which small variations in ages can be recorded by and extracted from the rocks.

Acknowledgements

The results presented in this paper are based on computations performed on the TerraWulf facility of the Centre for Advanced Data Inference of the Australian National University, in part funded by an Australian Research Council grant. The authors wish to thank P. Reiners and an anonymous reviewer for their helpful comments on an earlier version of this manuscript.

References

Bechtel T, Forsyth D, Sharpton V, Grieve R. 1990. Variations in effective elastic thickness of the North American lithosphere. *Nature* **343**: 636–638.

Braun J. 2002a. Estimating exhumation rate and relief evolution by spectral analysis of age–elevation datasets. *Terra Nova* **14**: 210–214.

Braun J. 2002b. Quantifying the effect of recent relief changes on age–elevation relationships. *Earth and Planetary Sciences Letters* **200**: 331–343.

Braun J. 2003. Pecube: A new finite element code to solve the heat transport equation in three dimensions in the Earth's crust including the effects of a time-varying, finite amplitude surface topography. *Computers and Geosciences* **29**: 787–794.

Braun J, Zwartz D, Tomkin J. 1999. A new surface processes model combining glacial and fluvial erosion. *Annals of Glaciology* **28**: 282–290.

Davis W. 1899. The geographical cycle. *Geography and Geomorphology Journal* **14**: 481–504.

Dodson MH. 1973. Closure temperature in cooling geochronological and petrological systems. *Contributions to Mineralogy and Petrology* **40**: 259–274.

Forsyth D. 1985. Subsurface loading and estimates of the flexural rigidity of continental lithosphere. *Journal of Geophysical Research* **90**: 12 623–12 632.

Grimmer J, Jonckheere R, Enkelmann E, Rauschbacher L, Hacker B, Blythe A, Wagner G, Wu Q, Liu S, Dong S. 2002. Cretaceous-Cenozoic hidtory of the southern Tan-Lu fault zone: apatite fission-track and structural constraints from the Dabie Shan (eastern China). *Tectonophysics* **359**: 225–253.

Hack T. 1960. Interpretation of erosional topography in humid temperate regions. *American Journal of Science* **258A**: 80–97.

Hilley G, Strecker M. 2004. Steady-state erosion of critical Coulomb wedges with application to Taiwan and the Himalaya. *Journal of Geophysical Research* **109**. DOI: B01411–10.1029/2002JB002284.

Huang J, Turcotte D. 1989. Fractal mapping of digitized images: application to the topography of Arizona and comparisons with synthetic images. *Journal of Geophysical Research* **94**: 7491–7495.

Jenkins GM, Watts DG. 1968. *Spectral Analysis and its Applications*. Holden-Day: Oakland, California.

Kooi H, Beaumont C. 1996. Large-scale geomorphology: classical concepts reconciled and integrated with contemporary ideas via a surface processes model. *Journal of Geophysical Research* **101**: 3361–3386.

Lague D, Crave A, Davy P. 2003. Laboratory experiments simulating the geomorphic response to tectonic uplift. *Journal of Geophysical Research* **108**. DOI: 10.1029/2002JB001785.

Maggi A, Jackson J, McKenzie D, Priestley K. 2000. Earthquake focal depths, effective elastic thickness, and the strength of the continental lithosphere. *Geology* **28**: 495–498.

Molnar P, England P. 1990. Late Cenozoic uplift of mountain ranges and global climate change: chicken and egg? *Nature* **346**: 29–34.

Montgomery DR. 1994. Valley incision and the uplift of mountain peaks. *Journal of Geophysical Research* **99**: 13 913–13 921.

Nunn J, Aires J. 1988. Gravity anomalies and flexure of the lithosphere at the Middle Amazon Basin, Brazil. *Journal of Geophysical Research* **93**: 415–428.

Penck W. 1924. *Die Morphologische Analyse: Ein Kapital der Physikalischen Geologie*. Engelhorn: Stuttgart.

Reiners P, Zhou Z, Ehlers T, Xu C, Brandon M, Donelick R, Nicolescu S. 2003. Post-orogenic evolution of the Dabie Shan, eastern China, from (U-Th)/He and fission-track thermochronology. *American Journal of Science* **303**: 489–518.

Roe G, Stolar D, Willett S. 2005. The sensitivity of a critical wedge orogen to climatic and tectonic forcing. In *Tectonics, Climate, and Landscape Evolution*, Willett S, Hovius N, Brandon M, Fisher D (eds). GSA Special Publication.

Sambridge M. 1999. Geophysical Inversion with a Neighbourhood Algorithm -I. Searching a parameter space. *Geophysical Journal International* **138**: 479–494.

Schmid R, Ryberg T, Ratschbacher L, Schulze A, Franz L, Oberhansli R, Dong S. 2001. Crustal structure of the eastern Dabie Shan interpreted from deep seismic reflection and shallow tomographic data. *Tectonophysics* **333**: 347–359.

Stüwe K, White L, Brown R 1994. The influence of eroding topography on steady–state isotherms. Application to fission track analysis. *Earth and Planetary Sciences Letters* **124**: 63–74.

Tomkin J, Braun J. 2002. The effect glaciation has on the relief of a fast growing orogen: a numerical modelling study. *American Journal of Science* **302**: 169–190.

Turcotte D. 1979. Flexure. *Advances in Geophysics* **21**: 51–86.

Turcotte DL, Schubert G. 1982. *Geodynamics: Applications of Continuum Physics to Geological Problems*. John Wiley and Sons: New York.

van der Beek P, Andriessen P, Cloetingh S. 1995. Morpho-tectonic evolution of rifted continental margins: Inferences from a coupled tectonic–surface processes model and fission-track thermochronology. *Tectonics* **14**: 406–421.

Wang Y, Mareschal J-C. 1999. Elastic thickness of the lithosphere in the Central Canadian Shield. *Geophysical Research Letters* **26**: 3033–3035.

Whipple K, Meade B. 2004. Controls on the strength of coupling among climate, erosion, and deformation in two-sided, frictional orogenic wedges at steady state. *Journal of Geophysical Research* **109**: F01011. DOI: 10.1029/2003JF000019.

Whipple KX, Tucker G. 1999. Dynamics of the stream-power incision model: implications for height limits of mountain ranges, landscape response timescales and research needs. *Journal of Geophysical Research* **104**: 17 661–17 674.

Wolf RA, Farley KA, Kass DM. 1998. Modeling of the temperature sensitivity of the apatite (U-Th)/He thermochronometer. *Computers and Geosciences* **148**: 105–114.

Zuber M, Bechtel T, Forsyth D. 1989. Effective elastic thickness of the lithosphere and mechanisms of isostatic compensation in Australia. *Journal of Geophysical Research* **94**: 9353–9367.

A.2 Analyse thermochronologique des sédiments Siwaliks de la Karnali, Népal de l'ouest

van der Beek et al. (2006) décrivent les premières données thermochronologiques sur les Siwaliks de l'ouest Népal, et les interprètent principalement en terme de sources.

Basin Research (2006) **18**, 413–434, doi: 10.1111/j.1365-2117.2006.00305.x

Late Miocene – Recent exhumation of the central Himalaya and recycling in the foreland basin assessed by apatite fission-track thermochronology of Siwalik sediments, Nepal

Peter van der Beek, Xavier Robert, Jean-Louis Mugnier, Matthias Bernet, Pascale Huyghe and Erika Labrin

Laboratoire de Géodynamique des Chaînes Alpines, Université Joseph Fourier, Grenoble Cedex, France

ABSTRACT

Thermochronological analysis of detrital sediments derived from the erosion of mountain belts and contained in the sedimentary basins surrounding them allows reconstructing the long-term exhumation history of the sediment source areas. The effective closure temperature of the thermochronological system analysed determines the spatial and temporal resolution of the analysis through the duration of the lag time between closure of the system during exhumation and its deposition in the sedimentary basin. Here, we report apatite fission-track (AFT) data from 31 detrital samples collected from Miocene to Pliocene stratigraphic sections of the Siwalik Group in western and central Nepal, as well as three samples from modern river sediments from the same area, that complement detrital zircon fission-track (ZFT) and U–Pb data from the same samples presented in a companion paper. Samples from the upper part of the stratigraphic sections are unreset and retain a signal of source-area exhumation; they show spatial variations in source-area exhumation rates that are not picked up by the higher-temperature systems. More deeply buried samples have been partially reset within the Siwalik basin and provide constraints on the thermal and kinematic history of the fold-and-thrust belt itself. The results suggest that peak source-area exhumation rates have been constant at $\sim$1.8 km Myr^{-1} over the last $\sim$7 Ma in central Nepal, whereas they ranged between 1 and $\sim$1.5 km Myr^{-1} in western Nepal over the same time interval; these spatial variations may be explained by either a tectonic or climatic control on exhumation rates, or possibly a combination of the two. Increasing lag times within the uppermost part of the sections suggest an increasing component of apatites that have been recycled within the Siwalik belt and are corroborated by AFT ages of modern river sediment downstream as well as the record of the distal Bengal Fan. The most deeply buried and most strongly annealed samples record onset of exhumation of the frontal Siwaliks along the Himalayan frontal thrust at $\sim$2 Ma and continuous shortening at rates comparable with the present-day shortening rates from at least 0.3 Ma onward.

INTRODUCTION

The Himalaya is by far the most important source of sediment input to the world's oceans (Summerfield & Hulton, 1994; Hay, 1998); its denudation history should, therefore, have major consequences for global climate change if atmospheric CO_2 drawdown from weathering and organic carbon burial plays a role in modulating climate (Raymo & Ruddiman, 1992; France-Lanord & Derry, 1997). Denudation rates within the Himalayan system may have fluctuated considerably through time, controlled by tectonic and/or climatic factors, such as the onset of the Asian Monsoon and global glaciations. The erosional history of the Himalaya, as inferred from mass-balance studies, is controversial: whereas some studies have inferred a significant Quaternary increase in sediment fluxes (e.g. Métivier *et al.*, 1999), others have suggested that fluxes have been decreasing since reaching a peak in middle-late Miocene times (e.g. Burbank *et al.*, 1993, Clift & Gaedicke, 2002). Vance *et al.* (2003) and Vannay *et al.* (2004) used detrital cosmogenic and *in situ* thermochronologic data, respectively, to argue that denudation rates in the western Himalaya have increased significantly during the last few million years. Burbank (1992) has demonstrated rebound of the Ganges foreland basin since $\sim$4 Ma, which he also attributes to increased denudation of the mountain belt since that time. Constraining the erosional history of the Himalaya is therefore important in order to elucidate both

Correspondence: Peter van der Beek, Laboratoire de Géodynamique des Chaînes Alpines, Université Joseph Fourier, BP 53, 38041 Grenoble Cedex, France. E-mail: pvdbeek@ujf-grenoble.fr

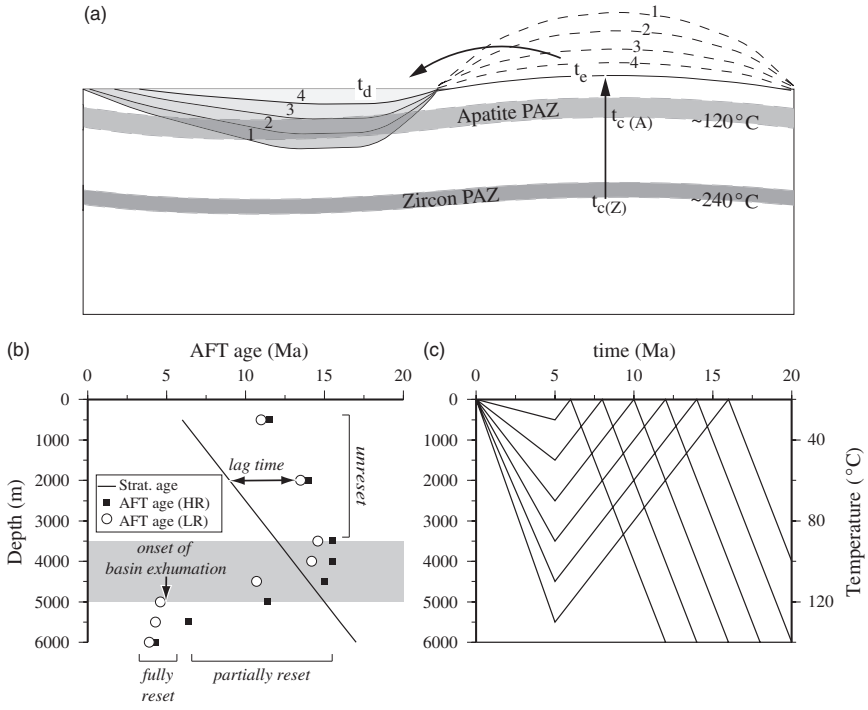

Fig. 1. (a) Concept of detrital thermochronology and principal differences between detrital apatite and detrital zircon fission-track thermochronology. Samples collected at stratigraphic horizons 1–4 record integrated exhumation rates between the time they passed through the closure temperature (t_c) and the time they arrived at the surface (t_e). t_d is time of deposition; it is generally assumed that $t_d = t_e$. Lag time equals t_c–t_d ($= t_c$–t_e). Subscripts (a) and (z) refer to the closure temperatures for the apatite and zircon fission-track systems, respectively; PAZ, partial annealing zone. Because of the relatively low closure temperature of the apatite fission-track system, samples may be partially or totally reset within the sedimentary basin. Modified from Garver *et al.* (1999). (b and c) Synthetic model for samples collected from an exhumed basin. Samples are initially exhumed from their source areas at a rate of 1 km Myr^{-1} and deposited in the basin from 16 Ma onwards. A single source terrain with uniform exhumation rates is considered here. Basin sedimentation rates are constant between 16 and 5 Ma at 500 m Myr^{-1}; the basin is exhumed from 5 Ma onward. For simplicity, a constant 20 °C km^{-1} geotherm is assumed for both the source area and the sedimentary basin. Predicted pattern of apatite fission-track (AFT) ages as a function of maximum stratigraphic depth is shown in (b), for highly retentive (HR) and low-retentive (LR) apatites, respectively. AFT ages are calculated using the forward model of Ketcham *et al.* (2000) using the thermal histories depicted in (c) and annealing kinetics characterized by D_{par} values of 2.0 and 1.0 μm for HR and LR apatites, respectively (cf. Carlson *et al.*, 1999; Barbarand *et al.*, 2003). The shaded box in (b) represents apatite partial annealing zone (PAZ). See text for discussion.

the mass fluxes at the Earth's surface and the climatic and tectonic controls on mountain building. Some of the questions that are of interest to us include: what is the recent cooling history of the Himalayas? Has exhumation of the Himalayas in Nepal been continuous or episodic since the mid-Miocene? Is the exhumation history of the Himalayas controlled purely by tectonics or can we isolate climatic controls?

Detrital thermochronology permits monitoring the evolution of cooling and exhumation rates through time by analysing samples from sediments of different ages derived from an eroding mountain belt. Thus, detrital thermochronology provides a much longer 'memory' of exhumation rates than *in situ* thermochronology, especially in regions of high exhumation rates and therefore young thermochronological ages such as the Himalaya. A key concept of detrital thermochronology is the 'lag time' (Garver *et al.*, 1999; Bernet *et al.*, 2001), defined as the difference between the thermochronological and the depositional ages of the sample and, therefore, the time the sample spent to reach the surface from its closure temperature and be deposited in the basin (Fig. 1). Transport times are generally considered negligible; the lag time is thus a direct measure of exhumation rates within the source area at the time of deposition. As synorogenic sediments may be derived from different sources in a mountain belt, characterized by varying denudation histories, detrital samples usually contain a range of cooling ages, which can be divided into different grain-age components or peaks (e.g. Bernet *et al.*, 2001, 2004; Stewart & Brandon, 2004).

Most detrital thermochronology studies have used thermochronometers with relatively high closure temperatures (T_c) such as zircon fission-track (ZFT; $T_c \approx 240$ °C; e.g. Cerveny *et al.*, 1988; Bernet *et al.*, 2004) or mica ^{40}Ar/^{39}Ar (T_c = 350–420 °C; e.g. Copeland & Harri-

son, 1990; White *et al*., 2002; Szulc *et al*., 2006). The effective closure temperature of any thermochronological system will determine what type of process can be addressed by its study: the time and length scales of constraint will depend on closure temperature, so that in any region, higher-temperature systems will constrain deeper, longer-term processes than lower-temperature systems (Fig. 1). Therefore, using a lower-temperature thermochronometer, such as the apatite fission-track (AFT) system ($T_c = 110 \pm 10\,^{\circ}C$), in conjunction with these higher-temperature systems makes it possible, in principle, to track short-term variations in denudation rates that are below the resolution of the higher-temperature systems. *In situ* bedrock AFT ages within the western and central Himalaya are consistently younger than a few Ma (e.g. Jain *et al*., 2000; Thiede *et al*., 2004; Blythe *et al*., 2006) so that, in principle, variations in exhumation rates can be monitored with a temporal resolution of 1–2 Myr.

The relatively low closure temperature of the AFT thermochronometer, however, makes this system also more sensitive to postdepositional heating within the sedimentary basin. As a sample is buried deeper in the sedimentary basin and reaches temperatures corresponding to the AFT partial annealing zone (PAZ; ~70–120 °C), the information it contains concerning source-area exhumation is progressively erased (Fig. 1). Samples that have been buried to depths less than the PAZ retain a source-area signal; their component ages are older than the depositional ages and increase down-section, indicating they are unreset and can be interpreted in terms of lag times (Fig. 1b). For samples exhumed from within the PAZ, in contrast, annealing will partially reset the peak ages, which thus lose their geological significance. Partially reset ages may be either older or younger than the depositional age; as the intensity of annealing increases with depth (temperature), peak ages of partially reset samples will thus generally decrease down-section. Moreover, as the kinetics of AFT annealing vary with apatite chemistry (e.g. Carlson *et al*., 1999; Barbarand *et al*., 2003), with low-retentive grains becoming (partly or fully) reset at lower temperature than high-retentive grains, we may expect a stronger variability in single-grain ages in such samples compared with unreset samples from the same source. This loss of information is, however, counterbalanced by complementary constraints on the postdepositional thermal history, which will be most clearly recorded by the deepest and most strongly annealed samples (Rohrman *et al*., 1996; Carter & Gallagher, 2004; Cederbom *et al*., 2004). In these samples, an increasing proportion of apatite grains will have been completely reset within the basin, such that the youngest component age peak will regain geological significance: it dates the onset of exhumation of the basin strata (Brandon *et al*., 1998; Locke & Garver, 2005). This situation manifests itself when minimum ages (that is, the age of the youngest component peak) are similar for different samples (Fig. 1b). Finally, if all of the apatites have been completely reset within the basin, a single peak age dating the onset of basin exhumation is expected. A more complete retrieval of the post-depositional thermal history is obtained when confined fission track-length distributions are considered together with the age distributions of the samples (Gallagher *et al*., 1998; Carter & Gallagher, 2004).

In this paper, we present detrital AFT data from 31 samples collected from Miocene to Pliocene stratigraphic sections of the Siwalik Group at the Karnali River, Surai Khola and Tinau Khola sections in western and central Nepal, as well as three samples from modern river sediments from the same area (Fig. 2). These data complement detrital ZFT ages from the same sections presented in a companion paper (Bernet *et al*., 2006). Samples from the upper part of the stratigraphic sections provide complementary constraints on source-area denudation rates, and show spatial variations in denudation rates that are not picked up by the higher-temperature systems, whereas more deeply buried samples provide constraints on the thermal and kinematic history of the Siwalik fold-and-thrust belt itself.

TECTONIC AND GEOMORPHIC SETTING

The Himalaya is classically subdivided into four tectonic zones (e.g. Hodges 2000, Yin & Harrison 2000) that can be followed along its ~2500 km length and are separated by north-dipping crustal-scale faults, branching off the main detachment overlying the underthrust Indian plate (Zhao *et al*., 1993; Yin & Harrison, 2000; Avouac, 2003). The northernmost Tethyan Himalayan zone forms the southern border of the Tibetan Plateau and consists of Cambrian to Eocene sedimentary to low-grade metamorphic rocks. It is separated from the structurally underlying Higher (or Greater) Himalayas by the extensional Southern Tibetan Detachment System (STDS; Burchfiel *et al*., 1992). The Higher Himalayan zone consists of high-grade metamorphic rocks and forms the topographic backbone of the range. It is intruded along its northern border by Miocene (~24–17 Ma) leucogranites (Burchfiel *et al*., 1992, Guillot *et al*., 1994, Hodges *et al*., 1996). The Higher Himalaya overthrusts the Lesser Himalaya along the main central thrust (MCT; Fig. 2). Precise dating of the activity of the STDS and MCT has shown that they were active simultaneously during the Early Miocene (around 22–18 Ma; Burchfiel *et al*., 1992, Hodges *et al*., 1996), giving rise to a model of extrusion of Greater Himalayan middle crust from under the overthickened Tibetan Plateau (Beaumont *et al*., 2001, Hodges *et al*., 2001).

The Lesser Himalaya consists mainly of Proterozoic to Palaeozoic (meta)sedimentary rocks and is bounded to the south by the main boundary thrust (MBT). In western Nepal, the Lesser Himalaya forms a complex structural duplex with several major internal thrusts (DeCelles *et al*., 2001). Overall, the timing of activation of thrusts in the Lesser Himalaya indicates a forward-propagating thrust sequence with activity of the MCT initiating > 20 Ma, the internal thrusts between 10 and 20 Ma (DeCelles *et al*., 2001; Huyghe *et al*., 2005) and the MBT between 5 Ma

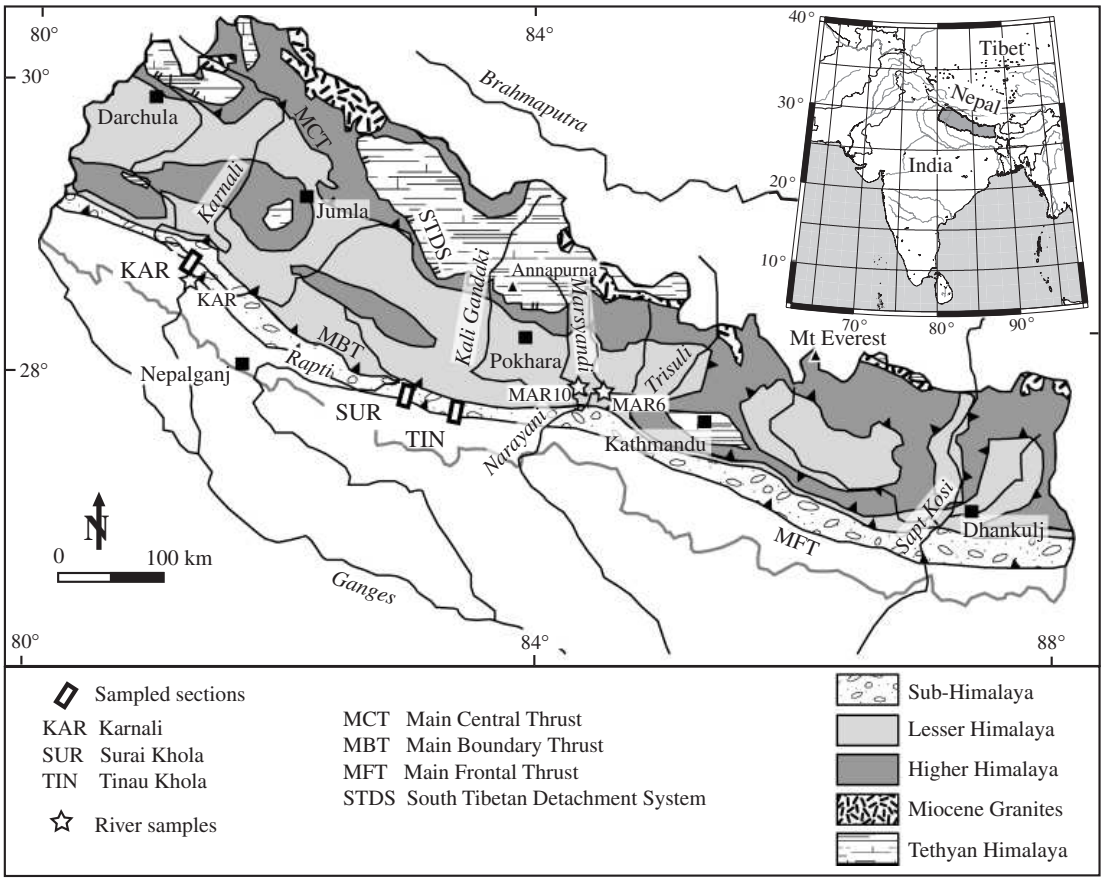

Fig. 2. Simplified geological map of Nepal showing major tectonostratigraphic units and faults (modified from DeCelles *et al*., 2001). Locations of sampled sections (KAR, Karnali; SUR, Surai; TIN, Tinau) and modern-day river samples are indicated. The inset shows the location of Nepal.

(DeCelles *et al*., 2001) and 10 Ma (Meigs *et al*., 1995; Huyghe *et al*., 2001). The MBT overthrusts the Sub-Himalaya or Siwalik thrust belt, composed of Mio-Pliocene syn-tectonic clastic deposits. The latter overthrusts the Ganges plain (known as Terai plain in Nepal) along the currently active main frontal thrust (MFT).

Present-day convergence rates across the Himalaya are $18 \pm 3\,\mathrm{mm\,year^{-1}}$ from GPS measurements (Bilham *et al*., 1997; Larson *et al*., 1999; Jouanne *et al*., 2004). Within error, these are equal to Holocene shortening rates across the MFT (Lavé & Avouac, 2000; Mugnier *et al*., 2004) inferred from folded and uplifted river terraces. They are also equal to Quaternary shortening rates across the Siwalik fold belt (Mugnier *et al*., 2004) and Mio-Pliocene shortening rates across the Lesser Himalaya (DeCelles *et al*., 2001) inferred from section balancing. Moreover, a frontal propagation rate that is equal to the convergence rate can be inferred from facies-migration patterns within the Ganges foreland basin, suggesting overall steady-state forward migration of the Himalayan orogenic wedge since ~15 Ma (Lyon-Caen & Molnar, 1985; Avouac, 2003; Mugnier & Huyghe, 2006). Combining present-day patterns and rates of uplift and deformation from geodetic studies with those obtained on geological timescales, Avouac (2003) has proposed a model in which convergence takes place over a mid-crustal detachment including a ramp underlying the topographic front of the Higher Himalaya (see also Bilham *et al*., 1997; Cattin & Avouac, 2000; Lavé & Avouac, 2001; Bollinger *et al*., 2004). From a detailed analysis of GPS data, Larson *et al*. (1999) and Berger *et al*. (2004) have proposed that the detachment is segmented and the crustal ramp more pronounced in central Nepal than in western Nepal. Recently, however, a competing model has been proposed that incorporates out-of-sequence activation of a newly formed thrust just south of the MCT, possibly controlled by climatic focusing of erosion on the topographic front of the Higher Himalaya (Wobus *et al*., 2003; Hodges *et al*., 2004).

A growing number of *in situ* fission-track thermochronology studies have emphasized the rapid rates of recent exhumation within the central Himalaya (e.g. Arita & Ganzawa, 1997; Jain *et al*., 2000; Burbank *et al*., 2003; Thiede *et al*., 2004; Vannay *et al*., 2004; Bojar *et al*., 2005; Blythe *et al*., 2006). Most of these studies have concentrated on the

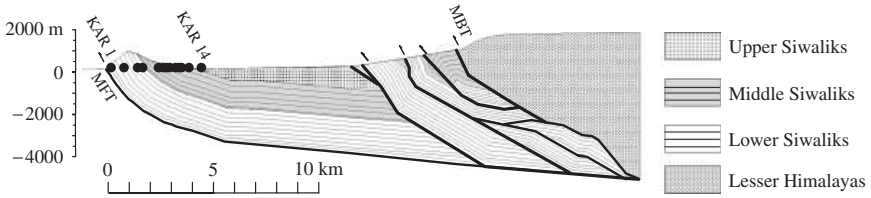

Fig. 3. Balanced cross section along the Karnali River showing sample locations and relationship with local structure. Modified from Mugnier *et al.* (1999).

Higher Himalaya and the Lesser Himalayan crystalline zones, due to the unfavourable lithologies in the other tectonic units of the central Himalaya. Within these zones, AFT ages of valley samples are commonly $\leq$ 1 Ma, rising to 2–4 Ma for the highest-elevation samples. In detail, however, there are some differences between the different results: extremely young AFT ages $<$ 0.5 Ma (e.g. Burbank *et al.*, 2003; Bojar *et al.*, 2005) are not reproduced in all studies, and whereas Burbank *et al.* (2003) report a jump in ages across the MCT in the Marsyandi area of central Nepal, Thiede *et al.* (2004), Vannay *et al.* (2004) and Bojar *et al.* (2005) show that AFT ages remain young in the Lesser Himalayan crystalline zone in the Goriganga and Sutlej regions ($\sim$400 and 700 km west of the Marsyandi, respectively). Higher closure-temperature $^{40}Ar/^{39}Ar$ mica ages show a similar pattern (Bollinger *et al.*, 2004, Vannay *et al.*, 2004): they are commonly 4–6 Ma in the northernmost Lesser Himalaya in the footwall of the MCT and increase to $\sim$20 Ma in the southernmost part of the Lesser Himalaya along the MBT hangingwall.

Stratigraphy and structure of the Siwalik belt in western Nepal

The Siwalik fold-and-thrust belt constitutes the active deformation front of the Himalaya and the deformed part of its Neogene foreland basin. The belt can be subdivided into a structurally simple outer belt, composed of laterally propagating fault-bend or fault-propagation folds associated with the MFT and their hanging-wall synclines, on which wedge-top basins or *Duns* have developed, and a more complex inner belt composed of a series of laterally relayed and transported thrust sheets (Fig. 3; Mugnier *et al.*, 1993, 1999; Champel *et al.*, 2002; Husson *et al.*, 2004). On the basis of growth strata recognized within the Surai Khola section in central Nepal, Mugnier *et al.* (2004) infer an onset of thrusting on the MFT between 1.8 and 2.4 Ma.

Siwalik Group sediments were deposited in the Ganges foreland basin during Middle Miocene–Pliocene times (e.g. Burbank *et al.*, 1996) and constitute an upward-coarsening fluvial megasequence (DeCelles *et al.*, 1998; Nakayama & Ulak, 1999; Huyghe *et al.*, 2005). The Siwalik Group is traditionally subdivided into the Lower, Middle, and Upper Siwalik subgroups (cf. Fig. 3). The Lower Siwaliks consist of mudstones and fine- to medium-grained sandstones with common palaeosol horizons and are interpreted as representing deposition in a fine-grained meandering fluvial system. The Middle Siwaliks are mainly massive coarse-grained micaceous sandstones and record a transition from sandy meandering to sandy braided fluvial environments. The Upper Siwaliks are composed of pebble- to boulder-sized conglomerates representing deposition in gravely braided streams and alluvial fans. Overall, the evolution of depositional environments records the forward propagation of the Himalayan thrust wedge and increasing proximity of the source area, although regional climate changes also influenced the depositional settings (Quade *et al.*, 1995; Nakayama & Ulak, 1999; Huyghe *et al.*, 2005).

The present-day drainage pattern of the Nepal Himalaya is characterized by a small number of through-going trunk rivers (the Karnali in western Nepal, Narayani in central Nepal and Sapt Kosi in eastern Nepal) that collect the drainage of many tributaries before cutting through the Siwalik ranges. The characteristic gridiron drainage pattern thus formed has been interpreted to result from thrust-related uplift along the MBT during Late Miocene times (Gupta, 1997). Lateral drainage diversion is also common within the Siwalik belt and is a response to uplift and lateral propagation of the active fault-related folds along the MFT (Champel *et al.*, 2002; van der Beek *et al.*, 2002). In contrast, flow directions measured within the Siwalik sediments are consistently towards the south, indicating transverse transport similar to the modern drainage pattern in the northern Ganges flood-plain (Tokuoka *et al.*, 1990; DeCelles *et al.*, 1998; Szulc *et al.*, 2006).

As the Siwaliks have been tilted and exhumed along the MFT, several continuous cross-sections through the sequence are exposed where rivers cut across the frontal structure (Figs 2 and 3), providing a well-constrained framework for sampling the tectonic and climatic record contained within the Siwalik Group sediments in magneto-stratigraphically dated sections (e.g. Harrison *et al.*, 1993; Quade *et al.*, 1995; DeCelles *et al.*, 1998; Huyghe *et al.*, 2001, 2005; Robinson *et al.*, 2001).

The first magneto-stratigraphic dating studies in western Nepal were carried out along the Surai Khola (Appel *et al.*, 1991) and Tinau Khola (Gautam & Appel, 1994) sections; these results have been reinterpreted and calibrated to the Cande & Kent (1995) magnetic polarity timescale by Gautam & Rösler (1999). The Surai Khola preserves the most completely dated stratigraphic section; the Tinau Khola section is cut off within the Middle Siwaliks by an internal thrust. Gautam & Rösler (1999) put the Lower-

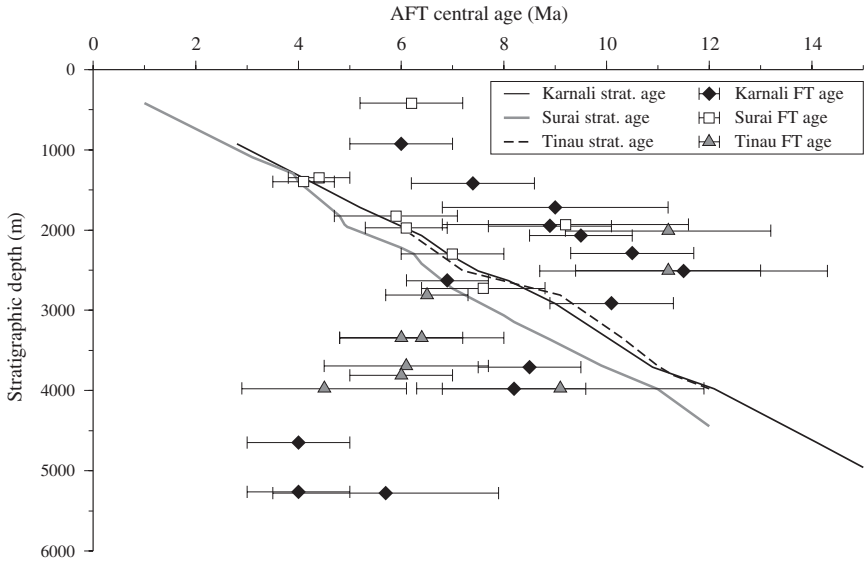

Fig. 4. Plot of apatite fission-track (AFT) central age against depth for all samples. Stratigraphic ages for the three sections [after Gautam & Fujiwara (2000) for the Karnali section; T. P. Ojha (pers. comm. 2003) for the Surai and Tinau sections] are also indicated.

Middle Siwalik boundary at ~9.8 Ma (base of chron 4a) in these sections and the Middle-Upper Siwalik boundary at 5.2 Ma (base of chron 3). This calibration has been questioned, however, on the basis of vertebrate fossil data, which would suggest that the Middle-Upper Siwalik limit should be younger than 3.5 Ma (Corvinus & Rimal, 2001). More recently, these sections have been resampled by a University of Arizona team (T. P. Ojha, pers. comm., 2003). Although the magneto-stratigraphic results themselves have not been published, they have been used to provide a temporal framework for several palaeo-climate and provenance studies (e.g. Hoorn *et al.*, 2000; Robinson *et al.*, 2001; Szulc *et al.*, 2006). Whereas the difference between the two magneto-stratigraphic frameworks for any horizon is never more than 1 Myr for the Tinau section, it reaches >2 Myr in the Middle Siwalik subgroup in the Surai section (cf. Fig. 4 in Szulc *et al.*, 2006). T. P. Ojha's unpublished data put the Lower-Middle Siwalik transition at 8.2 Ma in the Surai section and 10.3 Ma in the Tinau section, whereas they date the Middle-Upper Siwalik transition at 3.5 Ma in the Surai section. Szulc *et al.* (2006) provide a further discussion of these different magneto-stratigraphic studies. Finally, a long magnetostratigraphic record is available for the Karnali River section, encompassing Lower and Middle Siwalik subgroups between 15.9 and 5.2 Ma (Gautam & Fujiwara, 2000).

DETRITAL AFT THERMOCHRONOLOGY

Sampling and methods

We collected samples for detrital apatite and zircon analysis along the Surai, Tinau and Karnali River sections, aiming to collect a sample every million years represented by the sedimentary succession. For the Karnali section, we had access to detailed field logs, enabling us to locate and identify ~90% of the holes drilled for the Gautam & Fujiwara (2000) magnetostratigraphic study; we are thus able to tie our data very closely to the magnetostratigraphy. Samples KAR14 and KA30 were collected from Middle and Upper Siwalik series stratigraphically above the dated section; their ages were estimated by extrapolating the deposition rates recorded by the magnetostratigraphy. For the Surai and Tinau sections, we tied our data to the Appel *et al.* (1991) and Gautam & Appel (1994) studies using the most detailed maps and logs available (e.g. Tokuoka *et al.*, 1990; Corvinus & Rimal, 2001) and to the unpublished Ojha data by tying them to the sampling sites of Szulc *et al.* (2006). We estimate uncertainties on the stratigraphic ages to be of the order of the length of the recognized polarity chrons, i.e. ± 0.1–0.2 Myr, except for the youngest samples, which have larger errors because they are based on extrapolated deposition rates (in the Karnali section) or because the magnetostratigraphy has a low resolution (in the uppermost part of the Surai section).

In the following, we will use the stratigraphic depth of samples as a common reference for the different sections (cf. Figs 4 and 7). As none of the sections record continuous sedimentation to the present day, the maximum depth reached by the samples is not well constrained. The youngest Upper Siwalik sediments in the Surai Khola section have an estimated age of 1.0 ± 0.5 Ma and are overlain by a few hundred metres of younger conglomerates. In the Karnali section, a minimum estimated thickness of 1500 m of upper-Middle and Upper Siwalik series overlies the magneto-stratigraphically dated section. However, in both cases the Upper Siwaliks are clearly syntectonic

(Mugnier *et al.*, 2004; Huyghe *et al.*, 2005) and their thickness may vary strongly laterally, with thick deposits limited to the footwalls of major internal thrusts (Fig. 3). Because the Tinau section is cut off by an internal thrust, no estimate of the overlying sediment thickness can be made in the field. We estimated maximum stratigraphic depth in all three sections by extrapolating the sedimentation rates calculated from the magnetostratigraphic data to the present day (cf. Fig. 4). This approach tends to overestimate the maximum depth reached by the samples by minimizing the age of cessation of deposition at the section locations. However, the extrapolated sediment thickness is close to the thickness of overlying sediments observed in the field. Moreover, the stratigraphic age-depth curves we obtain are consistent between the three sections studied, lending a degree of confidence to our approach. Note that the use of stratigraphic depth is not central to our analysis; it mainly serves to compare the structural positions of samples from different sections and to estimate geothermal gradients from the data.

Apatites were recovered from whole-rock samples using standard magnetic and heavy liquid separation techniques, mounted in epoxy, polished and etched in a 5 M HNO_3 solution at 20 °C for 20 s. All samples were dated by the external detector method, using U-poor mica as an external detector and a ξ calibration factor for Fish Canyon and Durango age standards (Hurford 1990). Samples were irradiated at the well-thermalized ORPHEE facility of the *Centre d'Etudes Nucléaires* in Gif-sur-Yvette, France, with a nominal fluence of $\sim 5 \times 10^{15}$ neutrons cm^{-2}. Neutron fluences were monitored using NBS962 dosimeter glasses (National Bureau of Standards, Gaithersburg, MD, USA). Mica detectors were etched in 48% HF at 20 °C for 20 min. All datable grains (including zero-track grains) within a mount were included in the analysis; grains were selected for dating primarily on the basis of the grain images in the mica detectors. For the Karnali River section, where apatite yield was the highest, confined track-length measurements were performed on separate mounts, after irradiation with ^{252}Cf-fission fragments (at University College London) in order to increase the probability of revealing confined tracks. Track lengths were measured by digitizing the track ends using a drawing tube. For these apatite samples, the etch-pit width parallel to the *C*-axis (D_{par}) of 100 tracks crossing the etched internal surface was measured using the same digitizing technique, in order to constrain their annealing kinetics (e.g. Carlson *et al.*, 1999; Barbarand *et al.*, 2003).

RESULTS

AFT ages are reported as central ages (Galbraith & Laslett 1993) with $\pm 2\sigma$ uncertainties in Tables 1a and b. Although the use of central ages is common in reporting AFT results, these only have geological significance for samples that contain a single-age population (as indicated by a χ^2 probability $P(\chi^2) > 5\%$ and an age dispersion $D < 15\%$) and that are unreset. We determined the age populations making up our samples by binomial peak fitting (Brandon 1996, Stewart & Brandon 2004); Table 2 reports the fitted component ages for the samples containing multiple age populations. Samples collected within the same polarity chron at a single section (e.g. samples KA441+KAR1 in the Karnali section, samples BUT3+TIN5 and BUT1+TIN1 in the Tinau section) were first modelled individually and subsequently modelled together, in order to maximize the number of single-grain ages in the inversions. Thirteen of our samples can be fit by a single-age population; the single binomial peak-fit age is equal to the central age for these samples, which are characterized by age dispersions $D \leq 12\%$. In the following, we will thus quote the central ages for samples containing a single population of grain ages, and the component peak ages (termed P1, P2, etc.) for samples containing multiple populations. Representative radial plots and probability density plots of single-grain ages, together with the fitted age peaks, are shown in Fig. 5.

Three samples from modern river sands were analysed, from the Trisuli and Marsyandi rivers just upstream of their confluence within the Lesser Himalaya about 100 km ENE of the Tinau River section, and from the Karnali River as it enters the Ganges plain just south of the Karnali River section (Table 1b). All three samples contain a single AFT age population. The Trisuli and Marsyandi samples show a similar age structure with a central AFT age of $\sim 1.8 \pm 0.4$ Ma. The Karnali sample, in contrast, yields a surprisingly old AFT central age of 8.0 ± 1.4 Ma.

Within the Surai section, none of the three samples from the Lower Siwalik subgroup yielded sufficient apatite for meaningful age determinations; the deepest sample represented in this study is from a stratigraphic depth of ~ 2700 m (1720 m above the base of the section). Unexpectedly, all of the Surai samples contain a single-age population, consistent with the fact that they all pass the χ^2 test and are characterized by small age dispersions ($D < 10\%$ and mostly $\leq 1\%$). Except for samples SUR1 and SUR20, which are significantly older than the underlying samples, AFT central ages increase down-section (Fig. 4), suggesting that they are unreset. We thus interpret the central age to reliably date source-area exhumation for these samples. However, four out of the eight Surai samples have AFT central ages significantly younger than their depositional age, when using the Appel *et al.* (1991) magnetostratigraphic data (as recalibrated by Gautam & Rösler, 1999), and one sample (SUR15) has an AFT age equal to its depositional age (Fig. 6). The data appear more consistent with the unpublished magnetostratigraphy by T. P. Ojha, as all samples have AFT central ages older than their depositional age. For this reason, we will use this temporal framework, rather than the published data, in the remainder of this study for the Surai and Tinau sections. Lag times for most Surai section samples are ≤ 1 Myr, except for the two 'anomalously' old samples SUR1 and SUR20, which have lag times of 4.3 and 5.3 Myr, respectively. Of these two, SUR1 has a very low U content (as indicated by the low track counts) and its age may be spurious. In contrast, we think the age of SUR20 is reliable and will come back to it in the discussion section.

Table 1a. Detrital apatite fission-track data from the Siwaliks of western-central Nepal

Sample	Stratigraphic age (Ma)	Stratigraphic depth (m)	N	ρ_s ($\times 10^6$ cm^{-2})	N_s	ρ_I ($\times 10^6$ cm^{-2})	N_i	ρ_d ($\times 10^6$ cm^{-2})	N_d	$P(\chi^2)$ (%)	D (%)	Age $\pm 2\sigma$ (Ma)
Karnali Section												
KAR14	2.8 ± 0.3	925	41	0.087	303	1.416	4913	0.555	14 306	2	25	6.0 ± 1.0
KA 30	4.3 ± 0.2	1420	41	0.121	434	1.028	3695	0.374	15 841	46	28	7.4 ± 1.2
KAR13	5.2 ± 0.1	1720	16	0.130	165	1.359	1725	0.551	14 306	4	29	9.0 ± 2.2
KAR12	6.0 ± 0.1	1950	44	0.122	454	1.359	5041	0.554	14 306	1	20	8.9 ± 1.2
KA 34	6.4 ± 0.1	2070	63	0.116	694	0.807	4847	0.377	15 841	68	24	9.5 ± 1.0
KAR11	6.9 ± 0.1	2290	51	0.101	435	0.921	3976	0.553	14 306	59	6	10.5 ± 1.2
KA 36	7.5 ± 0.1	2510	11	0.118	93	0.674	531	0.378	15 841	44	12	11.5 ± 2.8
KAR10	8.1 ± 0.1	2630	59	0.073	365	1.049	5235	0.514	14 306	2	20	6.9 ± 0.8
KAR9	9.0 ± 0.1	2915	49	0.147	598	1.398	5704	0.550	14 306	62	17	10.1 ± 1.2
KAR7	10.9 ± 0.1	3710	56	0.115	546	1.271	6021	0.549	14 306	7	15	8.5 ± 1.0
KAR6	12.1 ± 0.1	3980	48	0.071	289	0.858	3469	0.544	14 306	1	31	8.2 ± 1.4
KAR3	14.1 ± 0.1	4650	51	0.032	139	0.804	3469	0.545	14 306	$\ll 1$	57	4.0 ± 1.0
KA 441	15.9 ± 0.1	5265	44	0.004	383	0.060	6344	0.370	15 841	$\ll 1$	76	4.0 ± 1.0
KAR1	15.9 ± 0.1	5280	37	0.026	88	0.662	2235	0.548	14 306	$\ll 1$	93	5.7 ± 2.2
Tinau Khola Section												
TIN13	6.1 ± 0.2	2010	44	0.108	243	1.105	2499	0.735	17 622	93.2	$\ll 1$	11.2 ± 2.0
TIN8	7.2 ± 0.2	2504	54	0.097	403	0.976	4076	0.735	17 622	26.8	22	11.2 ± 1.8
BUT4	9.1 ± 0.1	2811	29	0.209	529	2.847	7204	0.512	15 671	22.0	23	6.5 ± 0.8
TIN5	10.3 ± 0.2	3343	48	0.023	84	0.406	1493	0.735	17 622	98.7	$\ll 1$	6.4 ± 1.6
BUT3	10.3 ± 0.2	3343	29	0.209	487	3.328	7774	0.512	15 671	$\ll 1$	42	6.0 ± 1.2
TA18A	11.0 ± 0.1	3694	39	0.054	160	0.732	2154	0.519	13 449	35.0	49	6.1 ± 1.6
TA17	11.3 ± 0.2	3810	34	0.065	178	0.970	2672	0.519	13 449	60.9	13	6.0 ± 1.0
BUT1	12.0 ± 0.3	3976	9	0.137	58	3.266	1382	0.512	15 671	1.2	32	4.5 ± 1.6
TIN1	12.0 ± 0.3	3976	24	0.047	53	0.585	662	0.735	12 709	51.3	$\ll 1$	9.1 ± 2.8
Surai Khola Section												
SUR20	1.0 ± 0.5	417	25	0.416	215	6.367	3292	0.546	16 698	96	$\ll 1$	6.2 ± 1.0
SUR17	4.0 ± 0.2	1347	53	0.021	193	0.443	4101	0.545	16 698	84	1	4.4 ± 0.6
SUR16	4.0 ± 0.2	1397	63	0.036	192	0.829	4393	0.544	16 698	99	1	4.1 ± 0.6
SUR15	4.8 ± 0.3	1825	38	0.016	106	0.161	1696	0.546	16 698	98	1	5.9 ± 1.2
SUR1	4.9 ± 0.1	1932	20	0.157	69	1.613	709	0.543	16 698	100	$\ll 1$	9.2 ± 2.4
SUR3	5.0 ± 0.2	1972	34	0.079	210	1.236	3283	0.548	16 698	79	1	6.1 ± 0.8
SUR5	6.3 ± 0.2	2297	40	0.081	252	1.094	3536	0.548	16 698	67	10	7.0 ± 1.0
SUR8	7.0 ± 0.1	2727	68	0.031	179	0.386	2220	0.543	16 698	100	$\ll 1$	7.6 ± 1.2

Table 1b. Detrital apatite fission-track data from modern river sands, western-central Nepal.

Sample	River	Longitude	Latitude	N	ρ_s ($\times 10^6$ cm^{-2})	N_s	ρ_i ($\times 10^6$ cm^{-2})	N_i	ρ_d ($\times 10^6$ cm^{-2})	N_d	$P(\chi^2)$ (%)	D (%)	Age $\pm 2\sigma$ (Ma)
MAR6	Trisuli	84° 39′	27° 46′	32	0.025	74	1.308	3822	0.572	11 674	55.3	15	1.9 ± 0.4
MAR10	Marsyandi	84° 32′	27° 52′	54	0.016	85	0.896	4808	0.572	11 674	65.8	2	1.7 ± 0.4
KAR	Karnali	81° 17′	28° 38′	25	0.067	136	0.786	1600	0.547	14 306	99.6	$<<1$	8.0 ± 1.4

All age determinations were performed by E. Labrin; with $\xi = 346.6 \pm 6.3$ for glass dosimeter NBS962; all ages are reported as central ages (Galbraith & Laslett, 1993). N, number of grains counted; ρ_s, spontaneous track density; ρ_i, induced track density; ρ_d, dosimeter track density; N_s, N_i, N_d, number of tracks counted to determine the reported track densities. For irradiations with significant (> 3%) axial gradients in neutron fluence (as monitored by the dosimeters), ρ_d is interpolated between dosimeter values. $P(\chi^2)$, χ^2 probability that the single grain ages represent one population; D, age dispersion. Stratigraphic age and depth are calculated from the magnetostratigraphic data of Gautam & Fujiwara (2000) for the Karnali section, and from unpublished data by T. P. Ojha (pers. comm. 2003) for the Surai and Tinau sections.

Table 2. Results of binomial peak-age fitting for samples containing multiple age populations.

Sample	Stratigraphic age (Ma)	N	Age range (Ma)	P1 ± 2σ (Ma)	P2 ± 2σ (Ma)	P3 ± 2σ (Ma)
Karnali Section						
KAR14	2.8	41	2.7–25.3	5.0 ± 1.1 (74)	8.2 ± 4.3 (22)	14.1 ± 14.1 (4)
KA 30	4.3	41	1.1–22.4	5.9 ± 1.3 (65)	10.2 ± 2.3 (35)	
KAR13	5.2	16	5.8–16.8	7.1 ± 1.7 (76)	14.4 ± 4.5 (24)	
KAR12	6.0	44	3.2–28.2	7.9 ± 1.3 (79)	13.3 ± 6.0 (21)	
KA 34	6.4	63	1.1–25.7	3.6 ± 2.2 (9)	9.6 ± 1.7 (81)	13.9 ± 19.5 (10)
KAR10	8.1	59	2.7–34.3	6.5 ± 0.8 (98)	23.8 ± 29.0 (3)	
KAR9	9.0	49	3.8–49.4	9.9 ± 1.0 (97)	21.6 ± 36.8 (3)	
KAR7	10.9	56	1.4–31.6	5.1 ± 2.6 (20)	9.3 ± 1.3 (80)	
KAR6	12.1	48	0.9–26.0	2.1 ± 1.8 (13)	9.0 ± 1.3 (87)	
KAR3	14.1	51	0.4–22.3	1.8 ± 1.3 (43)	5.2 ± 1.8 (54)	17.2 ± 24.2 (3)
KA 441	15.9	44	1.2–22.0	2.4 ± 0.4 (82)	11.8 ± 2.0 (18)	
KAR1	15.9	37	0.3–60.5	1.7 ± 0.8 (58)	11.0 ± 6.9 (38)	25.8 ± 71.8 (4)
KA441+KAR1	15.9	81	0.3–60.5	2.4 ± 0.4 (75)	12.0 ± 2.1 (23)	19.2 ± 57.5 (2)
Tinau Khola Section						
TIN8	7.2	54	4.3–38.2	10.5 ± 1.8 (92)	19.3 ± 9.5 (8)	
BUT4	9.1	29	2.2–16.2	2.3 ± 1.2 (6)	7.0 ± 0.7 (94)	
BUT3	10.3	29	1.7–36.7	5.5 ± 0.6 (96)		34.9 ± 31.5 (4)
BUT3+TIN5	10.3	77	1.7–37.9	3.4 ± 1.2 (32)	6.9 ± 1.2 (67)	32.3 ± 32.3 (2)
TA18A	11.0	39	0.5–18.2	6.3 ± 1.5 (92)	14.7 ± 6.3 (8)	
TA17	11.3	34	1.6–24.5	5.4 ± 1.2 (83)	9.0 ± 5.9 (17)	
BUT1	12.0	9	2.2–16.2	3.5 ± 1.1 (88)	13.4 ± 21.5 (12)	
BUT1+TIN1	12.0	33	2.2–42.7	2.5 ± 0.7 (13)	6.9 ± 2.0 (83)	31.6 ± 29.7 (4)

N, number of grains counted; fitted binomial peak ages (P1–P3) are given ± 2σ (95 % confidence interval). Numbers in parentheses correspond to the percentage of grains in a given peak.

Samples from the Tinau section mostly come from greater stratigraphic depths than those from the Surai section, between ~2000 and ~4000 m. Out of nine samples analysed, three contain a single age population (Tables 1 and 2), but two of these (TIN5 and TIN1) were collected from the same polarity chron as samples that show multiple age populations (BUT3 and BUT1, respectively) and were ultimately combined with these for calculating age groups (Table 2). Only the two uppermost Tinau samples have AFT central ages (TIN13) or P1 ages (TIN8) older than the stratigraphic age; for the others, both P1 and P2 peak ages are younger than the depositional age (except for TA18A, which contains a minor P2 peak just older than the depositional age). These samples from below ~2800 m stratigraphic depth are thus partially reset; a downward-increasing intensity of annealing is indicated by the fact that central ages generally decrease down-section (Fig. 4). P1 ages do not become constant down-section, however, suggesting that none of them (except possibly the youngest ones) represent a fully annealed grain population. Thus, neither the P2 nor the P1 peak ages are geologically significant, the latter only provide a maximum estimate for the onset of basin exhumation in this area.

Sample recovery was most complete from the Karnali River section, represented here by 14 samples from between ~900 m and ~5300 m stratigraphic depth. All but two of the Karnali section samples (KAR11, KA36) are characterized by multiple age populations (Tables 1 and 2). Samples from ≤ 2500 m stratigraphic depth, have AFT central ages that increase with depth and that are

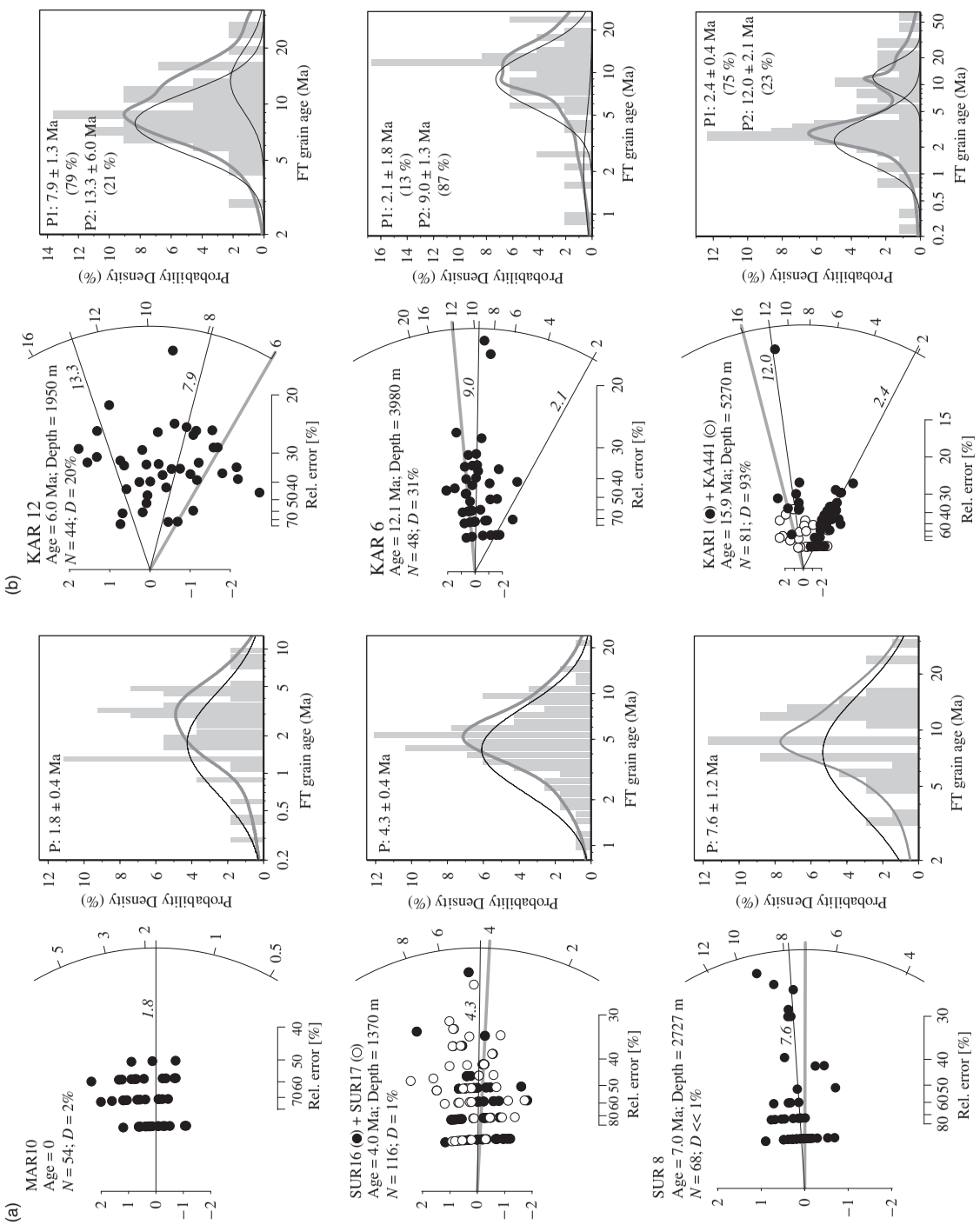

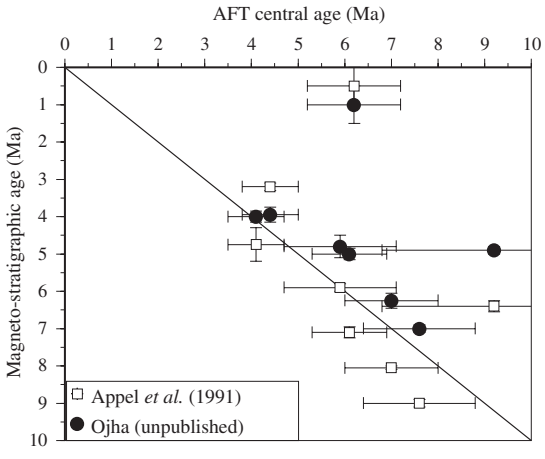

Fig. 6. Plot of apatite fission-track (AFT) central ages from the Surai section against the depositional age of the samples, using either the magnetostratigraphy of Appel *et al*. (1991), as recalibrated by Gautam & Rösler (1999), or the unpublished magnetostratigraphic data of T. P. Ojha (pers. comm., 2003). As all samples contain a single age population, the AFT central age is meaningful, and as these AFTages represent a source-area denudation signal, they should be older than the depositional age. See text for discussion.

significantly older than the depositional age (Fig. 4). For samples containing multiple age populations, minimum (P1) ages are also older than the depositional age (except for sample KA34 from 2070 m depth, which contains a small and anomalously young P1 peak). We interpret these samples as generally unreset and representing a source-area denudation signal. The differences between the P1 age and the depositional age define lag times increasing downward from ~2 to ~4 Myr for the samples above 2500-m depth (Fig. 7). The fact that lag times increase down-section for these samples is a strong indication that they are unreset, as partial annealing increases in intensity down-section and would reduce the peak ages and thus the lag times. Three samples (KA36, KAR10, KAR9) between ~2500 and ~2900 m depth have variable AFTages, with P1 peaks both older and younger than the depositional age. Samples from below ~3000 m stratigraphic depth (i.e. within the lowermost 2000 m of the section) have central ages generally decreasing down-section, and both P1 and P2 peaks that are younger than the depositional age, indicating partially reset samples. P1 ages generally decrease down-section but are constant, with a mean of 2.1 ± 0.3 Ma, for the lowermost four samples (Fig. 7, see also Fig. 5), suggesting that these represent a fully reset group of apatites and indicate the onset of final exhumation of the basin strata. This age overlaps the two youngest P1 peaks from the Tinau section samples (BUT4 and BUT1+TIN1).

Four samples from the Karnali section and two from the Tinau section show minor P3 populations with ages between 14 and 35 Ma, i.e. much older than the depositional ages, even for the deepest samples. If these are not artefacts, they must represent exceptionally resistant apatites derived from areas of relatively low denudation rates. However, because these age groups are defined by very small numbers of grains, the errors on the peak ages are typically larger than the peak age itself, rendering any interpretation of these very hazardous.

Track-length measurements were performed on eight samples from the Karnali River section and one from the Tinau section (Table 3). Track-length histograms for the Karanali samples are plotted in Fig. 7. Owing to the low track densities in these samples and the relative paucity of material, between 36 and 80 lengths only could be measured, even after ^{252}Cf irradiation. The mean track lengths vary between 11.0 and 12.0 μm for nonreset samples (with corresponding standard deviations of 2.0–3.0 μm), suggesting complex source-area exhumation paths. They decrease down-section to ~9.5 μm in the deepest, most strongly annealed samples. Samples from intermediate depths, between ~2000 and ~3000 m, show bimodal distributions (e.g. KAR12, KAR11, KAR9), whereas track-length distributions from deeper samples become positively skewed, indicative of increasing annealing intensities down-section (Gallagher *et al*., 1998). Etch-pit widths (D_{par}) show little variation, both within single samples and between samples. D_{par} values vary between 1.2 and 1.8 μm, with standard deviations of 0.3–0.4 μm. Six out of nine samples have a D_{par} between 1.6 and 1.8 μm (Table 3), indicating annealing behaviour close to that of Durango apatite (e.g. Carlson *et al*., 1999; Barbarand *et al*., 2003).

DISCUSSION

Interpreting the above results is not an easy task because our samples combine variable source signals with varying degrees of thermal resetting. This leads to a wide variety of single-grain age structures between the samples: some samples are characterized by a single grain-age population, whereas others have multiple component ages; both minimum and central ages can be either older or younger than the depositional age. Typical uncertainties on the AFT central or component ages are > 15% and will propagate into inferred source area or basin exhumation rates. Compared with these error bars, the uncertainties on the depositional ages are relatively small, but we have to accept the magnetostratigraphy at face value (except for the Surai

Fig. 5. Radial plots (Galbraith, 1990; left) and probability density functions (right) for a number of representative samples. Within the radial plots, thin black lines indicate the different peak ages recognized within the sample; thick shaded lines indicate the depositional age. *N*, number of grains represented; *D*, age dispersion (Galbraith & Laslett, 1993). Bars within probability density plots are histograms of single-grain age distribution; the thick shaded line is the single-grain age probability-density function of the entire population (Brandon, 1996); thin black lines are modelled probability-density functions for the fitted age populations.

section). Although formal 95% confidence limits on our reconstructed burial depths are very small (typically 10–15 m), we have no way of independently testing our stratigraphic depth model. This does not strongly influence our inferences, however, other than for determining the geothermal gradient. Finally, some of the results are spurious, falling outside of the trends defined by under- and overlying samples (e.g. SUR1, KAR10). Nevertheless, when combining all the data, some clear trends do arise and we will construct our interpretation of the data on the basis of these general trends.

Combining the data from all three sections (e.g. Fig. 4) shows a consistent transition from unreset to partially reset samples between 2500 and 2800 m reconstructed stratigraphic depth. Studies of AFT annealing from thermally calibrated wells (see Gallagher *et al.*, 1998 for a review), as well as annealing models based on experimental data (e.g. Ketcham *et al.*, 1999), indicate that significant AFT annealing under geological timescales begins at temperatures of 70–80 °C (cf. Fig. 1), thus providing us with a temperature benchmark in the sections. These inferred temperatures are consistent with vitrinite reflectance data from a limited number of samples from the upper part of the Karnali section (L. Martinez, Pers. Comm. 2003), which suggest maximum temperatures between 62 and 75 °C at depths between 1700 and 2600 m. Likewise, Mugnier *et al.* (1995) reported vitrinite reflectance (R_0) values of 0.3–0.5% for Middle Siwalik and 0.6–1.0% for Lower Siwalik sediments in west-central Nepal, corresponding to maximum burial temperatures of 60–90 °C and >100 °C, respectively. Huyghe *et al.* (2005) estimated temperatures of 70–95 °C at depths >2100 m in the Karnali section from illite crystallinity. These different depth–temperature couples indicate a geothermal gradient of 18–24 °C km^{-1} (assuming a mean surface temperature of 20 °C), consistent with temperature measurements in wells located in the Siwaliks of western India (Agarwal *et al.*, 1994). This overall consistency suggests that our palaeo-depth estimates from the extrapolation of sedimentation rates are reasonable.

Because of the fundamentally different information that is to be gained from unreset samples, retaining a source-area signal, and partially to fully reset samples, recording the postdepositional thermal evolution, we discuss these two sets of samples separately below.

Source-area denudation rates

Figure 8 shows a lag-time plot for all nonreset samples from the three sections analysed. The AFT ages plotted in this figure are either the central age (for samples with a single age population) or the youngest (P1) peak age (for samples with multiple age components).

Samples from the Surai section are aligned along a constant lag-time trend of ≤ 1 Myr, with the exception of the outliers SUR20 and SUR1, whereas samples from the Karnali section appear to indicate lag times that decrease up-section, from $\sim$4 Myr at $\sim$7 Ma (KAR11, KA36) to $\sim$2 Myr at the top of the section. Alternatively, the Karnali data can be interpreted as two more or less constant lag-time trends at $\sim$4 and $\sim$2 Myr, respectively, and a sharp jump from one to the other at $\sim$6.5 Ma. Note, however, that the three samples that define the $\sim$4 Myr lag time contain a single age population and we thus use their central ages, whereas for the younger samples with shorter lag times we use the P1 ages. On the other hand, bimodal track-length distributions in these lower samples (Fig. 7) indicate an onset of partial annealing that would tend to decrease the ages and lag times.

Bernet *et al.* (2001) suggested a simple test for constancy of lag times by performing a linear correlation of FT peak ages (t_c) to depositional ages (t_d): if lag times are constant, the slope to the correlation line should be $\sim$1; if it is >1, lag times decrease up-section and if it is <1, they increase up-section. For the Surai samples (excluding the outliers SUR20 and SUR1), the slope of the correlation line (weighted by the uncertainties on both the magnetostratigraphic and AFT ages; Williamson, 1968) is 1.18 ± 0.18 (95% confidence limit; $r^2 = 0.93$), consistent with a constant lag time of 0.8 ± 0.5 Myr (weighted mean $\pm$ 95% confidence limit). This mean lag time is consistent with published *in situ* AFT ages from samples closest to this section, in the upper Marsyandi valley in central Nepal (Blythe *et al.*, 2006), but significantly smaller than the central ages of the two present-day sediment samples, collected in rivers draining the central Nepal Himalaya (samples MAR6 and MAR10). Note that, at present, sediments from the Marsyandi and Trisuli catchments leave the Himalayan system along the Narayani River, approximately 120 km east of the Surai. Sedimentology and source area indicators for the Middle and most of the Upper Siwaliks of the Surai section, however, clearly indicate that these were fed by a drainage system originating in the Higher Himalaya (Huyghe *et al.*, 2001; 2005; Robinson *et al.*, 2001; Bernet *et al.*, 2006; Szulc *et al.*, 2006).

For the Karnali section, in contrast, the slope of the correlation line is 1.40 ± 0.22 (95% confidence limit; $r^2 = 0.93$), indicating lag times that decrease up-section, with a weighted mean of 2.5 ± 0.9 Myr. No *in situ* thermochronological data exist in Western Nepal to compare these with. The difference in lag times between the two sections, however, is significant.

These spatial variations in lag times do not show up as clearly in the detrital zircon data presented in the companion paper (Bernet *et al.*, 2006), principally because the zircon yield from the Karnali section is low. In order to compare the apatite and zircon data more quantitatively, we transformed lag times for both datasets to source-area exhumation rates using a modified version of the simple one-dimensional (1D) model of Brandon *et al.* (1998). This model takes into account the advective perturbation of an initially linear geotherm by rock exhumation, as well as the dependence of closure temperature on cooling rate (e.g. Dodson 1973). It does not, however, include 2D or 3D effects such as nonvertical rock-particle paths, spatial varia-

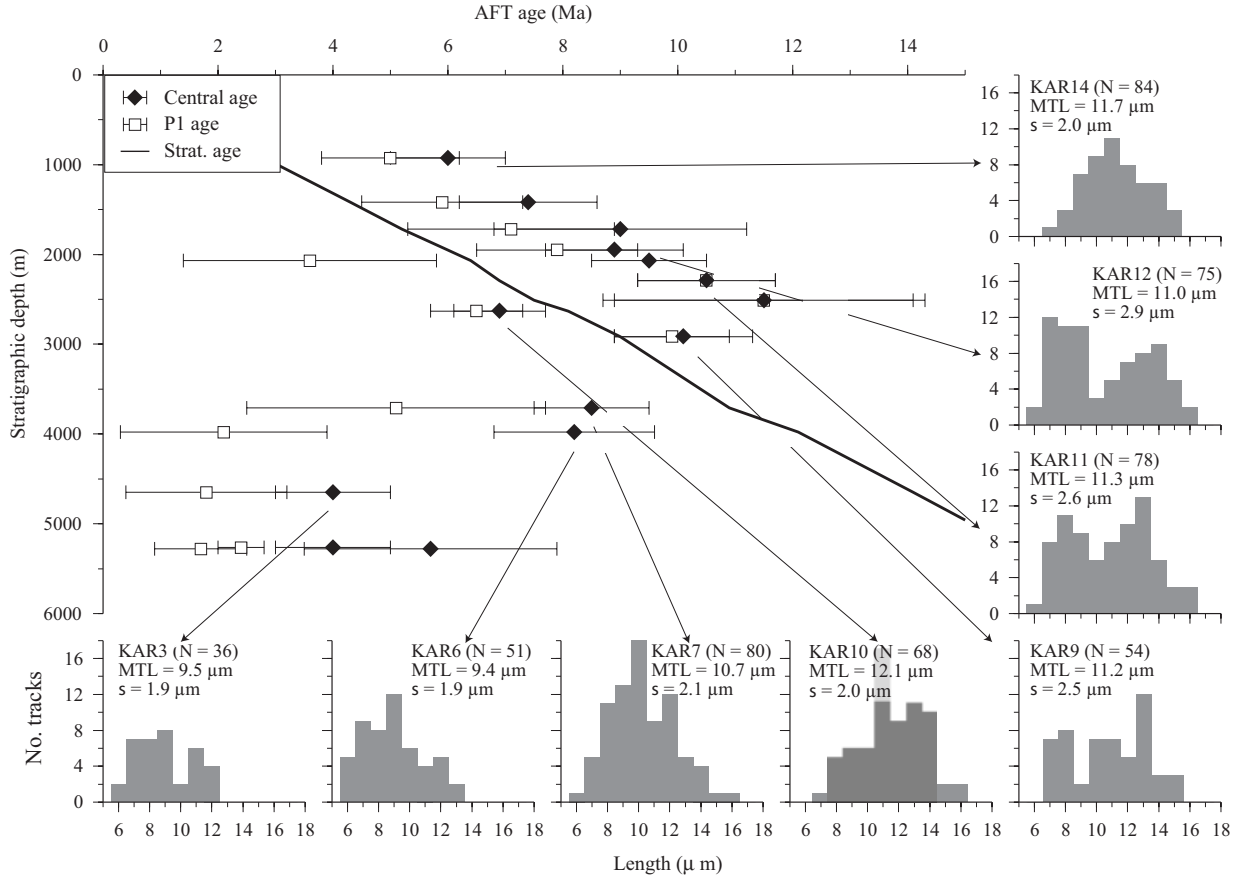

Fig. 7. Main panel shows plot of apatite fission-track (AFT) central ages (black diamonds) and P1 ages (i.e. peak age of the youngest population; white squares) against depth for samples from the Karnali River section. Small panels show track-length histograms for Karnali section samples (N, number of tracks lengths measured; MTL, mean track length, σ, standard deviation).

Table 3. Track-length and etch-pit width measurements

Sample	MTL ± 1σ (μm)	Standard deviation (μm)	*N*	D_{par}(μm)	Standard deviation (μm)
Karnali Section					
KAR14	11.7 ± 0.3	2.0	84	1.7	0.4
KAR13				1.7	0.3
KAR12	11.0 ± 0.3	2.9	75	1.6	0.3
KAR11	11.3 ± 0.3	2.6	78	1.6	0.3
KAR10	12.1 ± 0.2	2.0	68	1.8	0.3
KAR9	11.2 ± 0.3	2.5	54	1.3	0.4
KAR7	10.7 ± 0.2	2.1	80	1.6	0.4
KAR6	9.4 ± 0.3	1.9	51	1.2	0.3
KAR3	9.5 ± 0.3	1.9	36	1.5	0.4
Tinau Khola Section					
TIN8	10.9 ± 0.2	1.6	100		

Track lengths and etch-pit widths were measured by X. Robert. Samples were ^{252}Cf-irradiated before revealing confined horizontal tracks. MTL, mean track length; *N*, number of horizontal confined tracks measured. D_{par}, etch-pit width parallel to the *C*-axis. 100 etch-pit widths were measured for each sample.

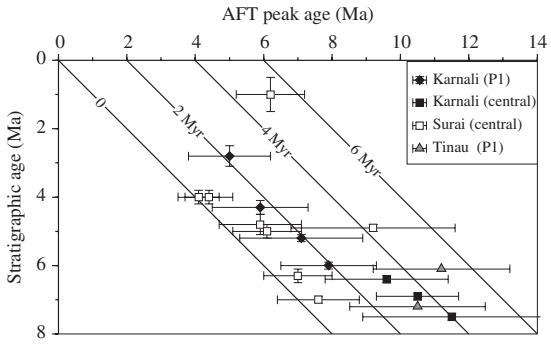

Fig. 8. Lag-time plot showing apatite fission-track (AFT) age against depositional age of nonreset samples from the Surai, Karnali and Tinau sections. For samples that contain a single age population (e.g. Surai and lower three Karnali samples), the central age is plotted; for samples with multiple age components, only the youngest age peak (P1) is reproduced. Diagonal lines represent constant lag times as indicated.

tion in exhumation rates or topographic effects. Where both zircon and apatite data are available for the same sample, we combine ZFT and AFT ages to predict an initial exhumation rate between the ZFT and AFT closure temperatures and a final rate between the AFT closure temperature and the surface. This procedure permits us to predict exhumation rates that are consistent with both sets of data. We predict exhumation rates using the central age for samples with a single age population, or the P1 age for samples containing multiple age components. The implication is that the model exhumation rate corresponds to the most rapidly exhuming part of the source area, which we will term 'peak exhumation rates' in the following.

Model results are shown in Fig. 9, for the Surai and Karnali sections. Error bars on the predicted exhumation rates are calculated from the 2σ error on the (peak or central) ages; where these overlap with the depositional age, the maximum exhumation rate becomes infinite. Within the Karnali section, apatite and zircon data consistently predict peak exhumation rates of 1.3 ± 0.3 km Myr^{-1}. Within the Surai section, ZFT data indicate relatively constant peak exhumation rates of 1.5 ± 0.4 km Myr^{-1}, whereas AFT data are more variable and predict higher peak exhumation rates of 3.5 ± 2.1 km Myr^{-1} between 7 and 4 Ma. The above values are simple arithmetic means of the predicted exhumation rates for each sample. When taking the uncertainties in exhumation rates (due to the error on the ages) into account and calculating weighted means, the difference between rates predicted using the two systems disappears. This is because the predicted high exhumation rates for AFT data in the Surai section result from very short lag times with large relative errors, mostly overlapping with the depositional age. The weighted mean predicted exhumation rate from both AFT and ZFT data for the Surai section (again excluding SUR1 and SUR20) is 1.8 km Myr^{-1}. AFT and ZFT data from present-day river sands upstream of the Siwaliks (the Marsyandi and Rapti rivers, respectively) also consistently indicate peak source-area exhumation rates of 1.5–1.6 km Myr^{-1}.

The inferred difference in peak source-area exhumation rate between the Karnali and Surai sections thus appears real, amounts to ∼500 m Myr^{-1} over the last ∼7 Myr and requires an explanation. Lower long-term exhumation rates in the Karnali catchment, with respect to central Nepal, are consistent with the preservation of klippen of Higher Himalayan and Tethyan rocks in western Nepal, whereas these have been removed by erosion in central Nepal (cf. Fig. 2). Both tectonic and climatic effects may control such lateral variations in exhumation rate along the Himalayan front. Thiede *et al.* (2004) and Bookhagen *et al.* (2005) suggested that Himalayan exhumation rates are the highest where monsoonal precipitation penetrates into the orogen along major river valleys and is focused on the orographic barrier formed by the High

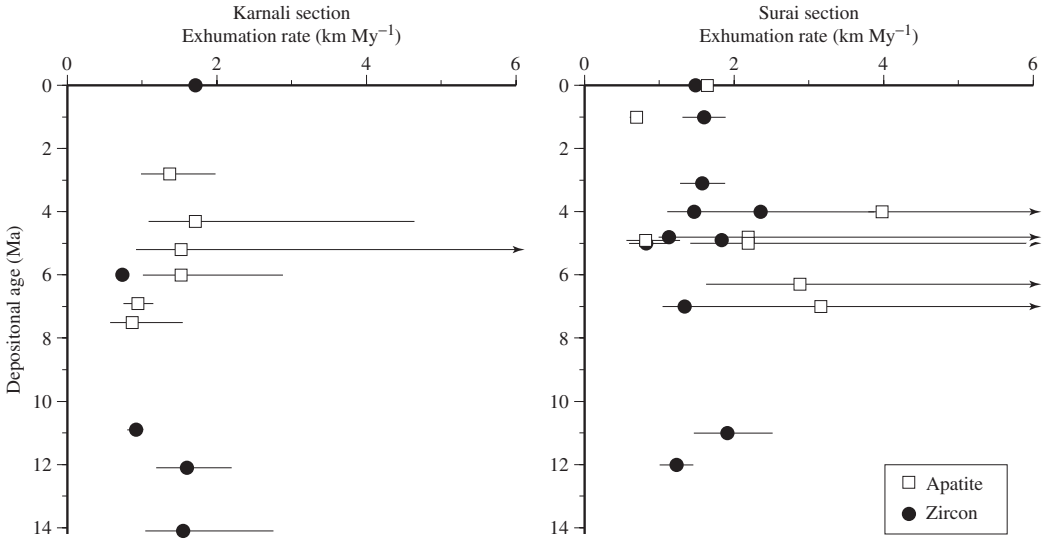

Fig. 9. Modelled peak exhumation rates as a function of time calculated from apatite fission-track (AFT) and zircon fission-track (ZFT) lag times observed in the Karnali and Surai section samples. A modified version of the one dimensional model of Brandon *et al.* (1998) is used in the calculation; closure temperature is estimated following Dodson (1973) using the kinetic parameters estimated from annealing experiments by Brandon *et al.* (1998); AFT: $E_a = 186.4\,\mathrm{kJ\,mol^{-1}}$, $D_0a^2 = 3.64 \times 10^{10}\,\mathrm{s^{-1}}$; ZFT: $E_a = 208.2\,\mathrm{kJ\,mol^{-1}}$, $D_0a^2 = 3.70 \times 10^{6}\,\mathrm{s^{-1}}$. Other parameter values used in the model: surface temperature $T_s = 20\,^{\circ}\mathrm{C}$, initial geothermal gradient $G = 20\,^{\circ}\mathrm{C\,km^{-1}}$, model thickness $L = 25\,\mathrm{km}$, thermal diffusivity $\kappa = 25\,\mathrm{km^2\,Myr^{-1}}$. Uncertainties in predicted exhumation rate are propagated from 2σ uncertainties in peak or central ages. See text for discussion.

Himalaya. The Narayani catchment in central Nepal may be one of these erosional 'hotspots', as shown by the precipitation maps published by Thiede *et al.* (2004) and Bookhagen *et al.* (2005), and the predicted stream power map of Finlayson *et al.* (2002), whereas precipitation appears not to penetrate deeply into the orogen in the Karnali catchment. From a tectonic point of view, Berger *et al.* (2004) modelled present-day deformation in Nepal to show that the mid-crustal ramp underlying the Himalayan topographic front is much larger in central Nepal than in western Nepal. As spatial variations in exhumation rates may be controlled to a large extent by material being pushed up this ramp (e.g. Lavé & Avouac, 2001; Avouac, 2003; Bollinger *et al.*, 2004), the Berger *et al.* (2004) results imply higher exhumation rates in central Nepal compared with western Nepal. It is possible that the tectonic and climatic controls are linked through the cross-sectional topography of the mountain belt, which is much more concave in central Nepal than in western Nepal (Berger *et al.*, 2004).

The data do not provide evidence for a significant increase in source-area denudation rates over the last few Myr, as has been inferred from the foreland basin stratigraphy (Burbank, 1992) and from comparisons of high- and low-temperature thermochronometers (Vance *et al.*, 2003; Vannay *et al.*, 2004). In contrast, the youngest samples appear to have intriguingly old AFT ages. SUR20 (depositional age 1.0 ± 0.5 Ma) has an AFT lag time of 5.2 Myr, longer than any of the other samples in this study and that cannot be attributed to artefacts due to low U contents such as in sample SUR1. The modern Surai is a minor stream draining only the Siwalik Hills, but the regional drainage pattern suggests that it was previously connected to the headwaters of the Rapti River before the latter was diverted by movement along the MFT (e.g. Champel *et al.*, 2002). We thus expect that the modern Surai exclusively carries sediments that have been recycled within the Siwaliks, which would explain this anomalously old AFT age. The appearance of an important recycled component within the Upper Siwaliks may therefore indicate the onset of movement along the MFT between 4.0 ± 0.2 and 1.0 ± 0.5 Ma (i.e. the depositional ages of samples SUR17 and SUR20, respectively). The importance of sediment recycling in the Siwaliks is also suggested by the modern sediment sample collected from the Karnali River where it leaves the Siwaliks and enters the Ganges plain. Although this sample yielded only 25 datable apatites, they have a surprisingly old central age of 8.1 ± 1.4 Ma. Amalgamating all Karnali section samples (611 single-grain ages) results in an indistinguishable central age of 7.6 ± 0.4 Ma. This virtual 'mixed Siwaliks' sample contains three age components of 3.0 ± 0.4, 8.1 ± 2.0 and 11.2 ± 3.0 Ma, respectively, the 8.1 Ma age peak representing $\sim$50% of the single-grain ages. It thus appears likely that the modern Karnali River sample downstream of the Siwaliks contains almost exclusively recycled apatites. A modern sediment sample taken upstream of the section and for which Bernet *et al.* (2006) report detrital ZFT ages would have been able to test this inference but unfortunately did not yield sufficient apatite for analysis.

Further evidence for significant recycling of apatites within the Siwalik sediments, however, comes from a comparison of our results from three proximal sections

Table 4. Results of binomial peak-age fitting for Bengal Fan data

Sample	Stratigraphic age (Ma)	*N*	Age range (Ma)	P1 ± 2σ (Ma)	P2 ± 2σ (Ma)
Site 717					
7–0	0.3 ± 0.3	30	1.0–25.7	4.4 ± 1.3 (95)	20.8 ± 26.9 (5)
7–220	3.0 ± 0.8	30	1.5–17.0	6.6 ± 1.8 (100)	
7–420	6.0 ± 0.4	30	1.8–21.3	7.7 ± 3.8 (65)	11.6 ± 8.3 (35)
7–620	8.0 ± 0.5	30	2.9–22.1	11.9 ± 2.4 (100)	
7–720	9.0 ± 0.5	30	9.1–37.5	14.3 ± 2.8 (100)	
Site 718					
8–290	9.0 ± 0.7	30	5.7–30.2	14.3 ± 3.1 (84)	25.5 ± 11.9 (16)
8–460	10.6 ± 0.3	30	8.1–190.3	18.9 ± 3.4 (97)	190.3 ± 82.8 (3)
8–660	14.4 ± 1.4	30	5.8–82.4	16.2 ± 6.8 (54)	21.4 ± 9.9 (46)
8–760	16.3 ± 0.6	30	10.2–32.8	18.0 ± 3.6 (100)	
8–860	17.0 ± 0.2	30	7.7–25.7	15.8 ± 3.0 (100)	

Data from Corrigan & Crowley (1990). Notations as in Table 2.

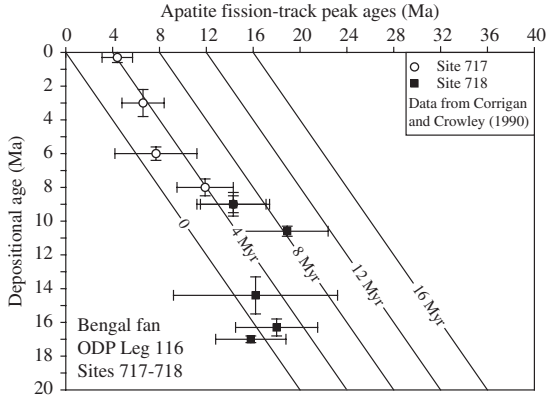

Fig. 10. Lag-time plot for the Bengal Fan data of Corrigan & Crowley (1990). The dataset was treated in the same manner as our own data (Table 4); the plot shows the P1 age peaks. Diagonal lines represent constant lag times as indicated. Compare with Fig. 8.

with those of Corrigan & Crowley (1990) from two ODP sites in the distal Bengal Fan. We calculated component ages from the Corrigan & Crowley (1990) dataset using the same approach as for our own data (Table 4) and plot the obtained minimum (P1) ages as a function of depositional age in Fig. 10. Except for the lowermost three samples from Site 718, which Corrigan & Crowley (1990) argue are partially reset, the data show lag times of 1.7–8.3 Myr with a weighted mean 4.4 ± 1.9 Myr, i.e. significantly longer than the lag times measured in our study.

Thus, it appears that sediment recycling within the Siwaliks has a major impact on detrital AFT age distributions of samples collected downstream. In contrast, no significant recycling of Siwalik sediments is evident from detrital zircon or mica ages, whether these were collected from the Upper Siwalik subgroup (Bernet *et al.*, 2006; Szulc *et al.*, 2006), from Bengal Fan sediments (Copeland & Harrison, 1990) or from the modern river sediment in the foreland (Clift *et al.*, 2004; Campbell *et al.*, 2005). We have no satisfactory explanation for this apparent contradiction at present. Further constraining the role of sediment recycling within Siwalik sediments will thus require more detailed multi-method analyses on present day and recent sediments.

Thermal and kinematic history of the foreland basin

Whereas the non-reset samples provide an insight into the history of source-area exhumation, the deeper, partially annealed samples record the postdepositional burial and exhumation history within the Siwalik basin. As all three sampled sections occur in the hanging wall of the MFT (e.g. Figs 2 and 3), the exhumation history is directly linked to the kinematics of the currently active deformation front of the Himalaya.

Minimum AFT ages of the lowermost four samples from the Karnali section (i.e. KAR6, KAR3, KA441+KAR1), as well as the lowermost two samples from the Tinau section (BUT1+TIN1) all overlap at 2.1 ± 0.4 Ma (Table 2), suggesting an onset of exhumation along the MFT around that time. In order to further constrain the exhumation history, we attempted to invert the track-length distributions of the most deeply buried samples from the Karnali section for thermal history using the AFTSolve modelling procedure (Ketcham *et al.*, 2000). Inverting track-length distributions in settings such as the one we study is far from straightforward and the resulting thermal histories should be considered with care. Firstly, the relatively short mean track lengths of the unreset samples (Table 3) indicate that the samples arrived in the basin with a relatively complex exhumation history that should be taken into account when modelling the postdepositional thermal history (e.g. Carter & Gallagher, 2004). Secondly, the number of track lengths we were able to measure in any sample is low, diminishing the constraint on predicted thermal history. Thirdly, we are dealing with partially annealed samples characterized by a relatively large spread in ages and wide track-length distributions, indicative of

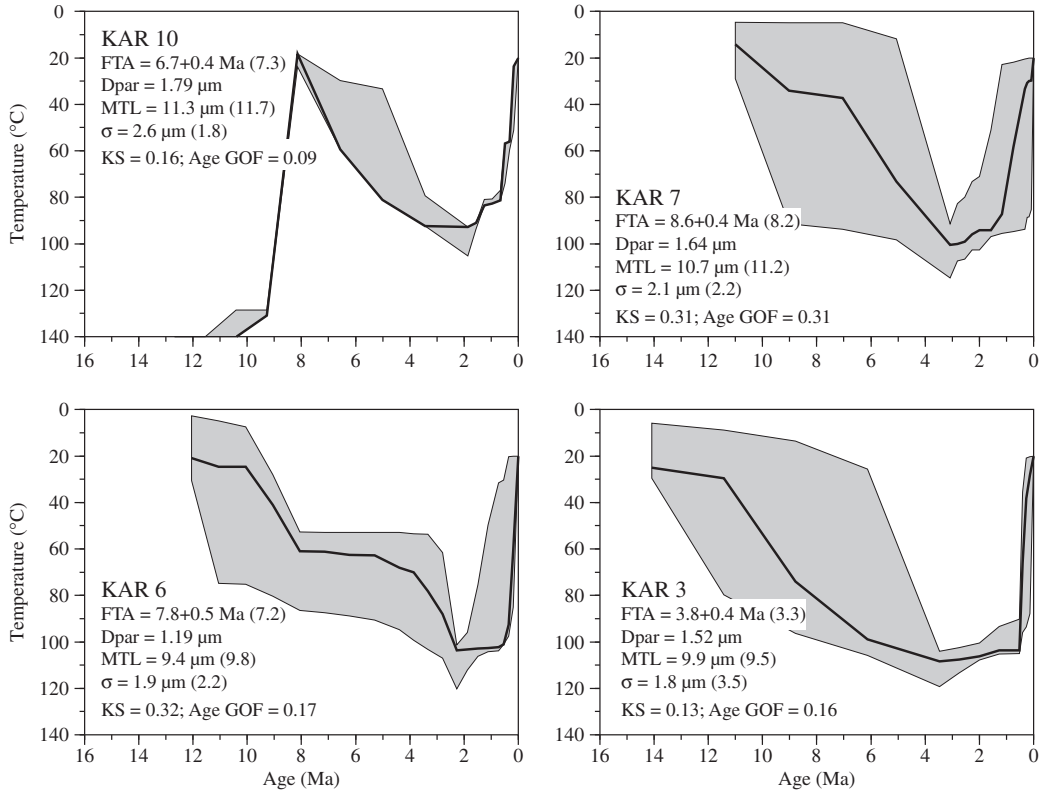

Fig. 11. Representative thermal histories for partially reset samples from the Karnali River section. The thick line is the best-fit model; the shaded area corresponds to acceptable model fits. For each sample, the legend provides the measured apatite fission-track (AFT) age, mean track length (MTL) and standard deviation of the track-length distribution (σ), compared with the best-fit model predictions in parentheses. Also quoted is the D_{par} value used in the inversion. The inversion used a constrained random search with 10 000 iterations to find a best-fit solution (cf. Ketcham *et al.*, 2000); model fit to the data is given by the KS statistic for the comparison of modelled and observed track-length distributions, and a goodness-of-fit criterion analogous to the KS statistic for the observed and predicted AFTage. For clarity, the predepositional cooling of samples KAR3, 6, and 7 has been omitted; this part of the thermal history is essentially unconstrained by the data.

variable predepositional thermal histories and/or variable resistance to annealing. In the Ketcham *et al.* (2000) modelling approach, these can be incorporated by defining multiple kinetic populations. Moreover, in detrital samples, thermal modelling should ideally be performed on a single age population in order to characterize a unique thermal history (e.g. Carrapa *et al.*, 2006). However, as we measured track lengths on separate ^{252}Cf-irradiated mounts and as we are working with relatively few track-length measurements, we refrained from separating our length measurements according to kinetic or age groups. We did, however, monitor the resistance to annealing of our samples by measuring etch-pit widths and found little variation in D_{par} values, both within and between samples (Table 3).

Keeping the above caveats in mind, modelled thermal histories for four samples from the Karnali section are shown in Fig. 11. We use the fact that samples were at the surface at the age of deposition as the principal constraint on these models, and use the source-area exhumation histories inferred for the shallow and lesser annealed samples to guide the predepositional histories of the deepest, most strongly annealed, samples. Because of the complications discussed above, none of the predicted thermal histories provide a very tight fit to the data, as indicated by the relatively low values for the fit statistics. The different thermal histories are, however, remarkably consistent with each other; they all indicate heating from the time of deposition until ~2 Ma, followed by a phase of thermal stability or slow cooling and a final phase of very rapid cooling from ~0.3 Ma onward. The final exhumation of basin strata is most tightly constrained by the deepest, most strongly annealed sample (i.e. KAR3), as expected. The maximum temperatures reached by the samples, as predicted by the inverse model, increase consistently with depth from 90–104 °C for KAR11 (2290 m depth) to 106–115 °C for KAR3 (4650 m depth), even though we modelled the samples individually. We chose not to use a combined inversion scheme (e.g. Gallagher *et al.*, 2005) as this would imply imposing a constant geothermal gradient *a priori*. Predicted maximum palaeotemperatures as a function of depth are shown in Fig. 12.

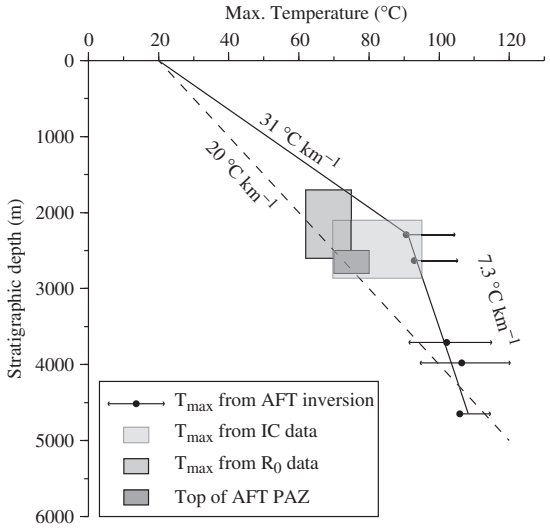

Fig. 12. Maximum palaeotemperature reached by the partially annealed samples from the Karnali River section, as predicted by the apatite fission-track (AFT) Solve inversions, plotted as a function of stratigraphic depth. Dots indicate maximum temperature of best-fit inversion; error bars correspond to maximum and minimum peak temperatures allowed by the 'acceptable' model fits (cf. Fig. 11). Shown for comparison are the maximum palaeotemperatures inferred from illite crystallinity (IC; Huyghe *et al.*, 2005) and vitrinite reflectance (R_0; L. Martinez, pers. comm. 2003) data in the upper part of the Karnali section, and the depth of the transition from unreset to partially reset samples and its associated temperature range. The peak temperatures from AFT inversions are consistent with a geothermal gradient of $7.3 \pm 3.8\,^{\circ}C\,km^{-1}$ (95% confidence limit; $r^2 = 0.92$) between ~2300 and ~4600 m depth and require a gradient of $\sim 30\,^{\circ}C\,km^{-1}$ above that depth range. A linear $20\,^{\circ}C\,km^{-1}$ gradient is plotted for comparison.

Although the predicted maximum palaeotemperatures are consistent with each other, they suggest a very low geothermal gradient of $7.3 \pm 3.8\,^{\circ}C\,km^{-1}$ (95% confidence limit; $r^2 = 0.92$) between ~2300 and 4650 m depth and imply a much higher geothermal gradient of $\sim 30\,^{\circ}C\,km^{-1}$ in the top 2 km of the section (Fig. 12). The peak temperatures predicted for the lowermost three modelled samples are consistent with the $\sim 20\,^{\circ}C\,km^{-1}$ geotherm inferred earlier from the depth of transition between unreset and partially annealed samples, but the predicted maximum palaeotemperatures for the two upper samples are 15–25 °C higher than expected. This discrepancy may reflect the difficulty of modelling the uppermost and least annealed samples. If the predicted palaeotemperatures are valid, they require a strongly nonlinear geotherm within the Siwalik basin, which could suggest convective heat transport by fluids in the basin. Although independent palaeotemperature indicators could be used to validate the model predictions, currently available vitrinite reflectance and illite crystallinity data (Huyghe *et al.*, 2005) do not permit to discriminate between a linear or nonlinear geotherm (Fig. 12).

Irrespective of the predicted maximum palaeotemperatures, the modelled thermal histories are readily explained within the tectonic setting of the frontal Siwalik belt. The initial postdepositional heating phase is clearly linked to postdepositional burial, the cessation of which at ~2 Ma would indicate onset of exhumation along the MFT. This timing is consistent with that inferred independently from the minimum AFT ages in the deepest samples, as well as with field observations of growth strata linked to the onset of movement along the MFT (Mugnier *et al.*, 2004). Finally, the strong acceleration of cooling at ~0.3 Ma is consistent with passage of the rocks from the basal décollement onto the MFT ramp during exhumation (cf. Fig. 3). As the flat-ramp transition occurs at ~3500 m depth in the Karnali section (Fig. 3), exhumation along a 30° dipping ramp in 0.3 Myr corresponds to a mean exhumation rate of $\sim 12\,mm\,year^{-1}$ and a mean shortening rate of $\sim 20\,mm\,year^{-1}$. These values are consistent with short-term rates of rock uplift and shortening along the MFT from tectonic geomorphology studies (Lavé & Avouac, 2000; Mugnier *et al.*, 2004), suggesting that the current shortening rates along the MFT have been maintained for at least the last 0.3 Myr.

One could argue that shortening at $\sim 20\,mm\,year^{-1}$ could have taken place along the MFT since 2 Ma, implying ~40 km of shortening along the MFT since its inception. However, such a scenario implies unrealistic depths of burial for samples at the base of the section. The dip of the décollement underlying the Siwaliks in western Nepal is 6–8° (Larson *et al.*, 1999; Berger *et al.*, 2004) and attaches to the ramp at a depth of ~3500 m. Shortening at $20\,mm\,year^{-1}$ during 1.7 Myr (before reaching the ramp) implies maximum burial depths for samples at the base of the section of 7.1–8.3 km, or maximum burial temperatures of 162–187 °C for a geothermal gradient of $20\,^{\circ}C\,km^{-1}$, largely sufficient to anneal fully all apatite in these samples regardless of composition. Even when adopting the nonlinear geotherm suggested by the track-length inversions, the maximum burial temperatures would be 126–135 °C, sufficient to anneal fully fission tracks in apatites of the composition encountered in this study. In contrast to these predictions, none of the samples in our study are totally annealed, with even the deepest samples (KAR1, KA441) retaining 25% of grains with AFT ages close to the depositional age (cf. Table 2; Fig. 5). These results require either intermittent operation of the MFT since 2 Ma or a recent increase in shortening rates along it. Preliminary thermal-kinematic forward modelling of the Karnali structure (Robert, 2005) suggests that intermittent operation of the MFT is most consistent with the thermochronological data presented here.

CONCLUSIONS

The low-temperature detrital AFT data presented here complement the detrital zircon data of Bernet *et al.* (2006) by highlighting spatial variations in source-area exhuma-

tion rates and by providing information on the postdepositional thermal and kinematic history of the Siwalik foreland basin. The most pertinent conclusions to be drawn from these data are the following:

Within the Surai section in central Nepal, the detrital AFT ages are inconsistent with the magneto-stratigraphic dating of this section as proposed by Appel *et al.* (1991) and recalibrated to the Cande & Kent (1995) magnetic polarity timescale by Gautam & Rösler (1999). In contrast, the data are consistent with more recent but unpublished magneto-stratigraphic data (T. P. Ojha, pers. commun., 2003). Using depositional ages constrained by this magneto-stratigraphic framework, the Surai section AFT ages yield a constant lag time of 0.8 ± 0.5 Myr, indicating rapid source-area exhumation rates of $\sim$1.8 km Myr^{-1} since $\sim$7 Ma. In contrast, nonreset samples from the Karnali River section in western Nepal yield minimum lag times that decrease from $\sim$4 Myr at $\sim$7 Ma to $\sim$2 Myr at the top of the section, implying peak source-area exhumation rates in the order of 1.0–1.5 km Myr^{-1}. These spatial variations in source-area exhumation rates can be explained by either tectonic or climatic controls, or possibly a combination of the two. No indications for a significant increase in source-area exhumation rates over the last few million years, as suggested by several authors, have been encountered. In contrast, lag times are conspicuously long for samples from the Upper Siwalik subgroup in the Surai section, suggesting an increasing influence of sedimentary recycling within the Siwaliks. Recycling is also indicated by the relatively old AFT age of present-day sediment in the Karnali River downstream of the Siwaliks, and by long lag times calculated from a published AFT dataset in the distal Bengal Fan.

Partially reset samples from the deeper parts of the sections provide insight into the kinematics of the Siwalik belt. In particular, they indicate onset of movement along the MFT at $\sim$2 Ma and suggest that present-day shortening rates along the MFT have been operating for at least 0.3 Myr. The data suggest intermittent operation of the MFT between 2 and 0.3 Ma.

ACKNOWLEDGEMENTS

We thank Adam Szulc and Ananta Gajurel for valuable field assistance, and Jérôme Lavé for providing pilot samples BUT and MAR. Andy Carter (University College London) performed Cf-irradiations on the Karnali samples. Luis Martinez (Université Henri Poincaré, Nancy) provided vitrinite reflectance values for a number of samples. Tank Ojha shared unpublished magneto-stratigraphic data. Detailed and constructive reviews by Doug Burbank, John Garver and Max Zattin helped to clarify the ideas contained in this paper. This study was supported by an INSU-CNRS *Intérieur de la Terre* programme grant to P. van der Beek and an INSU-CNRS *Eclipse* programme grant to P. Huyghe. M. Bernet was funded by a Marie Curie post-doctoral fellowship from the European Commission (contract HPMF-CT-2002-01779).

REFERENCES

Agarwal, R.P., Prasad, D.N., Samanta, U., Berry, C.M. & Sharma, J. (1994) Hydrocarbon potential of Siwalik Basin. In: *Siwalik Foreland Basin of Himalaya, Himalayan Geology*, **15**, pp. 301–320. Wadia Institute of Himalayan Geology, Dehra Dun.

Appel, E., Rösler, W. & Corvinus, G. (1991) Magnetostratigraphy of the Mio-Pliocene Surai Khola Siwaliks in west Nepal. *Geophys. J. Int.*, **105**, 191–198.

Arita, K. & Ganzawa, Y. (1997) Thrust tectonics and uplift of the Nepal Himalaya revealed from fission-track ages. *J. Geogr. (Chigaku Zashi)*, **106**, 156–167.

Avouac, J.P. (2003) Mountain building, erosion and the seismic cycle in the Nepal Himalaya. *Adv. Geophys.*, **46**, 1–79.

Barbarand, J., Carter, A., Wood, I. & Hurford, A. (2003) Compositional and structural control of fission-track annealing in apatite. *Chem. Geol.*, **198**, 107–137.

Beaumont, C., Jamieson, R.A., Nguyen, M.H. & Lee, B. (2001) Himalayan tectonics explained by extrusion of a low-viscosity channel coupled to focused surface denudation. *Nature*, **414**, 738–742.

Berger, A., Jouanne, F., Hassani, R. & Mugnier, J.L. (2004) Modelling the spatial distribution of present-day deformation in Nepal: how cylindrical is the Main Himalayan Thrust in Nepal? *Geophys. J. Int.*, **156**, 94–114.

Bernet, M., Brandon, M.T., Garver, J.I. & Molitor, B. (2004) Fundamentals of detrital zircon fission-track analysis for provenance and exhumation studies with examples from the European Alps. In: *Detrital Thermochronology – Provenance Analysis, Exhumation and Landscape Evolution of Mountain Belts* (Ed. by M. Bernet & C. Spiegel), Geol. Soc. Am. Spec. Pap., **378**, 25–36.

Bernet, M., van der Beek, P.A., Pik, R., Huyghe, P., Mugnier, J.L., Labrin, E. & Szulc, A.G. (2006) Miocene to recent exhumation of the central Himalaya determined from combined detrital zircon fission-track and U/Pb analysis of Siwalik sediments, western Nepal. *Basin Res.*, **18**, 393–412.

Bernet, M., Zattin, M., Garver, J.I., Brandon, M.T. & Vance, J.A. (2001) Steady-state exhumation of the European Alps. *Geology*, **29**, 35–38.

Bilham, R., Larson, K., Freymueller, J. & Project Idylhim Members. (1997) GPS measurements of present-day convergence across the Nepal Himalaya. *Nature*, **386**, 61–64.

Blythe, A., Burbank, D.W., Carter, A., Schmidt, K.L. & Putkonen, J. (2006) Plio-Quaternary exhumation history of the central Himalaya: 1. Apatite and zircon fission-track and apatite (U–Th)/He analyses. *Tectonics*, in press.

Bojar, A.-V., Fritz, H., Nicolescu, S., Bregar, M. & Gupta, R.P. (2005) Timing and mechanisms of Central Himalayan exhumation: discriminating between tectonic and erosion processes. *Terra Nova*, **17**, 427–433.

Bollinger, L., Avouac, J.-P., Catlos, E.J., Harrison, T.M., Grove, M., Beyssac, O., Goffé, B. & Sapkota, S. (2004) Thermal structure and exhumation history of the Lesser Himalaya in central Nepal. *Tectonics*, **23**, TC5015, doi:10.1029/2003TC001564.

Bookhagen, B., Thiede, R.C. & Strecker, M.R. (2005) Abnormal monsoon years and their control on erosion and sediment flux in the high, arid northwest Himalaya. *Earth Planet. Sci. Lett.*, **231**, 131–146.

Brandon, M.T. (1996) Probability density plot for fission-track grain-age samples. *Nucl. Tracks Radiat. Meas.*, **26**, 663–676.

Brandon, M.T., Roden-Tice, M. & Garver, J.I. (1998) Late Cenozoic exhumation of the Cascadia accretionary wedge in the Olympic Mountains, northwest Washington State. *Geol. Soc. Am. Bull.*, **110**, 985–1009.

Burbank, D.W. (1992) Causes of recent Himalayan uplift deduced from deposited patterns in the Ganges basin. *Nature*, **357**, 680–683.

Burbank, D.W., Beck, R.A. & Mulder, T. (1996) The Himalayan Foreland. In: *The Tectonic Evolution of Asia* (Ed. by A. Yin & T.M. Harrison), pp. 149–188. Cambridge University Press, New York.

Burbank, D.W., Blythe, A.E., Putkonen, J.K., Pratt-Situala, B.A., Gabet, E.J., Oskin, M.E., Barros, A.P. & Ojha, T.P. (2003) Decoupling of erosion and precipitation in the Himalaya. *Nature*, **426**, 652–655.

Burbank, D.W., Derry, L.A. & France-Lanord, C. (1993) Reduced Himalayan sediment production 8 Myr ago despite an intensified monsoon. *Nature*, **364**, 48–50.

Burchfiel, B.C., Zhiliang, C., Hodges, K.V., Yuping, L., Royden, L.H., Changrong, D. & Jiene, X. (1992) The South Tibetan detachment system, Himalayan orogen: Extension contemporaneous with and parallel to shortening in a collisional mountain belt. *Geol. Soc. Am. Spec. Pap.*, **269**, 41pp.

Campbell, I.H., Reiners, P.W., Allen, C.M., Nicolescu, S. & Upadhyay, R. (2005) He-Pb double dating of detrital zircons from the Ganges and Indus Rivers: implication for quantifying sediment recycling and provenance studies. *Earth Planet. Sci. Lett.*, **237**, 402–432.

Cande, S.C. & Kent, D.V. (1995) Revised calibration of the geomagnetic polarity timescale for the Late Cretaceous and Cenozoic. *J. Geophys. Res.*, **100**, 6093–6096.

Carlson, W.D., Donelick, R.A. & Ketcham, R.A. (1999) Variability of apatite fission-track annealing kinetics: I. Experimental results. *Am. Mineral.*, **84**, 1213–1223.

Carrapa, B., Strecker, M.R. & Sobel, E.R. (2006) Cenozoic orogenic growth in the Central Andes: evidence from sedimentary rock provenance and apatite fission track thermochronology in the Fiambala Basin, southernmost Puna Plateau margin (NW Argentina). *Earth Planet. Sci. Lett.*, **247**, 82–100.

Carter, A. & Gallagher, K. (2004) Characterizing the significance of provenance on the inference of thermal history models from apatite fission-track data – a synthetic data study. In: *Detrital Thermochronology – Provenance Analysis, Exhumation and Landscape Evolution of Mountain Belts* (Ed. by M. Bernet & C. Spiegel), Geol. Soc. Am. Spec. Pap., **378**, 7–24.

Cattin, E. & Avouac, J.P. (2000) Modeling mountain building and the seismic cycle in the Himalaya of Nepal. *J. Geophys. Res.*, **105**, 13389–13408.

Cederbom, C., Sinclair, H., Schlunegger, F. & Rahn, M. (2004) Climate-induced rebound and exhumation of the European Alps. *Geology*, **32**, 709–712.

Cerveny, P.F., Naeser, N.D., Zeitler, P.K., Naeser, C.W. & Johnson, N.M. (1988) History of uplift and relief of the Himalaya during the past 18 million years: evidence from fission-track ages of detrital zircons from sandstones of the Siwalik group. In: *New Perspectives in Basin Analysis* (Ed. by K.L. Kleinspehn & C. Paola), pp. 43–61. Springer Verlag, New York.

Champel, B., van der Beek, P.A., Mugnier, J.L. & Leturmy, P. (2002) Growth and lateral propagation of fault-related folds in the Siwaliks of western Nepal: rates, mechanisms and geomorphic signature. *J. Geophys. Res.*, **107**, 2111, doi:10.1029/2001JB000578.

Clift, P. & Gaedicke, C. (2002) Accelerated mass flux to the Arabian Sea during the middle to late Miocene. *Geology*, **30**, 207–210.

Clift, P.D., Campbell, I.H., Pringle, M.S., Carter, A., Zhang, X., Hodges, K.V., Khan, A.A. & Allen, C.M. (2004) Thermochronology of the modern Indus River bedload: new insight into the controls on the marine stratigraphic record. *Tectonics*, **23**, TC5013, doi:10.1029/2003TC001559.

Copeland, P. & Harrison, T.M. (1990) Episodic rapid uplift in the Himalaya revealed by $^{40}Ar/^{39}Ar$ analysis of detrital K-feldspar and muscovite, Bengal fan. *Geology*, **18**, 354–357.

Corrigan, J.D. & Crowley, K.D. (1990) Fission-track analysis of detrital apatites from sites 717 and 718, Leg 116, Central Indian Ocean. In: *Proceedings Ocean Drilling Program* (Ed. by J.R. Cochran, J.R. Curray, W.W. Sager & D.A.V. Stow), Ocean Drilling Program, Texas A&M University, College Station, TX, **Vol. 116B**, 75–83.

Corvinus, G. & Rimal, L.N. (2001) Biostratigraphy and geology of the Neogene Siwalik Group of the Surai Khola and Rato Khola areas in Nepal. *Palaeogeogr. Palaeoclimatol. Palaeoecol.*, **165**, 251–279.

Decelles, P.G., Gehrels, G.E., Quade, J., Ojha, T.P., Kapp, P.A. & Upreti, B.N. (1998) Neogene foreland basin deposits, erosional unroofing, and the kinematic history of the Himalayan fold-thrust belt, western Nepal. *Geol. Soc. Am. Bull.*, **110**, 2–21.

Decelles, P.G., Robinson, D.M., Quade, J., Ojha, T.P., Garzione, C.N., Copeland, P. & Upreti, B.N. (2001) Stratigraphy, structure, and tectonic evolution of the Himalayan fold-thrust belt in western Nepal. *Tectonics*, **20**, 487–509.

Dodson, M.H. (1973) Closure temperature in cooling geochronological and petrological systems. *Contrib. Mineral. Petrol.*, **40**, 259–274.

Finlayson, D.P., Montgomery, D.R. & Hallet, B. (2002) Spatial coincidence of rapid inferred erosion with young metamorphic massifs in the Himalayas. *Geology*, **30**, 219–222.

France-Lanord, C. & Derry, L.A. (1997) Organic carbon burial forcing of the carbon cycle from Himalayan erosion. *Nature*, **390**, 65–67.

Galbraith, R.F. (1990) The radial plot: graphical assessment of spread in ages. *Nucl. Tracks Radiat. Meas.*, **17**, 207–214.

Galbraith, R.F. & Laslett, G.M. (1993) Statistical models for mixed fission track ages. *Nucl. Tracks Radiat. Meas.*, **21**, 459–470.

Gallagher, K., Brown, R. & Johnson, C. (1998) Fission track analysis and its applications to geological problems. *Annu. Rev. Earth Planet. Sci.*, **26**, 519–572.

Gallagher, K., Stephenson, J., Brown, R., Holmes, C. & Fitzgerald, P. (2005) Low temperature thermochronology and modeling strategies for multiple samples 1: vertical profiles. *Earth Planet. Sci. Lett.*, **237**(1–2), 193–208.

Garver, J.I., Brandon, M.T., Roden-Tice, M. & Kamp, P.J.J. (1999) Exhumation history of orogenic highlands determined by detrital fission-track thermochronology. In: *Exhumation Processes: Normal Faulting, Ductile Flow and Erosion* (Ed. by U. Ring, M.T. Brandon, S.D. Willett & G.S. Lister), Geol. Soc., **154**, 283–304.

Gautam, P. & Appel, E. (1994) Magnetic-polarity stratigraphy of Siwalik Group sediments of Tinau Khola section in west central Nepal, revisited. *Geophys. J. Int.*, **117**, 223–234.

Gautam, P. & Fujiwara, Y. (2000) Magnetic polarity stratigraphy of Siwalik Group sediments of Karnali River section in western Nepal. *Geophys. J. Int.*, **142**, 812–824.

Gautam, P. & Rösler, W. (1999) Depositional chronology and fabric of Siwalik Group sediments in central Nepal from magnetostratigraphy and magnetic anisotropy. *J. Asian Earth Sci.*, **17**, 659–682.

Guillot, S., Hodges, K., Le Fort, P. & Pêcher, A. (1994) New constraints on the age of the Manaslu leucogranite: evidence for episodic tectonic denudation in the central Himalayas. *Geology*, **22**, 559–562.

Gupta, S. (1997) Himalayan drainage patterns and the origin of fluvial megafans in the Ganges foreland basin. *Geology*, **25**, 11–14.

Harrison, T.M., Copeland, P., Hall, S.A., Quade, J., Burner, S., Ojha, T.P. & Kidd, W.S.F. (1993) Isotopic preservation of Himalayan/Tibetan uplift, denudation, and climatic histories in two molasse deposits. *J. Geol.*, **100**, 157–173.

Hay, W.W. (1998) Detrital sediment fluxes from continents to oceans. *Chem. Geol.*, **145**, 287–323.

Hodges, K.V. (2000) Tectonics of the Himalaya and southern Tibet from two perspectives. *Geol. Soc. Am. Bull.*, **112**, 324–350.

Hodges, K.V., Hurtado, J.M. & Whipple, K.X. (2001) Southward extrusion of Tibetan crust and its effect on Himalayan tectonics. *Tectonics*, **20**, 799–809.

Hodges, K.V., Parrish, R.R. & Searle, M.P. (1996) Tectonic evolution of the central Annapurna Range, Nepalese Himalayas. *Tectonics*, **15**, 1264–1291.

Hodges, K.V., Wobus, C.W., Ruhl, K., Schildgen, T. & Whipple, K.X. (2004) Quaternary deformation, river steepening, and heavy precipitation at the front of the Higher Himalayan ranges. *Earth Planet. Sci. Lett.*, **220**, 379–389.

Hoorn, C., Ohja, T. & Quade, J. (2000) Palynological evidence for vegetation development and climatic change in the Sub-Himalayan Zone (Neogene, Central Nepal). *Palaeogeogr. Palaeoclimatol. Palaeoecol.*, **163**, 133–161.

Hurford, A.J. (1990) International union of geological sciences subcommission on geochronology recommendation for the standardization of fission track dating calibration and data reporting. *Nucl. Tracks Radiat. Meas.*, **17**, 233–236.

Husson, L., Mugnier, J.L., Leturmy, P. & Vidal, G. (2004) Kinematics and sedimentary balance of the Sub-Himalayan zone, western Nepal. In: *Thrust Tectonics and Petroleum Systems* (Ed. by K.R. McClay), *Am. Assoc. Petrol. Geol. Memoir*, **82**, 115–130.

Huyghe, P., Galy, A., Mugnier, J.L. & France-Lanord, C. (2001) Propagation of the thrust system and erosion in the Lesser Himalaya: Geochemical and sedimentological evidence. *Geology*, **29**, 1007–1010.

Huyghe, P., Mugnier, J.L., Gajurel, A.P. & Delcaillau, B. (2005) Tectonic and climatic control of the changes in the sedimentary record of the Karnali River section (Siwaliks of Western Nepal). *The Island Arc*, **14**, 311–327.

Jain, A.K., Kumar, D., Singh, S., Kumar, A. & Lal, N. (2000) Timing, quantification and tectonic modelling of Pliocene-Quaternary movements in the NW Himalaya: evidence from fission track dating. *Earth Planet. Sci. Lett.*, **179**, 437–451.

Jouanne, F., Mugnier, J.L., Gamond, J.F., Le Fort, P., Pandey, M.R., Bollinger, L., Flouzat, M. & Avouac, J.P. (2004) Current shortening across the Himalayas of Nepal. *Geophys. J. Int.*, **157**, 11–14.

Ketcham, R.A., Donelick, R.A. & Carlson, W.D. (1999) Variability of apatite fission-track annealing kinetics: III. Extrapolation to geological time scales. *Am. Mineral.*, **84**, 1235–1255.

Ketcham, R.A., Donelick, R.A. & Donelick, M.B. (2000) AFTSolve: a program for multi-kinetic modeling of apatite fission-track data. *Geol. Mater. Res.*, **2**, 18pp. http://gmr.minsocam.org/Papers/v2/v2n1/v2n1abs.html.

Larson, K.M., Bürgmann, R., Bilham, R. & Freymueller, J.T. (1999) Kinematics of the India-Eurasia collision zone from GPS measurements. *J. Geophys. Res.*, **104**, 1077–1093.

Lavé, J. & Avouac, J.P. (2000) Active folding of fluvial terraces across the Siwaliks Hills (Himalayas of central Nepal). *J. Geophys. Res.*, **105**, 5735–5770.

Lavé, J. & Avouac, J.P. (2001) Fluvial incision and tectonic uplift across the Himalayas of central Nepal. *J. Geophys. Res.*, **106**, 25561–25593.

Locke, B.D. & Garver, J.I. (2005) Thermal evolution of the eastern Serranía del Interior foreland fold and thrust belt, northeastern Venezuela, based on apatite fission-track analyses. In: *Caribbean–South American Plate Interactions, Vénezuela* (Ed. by H.G. Avé Lallemant & V.B. Sisson), Geol. Soc. Am. Spec. Pap., **394**, 315–328.

Lyon-Caen, H. & Molnar, P. (1985) Gravity anomalies, flexure of the Indian plate and the structure, support and evolution of the Himalaya and Ganga Basin. *Tectonics*, **4**, 513–538.

Meigs, A.J., Burbank, D.W. & Beck, R.A. (1995) Middle-Late Miocene (> 10 Ma) formation of the Main Boundary Thrust in the western Himalaya. *Geology*, **23**, 423–426.

Métivier, F., Gaudemer, Y., Tapponier, P. & Klein, M. (1999) Mass accumulation rates in Asia during the Cenozoic. *Geophys. J. Int.*, **137**, 280–318.

Mugnier, J.L., Chalaron, E., Mascle, G., Pradier, B. & Hérail, G. (1995) Structural and thermal evolution of the Siwaliks of western Nepal. *J. Nepal Geol. Soc.*, **11**, 171–178.

Mugnier, J.L. & Huyghe, P. (2006) The Ganges Basin geometry records a pre-15 Ma lithospheric isostatic rebound of the Himalaya. *Geology*, **34**, 445–448.

Mugnier, J.L., Huyghe, P., Leturmy, P. & Jouanne, F. (2004) Episodicity and rates of thrust sheet motion in the Himalayas (western Nepal). In: *Thrust Tectonics and Petroleum Systems* (Ed. by K.C. McClay), Am. Assoc. Petr. Geol. Memoir., **82**, 1–24.

Mugnier, J.L., Leturmy, P., Mascle, G., Huyghe, P., Chalaron, E., Vidal, G., Husson, L. & Delcaillau, B. (1999) The Siwaliks of western Nepal: I – Geometry and kinematics. *J. Asian Earth Sci.*, **17**, 629–642.

Mugnier, J.L., Mascle, G. & Faucher, T. (1993) Structure of the Siwaliks of western Nepal: an intracontinental accretionary prism. *Int. Geol. Rev.*, **35**, 32–47.

Nakayama, K. & Ulak, P.D. (1999) Evolution of fluvial style in the Siwalik Group in the foothills of the Nepal Himalaya. *Sediment. Geol.*, **125**, 205–224.

Quade, J., Cater, J.M.L., Ojha, T.P., Adam, J. & Harrison, T.M. (1995) Late Miocene environmental change in Nepal and the northern Indian subcontinent: stable isotopic evidence from paleosols. *Geol. Soc. Am. Bull.*, **107**, 1381–1397.

Raymo, M.W. & Ruddiman, W.F. (1992) Tectonic forcing of late Cenozoic climate. *Nature*, **359**, 117–122.

Robert, X. (2005) Analyse thermochronologique des sédiments Siwaliks : implications pour la séquence d'activité des failles et la mécanique du prisme frontal de l'Himalaya, Unpublished MSc. Thesis, Université Joseph Fourier, Grenoble, 36 pp.

Robinson, D.M., Decelles, P.G., Patchett, P.J. & Garzione, C.N. (2001) The kinematic evolution of the Nepalese Hima-

laya interpreted from Nd isotopes. *Earth Planet. Sci. Lett.*, **192**, 507–521.

Rohrman, M., Andriessen, P.A.M. & Van der Beek, P.A. (1996) The relationship between basin and margin thermal evolution assessed by fission track thermochronology: an application to offshore southern Norway. *Basin Res.*, **8**, 45–63.

Stewart, R.J. & Brandon, M.T. (2004) Detrital-zircon fission-track ages for the "Hoh Formation": implications for late Cenozoic evolution of the Cascadia subduction wedge. *Geol. Soc. Am. Bull.*, **116**, 60–75.

Summerfield, M.A. & Hulton, N.J. (1994) Natural controls of fluvial denudation rates in major world drainage basins. *J. Geophys. Res.*, **99**, 13871–13883.

Szulc, A.G., Najman, Y., Sinclair, H., Pringle, M., Bickle, M., Chapman, H., Garzanti, E., Ando, S., Huyghe, P., Mugnier, J.L., Ojha, T.P. & Decelles, P.G. (2006) Tectonic evolution of the Himalaya constrained by detrital ^{40}Ar–^{39}Ar, Sm–Nd and petrographic data from the Siwalik foreland basin succession, SW Nepal. *Basin Res.*, **18**, 375–391.

Thiede, R.C., Bookhagen, B., Arrowsmith, J.R., Sobel, E.R. & Strecker, M.R. (2004) Climatic control on rapid exhumation along the Southern Himalayan Front. *Earth Planet. Sci. Lett.*, **222**, 791–806.

Tokuoka, T., Takayasu, K., Hisatomi, K., Yamasaki, H., Tanaka, S., Konomatsu, M., Sah, R.S. & Rai, S.M. (1990) *Stratigraphy and Geologic Structures of the Churia (Siwalik) Group in the Tinau Khola – Binai Khola Area, West Central Nepal* (pp. 71–88). Faculty of Science, Shimane University, Matsue, Japan.

Van der Beek, P.A., Champel, B. & Mugnier, J.L. (2002) Control of detachment dip on drainage development in regions of active fault-propagation folding. *Geology*, **30**, 471–474.

Vance, D., Bickle, M., Ivy-Ochs, S. & Kubik, P.W. (2003) Erosion and exhumation in the Himalaya from cosmogenic isotope inventories of river sediments. *Earth Planet. Sci. Lett.*, **206**, 237–633.

Vannay, J.-C., Grasemann, B., Rahn, M., Frank, W., Carter, A., Baudraz, V. & Cosca, M. (2004) Miocene to Holocene exhumation of metamorphic crustal wedges in the NW Himalaya: evidence for tectonic extrusion coupled to fluvial erosion. *Tectonics*, TC1014, doi:10.1029/2002TC001429.

White, N.M., Pringle, M., Garzanti, E., Bickle, M., Najman, Y., Chapman, H. & Friend, P. (2002) Constraints on the exhumation and erosion of the High Himalayan Slab, NW India, from foreland basin deposits. *Earth Planet. Sci. Lett.*, **195**, 29–44.

Williamson, J.H. (1968) Least squares fitting of a straight line. *Can. J. Phys.*, **46**, 1845–1847.

Wobus, C.W., Hodges, K.V. & Whipple, K.X. (2003) Has focused denudation sustained active thrusting at the Himalayan topographic front? *Geology*, **31**, 861–864.

Yin, A. & Harrison, T.M. (2000) Geologic evolution of the Himalayan–Tibetan orogen. *Annu. Rev. Earth and Planet. Sci.*, **28**, 211–280.

Zhao, W., Nelson, K.D. & Project Indepth Team, . (1993) Deep seismic reflection evidence for continental underthrusting beneath southern Tibet. *Nature*, **366**, 557–559.

A.3 Données Traces de Fission sur Apatites

A.3.1 Calibration du Zeta

Observateur	Apatite	Date	Irradiation	Moniteur	ζ	$\pm 1\sigma$
X. Robert	Durango	11-09-2006	7-2005	NBS962	350.5	10.3
	Durango	18-09-2006	3-2006	NBS962	314.5	20.6
	Durango	04-04-2008	7-2007	540R	330.0	10.0
	Durango	28-04-2008	7-2007	NBS962	360.8	29.4
	Fish Canyon Tuff	07-09-2006	7-2005	NBS962	360.8	21.5
	Fish Canyon Tuff	21-04-2008	7-2007	540R	360.8	29.4

TAB. A.1 – *Valeurs du paramètre ζ utilisé pour cette étude.*

A.3.2 Coupe du Langtang

Langtang - Amlekhganj Section

Kakani Vertical Profil

Sample	Struct. Unit	Elevation	Roks	Long			Lat			Locality	N	ρs	Ns	ρi	Ni	ρd	Nd	P(χ2)	D	Age	±1σ
		(m)		°	min	s	°	min	s			($x10^6$ cm^{-2})		($x10^6$ cm^{-2})		($x10^6$ cm^{-2})		%	%	Ma	
NP05.06	Lesser Himal.	650	quartzite	85	8	50	27	55	12.1	Bidur	21	3.35	60	112.63	2015	6.00	9956	97.33	0	3.1	0.4
NP05.07	Lesser Himal.	674	sandstone	85	9	17	27	55	45.6	Simwutar	15	6.87	45	190	1244	5.62	11971	95.52	0	3.4	0.5
NP05.08	Lesser Himal.	739	sandstone	85	11	3.5	27	58	29.6	Betrawati	22	0.3	49	1.56	2884	6.00	9956	65.23	1	1.7	0.2
NP05.09	Lesser Himal.	1540	sandstone	85	20	39	28	10	3.6	Syabru Besi	21	0.58	12	49.6	1019	6.00	9956	90.16	1	1.2	0.4
NP05.10	Lesser Himal.	1621	gneiss	85	20	48	28	11	7.8	Wangal	23	1.86	42	71.67	1314	6.00	9956	79.62	2	2.7	0.4
NP05.11	High Himal.	1582	sandstone	85	21	15	28	12	11.8	Kagdinma	24	2.69	63	182.3	4265	6.00	9956	40.24	12	1.5	0.2
NP05.12	High Himal.	1600	quartzite	85	21	6.6	28	11	49	Lingling	25	1.59	39	190.27	4676	6.00	9956	0.26	76	0.9	0.2
NP05.13	High Himal.	1600	quartzite	85	20	54	28	11	23.6	Lingling	16	0.32	5	21.55	339	6.00	9956	14.86	1	1.5	0.7
NP05.14	Lesser Himal.	1833	quartzite	85	18	59	28	8	24.1	Thulo Barkhu	30	0.71	21	209.9	6190	6.00	9956	15.13	49	0.4	0.1
NP05.15	Lesser Himal.	1180	quartzite	85	12	10	27	59	33.5	Kalikasthan	21	3.92	81	140	2890	6.00	9956	80.74	0	2.9	0.3

Palung Section

Sample	Struct. Unit	Elevation	Roks	Long			Lat			Locality	N	ρs	Ns	ρi	Ni	ρd	Nd	P(χ2)	D	Age	±1σ
		(m)		°	min	s	°	min	s			($x10^6$ cm^{-2})		($x10^6$ cm^{-2})		($x10^6$ cm^{-2})		%	%	Ma	
NP05.17	Lesser Himal.	770	quartzite	85	7	38	27	44	8.1	Amarkhu	11	1.36	11	60.11	221	6.62	11971	95.04	0	2.1	1
NP05.18	Lesser Himal.	2027	sandstone	85	5	57	27	39	46.2	Tistung	18	3.17	43	172.47	2343	6.00	9956	99.89	0	1.9	0.3
NP05.20	Lesser Himal.	1935	granite	85	4	50	27	37	19.1	Palung	9	4.57	37	90.25	731	6.00	9956	90.3	0	4.7	0.8
NP05.21	Lesser Himal.	2360	granite	85	5	19	27	36	19.2	Daman	17	8.83	138	143.19	2238	6.00	9956	72.34	0	6.5	0.6
NP05.22	Lesser Himal.	2500	granite	85	5	3.8	27	35	27.6	Simbhanjang	22	19.73	419	287.15	6097	6.00	9956	84.13	0	7.2	0.4
NP05.23	Lesser Himal.	2190	granite	85	4	23	27	34	31.3		18	21.88	385	264.55	4655	6.00	9956	47.03	7	8.6	0.5
NP05.24	Lesser Himal.	1350	gneiss	85	2	54	27	33	4.4	Lamindanda	22	11.3	78	201.29	1389	6.00	9956	81.44	1	5.9	0.7
NP05.25	Lesser Himal.	611	diorite	85	2	37	27	29	30.7		-	-	-	-	-	6.00	9956	-	-	NON datable	
NP05.26	Lesser Himal.	530	schistes	85	2	31	27	28	34.4	Hetauda	-	-	-	-	-	6.00	9956	-	-	NON datable	

Hetauda Section (Detrital thermochronology)

Sample	Struct. Unit	Elevation	Roks	Long			Lat			Locality	N	ρs	Ns	ρi	Ni	ρd	Nd	P(χ2)	D	Age	±1σ
		(m)		°	min	s	°	min	s			($x10^6$ cm^{-2})		($x10^6$ cm^{-2})		($x10^6$ cm^{-2})		%	%	Ma	
NP05.27	Siwalik	510	sandstone	85	1	34	27	23	41.5		-	-	-	-	-	6.00	9956	-	-	NON datable	
NP05.28	Siwalik	330	sandstone	84	59	55	27	16	56.2	Amlekhganj	90	5.51	362	95.7	6284	5.62	11971	4.48	24	5.4	0.4

Gosaikung vertical section

Sample	Struct. Unit	Elevation	Roks	Long			Lat			Locality	N	ρs	Ns	ρi	Ni	ρd	Nd	P(χ2)	D	Age	±1σ
		(m)		°	min	s	°	min	s			($x10^6$ cm^{-2})		($x10^6$ cm^{-2})		($x10^6$ cm^{-2})		%	%	Ma	
T6	Lesser Himal.	1825	quartzite	85	12	32	28	0	47.3	Bhalayadanda	16	1.78	25	125.63	1766	5.93	12513	94.6	0	1.4	0.3
T7	Lesser Himal.	2000		85	13	25	28	3	57.5	Grang	19	2.22	37	158.79	2641	5.93	12513	96.65	0	1.4	0.2
T9	Lesser Himal.	1780	quartzite	85	18	50	28	6	34.7	Dunche	16	1.73	17	124.87	1225	5.93	12513	95.43	0	1.4	0.3
T10	Lesser Himal.	2540	schiste	85	19	35	28	6	11.2	Deurali	17	2.21	29	131.56	1729	5.93	12513	84.35	0	1.6	0.3
T11	Lesser Himal.	2960	gneiss	85	19	53	28	6	26.4	Dimsa	14	1.02	12	71.97	849	5.93	12513	95.92	0	1.4	0.4
T13	High Himal.	3640	gneiss	85	20	53	28	6	27.4	Cholangpati	18	1.74	29	117.4	1955	5.67	12016	97.05	0	1.4	0.3
T14	High Himal.	4500	gneiss	85	24	33	28	5	4.4	Gosaikund	21	1.03	19	49.57	916	5.67	12016	92.02	0	1.9	0.5
T15	High Himal.	4260	gneiss	85	23	47	28	5	7.5	holangpati Dad	18	1.58	26	57.57	945	5.67	12016	67.01	0	2.6	0.5
T17	High Himal.	3260	gneiss	85	22	16	28	6	29.1	Cholangpati	16	2.11	33	109.28	1708	5.67	12016	98.45	0	1.8	0.3

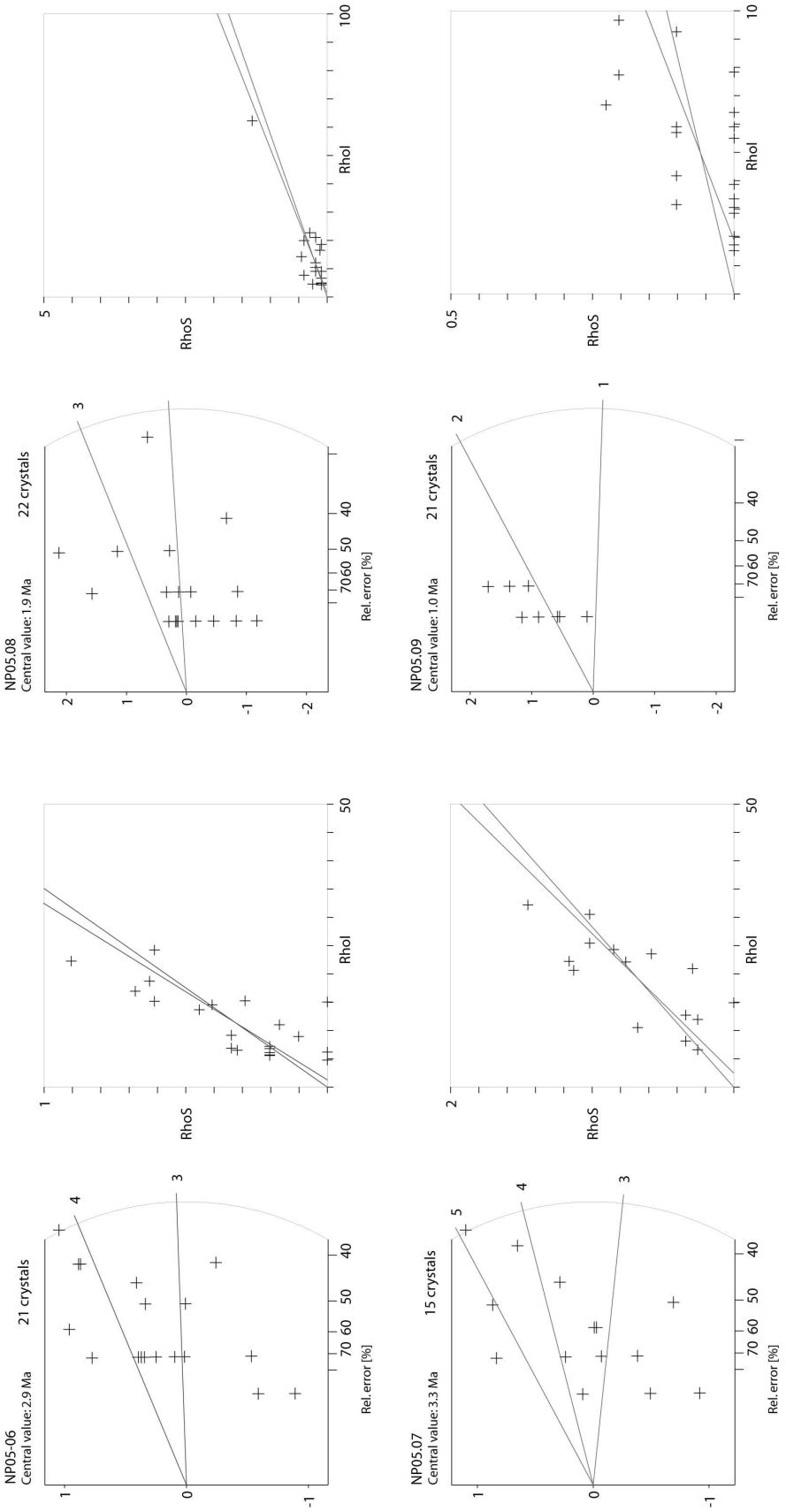
NP05-06
Central value: 2.9 Ma
21 crystals
NP05.08
Central value: 1.9 Ma
22 crystals
NP05.07
Central value: 3.3 Ma
15 crystals
NP05.09
Central value: 1.0 Ma
21 crystals
RhoS
RhoI
Rel.error [%]

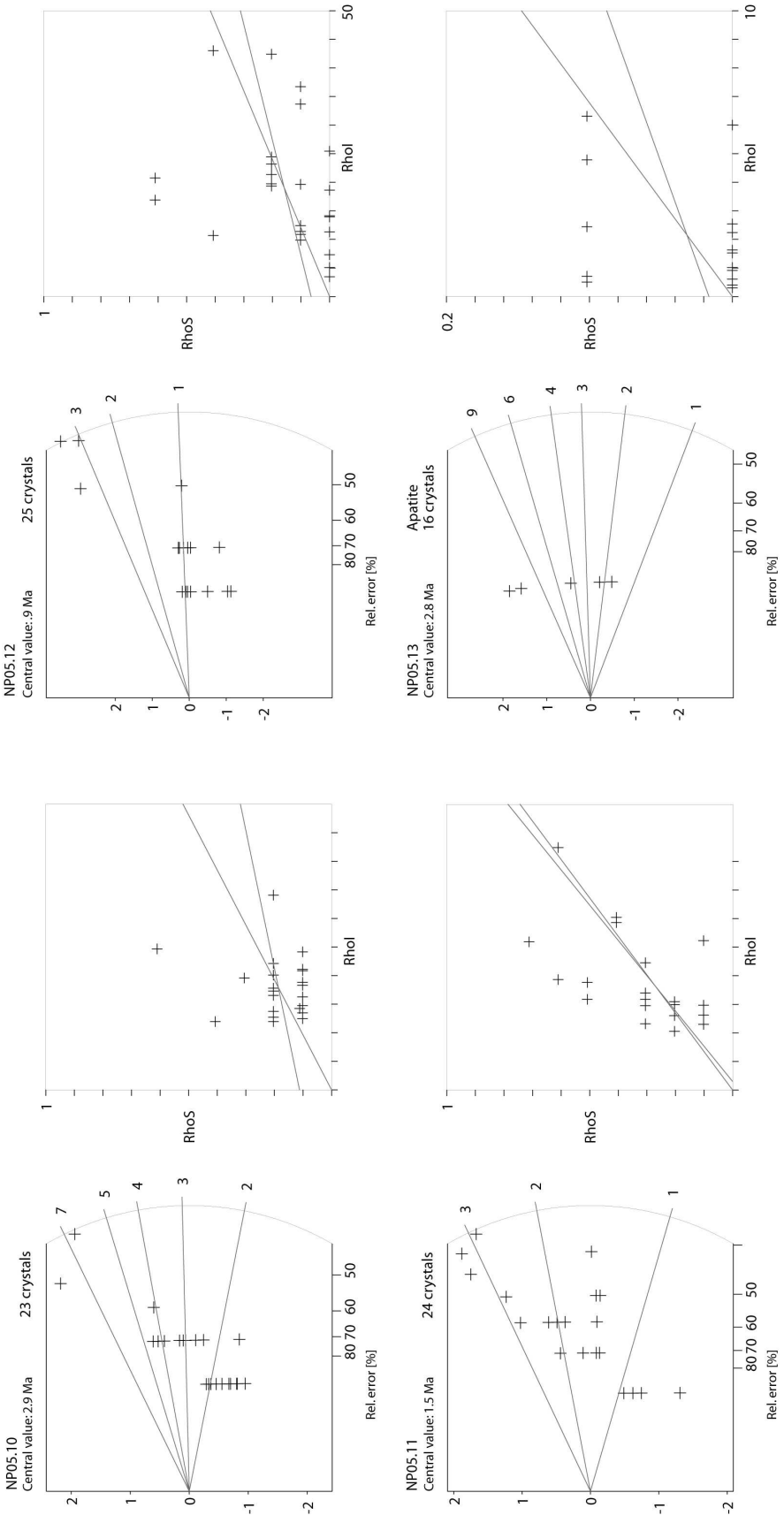
NP05.10
Central value:2.9 Ma
23 crystals
NP05.12
Central value:.9 Ma
25 crystals
NP05.11
Central value:1.5 Ma
24 crystals
NP05.13
Central value:2.8 Ma
Apatite
16 crystals
RhoS
Rhol
Rel.error [%]

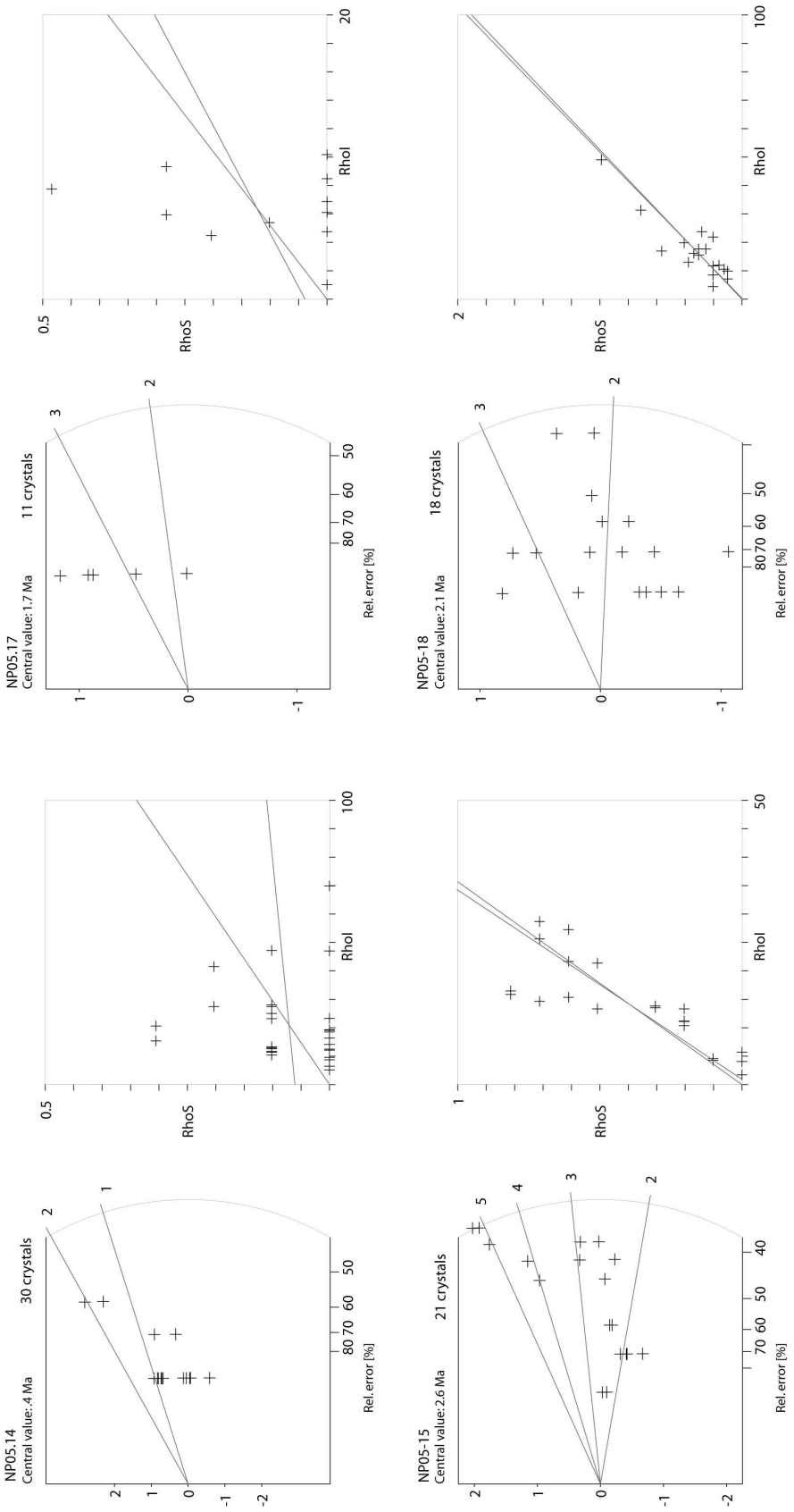
NP05.17
Central value: 1.7 Ma
11 crystals
NP05-18
Central value: 2.1 Ma
18 crystals
NP05.14
Central value: 4 Ma
30 crystals
NP05-15
Central value: 2.6 Ma
21 crystals
RhoS
Rhol
Rel. error [%]

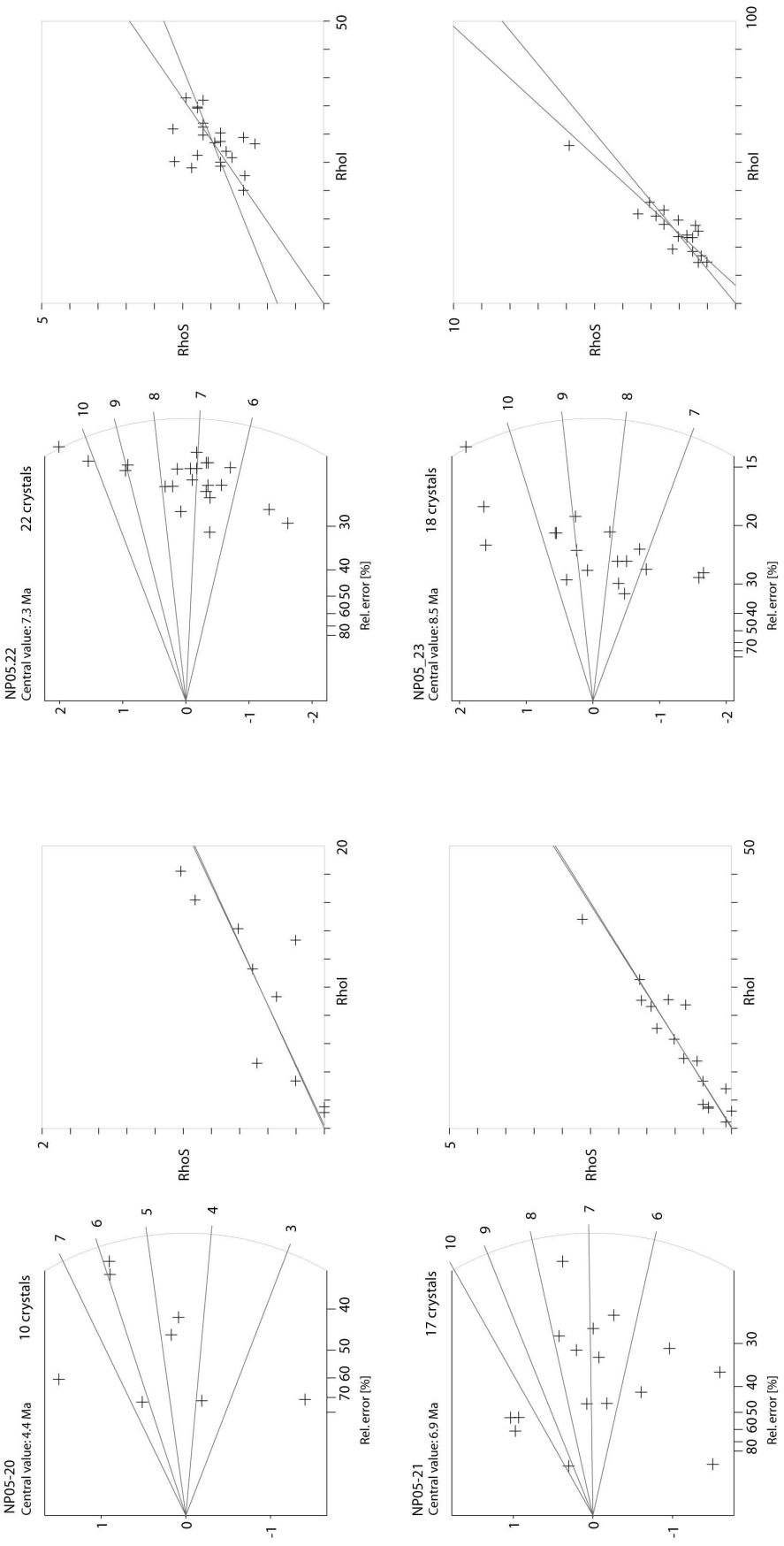
NP05-20
Central value:4.4 Ma
10 crystals
Rel. error [%]
RhoS
RhoI
NP05.22
Central value:7.3 Ma
22 crystals
Rel. error [%]
RhoS
RhoI
NP05-21
Central value:6.9 Ma
17 crystals
Rel. error [%]
RhoS
RhoI
NP05_23
Central value:8.5 Ma
18 crystals
Rel. error [%]
RhoS
RhoI

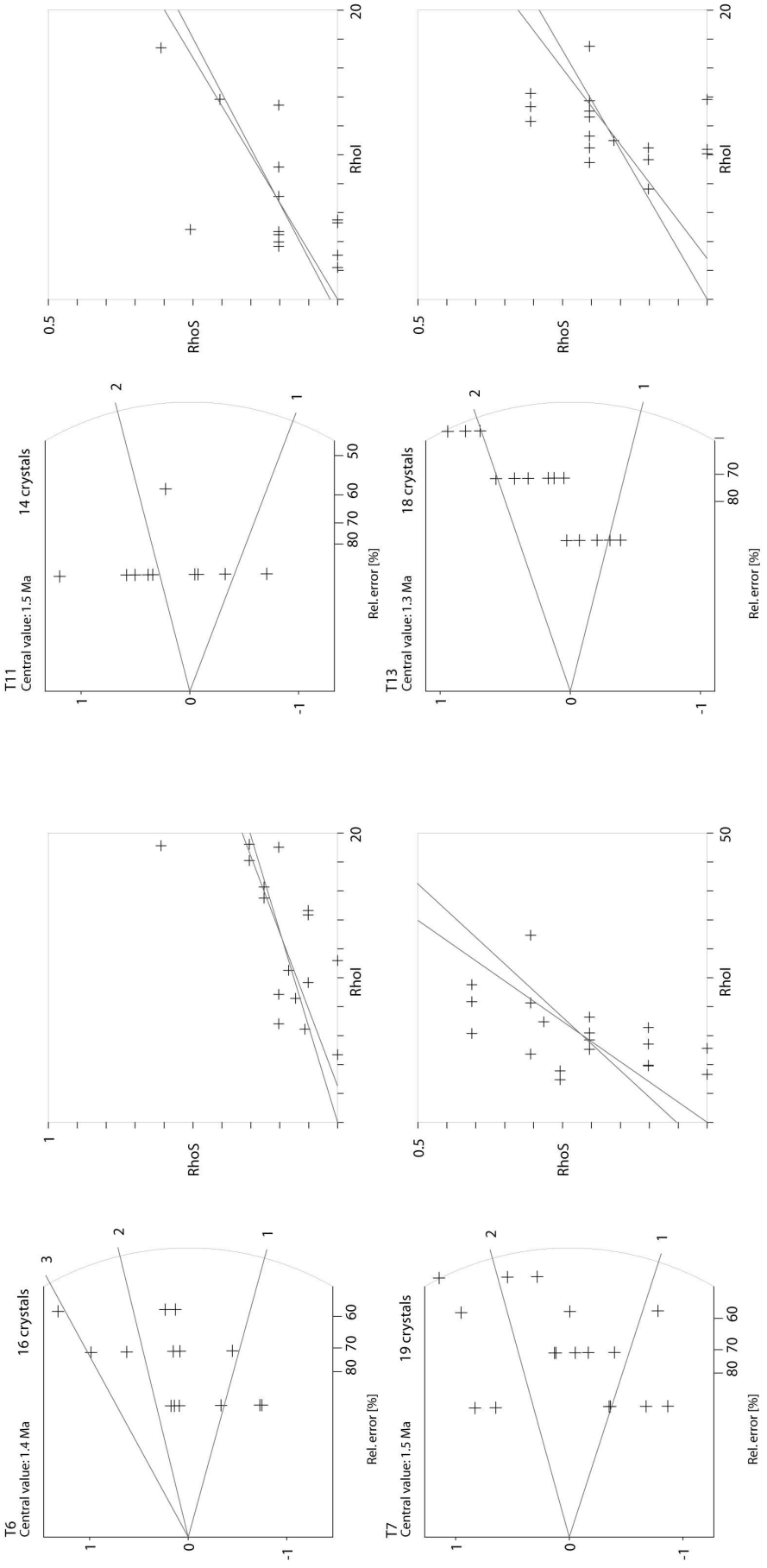
T11
Central value: 1.5 Ma
14 crystals
Rel. error [%]
RhoS
RhoI
T13
Central value: 1.3 Ma
18 crystals
Rel. error [%]
RhoS
RhoI
T6
Central value: 1.4 Ma
16 crystals
Rel. error [%]
RhoS
RhoI
T7
Central value: 1.5 Ma
19 crystals
Rel. error [%]
RhoS
RhoI

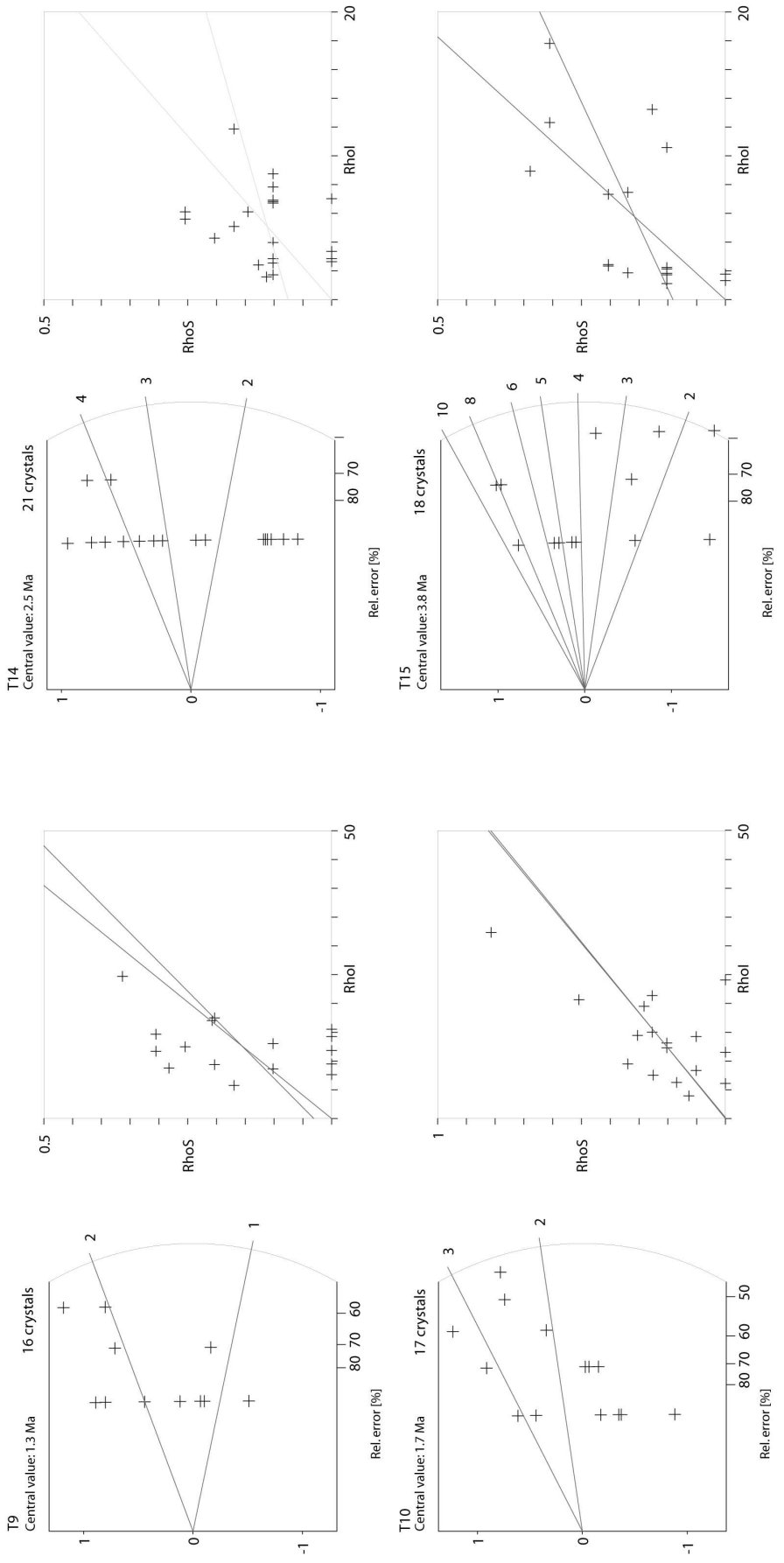
T14
Central value: 2.5 Ma
21 crystals
T15
Central value: 3.8 Ma
18 crystals
T9
Central value: 1.3 Ma
16 crystals
T10
Central value: 1.7 Ma
17 crystals
RhoS
Rhol
Rel. error [%]

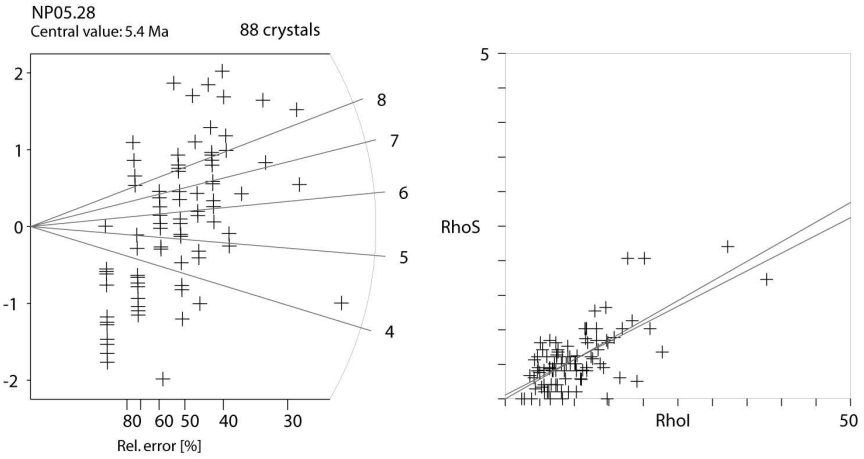
NP05.28
Central value: 5.4 Ma
88 crystals
Rel. error [%]
RhoS
RhoI

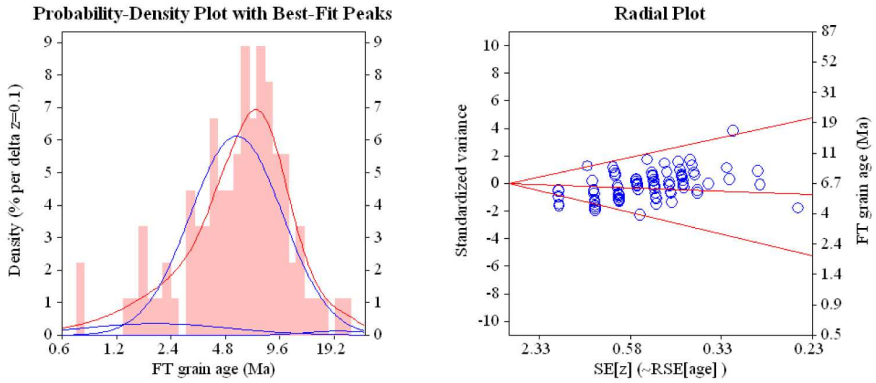
Probability-Density Plot with Best-Fit Peaks
Density (% per delta z=0.1)
FT grain age (Ma)
Radial Plot
Standardized variance
SE[z] (~RSE[age])
FT grain age (Ma)

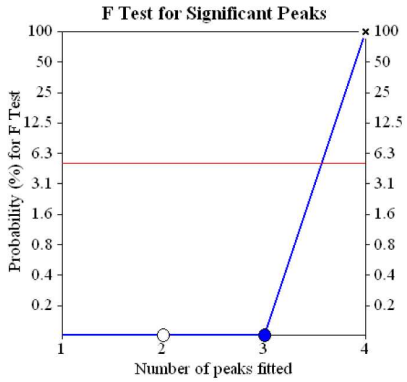
F Test for Significant Peaks
Probability (%) for F Test
Number of peaks fitted

A.3.3 Coupe des Annapurnas

Annapurna - Butwal Section

Ghorepani Vertical South Section

Sample	Struct. Unit	Elevation (m)	Roks	Long °	min	s	Lat °	min	s	Locality	N	ρs ($x10^6$ cm^{-2})	Ns	ρi ($x10^6$ cm^{-2})	Ni	ρd ($x10^6$ cm^{-2})	Nd	P(χ2) %	D %	Age Ma	±1σ
NP05.34	Lesser Himal.	2510	quartzite	83	42	39.1	28	23	2.4	Nangethanti	-	-	-	-	-	5.62	11971	-	-	NON datable	
NP05.36	Lesser Himal.	3190	quartzite	83	41	21.1	28	23	58.2	Poon Hill	-	-	-	-	-	5.62	11971	-	-	NON datable	
NP05.38	Lesser Himal.	2050	gneiss	83	40	27.9	28	26	11.8	Sikha	-	-	-	-	-	5.62	11971	-	-	NON datable	
NP05.40	Lesser Himal.	1200	Amphibolites	83	38	55.6	28	29	7.2	Tatopani Bridg	-	-	-	-	-	5.62	11971	-	-	NON datable	

High Kali Gandaki Section

Sample	Struct. Unit	Elevation (m)	Roks	Long °	min	s	Lat °	min	s	Locality	N	ρs ($x10^6$ cm^{-2})	Ns	ρi ($x10^6$ cm^{-2})	Ni	ρd ($x10^6$ cm^{-2})	Nd	P(χ2) %	D %	Age Ma	±1σ
NP05.41	High Himal.	1550	gneiss	83	37	57.5	28	33	21.5	Kabre Bridge	25	0.47	11	151.49	3559	5.62	11971	95	0	0.3	0.1
NP05.42	High Himal.	1450	gneiss	83	38	40.6	28	32	53.9	Titre	25	0.87	20	92.9	2137	5.62	11971	96.53	0	0.9	0.2
NP05.43	Lesser Himal.	1480	quartzite	83	38	54.1	28	32	6.0	Suke Bagar	-	-	-	-	-	5.62	11971	-	-	NON datable	
NP05.44	Lesser Himal.	1130	quartzite	83	38	1.98	28	28	14.68	Mahabir	27	1.19	26	137.19	3002	5.62	11971	94.25	0	0.8	0.2
NP05.47	Lesser Himal.	840	sandstone	83	34	1.1	28	20	23.9	Beni	-	-	-	-	-	5.62	11971	-	-	NON datable	
NP05.48	Lesser Himal.	1170	quartzite	83	35	10.2	28	17	53.6	Baglung	-	-	-	-	-	5.62	11971	-	-	NON datable	
NP05.49	Lesser Himal.	800	Amphibolites	83	39	35.2	28	14	31.9	Lampata	-	-	-	-	-	5.62	11971	-	-	NON datable	

Lower Kali Gandaki Section

Sample	Struct. Unit	Elevation (m)	Roks	Long °	min	s	Lat °	min	s	Locality	N	ρs ($x10^6$ cm^{-2})	Ns	ρi ($x10^6$ cm^{-2})	Ni	ρd ($x10^6$ cm^{-2})	Nd	P(χ2) %	D %	Age Ma	±1σ
NP05.50	Lesser Himal.	1140	sandstone	83	54	12.7	28	11	16.3		18	4.04	45	157.99	1758	5.62	11971	97.95	0	2.4	0.4
NP05.51	Lesser Himal.	1010	quartzites	83	51	34.8	28	8	23.4		-	-	-	-	-	5.62	11971	-	-	NON datable	
NP05.52	Lesser Himal.	850	sandstone	83	51	56.2	28	5	41.2		-	-	-	-	-	5.62	11971	-	-	NON datable	
NP05.53	Lesser Himal.	740	sandstone	83	43	8.1	27	58	27.5	Andhi Khola	-	-	-	-	-	5.62	11971	-	-	NON datable	
NP05.61	Lesser Himal.	434	sandstone	83	32	20.4	27	46	4.9	hola / Top MB	-	-	-	-	-	5.62	11971	-	-	NON datable	

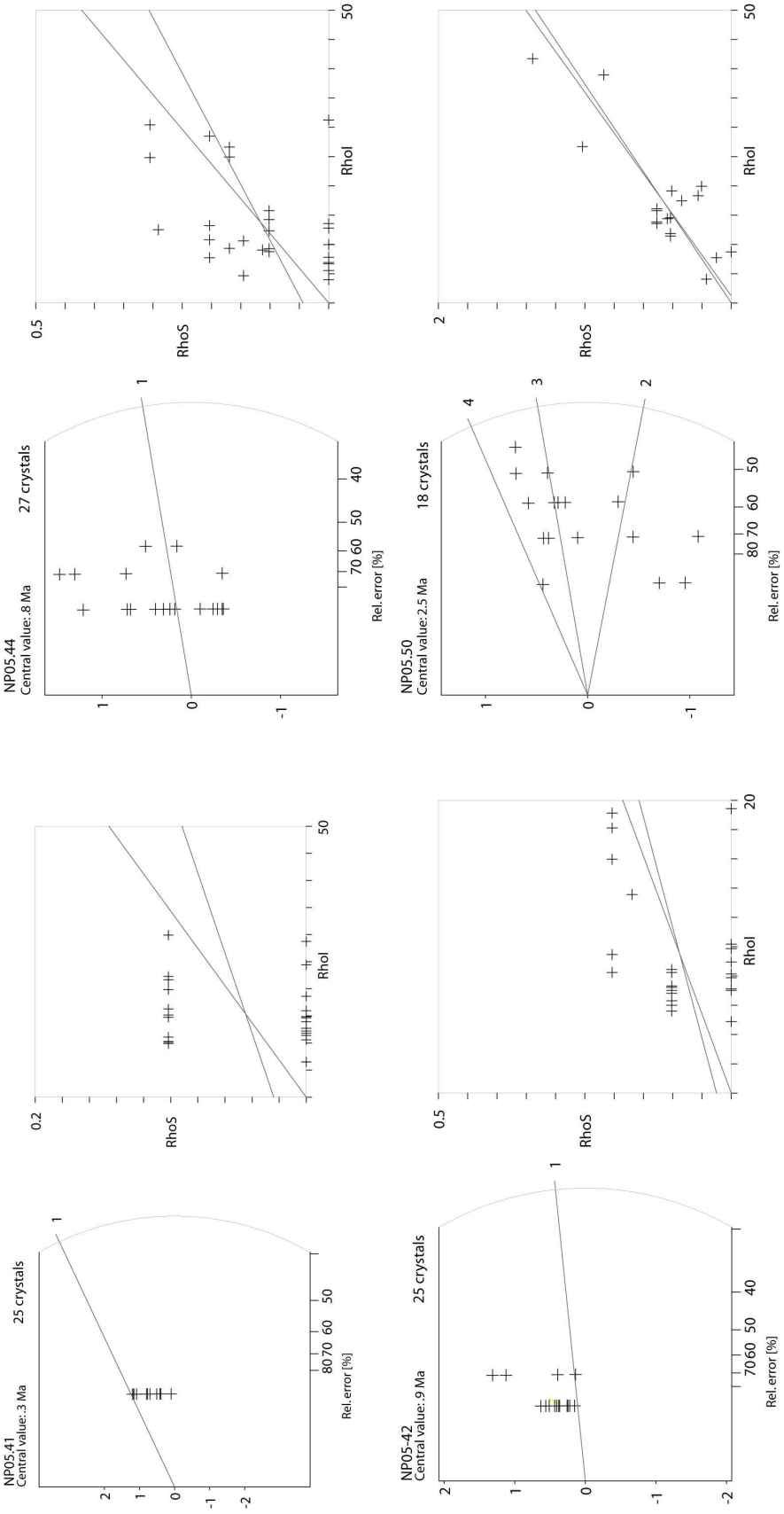
NP05.41
Central value: .3 Ma
25 crystals
Rel. error [%]
RhoS
Rhol
NP05.44
Central value: .8 Ma
27 crystals
Rel. error [%]
RhoS
Rhol
NP05-42
Central value: .9 Ma
25 crystals
Rel. error [%]
RhoS
Rhol
NP05.50
Central value: 2.5 Ma
18 crystals
Rel. error [%]
RhoS
Rhol

A.3.4 Projection des données

Pour chaque coupe, nous projetons les données le long d'un profil perpendiculaire au MFT, au plus porche des données. Pour cela, nous définissons (FAIRE UN SCHEMA) un repère par rapport au MFT en choisissant 2 points A et B sur celui-ci, qui donnent la direction générale du chevauchement, A étant au plus proche du profil.

Soit un point M que nous voulons projeter (M_p) sur la perpendiculaire au MFT passant par A. La longueur AM_p est calculé par :

$$AM_p = AM(\cos(\frac{\pi}{2} - \arccos\frac{BM^2 - AB^2 - AM^2}{2ABAM}))$$

Point	Annapurnas	Langtang	Bhutan
A	83.51 27.73	85.00 27.27	89.41 26.86
B	83.87 27.58	85.66 27.09	94.27 26.81

TAB. A.2 – *Coordonnées des points de références utilisés pour la projection de chaque coupe.*

A.4 Résumé des différentes présentations effectuées lors de congrès et workshops

Au cours des 3 années de thèse, j'ai participé à un certain nombre de conférences et de workshops. Les pages suivantes présentent les résumés respectivement à la Société Géologique de France en 2005 (Thrust Belts and Foreland Basins, Joint Earth Science Meeting, 14-16 décembre 2005), au workshop ModOSUG en 2006 puis au conférences internationnales European Geological Union (EGU) 2006, EGU 2007, Américan Geophysical Union (AGU) 2007, EGU 2008 et AGU 2008.

A.4.1 SGF 2005

Thermochronological analysis of Siwalik sediments from the Karnali River section (western Nepal): Constraints on the kinematics of the frontal Himalayan prism.

Xavier Robert, Peter Van der Beek, Jean-Louis Mugnier, Erika Labrin.
Laboratoire de Géodynamique des Chaînes Alpines, 38 000 Grenoble, France.

Foreland basin sediments contain a record of the dynamics of the orogenic prism in a continental collision context (e.g., Burbank, 1992; Cederbom et al., 2004; Harrison et al. 1993). Here, we study the dynamics of the Miocene-Recent Siwalik accretionary prism of the Himalayan orogen, which is constituted of several thrust slices adjacent to the active orogenic front. We report new detrital apatite fission-track data from Miocene to Pliocene Siwalik Group sediments. We have analysed 13 samples collected along the magneto-stratigraphically controlled Karnali River section in western Nepal (Gautam & Fujiwara, 2000). Both apatite and zircon fission-track ages were determined from these samples; they are reported in a companion paper at this meeting (van der Beek et al, this meeting).

The specific goal of this study was to quantify the onset of activity as well as the deformation history recorded by the Main Frontal Thrust (MFT), the active frontal thrust of the system. We use detrital apatite fission track (AFT) thermochronometry because this system is sensitive to post-depositional heating within the sedimentary basin due to its relatively low closure temperature (110 ± 10°C; Gallagher et al. 1998). As a sample is buried deeper in the sedimentary basin and reaches temperatures at which fission tracks start to anneal ($T \geq 60$°C), the information it contains concerning source-area exhumation is progressively erased. This loss of information is, however, counterbalanced by complementary constraints on the post-depositional thermal history, which will be most clearly recorded by the deepest and most completely reset samples (Carter & Gallagher, 2004; Cederbom et al., 2004; Rohrman et al., 1996). We complete the dataset presented by van der Beek et al. by including confined fission track length measurements (after Cf-irradiation of the samples improving confined-track revelation efficiency) to constrain the thermal history, as well as etch-pit width measurements to provide a kinetic proxy (e.g., Carlson et al., 1999; Barbarand et al., 2003).

The upper part of the Karnali section yielded samples with AFT ages older than the stratigraphic age and increasing downsection, characteristic of unreset samples. Deeper samples, in contrast, have an increasing proportion of single-grain AFT ages younger than the stratigraphic age and ages decrease downsection, characteristic of partly annealed samples (Figure 1). The transition between the two (i.e., the top of the pre-exhumation Partial Annealing Zone) occurs at ~2500 m depth, indicating a pre-exhumational geothermal gradient of 15-20°C within the basin, in accord with vitrinite reflectance data and heat flow measurements in Ganges basin wells. The annealed AFT samples from the lower part of the Karnali section have a consistent minimum age (i.e., youngest age population) peak of 2 Ma, suggesting that the onset of exhumation of this part of the Siwaliks along the Main Frontal Thrust took place at this time.

Mean confined track lengths vary from ~12 µm in unannealed samples to <10 µm in the deepest and most strongly annealed samples. We inverse the track-length data to further constrain the thermal history of the samples using the AFTSolve package (Ketcham et al. 2000) that allows incorporating kinetic data (Figure 2). Best-fit thermal histories show initial heating of the sediments related to burial within the foreland basin, followed by a phase of constant temperatures during a period of up to 5 My and extremely rapid cooling of the sediments since <1 Ma, which we interpret as being due to exhumation along the MFT. Predicted peak temperatures are between 80-110°C for all samples, suggesting a strongly non-linear geothermal gradient, possibly due to heat advection by fluids within the basin. The results also clearly show that the mean and minimal thermochronological ages of partially annealed samples are not simply related to a specific tectonic event.

Finally, we confront these inverse model results with predictions of a forward numerical tectono-thermal model using the IFP (Institut Français du Pétrole) Thruspack Package. From a reconstructed initial basin geometry and a tectonic scenario we calculate thermal histories for the rocks along the Karnali River section and use these to predict the corresponding apatite fission track ages and length distribution using AFTSolve. Taking into account all available constraints, our best-fit models suggest that initiation of the MFT took place after 2 Ma with an important recent shortening around 20 $mm.yr^{-1}$ from 0.3-0.1 Ma to today. The activity of MFT cannot have been homogenous through time; it has either accelerated recently or activity has been discontinuous through the last 2 My.

Keywords: orogenic prism, Himalaya, Siwaliks, Main Frontal Thrust, fold and thrust belt, thermal gradient, thermochronology, apatite fission tracks, numerical modelling, time - temperature paths

References:

Barbarand, J., Carter, A., Wood, I. & Hurford, A. 2003. Compositional and structural control of fission-track annealing in apatite. *Chemical Geology* **198**, 107-137.

Burbank, D. W. 1992. Causes of recent Himalayan uplift deduced from deposited patterns in the Ganges basin. *Nature* **357**, 680-683.

Carlson, W. D., Donelick, R. A. & Ketcham, R. A. 1999. Variability of apatite fission-track annealing kinetics: I. Experimental results. *American Mineralogist* **84**, 1213-1223.

Carter, A. & Gallagher, K. 2004. Characterizing the significance of provenance on the inference of thermal history models from apatite fission-track data - a synthetic data study. In: *Detrital thermochronology - Provenance analysis, exhumation and landscape evolution of mountain belts* (edited by Bernet, M. & Spiegel, C.). Geological Society of America Special Paper **378**, 7-24.

Cederbom, C., Sinclair, H., Schlunegger, F. & Rahn, M. 2004. Climate-induced rebound and exhumation of the European Alps. *Geology* **32**, 709-712.

Gallagher, K., Brown, R. & Johnson, C. 1998. Fission track analysis and its applications to geological problems. *Annual Review of Earth and Planetary Sciences* **26**, 519-572.

Gautam, P. & Fujiwara, Y. 2000. Magnetic polarity stratigraphy of Siwalik Group sediments of Karnali River section in western Nepal. *Geophysical Journal International* **142**, 812-824.

Harrison, T. M., Copeland, P., Hall, S. A., Quade, J., Burner, S., Ojha, T. P. & Kidd, W. S. F. 1993. Isotopic preservation of Himalayan/Tibetan uplift, denudation, and climatic histories in two molasse deposits. *Journal of Geology* **100**, 157-173.

Ketcham, R. A., Donelick, R. A. & Donelick, M. B. 2000. AFTSolve: A program for multi-kinetic modeling of apatite fission-track data. *Geological Materials Research* **2**(1) http://gmr.minsocam.org/Papers/v2/v2n1/v2n1abs.html.

Rohrman, M., Andriessen, P. A. M. & van der Beek, P. A. 1996. The relationship between basin and margin thermal evolution assessed by fission track thermochronology: an application to offshore southern Norway. *Basin Research* **8**, 45-63.

Van der Beek, P., Bernet, M., Pik, R., Huyghe, P., Mugnier, J.L. and Labrin, E. 2005. Orogenic exhumation of the central Himalaya recorded by detrital fission-track thermochronology of Siwalik sediments, Nepal. *This meeting*.

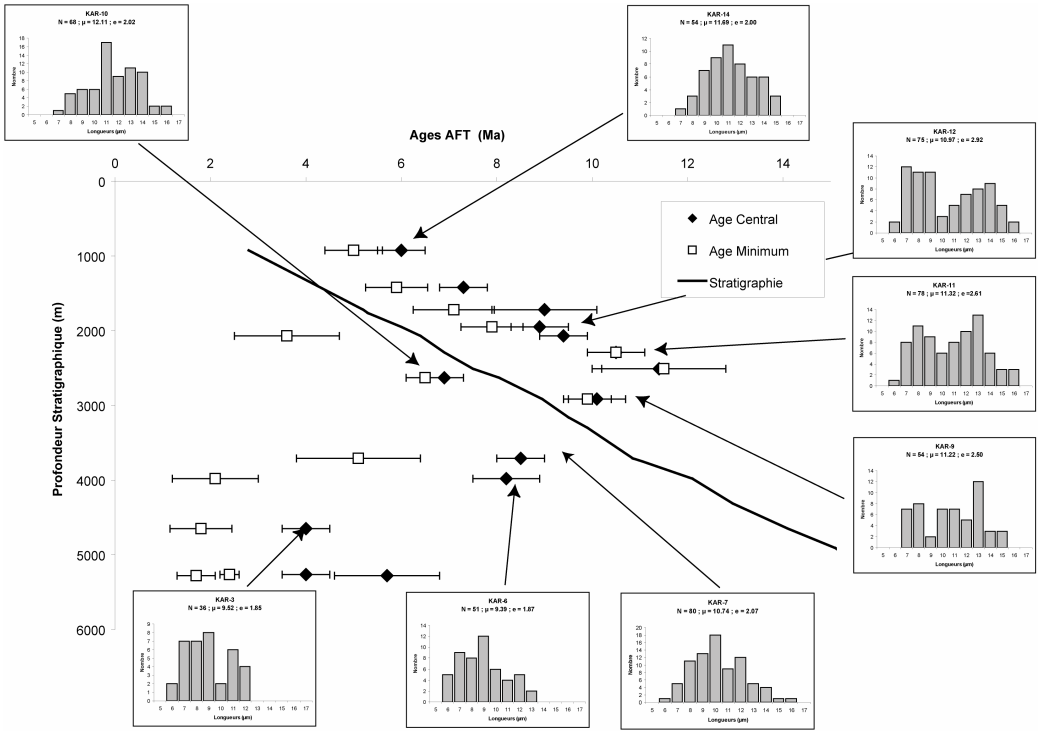

Figure 1. *Stratigraphic ages (thick continuous line), central (black diamonds) and minimum (white squares) AFT ages, and confined AFT length distributions for samples collected along the Karnali River section (μ is the mean confined track length and e the standard deviation). Note (1) the switch from unannealed to partially annealed samples at ~2500 m depth; (2) the consistent 2 Ma minimum age in the lowermost 4 samples, and (3) the decrease in mean track length downsection.*

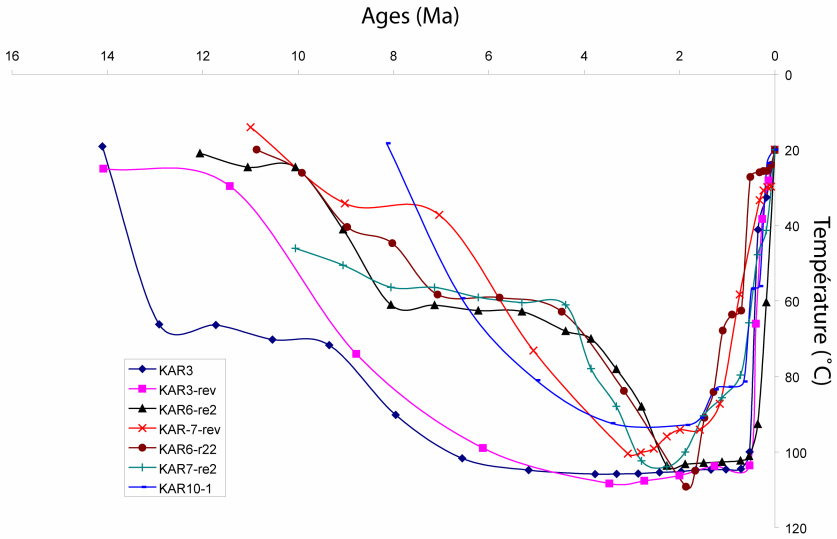

Figure 2. *Synthesis of the best-fitting thermal histories for the different samples from the Karnali River from inversion of thermochronological data using AFTSolve (Ketcham et al. 2000); thermal histories are cut off at the depositional age for readability, even though the complete history since initial exhumation in the source area was modelled for each sample. Note the extremely rapid recent cooling recorded by all samples and the small range of maximum temperatures attained.*

A.4.2 ModOSUG 2006

Couplage de modèles mécaniques, thermiques et érosifs

X. Robert, P. Van der Beek, J.-L. Mugnier, J. Braun

Mercredi 27 septembre 2006

Il est connu que les paysages sont fortement façonnés par un forçage tectonique, mais aussi par une interaction avec les phénomènes érosifs (Beaumont et al., 1992; Kooi and Beaumont, 1996). Ce couplage est difficilement quantifiable, ce qui nous a poussé à modéliser différents types de couplages Tectonique - Erosion. Pour contraindre nos modèles, nous reproduisons des marqueurs thermochronologiques issus de données de terrain, ce qui nous oblige à coupler nos modèles d'évolution à un modèle thermique.

Ici, nous présentons 3 études, une complète, et deux en cours de développement. La première (finalisée) consiste en une modélisation d'un rebond isostatique dans une zone montagneuse sans composante d'advection horizontale (Dabie Shan, Nord - Est de la Chine, Braun and Robert (2005)), la seconde en une modélisation du front d'un jeune bassin flexural (Karnali River, Siwaliks, Ouest du Népal), et la dernière en une modélisation du fonctionnement d'un chevauchement au sein d'un orogène (Main Central Thrust, Népal central).

References

C. Beaumont, P. Fullsack, and J. Hamilton. Erosional control of active compressional orogens. In *Thrust Tectonics*, pages 1–18, New York, 1992.

J. Braun and X. Robert. Constraints on the rate of post-orogenic erosional decay from low temperature thermochronological data: application to the Dabie Shan, China. *Earth Surface Processes and Landforms*, 30:1203–1225, 2005.

H. Kooi and C. Beaumont. Large-scale geomorphology: classical concepts reconsiled and integrated with contemporary ideas via a surface process model. *Journal of Geophysical Research*, 101: 3361–3386, 1996.

A.4.3 EGU 2006

Thermochronological analysis of Siwalik sediments from the Karnali River section (western Nepal): Constraints on the kinematics of the frontal Himalayan prism.

X. Robert (1), P. Van der Beek (1), J.-L. Mugnier (1), E. Labrin (1)

(1) Laboratoire de Géodynamique des Chaînes Alpines, UJF, Grenoble, France ; (xavier.robert@ujf-grenoble.fr)

We study the dynamics of the Miocene-Recent Siwalik accretionary prism of the Himalayan orogen with the specific goal of quantifying the onset of activity as well as the deformation history recorded by the Main Frontal Thrust (MFT), the active frontal thrust of the system. We report new detrital apatite fission-track data from Miocene to Pliocene Siwalik Group sediments along the magneto-stratigraphically controlled Karnali River section in western Nepal. We also measure confined fission track lengths to constrain the thermal history, as well as etch-pit width measurements to provide a kinetic proxy (e.g., Carlson et al., 1999; Barbarand et al., 2003). The upper part of the section yielded samples with AFT ages older than the stratigraphic age and increasing downsection (unreset samples). Deeper samples have an increasing proportion of single-grain AFT ages younger than the stratigraphic age and ages decrease downsection (partly annealed samples). The top of the pre-exhumation Partial Annealing Zone occurs at ˜2500 m depth, indicating a pre-exhumational geothermal gradient of 15-20°C, in accord with vitrinite reflectance data and heat flow measurements in Ganges basin wells. The annealed AFT samples from the lower part of the section have a consistent minimum age peak of 2 Ma, suggesting that onset of exhumation along the MFT took place at this time.

Mean confined track lengths decreased with depth. Inversions of track-length data show initial heating of the sediments related to burial, followed by a phase of constant temperatures during a period of up to 5 My and extremely rapid cooling of the sediments since $<$1 Ma, which we interpret as being due to exhumation along the

MFT. Predicted peak temperatures are between 80-110°C for all samples, suggesting a strongly non-linear geothermal gradient. The results also clearly show that the mean and minimum thermochronological ages of partially annealed samples are not simply related to a specific tectonic event.

Finally, from a reconstructed initial basin geometry and a tectonic scenario, we calculate, using the Thrustpack Package, thermal histories for the rocks along the Karnali River section and thus predict the corresponding apatite fission track ages and length distributions. Our best-fit models suggest that initiation of the MFT took place after 2 Ma with an important recent shortening around 20 mm/yr from 0.3-0.1 Ma to today. The activity of MFT cannot have been homogenous through time; it has either accelerated recently or activity has been discontinuous through the last 2 My.

A.4.4 EGU 2007

Constraints on recent Lesser Himalayan deformation from new apatite fission-track data along a North - South transect (Central Nepal).

X. Robert (1), P. Van der Beek (1), J.-L. Mugnier (1), J. Braun (2), B. Mucecku (1)

(1) Laboratoire de Géodynamique des Chaînes Alpines, UJF, Grenoble, France ; (xavier.robert@ujf-grenoble.fr), (2) Geosciences Rennes, Université de Rennes1, Rennes, France

We study the recent dynamics of the Himalayan orogen in central Nepal with the specific goal of quantifying the onset of activity as well as the deformation history recorded by the different thrusts. Here, we focus on the possible reactivation of the footwall of the MCT, which is marked by a strong topographic transition in the Nepalese Himalaya. We report 14 new apatite fission-track (AFT) ages collected along the Trisuli river and through the Palung granite (Langtang to Terail North - South transect).

The topographic transition corresponds to an AFT age transition, with very young ages to the north (<1.5 Ma), and much older ages to the south (up to 10 Ma). This transition is too sharp to be interprated as a simple consequence of erosion. Therefore, other mechanisms, such as out of sequence thrusting (Hodges et al., 2004) or underplating over a major crustal ramp (Bollinger et al., 2006) have to be considered. We perform numerical thermal-kinematic modelling, using a modified version of the PECUBE code (e.g. Braun, 2002), to quantify the respective roles of underplating and out-of-sequence thrusting in the shortening of this part of the Himalayan range. In these initial models, we assume a simple steady-state between tectonic accretion and surface erosion. Future model will incorporate physical erosion laws to study potential transient effects.

A.4.5 AGU 2007

Can we Detect Recent Activation of the Main Central Thrust Zone from Apatite Fission Track Data and Numerical Modelling?

X. Robert (1), P. Van der Beek (1), J. Braun (2), J.-L. Mugnier (1), B. Muceku (1)

(1) Laboratoire de Géodynamique des Chaînes Alpines, UJF, Grenoble, France ; (xavier.robert@ujf-grenoble.fr), (2) Geosciences Rennes, Université de Rennes1, Rennes, France

We study the recent dynamics of the Himalayan orogen in central Nepal with the specific goal of quantifying the onset of activity and the deformation history recorded by the different major thrusts. Here, we focus on the possible reactivation of the footwall of the MCT, which is marked by a strong topographic transition in the Nepal Himalaya. This transition is too sharp to be interpreted as a simple consequence of erosion and tectonic mechanisms, such as out of sequence thrusting (Hodges et al., 2004) or underplating over a major crustal ramp (Bollinger et al., 2006) have been suggested.

We report 14 new apatite fission-track (AFT) ages collected along a north – south transect from Langtang in the High Himalaya to the Terai Plain. AFT ages are consistently young ($<$ $3 \ My$) all along the N-S transect in the MCT zone and older (4 to $6 \ My$) in the southern part of the Lesser Himalaya. The topographic transition does not correspond to a sharp AFT age transition.

We perform numerical thermal-kinematic modelling, using a modified version of the PECUBE code (e.g. Braun, 2002), to quantify the respective roles of underplating and out-of-sequence thrusting in the shortening of this part of the Himalayan range. In these initial models, we assume steady state between tectonic accretion and surface erosion. The current dataset cannot discriminate the two models: although out-of-sequence thrusting and reactivation of the MCT shear zone are consistent with the data, they do not require such a mechanism. The presence of a crustal ramp below the topographic transition exerts the primary control on age patterns. Therefore, the question of possible out-of-sequence reactivation appears secondary in face of the current data set.

A.4.6 EGU 2008

Geophysical Research Abstracts,
Vol. 10, EGU2008-A-04728, 2008
SRef-ID: 1607-7962/gra/EGU2008-A-04728
EGU General Assembly 2008

Recent Kinematics and long-term Exhumation History of the central Himalaya (Nepal) from numerical Modelling of *in-situ* and detrital Thermochronology Data

P.A. van der Beek (1), X. Robert (1), H.K.C. Perry (1,2), J. Braun (2), M. Bernet (1)

(1) LGCA, Université Joseph Fourier, Grenoble, France, (2) Géosciences Rennes, Université Rennes I, Rennes, France (pvdbeek@ujf-grenoble.fr / Fax : +33 476 514058 / Phone : +33 476 514062)

Unravelling the kinematics and exhumation history of the Himalaya, the largest mountain belt on Earth and the largest provider of sediments to the world's oceans, has important implications for our understanding of mountain building processes, the interaction between tectonics, climate and erosion, as well as seismic risk assessment. We explore the capacity of thermochronological data to quantitatively constrain the kinematics of the central Himalaya at two different time scales: we use a transect of newly acquired *in-situ* apatite fission-track (AFT) ages across the central Nepal Himalaya to place constraints on the kinematics of the mountain belt over the last few million years, and we extract the kinematic and exhumation history of the belt since $\sim$20 Ma from a dataset of detrital zircon fission-track (ZFT) and mica Ar-Ar (MAR) thermochronology collected within the orogenic Siwalik deposits of central and western Nepal. To do so, we employ a newly developed 3-D thermal-kinematic model, based on the *Pecube* code, which allows the prediction of thermal histories and thermochronological ages for rocks exhumed along crustal-scale faults of any geometry. The model tracks the distribution of thermochronological ages at the surface throughout the model run, thus allowing comparison with both the *in-situ* and the detrital thermochronological record.

The central Himalaya underwent a major transition at $\sim$15-20 Ma, from an Early

Miocene phase characterised by localised exhumation in the Higher Himalayan crystalline belt along the Main Central Thrust (MCT) to a steady-state forward-propagating system in the Late Miocene-Pliocene. Detrital thermochronology records this transition as a major phase of exhumation; a significant proportion of both detrital ZFT and MAR single-grain ages falling within this age range throughout the stratigraphic sections. Our modelling of the detrital data aims at understanding this phase of rapid exhumation and the associated controls (climatic, tectonic?) on the change in kinematics. In recent years, controversy has arisen about the recent kinematics of the central Himalaya, with some authors arguing for Plio-Pleistocene reactivation of the MCT, possibly driven by climatically enhanced exhumation of the Himalayan topographic front. AFT ages increase linearly from $\leq$ 1 Ma in the MCT zone to 5-10 Ma in the outermost part of the Lesser Himalaya, without any sharp transition. Fitting the observed AFT-age pattern, using our themal-kinematic model with exhumation occurring simultaneously along several thrust faults, requires only minimal, if any, reactivation of the MCT.

A.4.7 AGU 2008

AGU 2008

How cylindrical is the Main Himalayan Thrust? Insights from low – temperature thermochronology and numerical modelling

X. Robert (1), P. van der Beek (1), J. Braun (2), J.-L. Mugnier (1)

(1) Laboratoire de Géodynamique des Chaînes Alpines, UJF, Grenoble, France ; (xavier.robert@ujf-grenoble.fr), (2) Geosciences Rennes, Université de Rennes1, Rennes, France

We study the recent dynamics of the Himalayan orogen in central Nepal with the specific goal of quantifying the onset of activity and the deformation history recorded by the different major thrusts along the Himalayan range, and propose a structural and kinematic model of the major crustal Himalayan thrust, the MHT. We report 27 new apatite fission-track (AFT) ages collected along north – south transects in western and eastern – central Nepal (Kali Gandaki and Trisuli Rivers). AFT ages are consistently young ($<$ $3 \ My$) along both N-S transects in the MCT zone and increase (4 to $6 \ My$) toward the south in the Lesser Himalaya. We present and compare 2 age – elevation transects, one in the MCT zone and one in the outer Lesser Himalaya, and interpret them in terms of exhumation rate that we use to constrain the geometry of the MHT ramp.

The Himalayan range is commonly presented as a cylindrical structure from west to east. However, geological structures, topography, precipitation rate, convergence rates and low – temperature thermochronological ages all vary significantly along strike. Here, we focus on the interpretation of thermochronological datasets in term of cylindricity in geometry and kinematics of the MHT along the Himalayan range.

We compare our new data to published low-temperature thermochronological datasets for western – central Nepal, eastern – central Nepal and the Bhutan Himalaya. We use these data to perform numerical thermal-kinematic modelling with a modified version of the PECUBE code, in order to constrain potential along-strike variations in the kinematics of the Himalayan range. Our results show that lateral variations in geometry of the MHT (in particular the presence or absence of a major ramp) strongly control the kinematics and exhumation history of the orogen.

Table des figures

Séquence d'activité des failles et dynamique du prisme himalayen : apports de la thermochronologie et de la modélisation numérique

L'influence de l'érosion sur la localisation de la déformation dans une chaîne de montagnes est un phénomène souvent envisagé à la suite de modélisations numériques. Or les données géologiques pertinentes en faveur de cette hypothèse sont encore fort peu nombreuses. Aussi, la mise en évidence d'une évolution temporelle et spatiale de la déformation constitue une observable clef pour tester les relations érosion/localisation de la déformation. Nous testons cet effet, sur un objet géologique soumis à des conditions de déplacements aux limites simples et sur un objet géologique soumis à des conditions climatiques et érosives variables latéralement : le flanc sud de l'Himalaya (située au dessus d'un décollement crustal majeur). Elle est soumise à une convergence continue et de valeur constante depuis au moins une dizaine de millions d'années et sa rhéologie est invariante au cours du temps ; elle est en revanche soumise à un gradient climatique d'est en ouest (transversalement par rapport à la direction de convergence), gradient de plus variable au cours du temps. Nous avons mis en oeuvre des techniques de thermochronologie basse température pour constituer une base de données conséquente, que nous avons utilisée dans des modélisations numériques thermo-cinématiques directes et inverses. Nous montrons que 1) au Népal central,le MHT présente une rampe crustale prononcée, et aucun mécanisme de chevauchement en hors-séquence n'est nécessaire pour expliquer les données, 2) la géométrie du MHT varie d'est en ouest, avec une rampe moins prononcée dans l'est de la chaîne, et 3) les variations latérales en terme de mise en place et de cinétique du MFT sont peu importantes.

Mots-clés *prisme orogénique, Himalaya, Main Frontal Thrust, Main Central Thrust, système chevauchant, gradient thermique, thermochronologie, traces de fission sur apatites, modélisation numérique, chemins temps - température*

Fault activity and timing of the himalayan prism : Constraints from thermochronology and numerical modeling

The influence of erosion on the location of deformation in mountain ranges has been demonstrated by numerical modelling. However, few relevant geological data in favour of this hypothesis exist. Thus, demonstrating a temporal or spatial evolution of the deformation/kinetics in the frontal units of the Himalayan range would provide a key observation to test the interactions between erosion and the location of the tectonic deformation at the scale of a mountain belt. We test this effect by the acquisition of low-temperature thermochronological data (apatite fission-track) and forward and inverse thermo-kinematic numerical modelling. The southern flank of the Himalaya, situated above a major crustal detachment, is well adapted to test the interactions between erosion and tectonics because it is submitted to convergence that is spatially continuous and homogeneous through time, and its rheology is invariable through time. However, it is submitted to a climatic gradient from east to west, perpendicular to the convergence direction. This gradient is moreover variable through time. We show that 1) in central Nepal, there is a well-expressed crustal ramp on the Main Himalayan Thrust (MHT) below the physiographic transition, out-of-sequence thrusting is not required by the data, 2) the geometry of the MHT varies from east to west, from a linearly dipping detachment to a well-expressed crustal ramp, and 3) the lateral variations of the kinetics or the initiation of the Main Frontal thrust are limited at the scale of the entire orogen.

Keywords *orogenic prism, Himalaya, Siwaliks, Main Frontal Thrust, Main Central Thrust, fold and thrust belt, thermal gradient, thermochronology, apatite fission tracks, numerical modelling, time - temperature paths*